204
3-9

applied

DWR #3

GEAP-10580-2
AEC RESEARCH AND DEVELOPMENT REPORT
JUNE 1972

20625

SODIUM-HEATED STEAM GENERATOR MODEL TESTS AT SGTR VOLUME 2

A. HUNSBEDT

PREPARED FOR THE
U. S. ATOMIC ENERGY COMMISSION
CONTRACT AT(04-3)-189 PROJECT AGREEMENT 61

MASTER

GENERAL ELECTRIC

DISTRIBUTION OF THIS DOCUMENT IS UNLIMITED

DISCLAIMER

This report was prepared as an account of work sponsored by an agency of the United States Government. Neither the United States Government nor any agency Thereof, nor any of their employees, makes any warranty, express or implied, or assumes any legal liability or responsibility for the accuracy, completeness, or usefulness of any information, apparatus, product, or process disclosed, or represents that its use would not infringe privately owned rights. Reference herein to any specific commercial product, process, or service by trade name, trademark, manufacturer, or otherwise does not necessarily constitute or imply its endorsement, recommendation, or favoring by the United States Government or any agency thereof. The views and opinions of authors expressed herein do not necessarily state or reflect those of the United States Government or any agency thereof.

DISCLAIMER

Portions of this document may be illegible in electronic image products. Images are produced from the best available original document.

NOTICE
This report was prepared as an account of work sponsored by the United States Government. Neither the United States nor the United States Atomic Energy Commission, nor any of their employees, nor any of their contractors, subcontractors, or their employees, makes any warranty, express or implied, or assumes any legal liability or responsibility for the accuracy, completeness or usefulness of any information, apparatus, product or process disclosed, or represents that its use would not infringe privately owned rights.

GEAP-10580-2
UC-79k
Volume 2
AEC Research and
Development Report
June 1972

SODIUM-HEATED STEAM GENERATOR MODEL TESTS AT SGTR
VOLUME 2
THERMAL-HYDRAULIC PERFORMANCE DATA AND ANALYSIS

A. Hunsbedt

Approved: F. E. Tippets, Manager
Heat Transfer Equipment Systems

Approved: L. F. Fidrych, Manager
Breeder Reactor Plant Engineering

Approved: J. M. Case
Program Manager

The work described herein was performed under and financed by ESADA FCR Component Development Program, by Foster Wheeler and General Electric Programs, and by the USAEC under Task C, PA-61, Contract AT(04-3)-189.

Prepared for the
United States Atomic Energy Commission
Contract AT(04-3)-189
Project Agreement No. 61

BREEDER REACTOR DEPARTMENT • GENERAL ELECTRIC COMPANY
SUNNYVALE, CALIFORNIA 94086

190p/275c/CDT
MKS/11-72

GENERAL ELECTRIC

MASTER

DISTRIBUTION OF THIS DOCUMENT IS UNLIMITED

FOREWORD

The work described in this report (Volume 2) covers the thermal-hydraulic performance data and analysis of the sodium-heated steam generator model tests at the Steam Generator Test Rig (SGTR). This work was initiated as part of the 300 MWe Fast Ceramic Reactor Component Development Program sponsored by the Empire State Atomic Development Associates, Incorporated (ESADA); the preparation of this report was financed by the USAEC under Task C of PA-61, LMFBR Steam Generator System Development. A companion report (Volume 1) covers the operational experience and the final inspection and disassembly of the test models.

NOTICE

This report was prepared as an account of work sponsored by the United States Government. Neither the United States nor the United States Atomic Energy Commission, nor any of their employees, nor any of their contractors, subcontractors, or their employees, makes any warranty, express or implied, or assumes any legal liability or responsibility for the accuracy, completeness or usefulness of any information, apparatus, product or process disclosed, or represents that its use would not infringe privately owned rights.

TABLE OF CONTENTS

ABSTRACT **1-1**

1. SUMMARY **1-1**
1.1 Heat Transfer Performance 1-1
1.2 Sodium Temperature Distributions 1-2
1.3 Departure from Nucleate Boiling 1-3
1.4 Steam-Side Stability 1-3
1.5 Sodium-Side Stability 1-3
1.6 Tube Thermal Conductivity 1-4

2. INTRODUCTION **2-1**
2.1 LMFBR Steam Generators 2-1
2.2 Development Program 2-1
2.3 Program Sponsors 2-1
2.4 Test Objectives and Data Obtained 2-1

3. BACKGROUND INFORMATION **3-1**
3.1 Sodium-Side Heat Transfer and Pressure Drops 3-1
3.2 Steam-Side Heat Transfer and Pressure Drops 3-1
3.3 Departure from Nucleate Boiling (DNB) in the Evaporator 3-4
3.4 Heater Tube Wall Thermal Conductivity 3-7

4. TEST APPARATUS **4-1**
4.1 Sodium-Heated Steam Generator Test Rig (SGTR) 4-1
4.2 Evaporator Test Section 4-1
4.3 Superheater Test Section 4-9
4.4 Auxiliary Equipment 4-12
4.5 Data Acquisition 4-16
4.6 Instrumentation and Calibration 4-16
4.7 Test Procedure 4-22

5. EVAPORATOR THERMAL PERFORMANCE **5-1**
5.1 Heat Transfer Performance 5-1
5.2 Determination of Sodium Bypass Flow in the Evaporator 5-12
5.3 Departure from Nucleate Boiling Measurements 5-14
5.4 Heat Transfer Performance Beyond DNB 5-26
5.5 Steam-Side Flow Distribution 5-41
5.6 Pressure Drops 5-43

6. SUPERHEATER THERMAL PERFORMANCE **6-1**
6.1 Heat Transfer Performance 6-1
6.2 Steam-Side Flow and Temperature Distribution in the Superheater 6-5
6.3 Pressure Drops 6-6

7. SYSTEM STABILITY **7-1**
7.1 Sodium-Side Stability 7-1
7.2 Steam-Side Stability 7-18

ACKNOWLEDGMENTS **R-1**

REFERENCES **R-1**

TABLE OF CONTENTS (Continued)

APPENDIXES

A. DATA REDUCTION CODES **A-1**
A-1 Summary Description of EVAP Code A-1
A-2 Summary Description of Super Code A-3

B. EXPERIMENTAL DATA **B-1**
B-1 Evaporator Performance Data B-1
B-2 Superheater Performance Data B-21
B-3 Steam-Side Stability Data B-25

C. ANALYSIS **C-1**
C-1 Tube Wall Transient Analysis C-1
C-2 Single Tube Stability Analysis C-3
C-3 DNB Correlation Factor C-4

DISTRIBUTION **D-1**

LIST OF ILLUSTRATIONS

Figure		Page
3-1	Schematic Diagram of the Bayonet Tube Assembly Used as the Basic Heat Transfer Device in the SGTR Evaporator Model	3-2
3-2	Schematic Diagram of a Portion of the Bayonet Tube Assembly Showing Swirl Generator Device	3-3
3-3	Diagram Illustrating Transition Boiling Heat Transfer Dependence on Steam Quality or Axial Position for a Constant Heat Flux System	3-6
3-4	Schematic Diagram Showing the Similarities between Flows in the Annular Swirl Flow Geometry and the Coiled Tube Geometry	3-8
3-5	Comparison of Tube inside Wall Temperature Behavior in the Transition Boiling Regime for a Straight Vertical Tube and a Coiled Tube, Both with Constant Heat Flux (Modified Form of Figure 24 In Reference 32)	3-9
3-6	Comparison of Available Thermal Conductivity Data for the Heater Tube Reference 2-1/4 Cr — 1 Mo Alloy (T-22)	3-10
4-1	Schematic Diagram of the 2000 kWt Sodium-Heated Steam Generator Test Rig (SGTR)	4-2
4-2	Flow Diagram of the Steam Generator Test Rig	4-3
4-3	Steam Generator Test Rig—Instrument Connection Details	4-4
4-4	View of the Upper Portion of the Steam Generator Test Rig with the Foster Wheeler Evaporator Model in the Background	4-5
4-5	View from below the Steam Generator Test Rig Showing the Foster Wheeler Superheater Model and Connecting Piping	4-6
4-6	Evaporator Test Section—Details (Courtesy Foster Wheeler Corporation)	4-7
4-7	Details of Evaporator Near Sodium Inlet Nozzle (Courtesy Foster Wheeler Corporation)	4-8
4-8	Details of the Insulated Bayonet Tube Design Used with the P/D = 3 Swirl Generator Insert	4-10
4-9	Schematic Diagram of Evaporator Tube Support	4-11
4-10	Internal Arrangement of Superheater Test Section (Courtesy Foster Wheeler Corporation)	4-13
4-11	Coiled-Tube Superheater Test Section Bundle During Assembly (Courtesy Foster Wheeler Corporation)	4-14

LIST OF ILLUSTRATIONS (Continued)

Figure		Page
4-12	Upper Portion of Tube Bundle for Coiled-Tube Superheater Test Section (Courtesy Foster Wheeler Corporation)	4-15
4-13	Diagram Showing Positions of Evaporator Test-Section Thermocouples	4-17
4-14	Diagram Showing Positions of Superheater Test Section Thermocouples	4-18
4-15	Details of Departure from Nucleate Boiling Thermocouples (Courtesy Foster Wheeler Corporation)	4-19
4-16	View of the Evaporator Test Section Tube Bundle with the DNB and Sodium Thermocouples Attached (Courtesy Foster Wheeler Corporation)	4-20
5-1	Comparison of Measured Axial Sodium Temperature Profiles for the Evaporator at Approximately 1500 kWt	5-3
5-2	Comparison of Measured Axial Sodium Temperature Profiles and Analytic Profiles for the Evaporator at Approximately 750 kWt	5-4
5-3	Schematic Diagram of a Typical Cross-Section in the Evaporator Test Section	5-5
5-4	Schematic Diagram of Thermocouple Measurements Used to Calculate the Log Mean Temperature Difference and the Overall Heat Transfer Coefficient	5-7
5-5	Wilson-Plot of the Average Sodium Side Heat Transfer Coefficient Deduced from Measurements in the Boiling Region of the Evaporator	5-11
5-6	Comparison of Measured Sodium Side Nusselt Number to Existing Correlations	5-13
5-7	Measured Axial Sodium Temperature Profiles in the Bypass Channel Compared to Analytic Predictions with Various Bypass Flow Rates	5-15
5-8	Schematic Diagram of the Double Wall Section of the Bayonet Tubes Used with the P/D = 3 Swirl Generator Insert and Corresponding Temperature Profiles	5-16
5-9	Measured Overall Heat Transfer Coefficients of the Insulated (Double Wall) Bayonet Tubes versus the Log Mean Temperature	5-18
5-10	Details of Departure from Nucleate Boiling Thermocouple Locations Relative to Swirl Generator	5-20
5-11	Typical Sanborn Tracees of the DNB Thermocouples during a DNB Run with the P/D = 6 Insert	5-21
5-12	Typical Sanborn Traces of the DNB Thermocouples during a DNB Run with the P/D = 3 Insert	5-22
5-13	Schematic Diagram of Assumed Relationship between Recirculation Flow Rate and the Average Temperature Rise of the Heater Tube in the DNB Criterion	5-23

LIST OF ILLUSTRATIONS (Continued)

Figure		Page
5-14	Critical Heat Flux with Correlation Factor Applied versus Local Steam Quality for the SGTR Bayonet Tube Evaporator Test Model with the P/D = 6 and P/D = 3 Swirl Generator Inserts	5-25
5-15	Phase Distribution of Air/Water Mixture in Annular Swirl Flow Geometry at Approximately 82 Percent Quality (Photograph Courtesy General Electric Missile and Space Division, Cincinnati, Ohio)	5-27
5-16	Phase Distribution of Air/Water Mixture in Annular Swirl Flow Geometry at Approximately 92 Percent Quality Showing the Presence of Rivulets (Photograph Courtesy of General Electric Missile and Space Division, Cincinnati, Ohio)	5-28
5-17	Phase Distribution of Air/Water Mixture in Annular Swirl Flow Geometry at Approximately 95 Percent Quality Showing Water Flow along the Center Body (Photograph Courtesy of General Electric Missile and Space Division, Cincinnati, Ohio)	5-29
5-18	Diagram of Bayonet Tube at the DNB Thermocouples	5-30
5-19	Local Steam Side Heater Tube Heat Transfer Coefficient at the Upper DNB Thermocouple Location versus Local Steam Quality for Both the P/D = 6 and P/D = 3 Swirl Generator Inserts	5-33
5-20	Inside Heater Tube Wall Temperature at the Upper DNB Thermocouple Location versus Local Steam Quality for Both the P/D = 6 and P/D = 3 Swirl Generator Inserts	5-35
5-21	Theoretical Maximum Heater Tube Wall Temperature Fluctuation versus Frequency at an Angular Location of 90° away from the Swirl Generator for the Total Steam Side Surface Subjected to Various Periodic Cycling of the Steam Side Heat Transfer Coefficient	5-37
5-22	Sanborn Traces of the DNB Thermocouples during a DNB Run with P/D = 6 Swirl Generator Insert	5-38
5-23	Comparison of Theoretical Maximum Heater Tube Wall Temperature Fluctuations Compared to Measured Wall Temperature Fluctuations	5-40
5-24	Diagram of Orifices Installed on the Bayonet Tubes and Used to Measure the Steam Side Flow Distributions with the P/D = 6 Inserts	5-42
5-25	Sanborn Trace of Pressure Drops Across the Bayonet Tube Orifices with the P/D = 6 Insert	5-43
5-26	Comparison of Predicted Sodium Side Friction Pressure Drop to Measured Friction Pressure Drop for the Evaporator versus the Sodium Average Peclet Number	5-45

LIST OF ILLUSTRATIONS (Continued)

Figure		Page
5-27	Comparison of Predicted Total Steam Side Friction Pressure Drop to Measured Friction Pressure Drop for the Evaporator versus the Bayonet Tube Reynolds Number and for Exit Steam Qualities in the Range of Approximately 30 - 94 Percent	5-46
6-1	Comparison of Measured and Calculated Axial Sodium Temperature Profile in Segment No. 2 of the Superheateer	6-2
6-2	Comparison of Experimental and Analytic Circumferential Sodium Temperature Variations near the Lower End of the Coiled Section in the Superheater	6-3
6-3	Comparison of Measured and Predicted Steam Side Pressure Drop in the Superheater	6-9
7-1	Schematic Diagram of Sodium System	7-2
7-2	Sanborn Traces of Sodium Flow and Level Variations in the SGTR at Isothermal Conditions and Sodium Flow Rate of 205 gpm, Superheater and Evaporator on Line	7-3
7-3	Sanborn Traces of Sodium Flow and Level Variations in the SGTR at Isothermal Conditions and Sodium Flow Rate of 205 gpm, Superheater and Evaporator on Line	7-4
7-4	Sanborn Traces of Sodium Flow and Level Variations in the SGTR at Non-Isothermal Conditions and Sodium Flow Rate of 120 gpm, Superheater and Evaporator on Line	7-5
7-5	Sanborn Traces of Sodium Flow and Level Variations in the SGTR at Isothermal Conditions and Sodium Flow Rate of 34 gpm, Superheater and Evaporator on Line	7-6
7-6	Sanborn Traces of Sodium Flow and Level Variations in the SGTR at Isothermal Conditions and Sodium Flow Rate of 205 gpm, Superheater Isolated, Evaporator on Line	7-8
7-7	Sanborn Traces of Sodium Flow and Level Variations in the SGTR at Isothermal Conditions and Sodium Flow Rate of 34 gpm, Superheater Isolated, Evaporator on Line	7-9
7-8	Sanborn Traces of Sodium Flow and Level Variations in the SGTR at Isothermal Conditions and Sodium Flow Rate of 180 gpm, Superheater on Line, Evaporator Isolated	7-11
7-9	Sanborn Traces of Sodium Flow and Level Variations in the SGTR at Isothermal Conditions and Sodium Flow Rate of 170 gpm, Superheater on Line, Evaporator Isolated	7-12
7-10	Sanborn Traces of Flow and level Variations in the SGTR at Isothermal Conditions and Sodium Flow Rates of 190 and 68 gpm, Superheater and Evaporator Isolated	7-13

LIST OF ILLUSTRATIONS (Continued)

Figure		Page
7-11	Sanborn Traces of Sodium Flow and Level Variations in the SGTR at Isothermal Conditions and Showing Effect of Introducing Flow Resistance in the Line between the Superheater and Evaporator Test Sections, Sodium Flow Rate 175 gpm	7-14
7-12	Sanborn Traces of Sodium Flow and Level Variations in the SGTR at Isothermal Conditions Showing Effect of Introducing Flow Resistance in the Line between the Superheater and Evaporator Test Sections, Sodium Flow Rate 90 gpm	7-15
7-13	Sanborn Traces of Temperature Variations in the Sodium below and above the Calming Plates in the Superheater and Evaporator Models Operating at Near-Rated Conditions, Sodium Level in the Superheater Nine Inches above the Calming Plate, Sodium Level in Evaporator 25 Inches above the Calming Plate	7-16
7-14	Sanborn Traces of Temperature Variations in the Sodium below and above the Calming Plates in the Superheater and Evaporator Models Operating at Near-Rated Conditions, Sodium Level in Superheater 12 Inches above Calming Plate, Sodium Level in Evaporator 11 Inches above Calming Plate	7-17
7-15	Schematic Diagram of the Evaporator Steam System Showing Locations of Stability Instrumentation Recorded on the Sanborns	7-20
7-16	Sanborn Traces of Selected Stability Instrumentation on the Evaporator During Stable Operation at Approximately 1100 kWt and 65 Percent Exit Steam Quality, Time Approximately 1342 Hours	7-21
7-17	Sanborn Traces of Selected Stability Instrumentation on the Evaporator during Stable Operation at Approximately 1100 kWt Showing Transition to Partial and Film Boiling at the DNB Thermocouple Locations, Time between 1421 and 1441 Hours	7-22
7-18	Sanborn Traces of Selected Stability Instrumentation on the Evaporator Operating at Approximately 1100 kWt Showing Initiation of Instabilities in the Center Tube at Net Superheat Conditions, Time Between 1501 and 1521 Hours	7-23
7-19	Sanborn Traces of Selected Stability Instrumentation on the Evaporator During Unstable Operation at Approximately 1100 kWt and Net Superheat Conditions, Time Approximately 1521 Hours	7-24
7-20	Sanborn Traces of Selected Stability Instrumentation on the Evaporator During Unstable Operation at Approximately 1100 kWt and Net Superheat Conditions, Time Approximately 1541 Hours	7-25
7-21	Sanborn Traces of Selected Stability Instrumentation on the Evaporator Operating at Approximately 1100 kWt Showing Transition to Stable Boiling Conditions, Time Between 1541 and 1601 Hours	7-26

LIST OF ILLUSTRATIONS (Continued)

Figure		Page
7-22	Measured Sodium Temperature Profiles in the Evaporator Test Model During Different Modes of Operation	7-28
7-23	Sanborn Traces of Selected Stability Instrumentation on the Evaporator During Stable Operation at Approximately 1500 kWt and 72 Percent Exit Steam Quality, Time Approximately 945 Hours	7-29
7-24	Sanborn Traces of Selected Stability Instrumentation on the Evaporator Operating at Approximately 1500 kWt Showing Initiation of Instabilities in the Center Tube at Net Superheat Conditions, Time Approximately 1104 Hours	7-30
7-25	Sanborn Traces of Selected Instrumentation on the Evaporator During Unstable Operation at Approximately 1500 kWt and Net Superheat Conditions, Time Approximately 1124 Hours	7-31
7-26	Sanborn Traces of Selected Stability Instrumentation on the Evaporator Operating at Approximately 1500 kWt Showing Transition to Stable Boiling Conditions, Time Approximately 1143 Hours	7-32
7-27	Sanborn Traces of Selected Stability Instrumentation on the Evaporator During Stable Operation at Approximately 900 kWt and 62 Percent Exit Steam Quality, Time-Approximately 1242 Hours	7-33
7-28	Sanborn Traces of Selected Stability Instrumentation on the Evaporator Operating at Approximately 900 kWt Showing Initiation of Instabilities in the Center Tube at Net Superheat Conditions, Time between 1402 and 1422 Hours	7-34
7-29	Sanborn Traces of Selected Stability Instrumentation on the Evaporator During Stable Operation at Approximately 1100 kWt and 65 Percent Exit Steam Quality, Time Approximately 1342 Hours	7-35
7-30	Sanborn Traces of Selected Stability Instrumentation on the Evaporator Operating at Approximately 900 kWt Showing Transition to Stable Boiling Conditions, Time Approximately 1502 Hours	7-36
7-31	Diagram of Stable and Unstable Mode of Operation for One Bayonet Tube Assembly Idealized as a U-Tube	7-38
7-32	Results of Transient Analysis of Single Bayonet Tube with Boundary Condition 1 for $t<0$ and Boundary Condition 2 for $t>0$	7-39
7-33	Transient Analysis of Single Bayonet Tube Showing Variation of the Mass Flow Rate, Water Temperature, and Steam Void Fraction at Elevation 450.5 Inches Using the Boundary Conditions in Figure 7-32	7-40
7-34	Results of Transient Analysis of Single Bayonet Tube with Boundary Condition 1 for $t<0$ and Boundary Condition 2 for $t>0$ Using Bayonet Tube Overall Heat Transfer Coefficient of U = 280 for the Entire Length	7-41

LIST OF ILLUSTRATIONS (Continued)

Figure		Page
A-1	Cross-Section of Evaporator Test Section Showing Basic Nodal Structure Used in the Evap Code	A-2
A-2	Cross-Section of Superheater Test Section Showing Basic Nodal Structure Used in the "Super" Code	A-5
A-3	Diagram of the Three Different Kinds of Nodes Used in the "Super" Code	A-6
C-1	Computer Model Useed in the Transient Heater Tube Wall Analysis	C-2
C-2	Computer Model Used in the Single Tube Stability Analysis	C-5
C-3	Multiplication Factor in the DNB Correlation for the P/D = 6 Insert	C-7
C-4	Multiplication Factor in the DNB Correlation for the P/D = 3 Insert	C-8

LIST OF TABLES

Table		Page
4-1	Dimension of Evaporator Tubes	4-9
5-1	Summary of Evaporator Thermal Performance for the Boiling Region at Near-Rated Conditions	5-8
5-2	Insulated (Double Wall) Bayonet Tube Heat Transfer Data and the Calculated Overall Heat Transfer Coefficients	5-17
5-3	Outside Wall Temperature Fluctuation and Frequency Data in the Transition Regime from Sanborn Traces of the DNB Thermocouples	5-39
5-4	Steam Side Flow Distribution Data for the Evaporator Operating at Near Rated Conditions	5-41
5-5	Sodium-Side Pressure Drop Data for the Evaporator	5-47
5-6	Steam-Side Pressure Drops for the Evaporator	5-48
6-1	Summary of Superheater Thermal Performance for the Coil Region at Near-Rated Conditions	6-4
6-2	Steam Exit Temperature Data for the Superheater	6-5
6-3	Sodium-Side Pressure Drops for the Superheater	6-6
6-4	Steam-Side Pressure Drops for the Superheater	6-8
B-1	Overall Heat Transfer Coefficients	B-2
B-2	Summary of Evaporator Thermal Performance Data For P/D = 6	B-6
B-3	DNB Thermocouple Data and Recirculation Flow Rates	B-10
B-4	Reduced Departure from Nucleate Boiling Results	B-13
B-5-1	DNB Thermocouple Data for Nucleate Boiling Conditions and the Evaluated Effective Heat Transfer Coefficient for the DNB Thermocouple "Insulation"	B-15
B-5-2	DNB Thermocouple Data Near Departure from Nucleate Boiling Conditions and the Corresponding Steam Side Heat Transfer Coefficient	B-17
B-5-3	DNB Thermocouple Data for Film Boiling Conditions and the Corresponding Steam-Side Heat Transfer Coefficient	B-19

B-6 Superheater Thermal Performance Results....B-22

B-7 Superheater Thermal Performance Data....B-23

B-8-1 Data for the Bayonet Tube Evaporator with the P/D = 3 Insert....B-26

B-8-2 Data for the Bayonet Tube Evaporator with the P/D = 3 Insert....B-27

B-8-3 Data for the Bayonet Tube Evaporator with the P/D = 3 Insert....B-28

NOMENCLATURE

Engineering Symbols

A	Heat Transfer Surface (ft²)
A_R	Radial Acceleration Caused by the Swirl Generator (g's)
C	Correlation Factor in DNB Design Limit (dim. less)
C_1, C_2	Constants in Sodium-Side Correlation (dim. less)
C_3	Multiplier in Film Boiling Correlation (dim. less)
C_p	Specific Heat at Constant Pressure (Btu/h-lb-°F)
D	Diameter (in.)
D_H	Hydraulic Diameter (in.)
d	Diameter (in.)
e	2.718 (dim. less)
F	Function in Chen's Correlation (dim. less)
f	Friction Factor Based on D_H (dim. less)
G	Mass Velocity (lb/sec ft²)
g	Acceleration of Gravity (ft/sec²)
H	Enthalpy (Btu/lb)
H_{fg}	Latent Heat of Evaporation (Btu/lb)
h	Heat Transfer Coefficient (Btu/h-ft²-°F)
k	Thermal Conductivity (Btu/h-ft-°F)
L	Length of Flow Channel (in.)
LMTD	Logarithmic Mean Temperature Difference (°F)
P	Pressure (lb/ft² or psi)
P	Swirl Generator Pitch (in.)
ΔP	Pressure Drop (lb/ft² or psi)
Q	Rate of Heat Transfer (Btu/h)
q	Heat Flux (Btu/h-ft²)
R	Coil Radius (in.)
r	Tube Radius (in.)
r	Radial Coordinate (in.)
S	Slip Ratio (dim. less)
S	Function in Chen's Correlation (dim. less)
S	Slope (lb/h-°F)
T	Temperature (°F)
ΔT	Temperature Difference (°F)
ΔT_{sat}	$T_{wall} - T_{sat}$ = Wall Superheat (°F)
t	Temperature of Steam (°F)
t	Time Variable (sec)
U	Overall Heat Transfer Coefficient (Btu/h-ft²-°F)
v	Specific Volume (ft³/lb)
W	Flow Rate (lb/h)
X	Steam Quality (dim. less)
X_{tt}	Lockhart and Martinelli Parameter (dim. less)
x	Abscissa (dim. less)
y	Ordinate (dim. less)
z	Elevation along Evaporator (in.)
z	Coordinate (dim. less)
Δz	Node Length (in.)

Greek Letters

α	Thermal Diffusivity (ft^2/h)
α	Void Fraction (dim. less)
ϵ	Surface Roughness (ft)
θ	Coordinate (rad.)
μ	Viscosity (lb/ft-sec)
Π	3.1416 (dim. less)
ρ	Density (lb/ft)
σ	Surface Tension (lb/ft)
ϕ	Angular Coordinate (rad.)

Superscripts

	Mean Value

Subscripts

b	Boiling Region
c	Critical Conditions
e	Exit Conditions
e	Equivalent Quantity
eff	Effective Value
f	Fouling
f	Film Temperature
fg	Change from Liquid to Steam
g	Saturated Steam Condition
i	Inner Diameter
i	Denotes i^{th} Node
in	Inlet Conditions
j	Denotes j^{th} Node
Na	Sodium-Side
out	Outlet Conditions
m	Mean Value
o	Outer Diameter
s	Steam-Side
s	Standard Value
w	Wall Condition
LO	Local Value
LPF	Single-Phase Flow Only
TPF	Two-Phase Friction
DNB	DNB Condition
LMTD	LMTD Quantity Obtained from LMTD Method

Nondimensional Groups

Nu	Nusselt Number ($h D/k$)
Pr	Prandtl Number ($C_p \mu/k$)
Re	Reynolds Number ($\rho VD/\mu = DG/\mu$)
Pe	Peclet Number (Re Pr)

ABSTRACT

The results of steam generator model tests conducted in a sodium-heated test facility at sodium temperatures up to 950°F and steam pressures of 1600 psia are presented. The results include overall heat transfer coefficients and sodium-side heat transfer correlation for a seven-tube bayonet tube evaporator employing swirl flow generator inserts on the steam-side as well as departure from nucleate boiling (DNB) data and a heat transfer correlation for this geometry. The steam-side heat transfer characteristic beyond DNB was evaluated and the wall temperature fluctuations associated with DNB were studied. The steam-side stability characteristics of the evaporator were tested and evaluated.

The results also include overall heat transfer coefficients for the coil region of a helical coil superheater containing two active tubes with steam exit temperatures up to 930°F. Sodium temperature distribution data for both models are presented along with data on sodium flow, temperature, and level fluctuations which were observed during the tests.

1. SUMMARY

A seven-tube model of a candidate forced-recirculation demonstration plant bayonet tube evaporator and a helical coil superheater containing three tubes (two active) were tested in the Steam Generator Test Rig (SGTR) under prototypical plant conditions. The main objectives of the testing were to provide a rigorous proof-of-principle test of the integrity and durability of the tubes and associated weld-joints at representative plant conditions and obtain practical experience in the total process of component specification, design, manufacture, quality control, installation and startup, and operation at plant sodium and steam conditions. Furthermore, the objective was to obtain detailed thermal performance data needed to confirm or correct the thermal design bases, in particular with respect to heat transfer surface area, departure from nucleate boiling in the evaporator, and steam-side boiling stability and flow uniformity. Substantial amounts of thermal performance data were obtained in addition to sodium temperature fluctuation data near the sodium levels in the two models. Sodium-side flow instability data associated with series operation of components containing cover gas spaces were also obtained. The results of the tests with respect to these subjects are summarized below, along with design implications and recommendations for further work.

1.1 HEAT TRANSFER PERFORMANCE

The overall heat transfer coefficient for the boiling region of the evaporator was found to be more than 50% higher than predicted in the design of the test section. This is attributed mainly to the presence of the tube support plates, which increase mixing effects on the sodium-side, and to the thermal conductivity of the tubes, which is believed to be higher than originally assumed. A correlation for the sodium-side Nusselt number was obtained and it is recommended that this, along with the thermal conductivity data used in this report, be applied to the prototypical evaporator design. This will result in a considerable reduction of the heat transfer surface area. It is believed that additional savings can be realized by an appropriate selection of the sodium exit temperature (a few degrees higher sodium exit temperature has a large effect on the surface requirement) and an optimization study in this direction is recommended. It was shown that insulation of the bayonet tubes to reduce the regenerative effect above the sodium level is practical; however, the double bayonet tube wall arrangement tested was not as effective as expected, and a careful selection and testing of different arrangements is recommended.

Although uncertainties exist in the pressure drop measurements, it appears that the steam-side drop in the evaporator is approximately as predicted, while the sodium-side pressure drop was overpredicted approximately by a factor of two.

The overall heat transfer coefficient for the coil region of the superheater was found to be more than 30% higher than predicted. This is attributed mainly to the steam-side heat transfer coefficient which, due to secondary flow patterns, is larger for flow in curved tubes than in straight tubes. Also, the wall thermal conductivity of the coils is believed to be higher than was originally assumed. It is recommended that the curvature effect on the steam-side heat transfer coefficient be accounted for as suggested in this report and that the tube thermal conductivity data used here be applied to future helical coil superheater designs. Although uncertainties exist in the pressure drop measurements, it appears that the predicted steam-side pressure drop for the superheater is in general agreement with the measurements. The sodium-side pressure drop is too small to be measured.

1.2 SODIUM TEMPERATURE DISTRIBUTIONS

Large axial sodium temperature gradients were measured near and immediately below the sodium level in the evaporator at full load operation, becoming increasingly worse at lower power levels. The temperature gradients near the sodium level were caused by the high heat transfer rates in the calming region which is used to calm surface disturbances, and thus reduce the thermal cycling of the tubes at the sodium level cover gas interface. This produces a cold sodium region above the calming plate with the hottest sodium in the unit immediately below. Below the calming region, the axial temperature gradients were caused by the high heat transfer rates in the region near the sodium inlet. Cross-sectional sodium temperature maldistributions near the sodium inlet were also measured. These are caused by a combination of high heat transfer rates and a loss in temperature as the sodium flows radially inward across the outer row of tubes. There was also a contribution from cold sodium mixing into the center region from the calming region, further lowering the temperature in the center channel. This intermittent mixing in of cold sodium also caused sodium temperature fluctuations immediately below the calming region of up to ± 50°F at high sodium level and less than this with lower sodium levels. The present calming region arrangement was effective in reducing the thermal cycling of the tubes at the interface, but extensive redesign is necessary to reduce the harmful side effects. In particular, it is recommended that sodium flow and heat transfer rates in and out of the calming region be restricted or adjusted.

Cross-sectional sodium temperature maldistribution will always exist when the sodium has to flow radially across rows of tubes before parallel flow starts. Application of the present tests results to the prototypical plant evaporator unit indicates that a radial temperature drop of 50°F or more may occur near the top of the unit; this will result in a substantial steam-side enthalpy unbalance being the worst in the case of the parallel sodium flow arrangement vs the disc and donut baffle arrangement. Modularization would be advantageous in this respect, since the sodium would have to flow radially across fewer rows of tubes.

The available sodium temperature data in and near the calming region of the superheater indicate that the problems noted in the evaporator are much less severe in the superheater. The sodium in the calming region is generally lower than the sodium inlet temperature; thus, the thermal cycling of the tubes, particularly the cool downcomers, is reduced in the superheater. The sodium temperature gradients are much smaller than in the evaporator because the overall sodium temperature drop between the sodium inlet and outlet is substantially less in the superheater. Also, sodium temperature fluctuations in and near the calming region were virtually nonexistent. The main reason for the more favorable results in the superheater, apart from different geometry, is the much lower heat transfer rates in the superheater (film boiling vs nucleate boiling).

Circumferential sodium temperature maldistributions of up to 30°F were found to exist in the superheater at the exit from the coil region near the inactive downcomer. The maldistribution resulted from having one of the three tubes purposely plugged, eliminating the cooling effect locally in one of the three downcomers. This will result in thermal stresses in the flow shrouds and tends to emphasize the need for caution when leaky tubes are plugged in larger helical coil units similar in design to the one tested.

1.3 DEPARTURE FROM NUCLEATE BOILING (DNB)

Departure from nucleate boiling was obtained for two different swirl generator inserts in the evaporator. It was found that the insert with the lower pitch-to-diameter (P/D) ratio (P/D = 3) did not perform any better than the P/D = 6 insert (i.e., the onset of DNB at a given heat flux started at about the same local steam quality for both inserts). It is recommended that the P/D = 6 swirl generator inserts be used in the high quality high heat flux region, mainly because these inserts result in less pressure drop.

Based on the critical heat flux design limit obtained from these experiments, the local steam quality in the "hottest" tube is approximately 60%, as compared to a design value of 38%. Local partial film and pure film boiling steam-side heat transfer coefficients and the inside wall temperature for these boiling modes were evaluated. The results indicate that the wall temperature increases gradually after onset of DNB approximately the same way as has been observed in coiled tubes without the traditional steep temperature rise observed in straight boiling channels. This suggests that the magnitude of the wall temperature fluctuations associated with transition boiling may be decreased by the use of helical inserts in the boiling channel. This may prove to be very useful in the design of once-through steam generators.

It is recommended that the effectiveness of various swirl generator devices be investigated with respect to ability to delay onset of DNB if operation below DNB is desired, and with respect to ability to reduce wall temperature fluctuations in the case of once-through operation. The maximum inside wall temperature fluctuation was deduced from measurements of magnitude and frequency at the outside wall by means of a transient analysis. The temperature fluctuation was found to be approximately 40°F (peak to peak) with a frequency of approximately 0.3 Hz. This is less than the design limit of 60°F and indicates that operation with DNB may be feasible; however, more detailed experiments are necessary to confirm the present results. There is considerable economic incentive for once-through operation and most of the sodium temperature gradients and sodium temperature fluctuations observed in the evaporator may be greatly reduced due to the lower heat transfer rates in the sodium inlet region, which is in film boiling with once-through operation. The cross-flow sodium temperature unbalance would also be reduced in this case.

1.4 STEAM-SIDE STABILITY

The steam-side flow distribution in the evaporator was measured using orifices at the bayonet tube inlets and was found to be very uniform at normal operating conditions. The water flow in the center tube was approximately 4% less than the average flow and this was the maximum deviation observed. The steam-side stability was checked in the load range of approximately 60 to 100% and was found to be stable. However, if the unit is pushed far beyond the steam-side design range where the exit steam conditions become superheated by approximately 100°F or more, severe boiling instabilities were observed. The instabilities were characterized by very low overall pressure drop and periodic flow oscillations and possibly complete flow stoppage occurring in the tubes in some sequential order. Temperatures corresponding to superheated steam conditions were measured in the bayonet tubes that normally contained subcooled water, which indicate boiling conditions in the bayonet tubes (possible with superheated conditions in the annulus only). This was investigated analytically by performing a transient analysis of a single bayonet tube and the analysis predicted that the observed instability would occur. Furthermore, it was shown analytically that the cause of the instability (boiling in the bayonet tube) could be removed by insulating the bayonet tubes. The observed boiling instabilities are of no practical interest at the present time, since they occurred far outside the steam-side operating range considered; therefore, no further work on this particular data seems necessary. However, more steam-side stability testing at very low power levels is desirable.

1.5 SODIUM-SIDE STABILITY

The superheater and evaporator, both containing cover gas spaces, were operated in series. Sudden increases or decreases in the sodium flow between the two units and corresponding sodium level changes in the superheater and evaporator were observed. The sodium flow gradually restored itself to the original value if not interrupted by another flow rate perturbation in the opposite direction. It was not possible to identify the mechanism that triggered the sodium flow rate perturbation, but low sodium-side pressure drop

in the superheater is believed to be a contributing factor. The sodium-side instability disappeared when hydraulic flow resistance (throttling of the superheater exit isolation valve) was introduced in the line between the two units. Since sodium level changes introduce thermal cycling of the tubes, it is recommended that the instability problem be investigated further, possibly by simulation in a water loop.

1.6 TUBE THERMAL CONDUCTIVITY

Since the thermal resistance of the reference alloy (2-1/4 Cr-1 Mo) used for the heater tubes in the evaporator in general constitutes more than 60% of the overall resistance, it is recommended that tests be run on representative samples of tubing to be used for the demonstration plant to determine the thermal conductivity accurately. This is particularly important in view of the apparent large scatter in available data and strong influence of small variations in alloy composition.

2. INTRODUCTION

2.1 LMFBR STEAM GENERATORS

It has long been recognized that a reliable steam generator system is essential for successful operation of a Liquid Metal Fast Breeder Reactor (LMFBR) plant. The structural integrity of the steam generator internals is of utmost importance in this respect, but the ALCO/BLH steam generator tests at the Liquid Metal Engineering Center[1] show that the stability and performance characteristics of steam generators are important as well. The thermal-hydraulic performance of the steam generator system must be predictable over the range of load conditions experienced under prototypical LMFBR plant conditions. This includes the ability to predict the overall heat transfer coefficients and the departure from nucleate boiling point as well as the thermo-hydraulic stability and flow uniformity of the steam-side. On the sodium-side, it is important to ensure that the sodium flow and temperature distributions are as uniform as is practical.

2.2 DEVELOPMENT PROGRAM

In support of the development efforts in these areas, under a joint Foster Wheeler—General Electric program, models of candidate steam generator units were designed and built. The models were installed and tested in the 2 MWt sodium-heated SGTR in San Jose, California, during the period of approximately mid-1970 through 1971. The evaporator test section was a bayonet tube forced-recirculation evaporator employing seven full-size tubes approximately 49 ft long, which were about the same as the reference design. The nominal design-point power was 1500 kWt at 1600 psia steam pressure. The superheater test section was a helical coil unit employing three full-size tubes with nominal design-point power of 500 kWt at 1525 psia, 905°F outlet steam pressure and temperature. Both models were operated at prototypical sodium inlet and outlet conditions.

2.3 PROGRAM SPONSORS

The sodium-heated steam generator model tests conducted at the SGTR comprised Subtask F of Task VI of the 300 MWe Fast Ceramic Reactor Component Development Program sponsored by the Empire State Atomic Development Associates, Incorporated (ESADA). The ESADA support for this work was supplemented by Foster Wheeler Corporation, who provided the design and fabrication of the evaporator and superheater test sections, and by General Electric Company, who financed the 1971 test operations and the Breeder Test Facility (BTF) building. ESADA funding was employed to design and construct the SGTR facility and to conduct the test program from mid-1967 through 1970. Much of the test data analysis and the preparation of this report were financed by the USAEC under Task C of PA-61, LMFBR Steam Generator System Development (in the period beginning January 1972).

2.4 TEST OBJECTIVES AND DATA OBTAINED

The general objective of the SGTR operation was to discover areas in which the perception and quantitative understanding of factors affecting the design and operation of a long-lived steam generator may be inadequate. A summary of the overall objectives and program priorities is as follows:

1. Provide a proof-test of the completeness of design and operating assumptions, and explore and define practical remedies where such deficiencies are found.

2. Provide a proof-test of critical mechanical components, including portions of the tube-sheet, tube-sheet welds, end-cap welds, and tube integrity under the thermal and flow forces experienced in service.

3. Provide extended term performance tests with multiple tube models to observe time-dependent effects, and develop and practice surveillance methods to ensure continued satisfactory condition of all critical components of the steam generator.

4. Determine adequacy of thermal design with respect to stability and uniformity of flow distribution on the steam side.

5. Confirm, experimentally, and provide basis for improved modification of design prediction, overall thermal performance of the steam generator, including shell-side flow and temperature distributions.

During the present test program conducted in the period from July 1970 to December 1971, large amounts of steady-state thermal performance data for both the evaporator and superheater test sections were collected over the operating range that can be expected in practice, as well as operation of the evaporator on natural circulation and once-through boiling conditions. Data on departure from nucleate boiling in the evaporator for two different swirl generator inserts were obtained and a check on the steam-side flow distribution was made. The boiling stability characteristics of the evaporator were determined in the range from approximately half- to full-load operation. The overall pressure drops on the sodium-side and on the steam-side of the evaporator and superheater were measured. Sodium flow and level instabilities were studied during operation of the combined system and sodium temperature fluctuations believed to be associated with sodium level changes and cross-flow in the evaporator were examined.

In this report, the thermal-hydraulic test results and associated data reduction and analysis of the data obtained mainly during the latter part of the 1971 operation are presented. A companion report[2] covers the SGTR operating experience and the post-test examination of the evaporator and superheater tube bundles.

3. BACKGROUND INFORMATION

3.1 SODIUM-SIDE HEAT TRANSFER AND PRESSURE DROPS

The prediction of heat transfer in liquid metal heat transfer systems encountered in practice is often a difficult task. Analysis and experiments performed with well-defined or "clean" geometries, such as in-line flow-through unbaffled rod bundles with constant or approximately constant heat flux and fully developed velocity and temperature profiles, are available in the literature.[3,4,5] However, in practical heat transfer systems, such as are found in liquid metal steam generators, the applicability of such "clean geometry" correlations is often questionable for several reasons. As an example, consider the SGTR evaporator model. The basic feature of this model is a seven-rod, triangular array bundle with in-line downward flow; thus, one might at first think that available data for this geometry are applicable. However, there are many complicating factors. First, the bundle has tube support plates approximately every eight hydraulic diameters; thus, the velocity and temperature profiles may not become fully developed. Second, the presence of the support plates and the springs between the tubes increases mixing and heat transfer. Finally, the heat flux is far from constant along the axial length, and, in fact, constant wall temperature would probably be a better approximation to the real system. An additional complicating factor found in real heat transfer systems is the presence of nonuniform flow distribution that can make the heat transfer prediction a very difficult task.

The available literature on liquid metal heat transfer in rod bundles is summarized in Reference 3 for the period up to 1968. The paper by Borishanskii et al.[4] presented what are probably the most recent data for spacerless rod bundles, and are believed to be the best available at this time. In the design of the evaporator, the correlation given by Seban and Shimazaki[5] was used. This correlation was selected because it is believed to be the most conservative.

The sodium-side pressure drop in the SGTR evaporator is due mainly to the support plates. The pressure drop across a plate was predicted by treating the plate as an orifice for which standard methods are available.

For the superheater, the sodium-side heat transfer for the coils was predicted by using the correlation proposed by Rickard, et al.[6] The pressure drop across the coil bank was predicted by the methods proposed by Gunter and Shaw.[7]

3.2 STEAM-SIDE HEAT TRANSFER AND PRESSURE DROPS

3.2.1 Evaporator

A diagram of the basic heat transfer device used in the SGTR evaporator test model (the bayonet tube assembly) is shown in Figure 3-1. A unique feature of this heat transfer geometry is a swirl generator device mounted in the annulus between the heater tube and bayonet tube, as shown in Figure 3-2. Subcooled water enters at the top of the bayonet tube and flows downward while picking up heat through the bayonet tube wall. As the water turns at the bottom of the tube and enters the annular region between the bayonet tube and the heater tube, the water temperature is about 6 to 10°F below saturation temperature. The water now receives heat through the heater tube wall from downward-flowing sodium and reaches saturation condition about 10 ft above the bottom end of the tube, depending on operating conditions.

The heating of the water continues in the nucleate boiling regime, whose main characteristic is a relatively high heat transfer coefficient over the tube length up to the position of the sodium/cover gas interface. It is in this boiling region that the swirl generator serves its function by separating the phases and keeping the inner wall of the tube wetted with water. The design steam quality at this point is 33 wt % for the SGTR evaporator.[8] Above the sodium level, heat is lost from the steam-water mixture to the entering subcooled water through the bayonet tube wall, referred to as the regeneration effect of this heat transfer device.

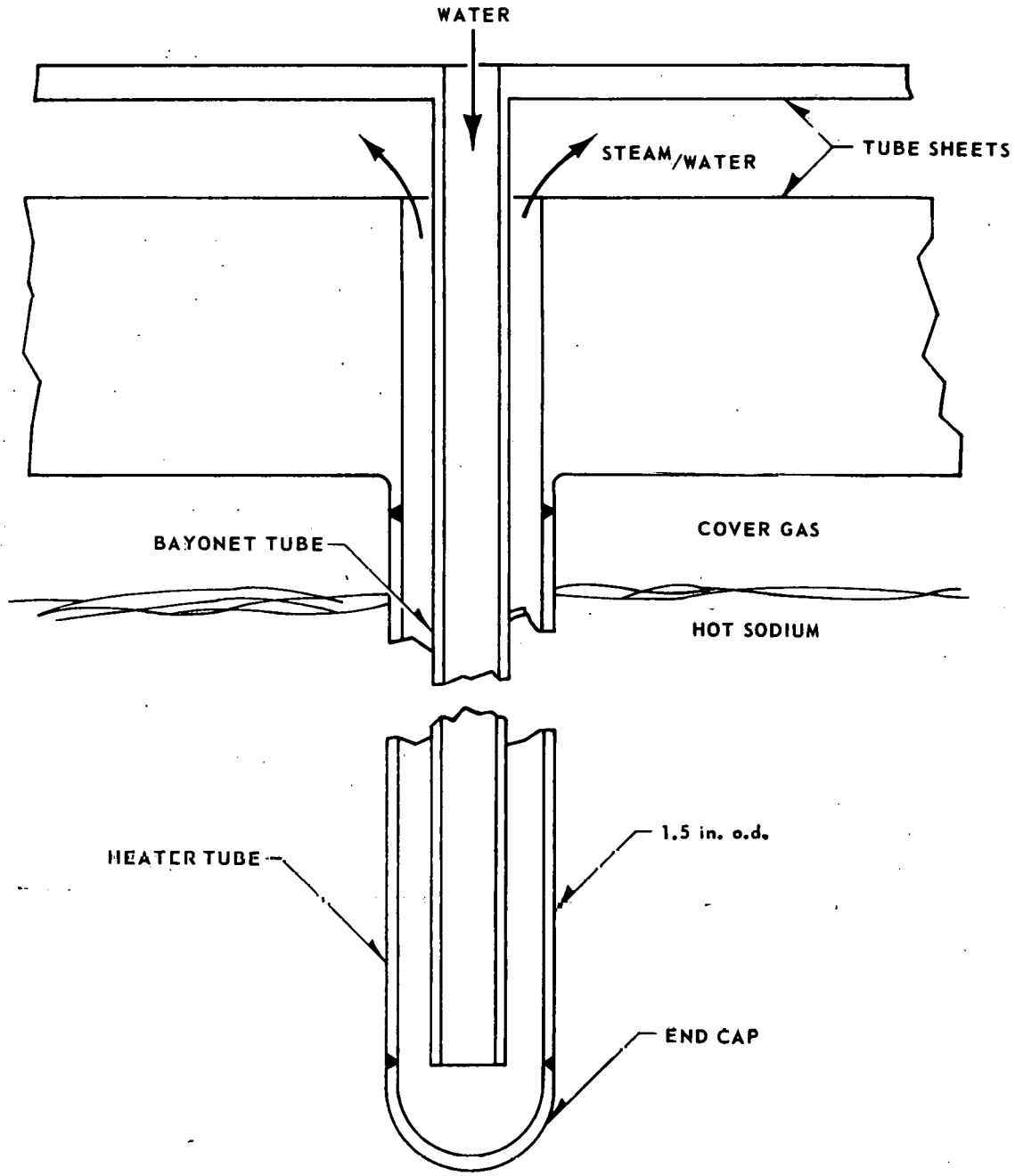

Figure 3-1. *Schematic Diagram of the Bayonet Tube Assembly Used as the Basic Heat Transfer Device in the SGTR Evaporator Model*

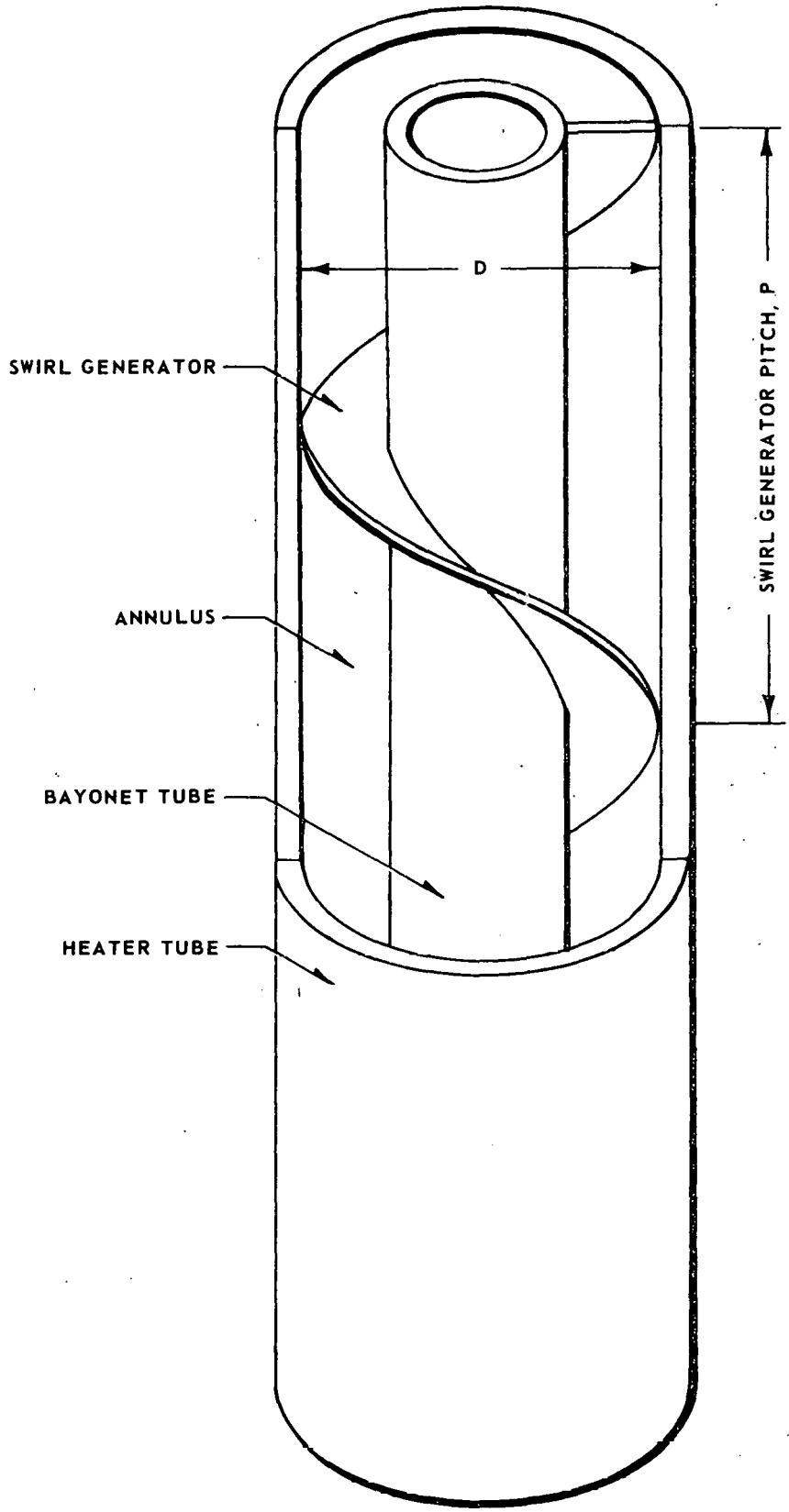

Figure 3-2. Schematic Diagram of a Portion of the Bayonet Tube Assembly Showing Swirl Generator Device

The subcooled liquid phase heat transfer in the bayonet tube is well defined by the Dittus-Boelter correlation,[9] and the pressure drop can be calculated by standard methods used for pipe flow.[10] Initially, the water entering the annulus between the heater tube and the bayonet tube contains no steam bubbles. The heat transfer and pressure drop for swirl flow of water in an annulus has recently been investigated by Seban and Hunsbedt.[11]

Continued heating of the subooled water eventually results in subcooled boiling and bubble formation along the heater tube wall. The heat transfer for this condition in straight pipes has been investigated by Jens and Lottes;[12] however, the presence of the swirl generator complicates the prediction of the heat transfer. In the design analysis, this problem was handled in an approximate way by assuming that the subcooled heat transfer coefficient applied to the point where the mean steam quality was less than 0 and nucleate boiling for the mean steam quality larger than 0.

When net bulk saturation conditions have been reached, the flow regime traditionally denoted by the bubbly flow regime starts and the boiling process is denoted nucleate boiling. The traditional sequence of flow patterns the steam-water mixture will go through as the heating continues are the slug, slug-annular, and the annular regime, respectively, nucleate boiling being the boiling process. It is believed that the wall is completely wetted in the nucleate boiling regime. In the higher quality regions of the regime, it is thought that part of the liquid flows as a continuous liquid film on the tube wall, the remainder being entrained in the vapor core. Heat can be transferred in the nucleate boiling region by conduction through the postulated liquid film and subsequent evaporation into the vapor core ("film evaporation"), and by boiling with bubble formation from nucleation sites in the boiler tube wall.

Data on nucleate boiling for swirl flow appear to be nonexistent; however, since the nucleate boiling heat transfer coefficient is in general high, it contributes little to the overall thermal resistance of the heater tube; therefore, to a good approximation, the nucleate boiling coefficient is given by Chen's correlation.[13]

Peterson, Converse, and Gutstein[14] performed two-phase pressure drop experiments using air/water mixtures and found that the Martinelli-Nelson[15] correlation for prediction of two-phase pressure drop is applicable for the present geometry when the liquid phase pressure drop is known.

3.2.2 Superheater

The steam-water mixture exiting the evaporator flows to the steam drum where the two phases are separated. The saturated or near-saturated steam enters the helical coil superheater test section and flows downward in the downcomer tubes while being heated by sodium in cocurrent flow. The steam flow direction is then reversed at the bottom of the unit, enters the helical coil section, and exits the superheater at the top at about 905°F under normal operating conditions. The steam-side heat transfer in the superheater is by film boiling and is well defined in the straight downcomers by the Hienemann correlation.[16] Also, the pressure drop can be calculated by the standard methods used for pipes.[10] In the helical coil section, the heat transfer and pressure drop characteristics are modified due to the tube curvature. The curved flow path introduces centrifugal force fields that result in secondary flow patterns perpendicular to the main flow direction, the magnitude of which depends on the curvature. The pressure drop in curved pipes has been investigated by Ito[17] and the heat transfer characteristics have been well-defined by Seban and McLaughlin.[18]

3.3 DEPARTURE FROM NUCLEATE BOILING (DNB) IN THE EVAPORATOR

At the beginning of the ESADA steam generator development program, it was specified that departure from nucleate boiling should not occur in the evaporator unit, since it was anticipated that the thermal cycling associated with DNB might strain cycle the heater tubes and thus reduce their lifetime. The design specification is still in effect; however, there are economic incentives to relax this specification and operate the evaporator with DNB at about 100% exit steam quality. This would reduce the size and cost of the recirculation system and would reduce the recirculation pumping costs.

The DNB point (sometimes called "dry-out," "critical heat flux," or "burn-out"), where the thin liquid film is thought to be destroyed, terminates the high performance nucleate boiling region and marks the onset of the lower performance "transition boiling" region. The lower heat transfer coefficients determined for the transition region are thought to be caused by the heat transfer surface being only partially wetted. Heat transfer in this region is visualized as a combination of heat transfer to patches or droplets on the boiler tube wall and vapor phase heat transfer from the dry areas. The transition region is terminated by the onset of "film boiling," at which point the liquid droplets and patches, thought to wet the wall in the transition region, become insulated from the heat transfer surface by a superheated vapor film. The film boiling region extends to the point at which bulk superheating commences, and the subsequent "film boiling region" is the final step in a "once-through" boiling process.

The problem of determining the point of critical heat flux with various geometries and conditions has been given a lot of attention in recent years; however, data directly applicable to the annular swirl flow geometry apparently do not exist. The annular geometry without the swirl generator has been studied. Janssen and Kervinen[19] ran tests with the inner surface of the annulus heated at pressures ranging from 600 to 1400 psig; DNB data for an annulus with the inner and outer surfaces heated at 1500 psia have been obtained.[20] Tippets[21, 22] did an extensive analytical study of the problem of predicting DNB and arrived at a general relationship for the critical heat flux vs steam quality curve. This result is applicable to the present swirl flow geometry after a suitable correction to account for the acceleration field set up by the swirl generator has been made; but the final correlation requires the determination of two constants from experimental data.

Extensive experimental measurements have been obtained of heat transfer behavior beyond the DNB point. These tests were run with forced flow at high pressure and intermediate steam qualities by Hench,[23, 24] Quinn,[25] and Kunsemiller.[26] Beyond DNB, wall temperature fluctuations were found to occur over a very narrow range of conditions. Hench reports the magnitude of the wall temperature fluctuations to be as much as 700°F at a frequency of approximately 0.5 Hz for a constant heat flux system. Further, it was found that the temperature oscillations are reduced in magnitude as the steam quality and mass velocity are increased.

Concurrent measurement of wall temperatures at various positions along the heated wall and high-speed photography of heated surface fluid behavior during transition boiling[27] have led to the conclusion that, in the flow regime studied, transition temperature fluctuations are caused by temporal movements of the liquid film terminus on the wall. The effects of the oscillating movement of the liquid film terminus on heat transfer behavior are shown in Figure 3-3* for the two extreme positions. The lowermost position is seen in the figure to be the location of the DNB condition. The uppermost position is near the location of the onset of stable film boiling, because the wall does not rewet beyond this position. However, significant variations in the heat transfer coefficient occur for a short distance beyond the uppermost film terminus position, making the transition boiling length slightly longer than the terminus travel.

The movement of the liquid film terminus is ordinarily very slow and travels over a short distance found to be approximately 10 to 20 sec/cycle and less than three hydraulic diameters for the single rod tests reported in Reference 25. Ordinary irregularities of two-phase flow and slight unsteadiness of loop conditions, such as small oscillations of absolute pressure, appear to be the cause of terminus movement. The spatial dependence of wall temperature and heat transfer coefficient beyond the transition boiling location are also shown in Figure 3-3.

The previous description of the transition boiling phenomenon applies to straight flow in a pipe, an annulus, or a heated rod, and for constant heat flux systems (e.g., electrically resistance heated test sections). In liquid-liquid systems, such as the liquid metal heated steam generators, the local heat flux is not constant in the transition boiling region and the potential for obtaining large magnitude wall temperature fluctuations is reduced. The presence of the swirl generator and the corresponding radial acceleration field also modifies

* The heat flux is uniform and constant in the figure.

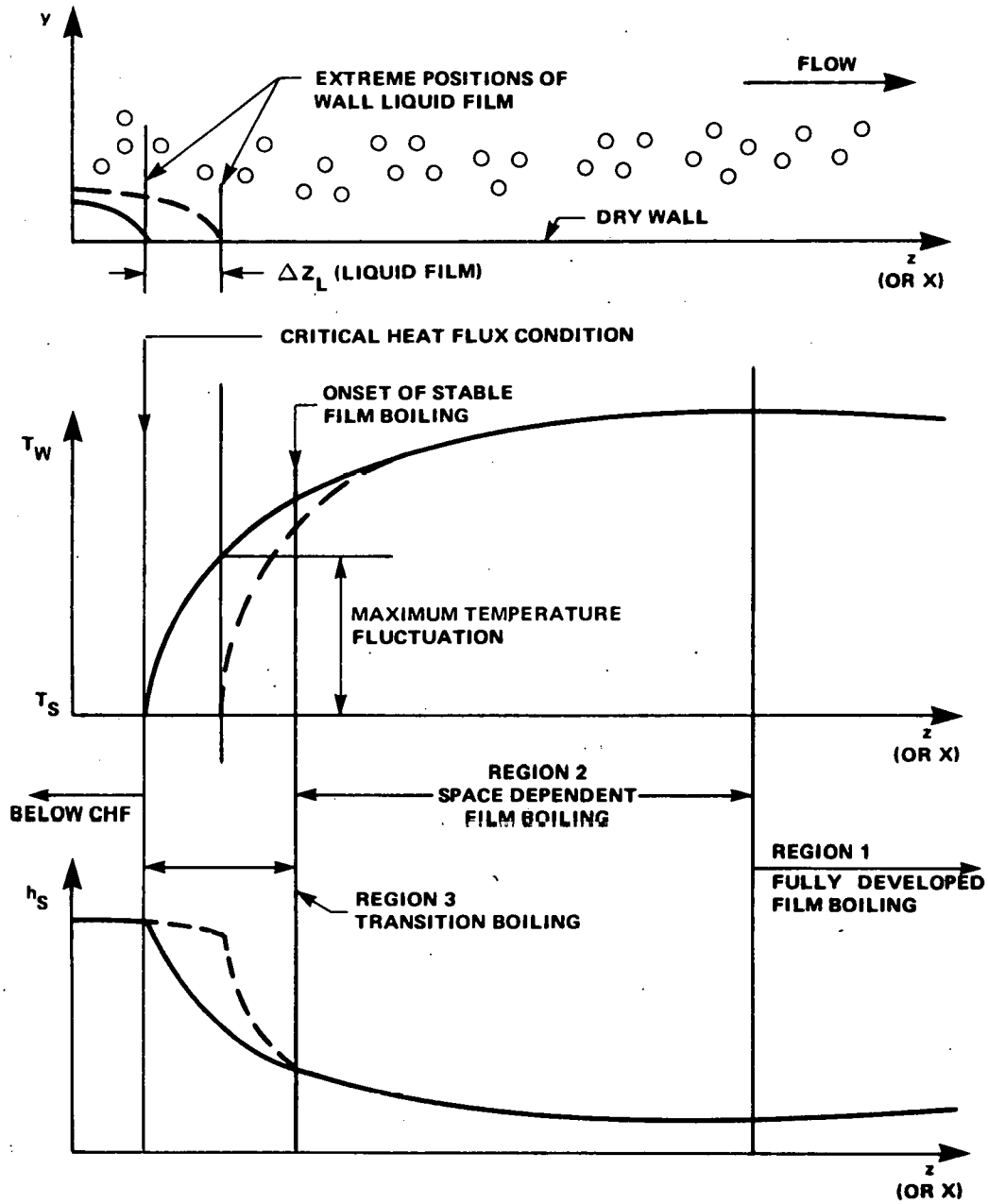

Figure 3-3. Diagram Illustrating Transition Boiling Heat Transfer Dependence on Steam Quality or Axial Position for a Constant Heat Flux System

the straight flow description of the transition boiling region. Air/water flow tests* show that with the swirl generator the heater tube inside wall stays wetted up to about 80% qualities (Figures 5-15, 5-16, and 5-17). At higher qualities, rivulets start to form at this surface and persist to about 95% qualities while the bayonet tube outer wall remains wetted or partially wetted after the heater tube wall is completely dry.

A special feature with the present evaporator is the relatively low sodium to steam temperature difference and the high temperature drop in the heater tube wall, along with the correspondingly low heater tube wall to steam temperature difference. It has been observed[28] that there is an abrupt drop in the wall wettability above surface to steam temperature differences of 250 to 450°F. The maximum wall-to-steam temperature difference in the present system is approximately 150°F and it appears, therefore, that the wall will rewet after having been blanketed momentarily.

These observations suggest that the wall temperature fluctuations associated with DNB are not as large as in straight channel flow. Also, it appears possible to delay the onset of DNB further if the water film on the bayonet tube surface and swirl generator could be moved to the heater tube surface.

Experiments[29] with once-through steam generators using twisted tapes in straight tubes show that there was a considerable increase in steam quality at DNB and the wall temperature fluctuations in the transition region were much lower than for straight channel flow. Similar results were obtained[30] with coiled tubes and it is clear from the illustration of Figure 3-4 that the annular swirl geometry can be interpreted as a coiled tube in the limit, and therefore would be expected to have some of the same characteristics as the coiled tube.

An interesting feature of the coiled tube vs the straight tube[30] is illustrated in Figure 3-5. A much smoother transition to film boiling occurs with the coiled tube than with the straight tube; a similar behavior may be expected in the annular swirl flow geometry in view of the analogy pictured in Figure 3-4.

As illustrated in Figure 3-3, the heat transfer coefficient decreases from a very high nucleate boiling coefficient to a fully developed film coefficient, and the film coefficient has been observed[25] to be space dependent. This is a characteristic of any developing thermal boundary layer, but Quinn[31] shows that there is also a bulk superheat accumulation effect due to entrained droplets.

3.4 HEATER TUBE WALL THERMAL CONDUCTIVITY

The thermal resistance of the heater tube is a large fraction of the total thermal resistance (approximately 60% for the evaporator and approximately 30% for the superheater). The accuracy of the thermal conductivity data will thus determine to a large degree the accuracy by which the overall evaporator and superheater performance can be predicted. It turns out that there is a large scatter in the available data for the thermal conductivity of the 2-1/4 Cr-1 Mo steel. This is apparent from Figure 3-6, where the data for the above reference alloy and alloys with composition close to the above from four references are summarized.

It is not possible to tell with certainty the reasons for the discrepancies between the data. One possible reason is that the thermal conductivity is sensitive to exact composition, impurities, etc., and may vary from batch to batch. This suggests that the steel supplier should be required to run thermal conductivity experiments on each batch; this requirement should be specifically stated in the purchase specification.

* Unpublished work performed at General Electric Missile and Space Division, Cincinnati, Ohio.

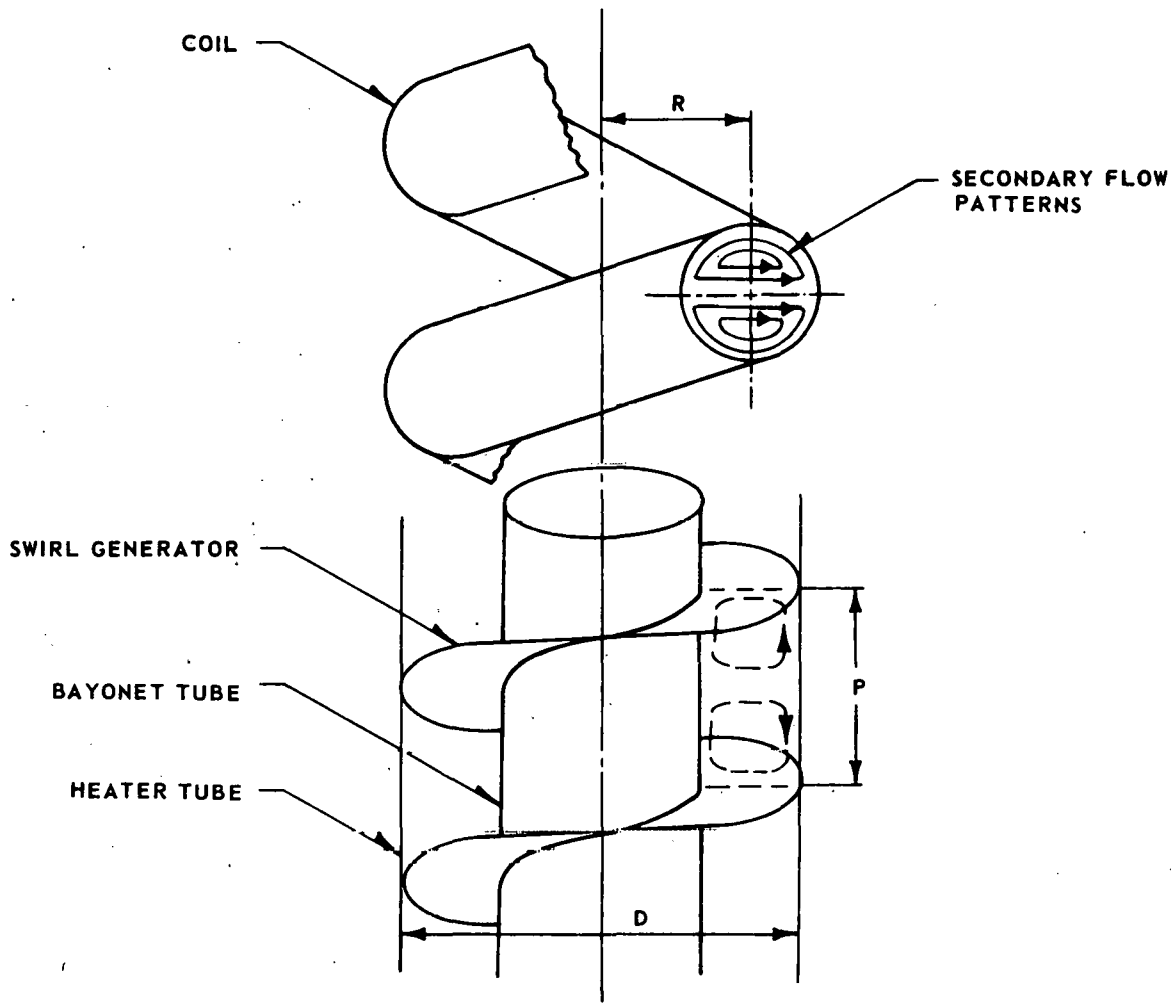

Figure 3-4. Schematic Diagram Showing the Similarities between Flows in the Annular Swirl Flow Geometry and the Coiled Tube Geometry

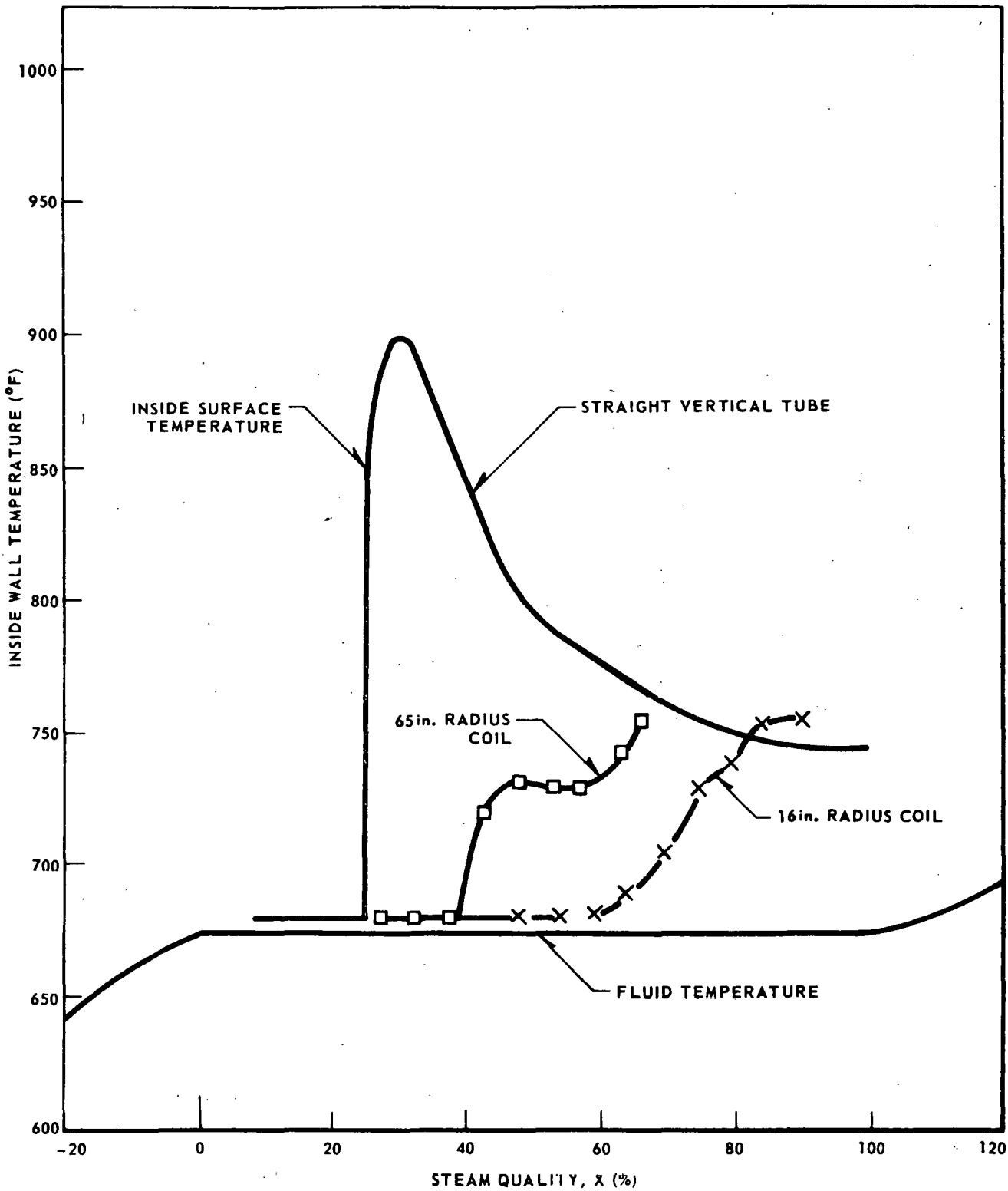

Figure 3-5. *Comparison of Tube inside Wall Temperature Behavior in the Transition Boiling Regime for a Straight Vertical Tube and a Coiled Tube, Both with Constant Heat Flux (Modified Form of Figure 24 in Reference 32)*

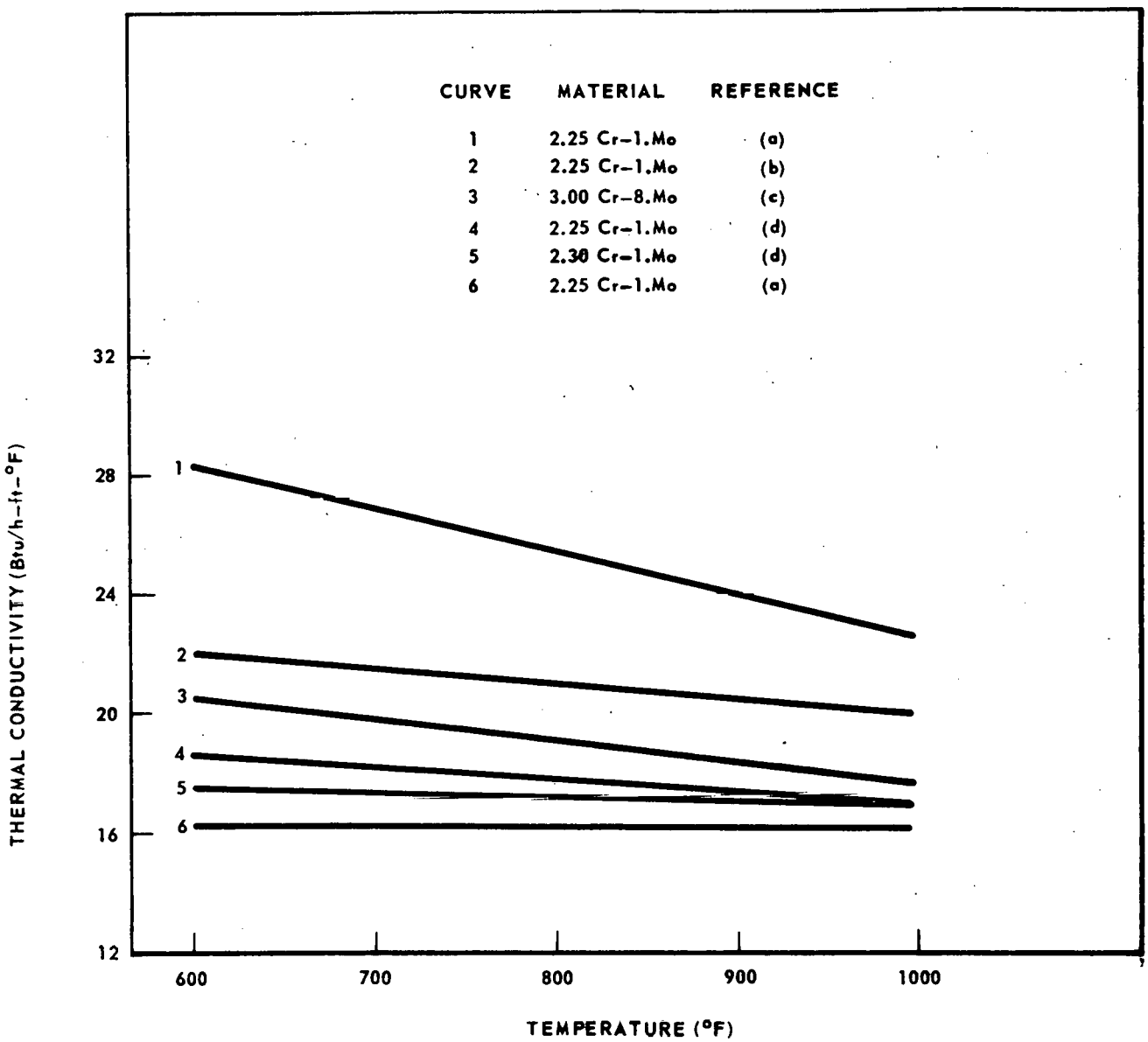

a. "Design Guide for LMFBR Sodium Piping," Report SAN-781-1, Prepared for USAEC by C. F. Braun and Company, February 1, 1971.

b. *Standards of Tubular Exchanger Manufacturers Association*, Fifth Edition, 1968.

c. *Properties of Steel,* 1969 Internationale Atomteaktorbau G.M.B.H. Bensberg, West Germany, NP-18080.

d. Sandrik Steel Manufacturing Company, Sweden, Products Catalogue.

Figure 3-6. ***Comparison of Available Thermal Conductivity Data for the Heater Tube Reference 2-1/4 Cr - 1 Mo Alloy (T-22)***

4. TEST APPARATUS

4.1 SODIUM-HEATED STEAM GENERATOR TEST RIG (SGTR)

The Steam Generator Test Rig (SGTR), located at a General Electric site in San Jose, California, is a gas-fired, air-cooled system. The rig is constructed primarily of Type-304 stainless steel, with bimetallic joints to accommodate the chrome-molybdenum evaporator and superheater test sections. A schematic diagram of the rig is shown in Figure 4-1. The operating capabilities of the test rig are:

- Power ..... 2000 kWt
- Top Sodium Temperature ..... 1100°F
- Sodium Flow Rate ..... 200 gpm
- Top Steam Temperature and Pressure ..... 1000°F/2400 psi
- Steam Flow Rate ..... 8000 lb/h
- Recirculation Water Flow Rate ..... 60 gpm (one recirculation pump)

The SGTR includes a complete sodium-water reaction vent-relief system and a leak detector system which is representative of that planned for the reference plant steam generator (gas chromatograph, gas thermal conductivity analyzer, and diffusion-tube hydrogen detector).

Figure 4-2 shows the flow diagram for the system, and instrument connection details are shown in Figure 4-3. (The system isometric and system plan and elevation drawings, etc., are included in Volume 1.[2]) Figure 4-4 shows a view inside the Breeder Test Facility (BTF), with the upper portion of the SGTR and evaporator test section in view in the background. Figure 4-5 is a view of the SGTR from below the superheater model which is mounted adjacent to the evaporator model.

4.2 EVAPORATOR TEST SECTION

The evaporator model was manufactured in the Foster Wheeler factory at Mountaintop, Pennsylvania, and was delivered to the SGTR in October 1969. The model is a sodium-heated bayonet-tube recirculating evaporator containing seven full-size tubes whose dimensions, weld-joints, and other structural features are identical or similar to those for the reference evaporator design (except that the tube support devices approximate rather than duplicate the reference design). The nominal design evaporator model power is 1500 kWt at 1635 psia boiling pressure and 855°F sodium inlet temperature (same pressure and temperatures as the reference plant evaporator).

The outline of the test section is shown in Reference 2. The subcooled recirculation water enters through Nozzle N-1, flows downward through the inner bayonet tubes, reverses, and flows upward through the annuli formed by the outer heat transfer tubes and the inner bayonet tubes where a portion of the water is converted to steam. The two-phase mixture then leaves the evaporator through Nozzle N-2. The design point exit steam quality from the evaporator is 30% (same as plant evaporator—see Reference 8). Fins are welded to the outside surface of the bayonet tube to impart a swirling motion to the water in the annulus.

Figure 4-6 shows the details of the evaporator test section; Figure 4-7 shows details of the region near the sodium inlet at the top. The heat transfer tubes are approximately 49 ft long and are constructed of 2-1/4 Cr-1 Mo (T-22) alloy (same as the reference evaporator design).

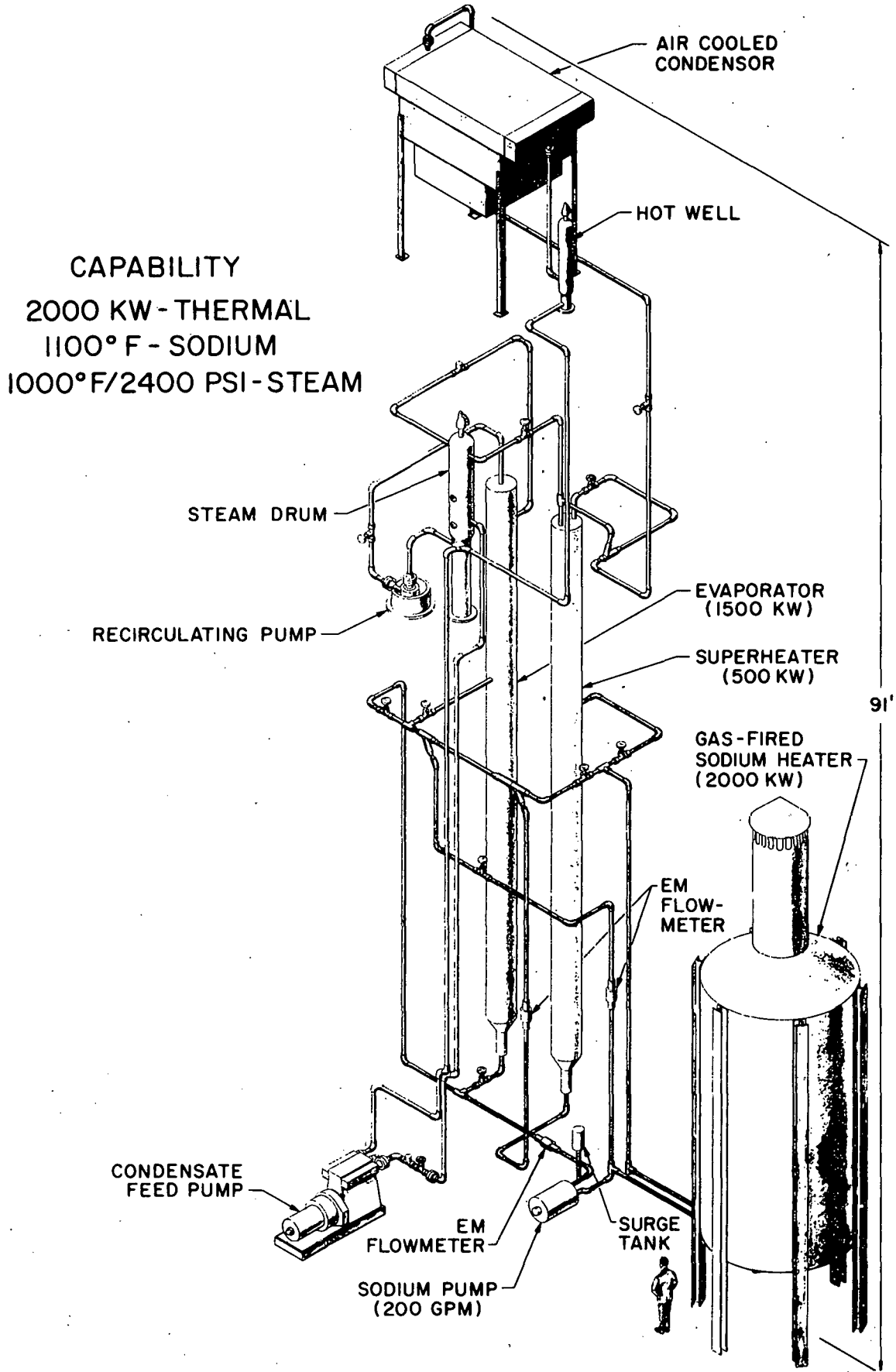

Figure 4-1. Schematic Diagram of the 2000 kWt Sodium-Heated Steam Generator Test Rig (SGTR)

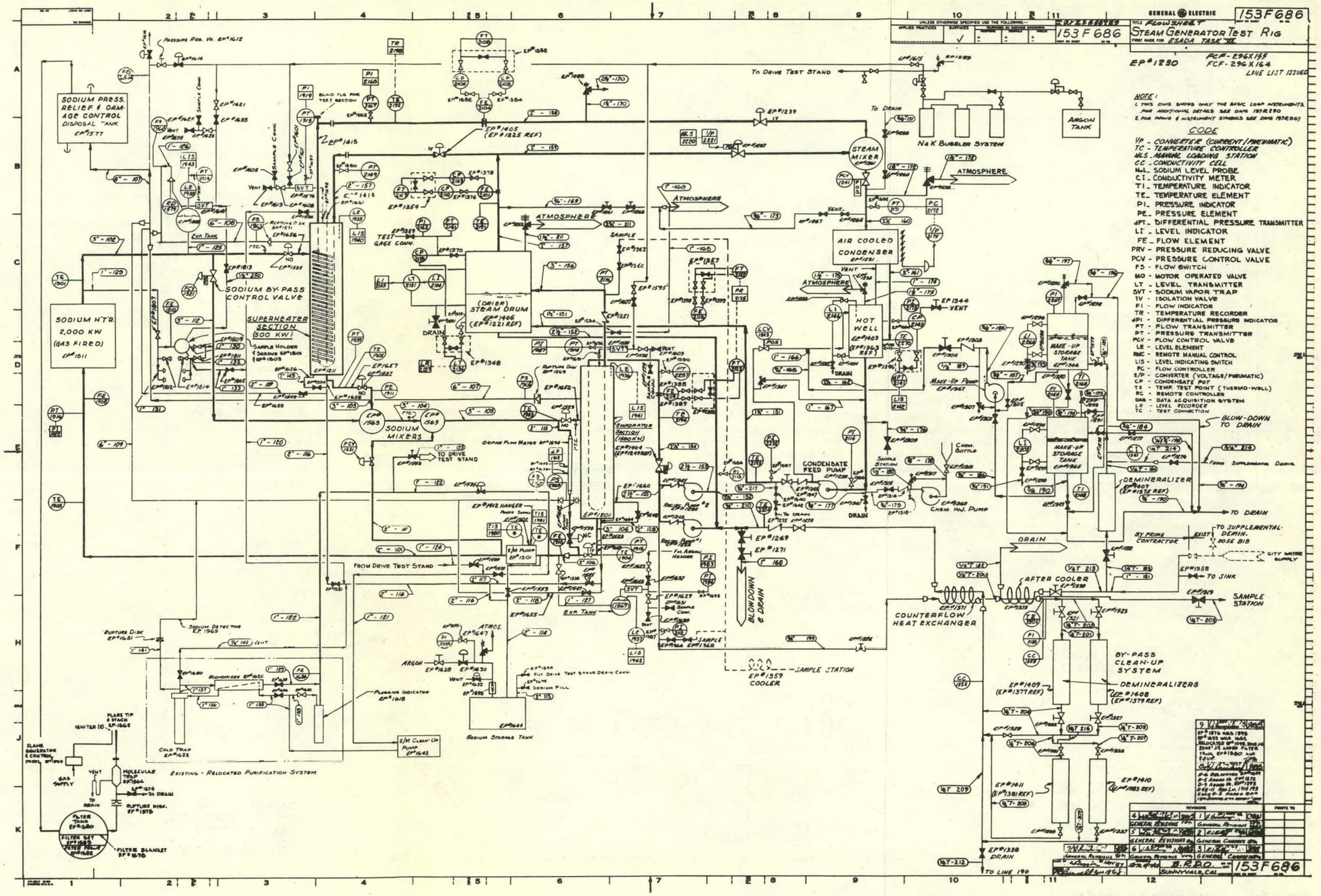

Figure 4-2. Flow Diagram of the Steam Generator Test Rig

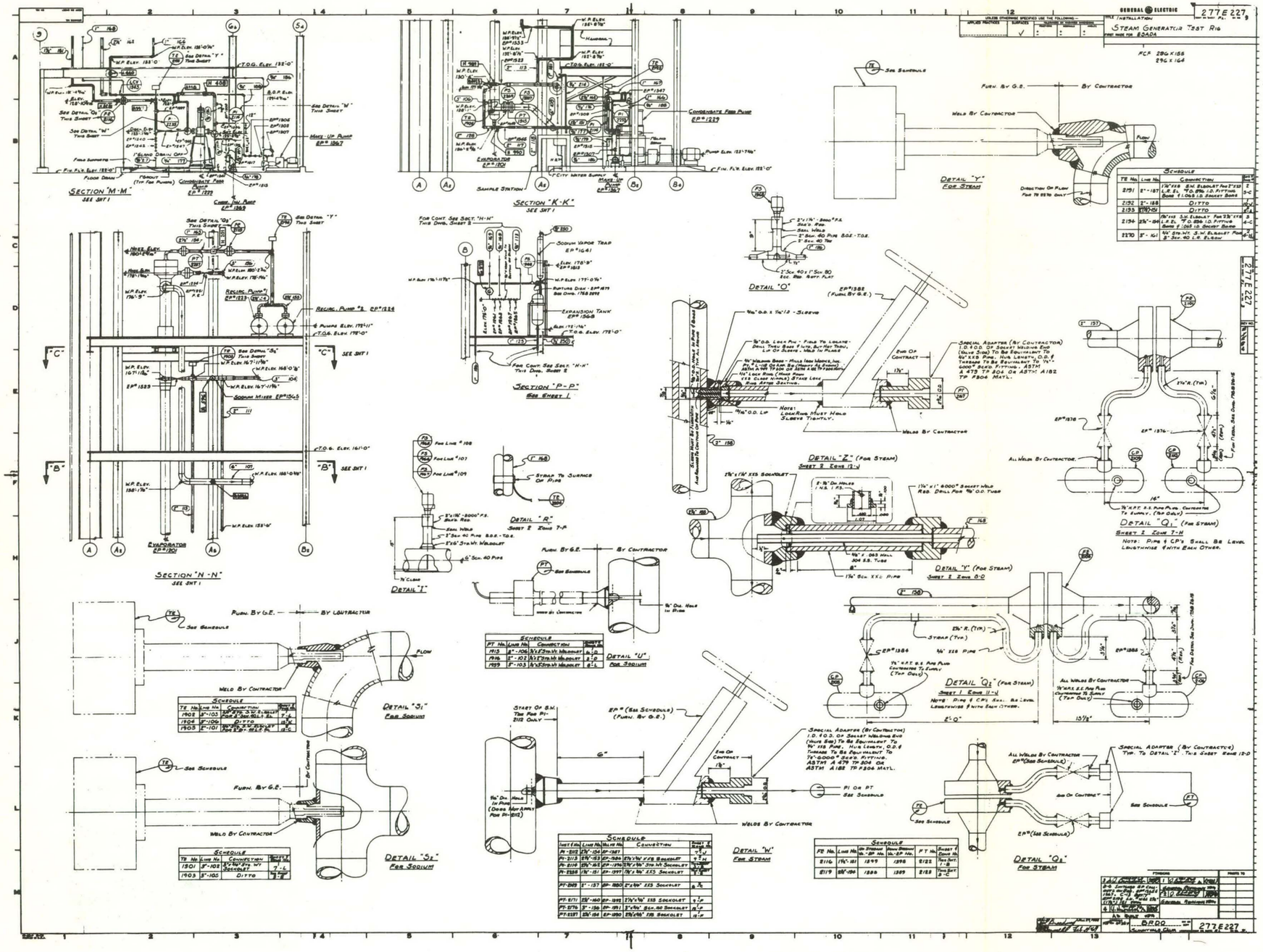

Figure 4-3. Steam Generator Test Rig - Instrument Connection Details

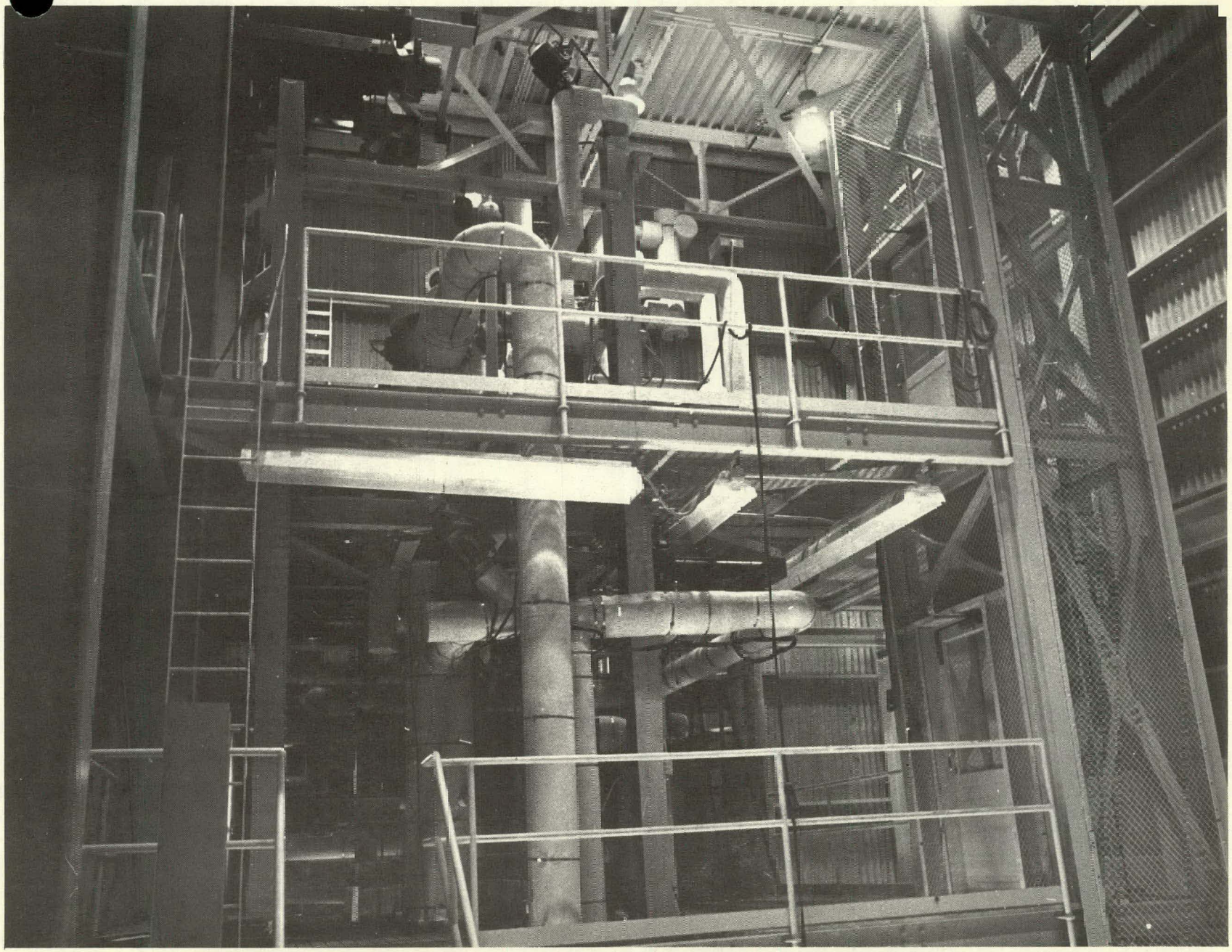

Figure 4-4. View of the Upper Portion of the Steam Generator Test Rig with the Foster Wheeler Evaporator Model in the Background

THIS PAGE

WAS INTENTIONALLY

LEFT BLANK

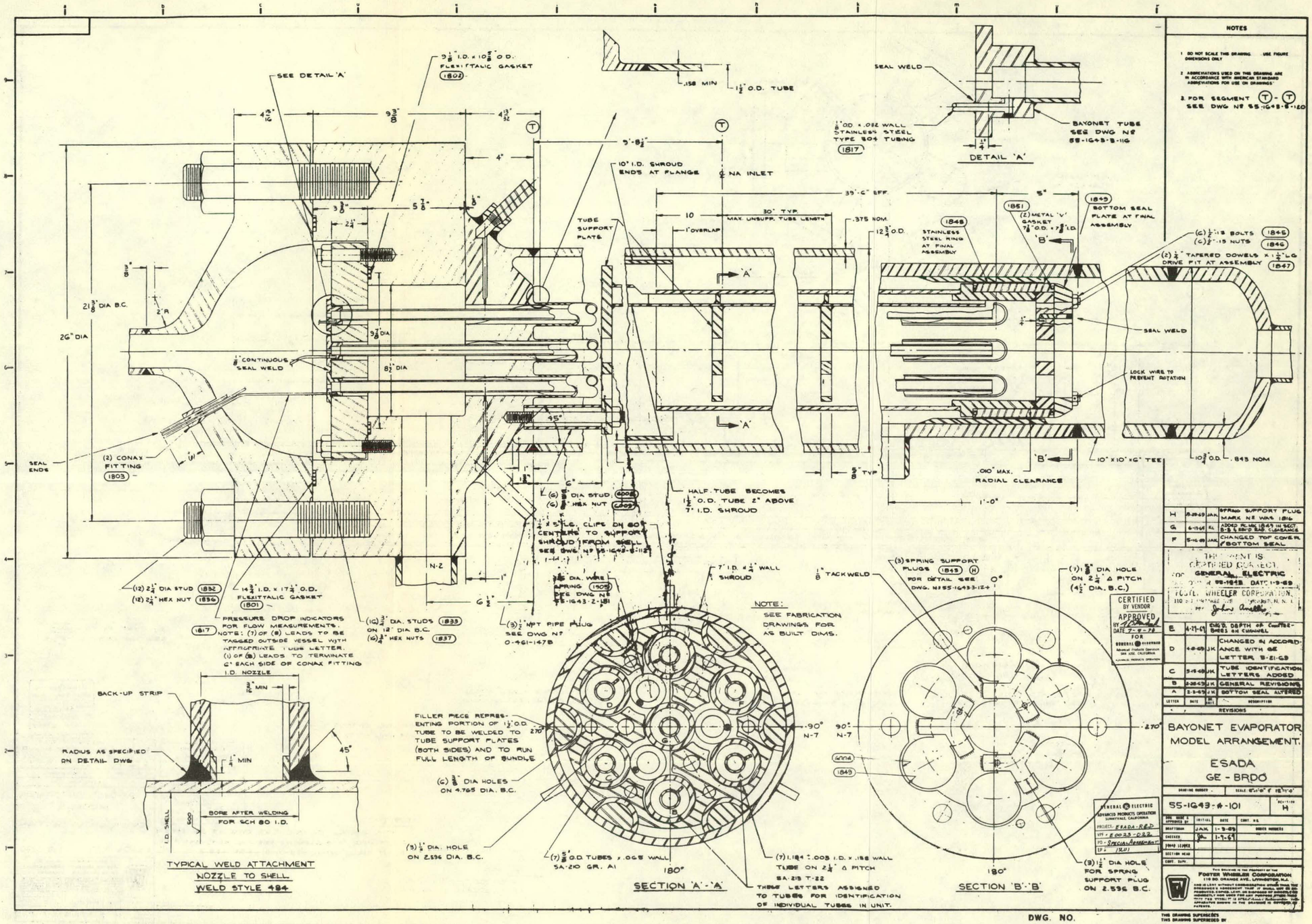

Figure 4-6. Evaporator Test Section - Details (Courtesy Foster Wheeler Corporation)

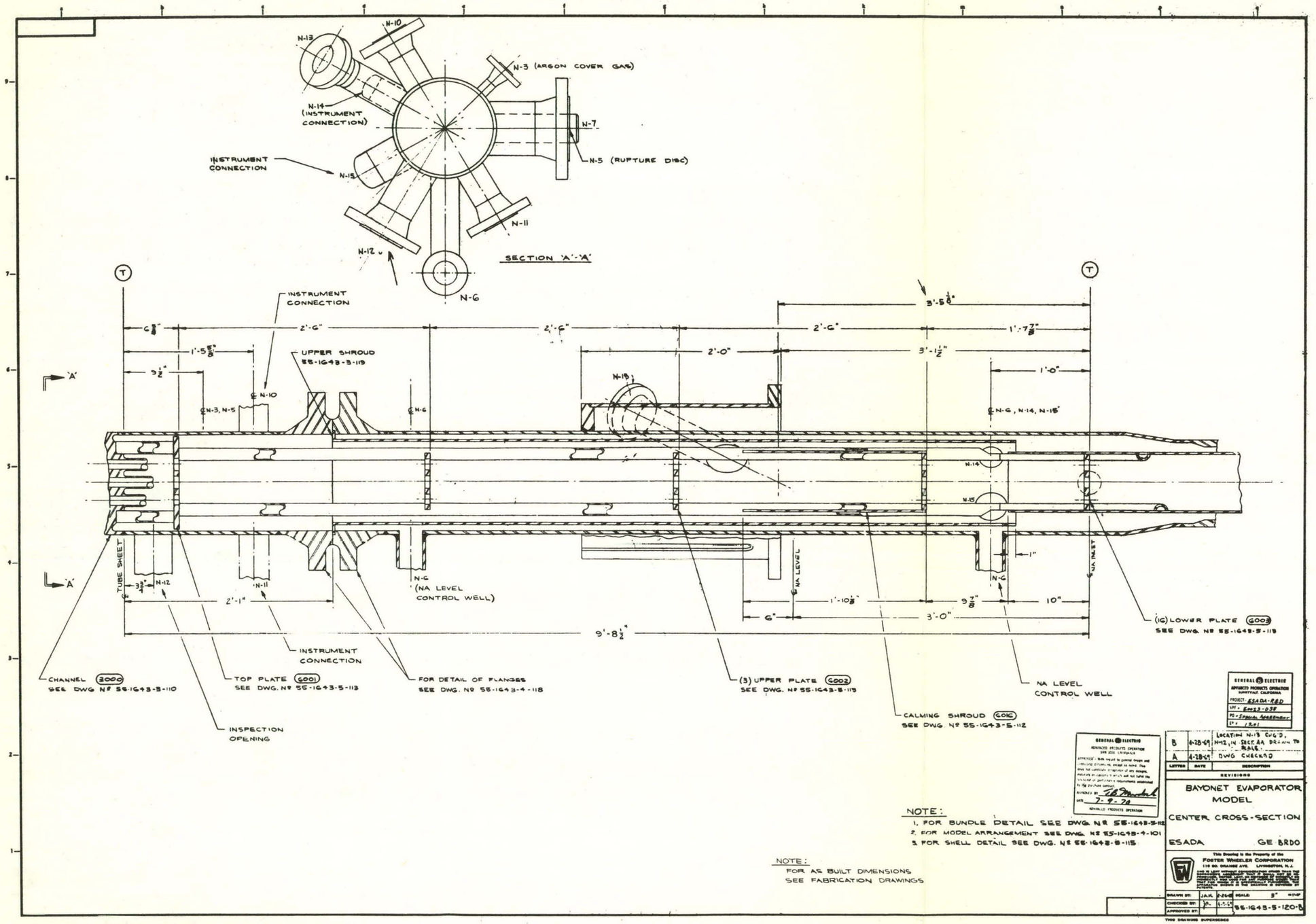

Figure 4-7. Details of Evaporator Near Sodium Inlet Nozzle (Courtesy Foster Wheeler Corporation)

Two different pitch/diameter ratio (P/D ratio; for definitions, see Figure 3-2) swirl generator inserts were tested. Initially, the reference design employed noninsulated bayonet tubes over the total length; this arrangement was also used in the model with the first swirl generator insert. The second swirl generator insert used water-filled, double wall bayonet tubes for the upper 10 ft corresponding approximately to the section of tubing above the sodium inlet, to reduce the regenerative heating and the corresponding reduction in steam exit quality. Details of the insulated bayonet tube design are shown in Figure 4-8. Details of the two swirl generator inserts and the tube dimensions are given in Table 4-1 below:

Table 4-1
DIMENSION OF EVAPORATOR TUBES

	Swirl Generator		Tube Lengths (feet)			Diameters (inches)					
			Heater	Bayonet	Insulated	Heater Tube		Bayonet Tube		Insulation	
P/D	Width	Thickness	Tube	Tube	Portion	o.d.	i.d.	o.d.	i.d.	o.d.	i.d
6	0.252	0.06	48.4	49.4	–	1.500	1.184	0.625	0.500	–	–
3*	0.252	0.06	48.4	49.4	10	1.500	1.184	0.625	0.500	0.437	0.321

* This was the swirl generator P/D ratio used in the upper approximately 24-ft section; in the lower approximately 25-ft section, the old P/D = 6 swirl generator inserts were used (Figure 4-8).

The problem of tube vibration is minimized by the use of tube support springs as shown schematically in Figure 4-9. The springs are 1-3/32 in. o.d. and are made of 3/16 in. o.d. wire with a coil pitch of 6 in. One coiled spring is inserted between three adjacent heat transfer tubes. The spring extends the full length of the tubes. The force of the spring holds the tubes against the tube support/baffle plates, thereby dampening any vibration that may arise. (Subsequent development resulted in the elimination of the spring in the reference steam generator design.)

The heat transfer tubes were welded to annular projections on the tube-sheet by the internal bore-welding torch developed by Foster Wheeler.[8]

The sodium enters Nozzle N-7 (Figures 4-6 and 4-7), flows upward for a distance of 10 in., and into the shroud enclosing the tube bundle assembly. The sodium then flows downward in parallel with the heat transfer tubes, and exits at the bottom through Nozzle N-8. An annular seal at the bottom of the shroud prevents bypass of the sodium around the tube bundle. In addition to channeling the sodium flow through the tube bundle, the shroud serves as a protective shield for the vessel shell to prevent direct impingement of sodium-water reaction products that would result from a tube leak.

The vessel shell is constructed of standard commercial pipe and fittings. The material of construction is 2-1/4 Cr-1 Mo alloy. The lower portion of the shell is fabricated from heavy wall pipe (Schedule 120) to minimize any damage that could result from the high peak pressures and temperatures that might occur in the event of a large tube leak and associated sodium-water reaction. In addition to this precautionary measure, rupture discs were mounted on the 6-in. nozzles (N-5 and N-16) at the top and bottom of the shell, respectively, to relieve the generated pressure. A standpipe (N-6) is mounted on the side of the shell for sodium level indication.

4.3 SUPERHEATER TEST SECTION

The superheater model was also manufactured in the Foster Wheeler factory and was delivered to the SGTR in July 1970. The superheater model is a helical coil superheater consisting of three, 74-ft-long, full-size (1-1/4 in. o.d. X 0.065 in. wall) heater tubes nested together in a single 18-in.-diameter coil bank. The tubes were made up with representative samples of four candidate alloys: normal 2-1/4 Cr-1 Mo (SA-213, Grade T-22), low carbon chrome-moly (0.03% C), niobium-stabilized chrome-moly (1% Nb), and titanium-niobium-stabilized chrome-moly (1/4 Ti, 1/2 Nb). Except for the associated differences in tubing materials,

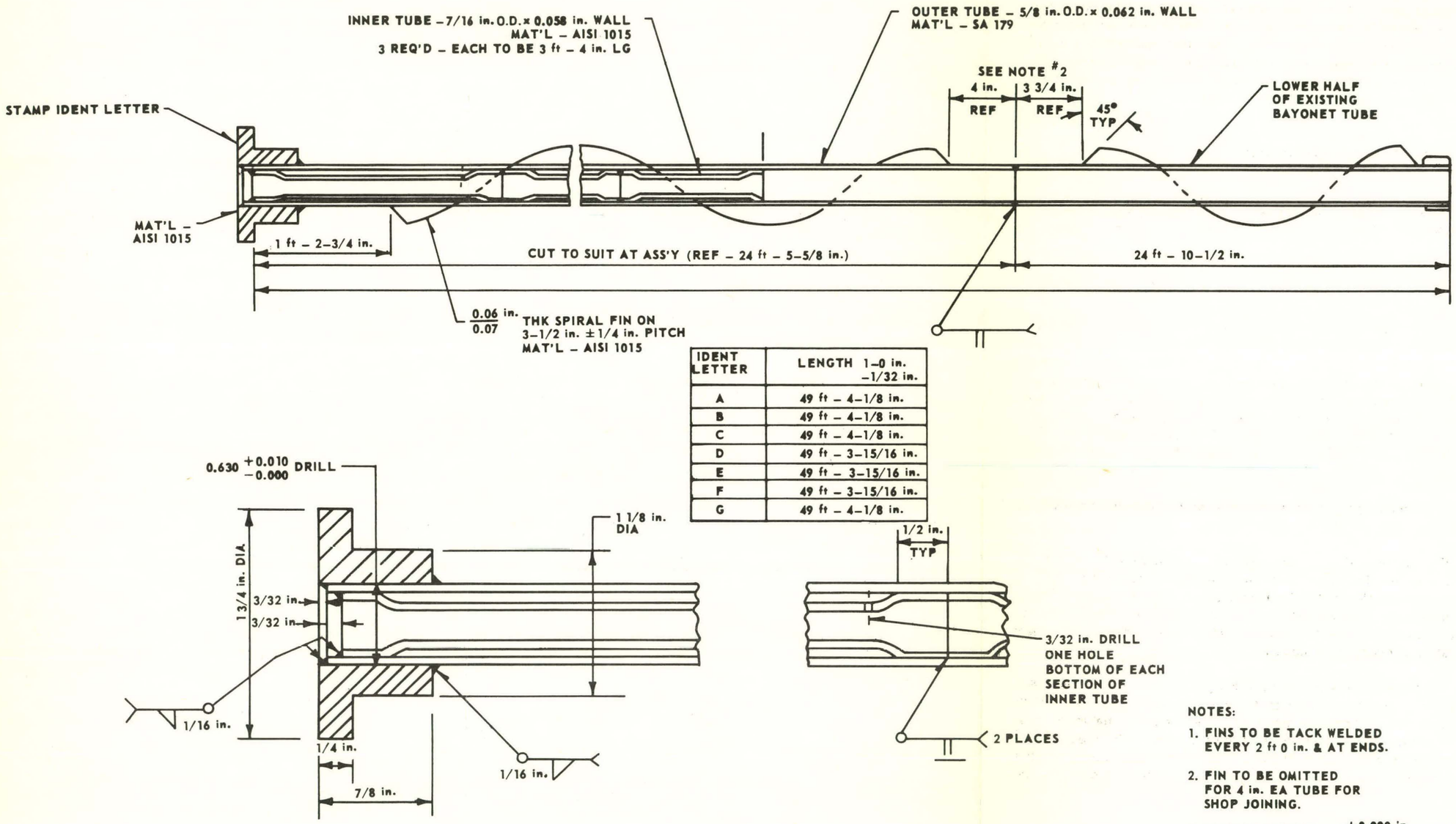

IDENT LETTER	LENGTH 1–0 in. –1/32 in.
A	49 ft – 4–1/8 in.
B	49 ft – 4–1/8 in.
C	49 ft – 4–1/8 in.
D	49 ft – 3–15/16 in.
E	49 ft – 3–15/16 in.
F	49 ft – 3–15/16 in.
G	49 ft – 4–1/8 in.

NOTES:

1. FINS TO BE TACK WELDED EVERY 2 ft 0 in. & AT ENDS.
2. FIN TO BE OMITTED FOR 4 in. EA TUBE FOR SHOP JOINING.
3. FIN O.D. TO BE $1.175^{+0.000}_{-0.032}$ in.
4. ALL FINS TO BE DEBURRED.

Figure 4-8. Details of the Insulated Bayonet Tube Design Used With the P/D = 3 Swirl Generator Insert

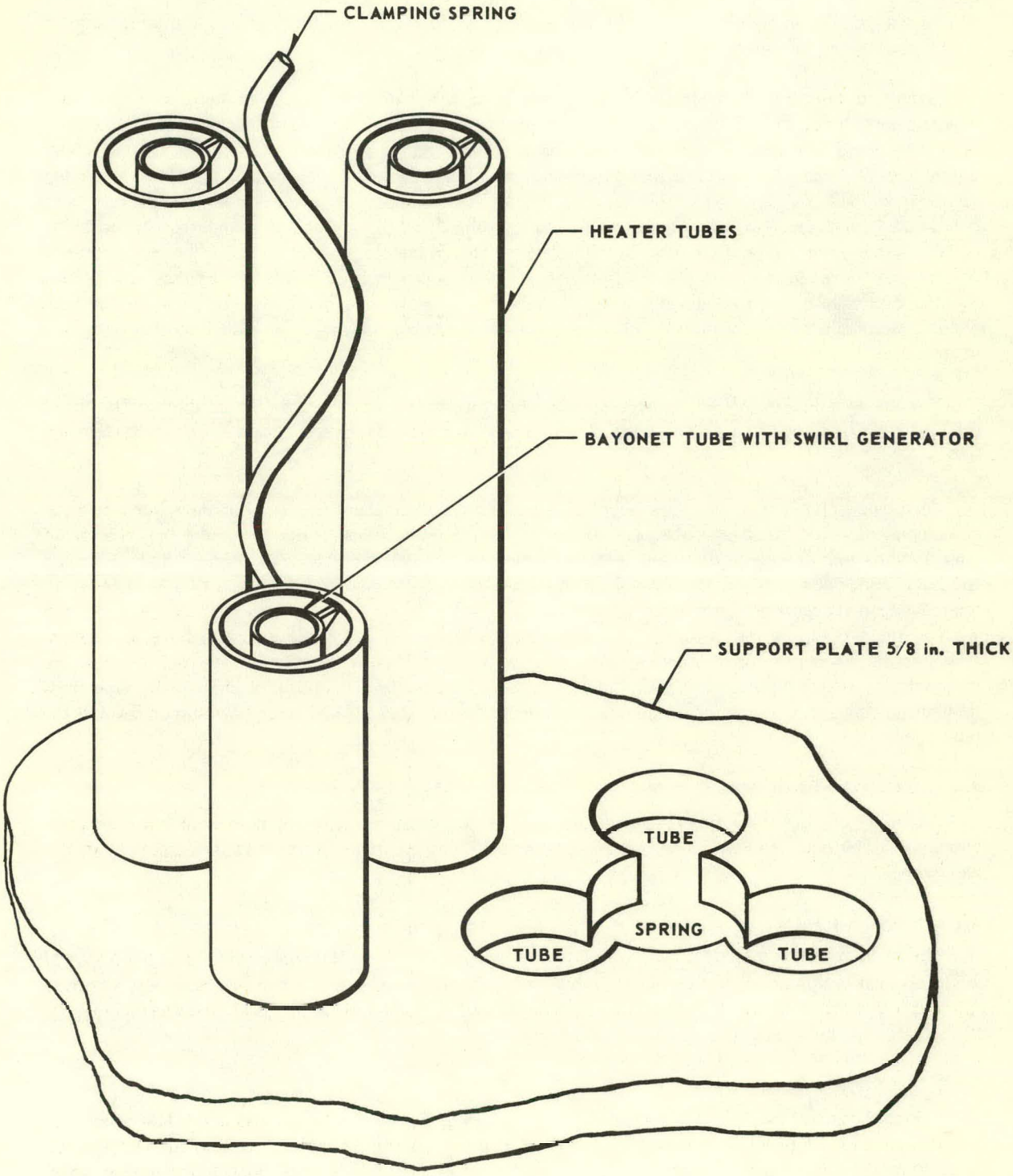

Figure 4-9. Schematic Diagram of Evaporator Tube Support

the same types and locations of welds were used as were planned to be used on the reference design superheater.* Two of the three tubes are active heat transfer tubes, and one tube is inactive (plugged) in order to provide a mechanical test of a tube that is out of service. The nominal design point thermal power is 500 kWt at 1525 psia, 905°F outlet steam pressure and temperature. An outline drawing of the test section is given in Reference 2. Figure 4-10 shows the internal arrangement. Views of the tube bundle for the superheater are shown in Figures 4-11 and 4-12.

Saturated steam from the test rig steam drum enters Nozzle N-1, flows downward through the downcomers, flows upward through the helical coil receiving heat from the sodium that flows downward in counterflow, enters the risers, and exits through Nozzle N-2 as superheated steam. Hot sodium from the test rig heater enters through Nozzle N-3 and is distributed around the coil circumference by a distributor plate. A calming baffle is located above the entrance nozzle to minimize fluctuations of the sodium level. The sodium flows downward over the coil in the annulus formed by the inner and outer shrouds. A high resistance baffle is located in the annulus at the bottom of the coil to maintain a uniform sodium flow over the circumference of the coil. The sodium then flows inside a bellows seal, which is used to prevent bypass flow around the coil, and exits through Nozzle N-4. The tube/tube-sheet welds were made by use of the internal bore welding technique.[8] The tube/tube welds were made by an orbital welding torch, which is also described in Reference 8.

The coil is supported by three radial support plates which are welded to the inner shroud. The tubes are clamped to the support plate by means of a clamping bar arrangement which uses a shear-type clamping action.

To provide pressure relief in the event of a sodium-water reaction, two 6-in.-diameter rupture discs are employed — one located in Nozzle N-10 at the top and the other in the bottom of the inner relief duct. In the event of a large tube leak and associated sodium-water reaction, the rupture disc at the top will burst and, depending on the location of the leak, the rupture disc at the bottom may also burst; in this case, the reaction products will bypass the high-resistance flow path through the coil assembly and will flow up through the inside of the inner relief duct, which is gas-filled and extends above the sodium level into the cover gas space. Bursting of the rupture disc in Nozzle N-10 will allow the reaction products to flow to the reaction products disposal tank provided in the test rig. Further protection of the shell from damage in the event of a large sodium-water reaction is provided by the outer flow shroud around the tube bundle.

4.4 AUXILIARY EQUIPMENT

A brief description of the major auxiliary equipment will be given below. For a more complete description of this and other equipment and their operating experience, see the topical report on this subject, Volume 1, Reference 2.

4.4.1 Sodium Heater

The sodium heater employed as the heat source is designed for a nominal heat load of 2000 kWt at a sodium exit temperature of 1300°F. The sodium is heated inside a single helical coil, 558 ft long and 4.5 in. o.d. with 0.237-in. wall thickness, providing a total heat transfer surface of 656 ft^2. The design pressure is 250 psig and the sodium flow capacity is 200 gpm.

4.4.2 Air-Cooled Condenser

For dissipation of the heat transferred to the steam, an air-cooled condenser was used. The condenser was designed for 2000 kWt at maximum pressure of 600 psi and 900°F. The horizontal tube bundle manufactured from Type-304 stainless steel consisted of three rows of 10-in. o.d., 10 ft-long tubes across which atmospheric air was blown upwards by a 6-ft-diameter fan positioned below the tube bank. The air flow and the corresponding cooling capacity were controlled by louvers positioned above the tube bank.

* The helical coil concept for the reference design superheater for the demonstration plant has now been replaced with a bayonet tube concept.

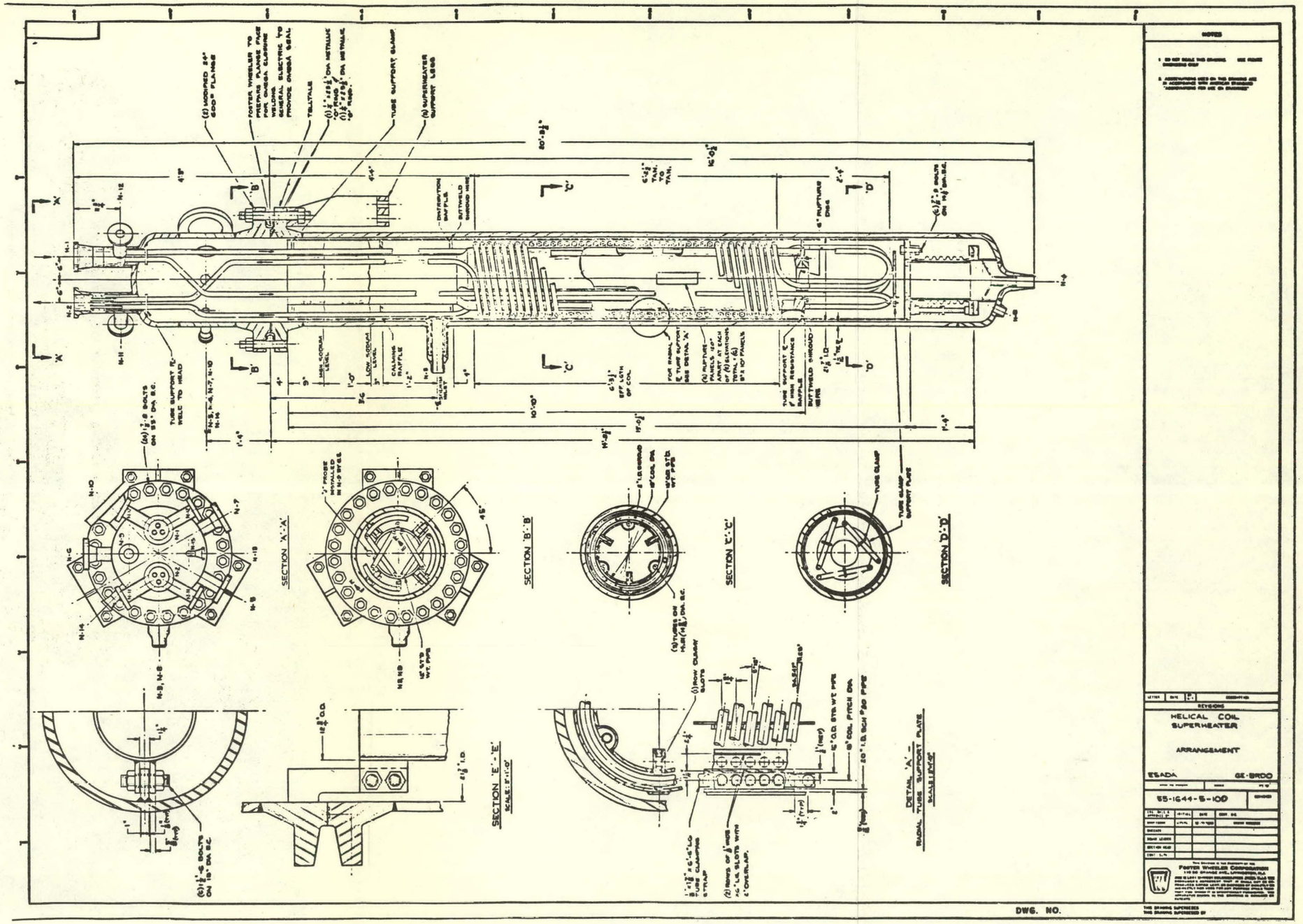

Figure 4-10. Internal Arrangement of Superheater Test Section (Courtesy Foster Wheeler Corporation)

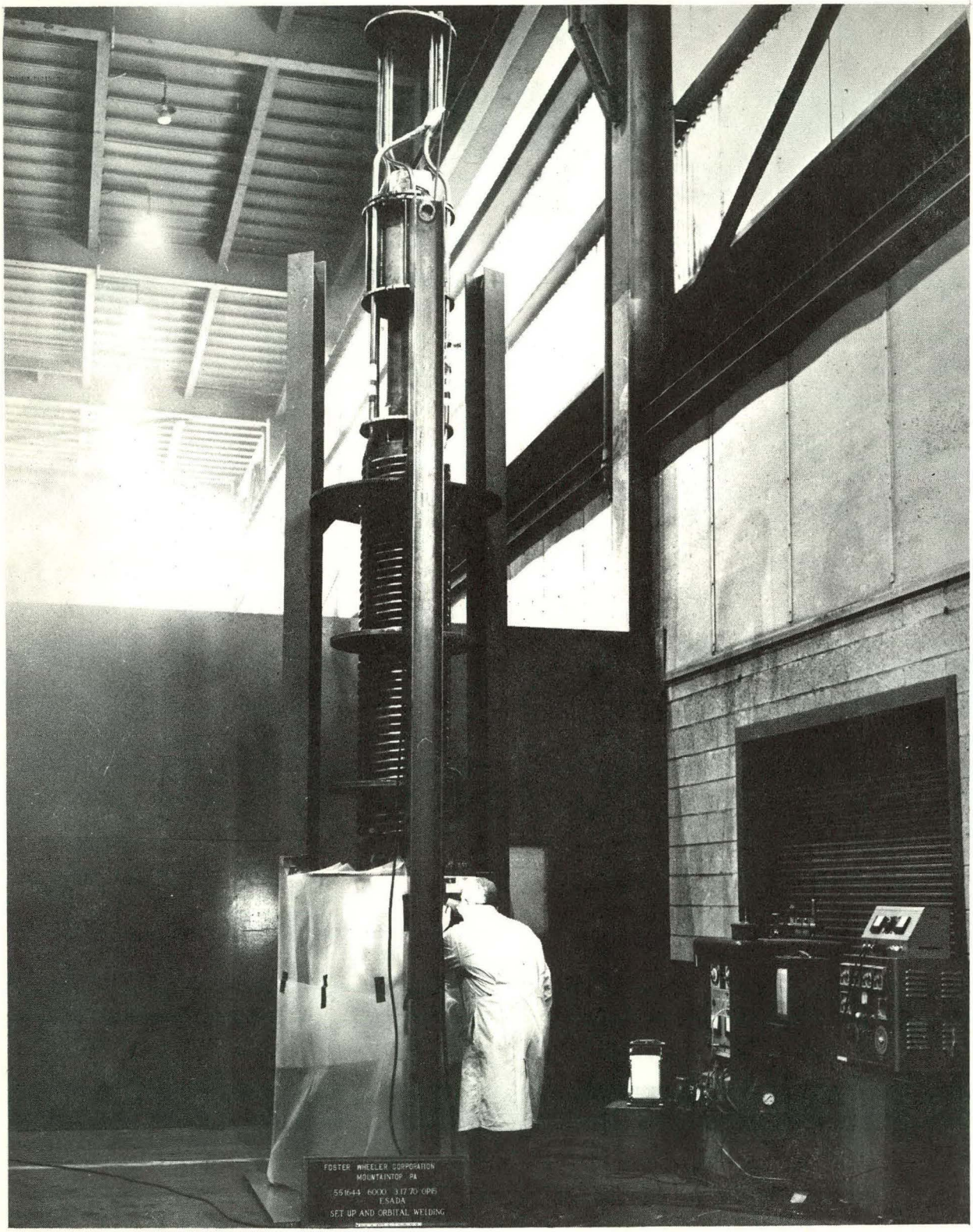

Figure 4-11. ***Coiled-Tube Superheater Test Section Bundle during Assembly (Courtesy Foster Wheeler Corporation)***

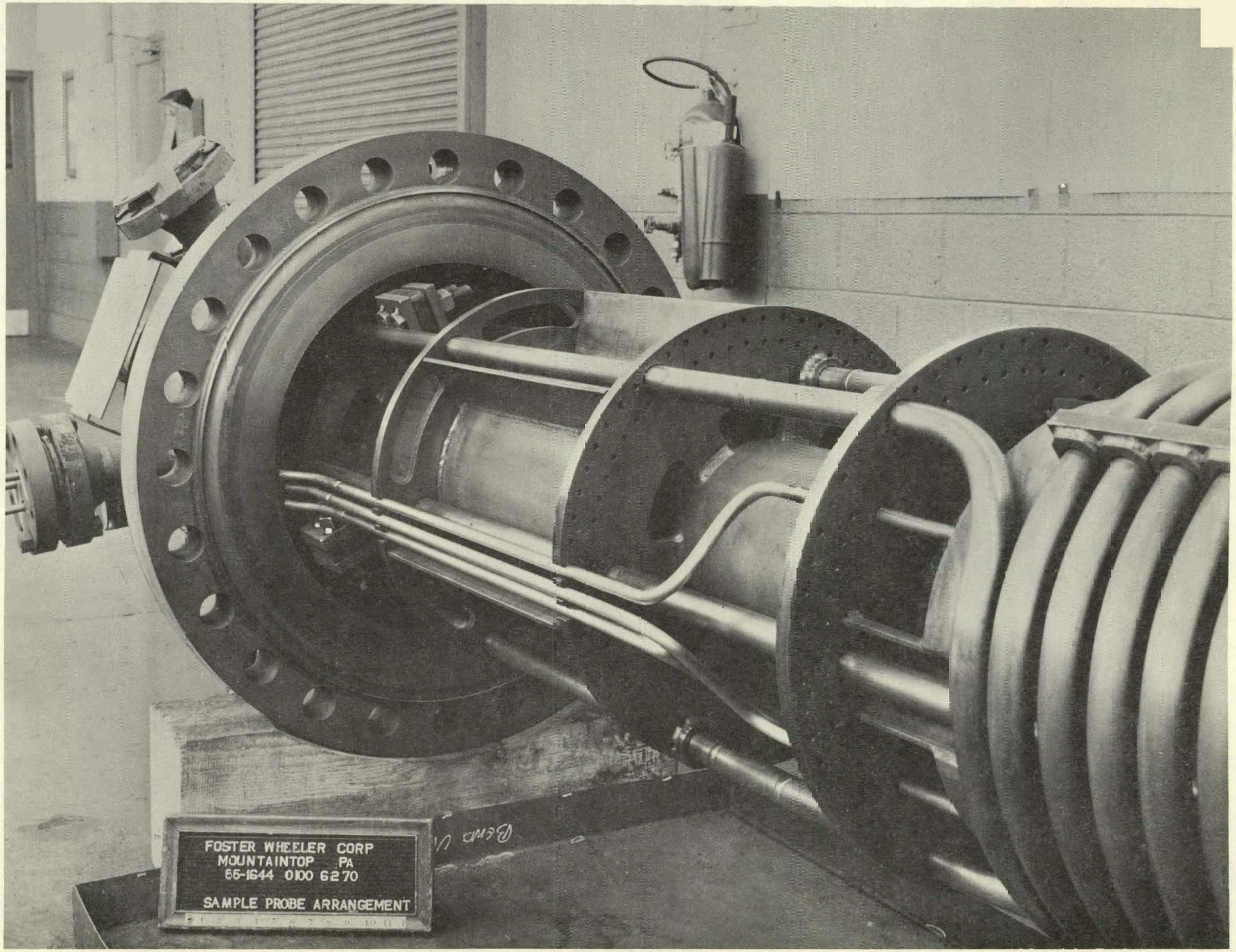

Figure 4-12. Upper Portion of Tube Bundle for Coiled-Tube Superheater Test Section (Courtesy Foster Wheeler Corporation)

4.4.3 Pumps

The electromagnetic pump used in the sodium loop is of the helical induction type rated at 200 gpm and 125 psi developed pressure with a top sodium temperature of 800°F. The power supply is three-phase, 480 V, 60 Hz.

The water recirculation system contained a centrifugal pump rated at 60 gpm (20000 lb/h) with a head of 100 psi. The control of the recirculation flow rate was by a throttling valve located between the pump and the evaporator inlet.

The condensate feed pump was of the reciprocal piston type rated at 20 gpm (8000 lb/h) with a design head of 2500 psia.

4.5 DATA ACQUISITION

The main component in the data acquisition system is a Hewlett Packard HP 2114A small, general-purpose computer with a 8K memory. With appropriate programming and auxiliary hardware, this computer stores transducer signals, performs preliminary data reduction, and provides a permanent record of operating conditions for subsequent analysis.

In addition to the above, one six-channel and one eight-channel Sanborn oscillograph recorder were available and used for the DNB and stability tests.

The recorded data were used as input to the two data reduction codes (EVAP and SUPER) prepared for this purpose, from which detailed information on the performance was deduced. These codes perform complete thermal-hydraulic analysis of the two test sections using finite difference approximations and appropriate physical models of the two units. The codes use the actual measured inlet conditions as a starting point. The calculated exit conditions and the sodium temperature profiles are compared to the actual measured quantities and a near complete match is achieved by adjusting parameters in the heat transfer correlations used in the codes. A summary description of these codes is given in Appendix A.

4.6 INSTRUMENTATION AND CALIBRATION

The initial test operation with the complete system on-line revealed a number of anomalies in the instrumentation. A complete check of the instrumentation system was necessary in order to obtain useful test data.

4.6.1 Temperature Measurements

The locations of the thermocouples used to determine the sodium temperature distributions in the evaporator and superheater test sections are shown in Figures 4-13 and 4-14, respectively. Also, the thermocouples located on the outside of the evaporator are shown in Figure 4-13. The thermocouples used to measure the departure from nucleate boiling characteristic of the evaporator were attached to the heater tube walls as shown in Figure 4-15; a view of the tubes with the DNB thermocouples attached is given in Figure 4-16.

Most of the chromel-alumel thermocouples were connected by continuous lengths of insulated cable to a controlled reference junction maintained at 150°F ±0.01. Thermocouples measuring the sodium inlet/outlet temperatures of the models were connected to the cold junction by continous lengths of chromel-alumel cable to minimize errors.

For measurements of loop temperatures such as heater inlet and outlet temperatures, evaporator inlet and outlet temperatures, etc., chromel-alumel thermocouples were installed in commercially designed thermowells as shown in Figure 4-3.

To ensure accurate and consistent sodium temperature measurements, an isothermal calibration was performed in which sodium was circulated at various temperature levels through the rig and test sections. Subsequent analysis of the data in which the sodium heater exit temperature reading was selected as a reference showed that the maximum deviation from this occurred at the evaporator exit which read about 7°F lower in temperature than the reference at the lowest sodium flow rate.

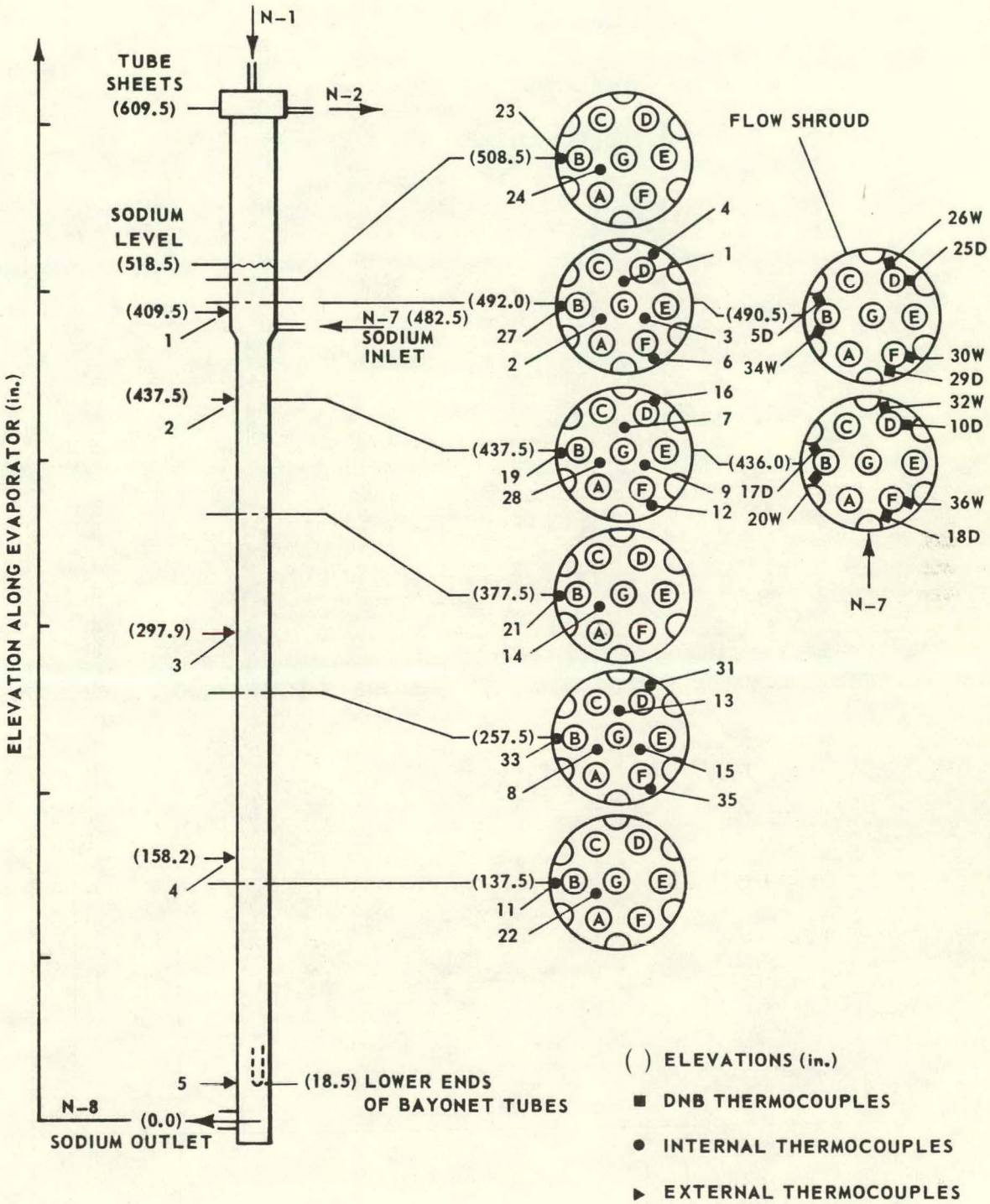

Figure 4-13. Diagram Showing Positions of Evaporator Test Section Thermocouples

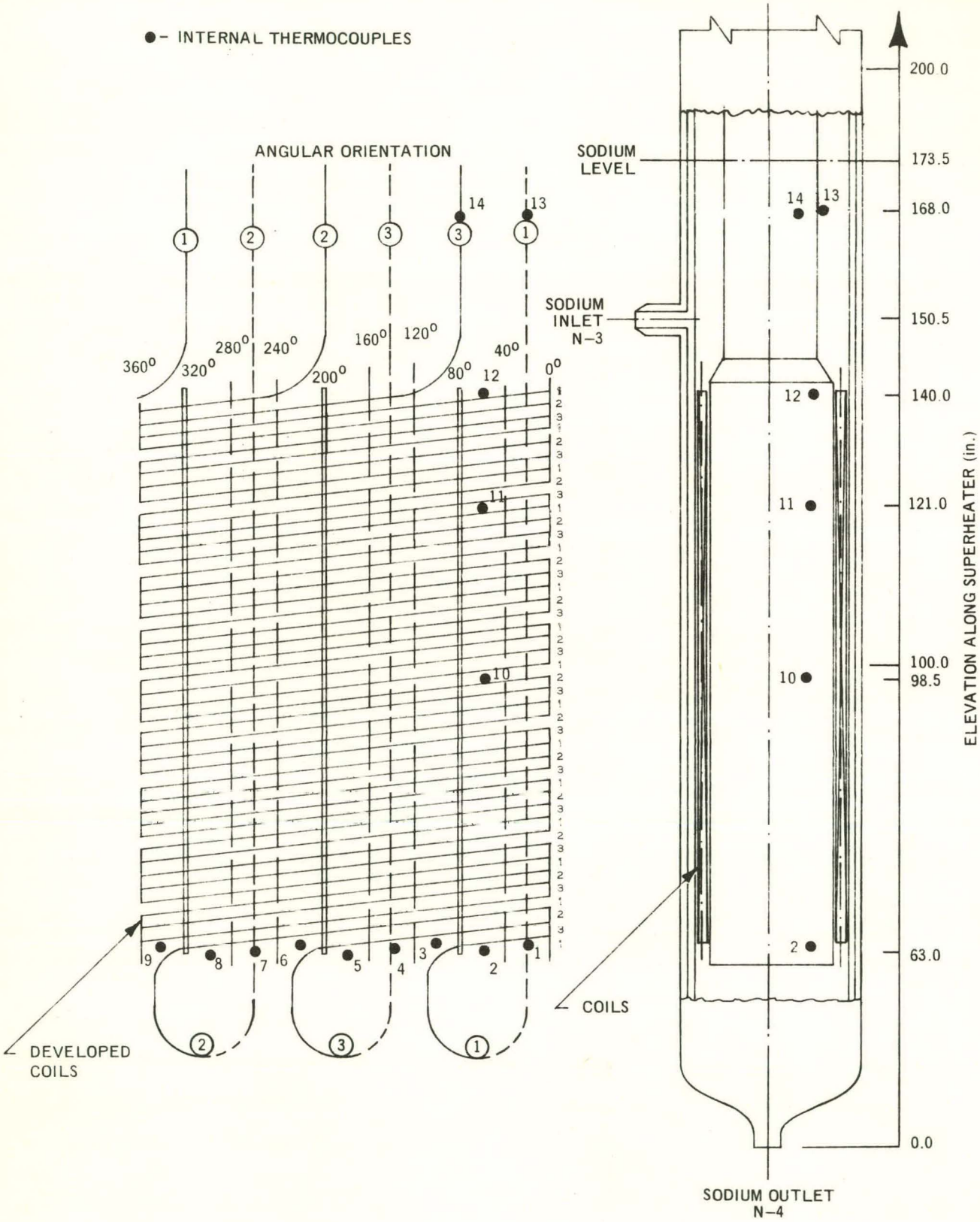

Figure 4-14. Diagram Showing Positions of Superheater Test Section Thermocouples

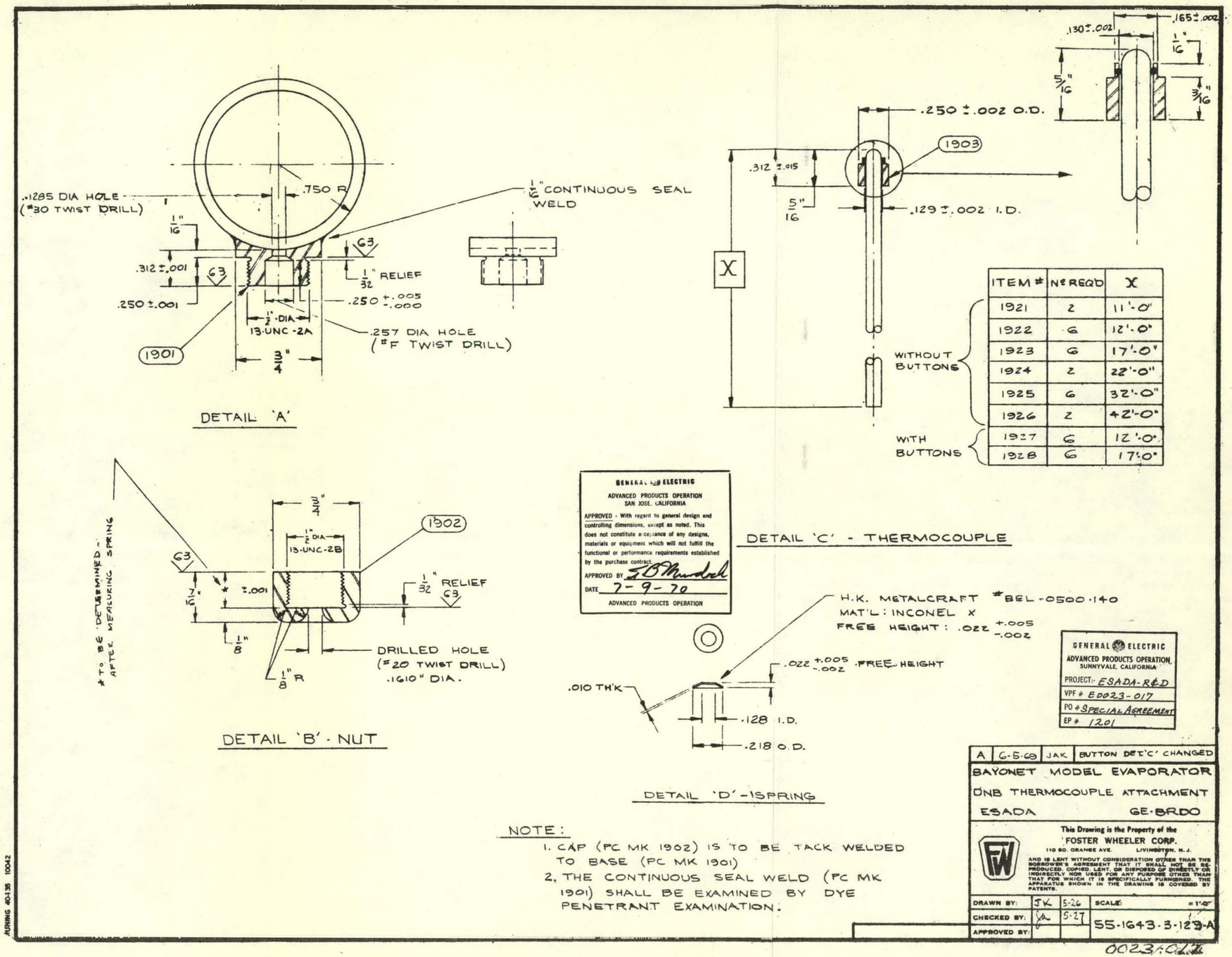

NOTE:

1. CAP (PC MK 1902) IS TO BE TACK WELDED TO BASE (PC MK 1901)
2. THE CONTINUOUS SEAL WELD (PC MK 1901) SHALL BE EXAMINED BY DYE PENETRANT EXAMINATION.

ITEM #	Nº REQ'D	X
1921	2	11'-0"
1922	6	12'-0"
1923	6	17'-0"
1924	2	22'-0"
1925	6	32'-0"
1926	2	42'-0"
1927	6	12'-0"
1928	6	17'-0"

Figure 4-15. Details of Departure from Nucleate Boiling Thermocouples (Courtesy Foster Wheeler Corporation)

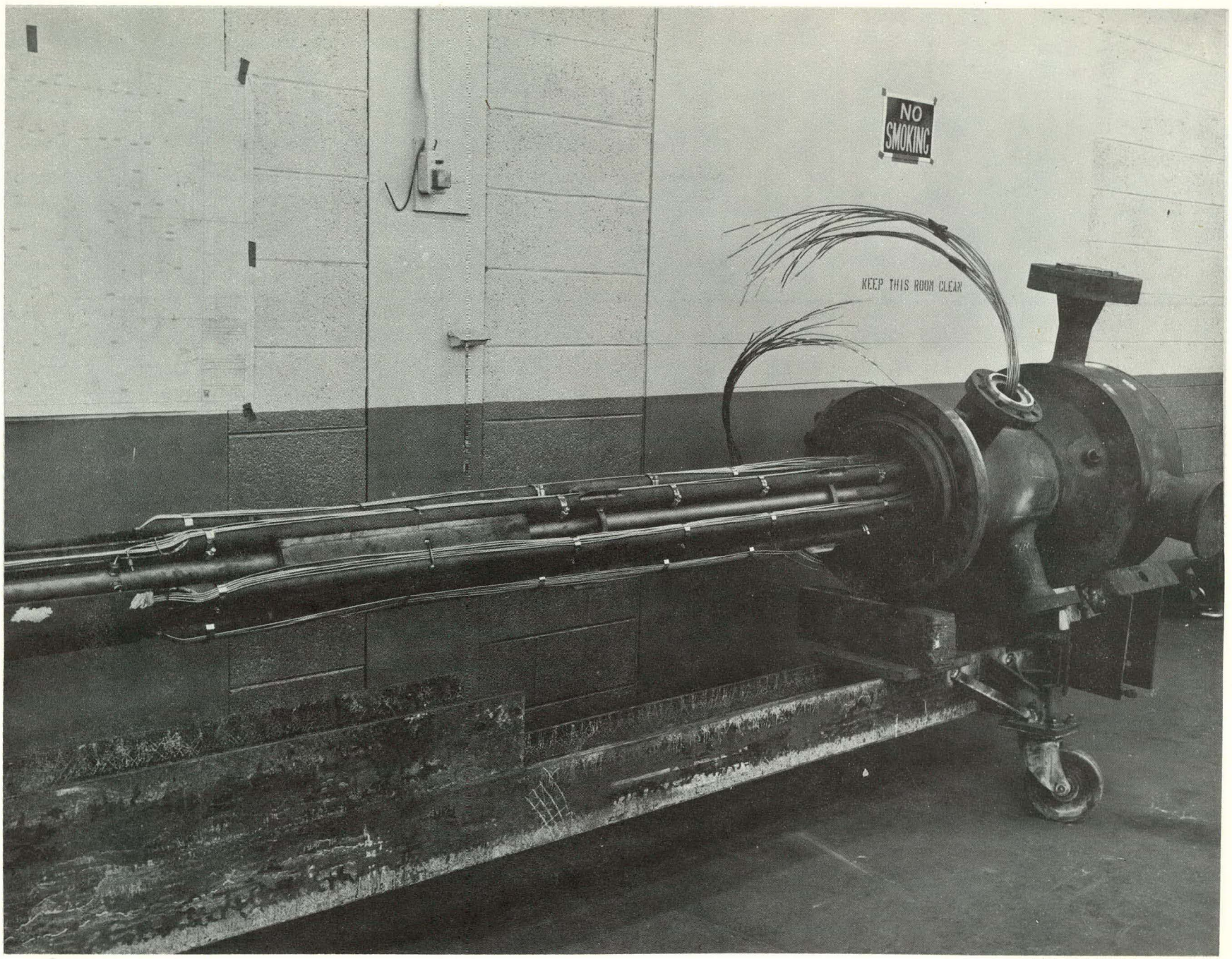

Figure 4-16. View of the Evaporator Test Section Tube Bundle with the DNB and Sodium Thermocouples Attached (Courtesy Foster Wheeler Corporation)

The thermocouples attached to the outside surface of the vessel were subjected to considerably larger errors (approximately 60°F) due to convection of air vertically between the vessel and the insulation (approximately one-in. gap). This condition was corrected on several key thermocouples and the deviation from the reference isothermal sodium was reduced to approximately 12°F.

Since the deviations from the reference thermocouple reading did not vary much with flow rate or temperature level and the heat losses were relatively small, a standard set of corrections at intermediate flow rate and temperature level was selected and applied in the subsequent data analysis. Time limitations did not permit the isothermal tests to be performed at regular intervals and some instrument drift could have occurred; however, in subsequent data analysis, no anomalies were uncovered. Thus, the accuracy of the sodium temperature measurements is believed to be within ±0.5% of the reading after the standard set of correction factors had been applied. The sodium thermocouples mounted inside the test sections are believed to be more accurate than this. It should be noted that only two of a total of 50 internal sodium and DNB thermocouples failed during the test program.

Steam temperature measurements such as condenser outlet, feedwater inlet, superheater outlet, etc., were measured using chromel-alumel thermocouples in thermowells of the same design and output provision as were used for the sodium loop temperature measurements. These thermocouples were calibrated by circulating water at approximately 500 psia pressure through the entire steam-side system. It was impossible to obtain completely isothermal conditions around the loop because sodium was present in the system during the tests and some heat losses could not be avoided in the inactivated condenser and the connecting piping. The thermocouples were found to be within 10°F of each other and the temperature readings at locations where it was known that saturation conditions existed were in excellent agreement with the corresponding saturation temperature at the existing pressure. This provided a check on the pressure measurements as well. The accuracy of the steam-side temperature measurements is believed to be within ±1%.

Additional thermocouples were installed later in the test program as the need arose. This included the insertion of two approximately 50-ft-long thermocouples into bayonet tubes B and G to measure the subcooling of the water as it enters the annuli. These thermocouples were later pulled up to approximately the elevation of the upper set of departure from nucleate boiling thermocouples. One thermocouple was inserted into one of the stability pressure taps in the tube-sheet to indicate superheat in the once-through boiling and stability experiments. In order to evaluate the steam temperature unbalance at the superheater exit, two thermocouples were installed in the two active tubes through holes drilled in the tube-sheets.

4.6.2 Pressure Measurements

System pressures and pressure differences were monitored on the sodium-side and on the steam-side (see Figure 4-2 for measurement points). The pressure taps were installed in accordance with the manufacturer's instructions as shown in Figure 4-3.

The cover gas pressures in the two test models were measured using GEMAC pressure transducers connected directly to the data acquisition system; sodium outlet pressures were measured by Taylor pressure transducers. The differential pressure drops were obtained from these by subtraction of the signals in electronic summers. In-loop calibration procedures to check the pressure readings relative to each other were not feasible; therefore, the transducers were bench calibrated using a dead weight tester. The accuracy of the sodium-side pressure readings was estimated to be ±2%; however, pressure differentials based on electronic summation of absolute readings were not very accurate, especially when small pressure differentials were involved. It was found that the pressure differentials obtained by subtraction of absolute pressures were often more consistent; however, for small pressure differentials, the accuracy obtained by this method too must be considered poor.

The steam-side pressure measurements included the evaporator inlet and outlet, the steam drum, and the superheater inlet and outlet pressures (Figure 4-2). Differential pressure drops were obtained from these by subtraction of the signals in electronic summers. The pressure transmitters were bench calibrated and

the relative readings compared under near isobaric loop conditions at normal operating pressure and were found to be in satisfactory agreement. The pressure readings were also in good agreement with the saturation pressure deduced from simultaneous reading of the saturation temperature. The accuracy of the steam-side pressure readings is estimated to be ±1%.

In addition to the above, a Barton differential pressure gauge was used to measure the pressure drops across especially designed orifices at the bayonet tube inlets to measure the steam-side flow distribution (Figure 5-24). This transmitter was later used to measure steam-side pressure drops during the steam-side stability testing.

4.6.3 Sodium Flow Measurements

The sodium flow measurements were provided by three different electromagnetic flowmeters, one located in the line between the superheater and evaporator, one in the exit line from the evaporator, and one between the electromagnetic pump and sodium heater (Figure 4-2). The flowmeters were of the permanent magnet type using 2-in. i.d. X 0.165-in. wall stainless steel piping with approximately 3 ft of straight tubing upstream and downstream of the flowmeters.

The flowmeters were calibrated using an ASME orifice plate installed in a bypass line for this purpose (Figure 4-2) as a standard. The magnetic flux strengths of the magnets were checked and the magnets stabilized. After these corrections, a final calibration was made in which it was found that the sodium flow calculated from the pressure differential across the orifice plate was within 2% of the predicted flow rates of the electromagnetic flowmeters. Time limitations did not permit this calibration procedure to be performed periodically; however, there were no indications of any major drift between the individual meters. The signals from the electromagnetic flowmeters were connected directly into the data acquisition system.

4.6.4 Water/Steam Flow Measurements

Water/steam flow measurements were made at three locations using ASME orifice plates. The feedwater flow rate was measured between the condensate feed pump and the steam drum, the recirculation flow rate between the recirculation pump and the evaporator inlet, and the steam flow rate between the steam drum and the superheater (Figure 4-2).

The orifice plates were installed using flange taps in accordance with the ASME code (Figure 4-3). The impulse lines were connected to differential pressure transducers and the transducer signals were taken directly to the data acquisition system using shielded cables.

Correction factors accounting for variations in the actual fluid densities which were often considerably different from the reference calibration fluid conditions were applied to the output signals in the data acquisition system using measured actual fluid conditions. The measured flow rates were found to be within 2% of each other. This is well within the ±5% accuracy quoted by the manufacturer.

The recirculation flow rate turned out to be one of the most important measurements and no direct comparison could be made since there was only one measurement point. Indirect checks could be made by using a sodium heat balance on the evaporator and the steam flow measurement. The accuracy was found to be within ±5% when correction for the fluid density was made.

4.7 TEST PROCEDURE

4.7.1 Thermal Performance Tests

The test procedure generally followed was to establish the desired operation conditions. The system was then allowed to stabilize at these conditions for approximately 30 min before the data were recorded by the data acquisition system. Difficulties were sometimes encountered in holding for 30-min truly steady-state conditions as a result of system control dynamics triggered by a slight drift in heater temperature.

4.7.2 Departure from Nucleate Boiling Tests

In order to simplify the operation of the system, the evaporator was operated alone with the superheater bypassed during the departure from nucleate boiling tests. The main parameters varied were the sodium flow and inlet temperature and the recirculation flow rate. The general test procedure was to establish conditions below the DNB point and let the system stabilize for about 25 min. The steam exit quality was then generally about 50% with nucleate boiling over the entire boiling region. The recirculation flow rate was then reduced in small steps, corresponding to increasing the exit steam quality, until the DNB thermocouple traces on the Sanborn recorders started to deflect, indicating a change in heat transfer characteristics from fully nucleate to partial film boiling. A complete recording of data was then made using the data acquisition system. The recirculation flow rate was further reduced in steps until the exit quality exceeded 100% and film boiling prevailed near the DNB measurement point. This procedure was repeated for different sodium inlet conditions in order to vary the heat flux and power level in the evaporator at DNB.

4.7.3 Stability Tests

The steam-side stability test procedure was similar in most respects to the DNB test procedure. The recirculation flow was reduced slowly in steps, allowing about 20 min between steps for one complete data set to be recorded. Important hydraulic stability parameters were recorded on the Sanborn recorders, such as steam-side plenum pressures, pressure drops, and thermocouples located in the boiling tubes and in the sodium. The recirculation rate was reduced until instabilities were detected on the recorders. The unstable mode was maintained long enough to allow several complete data sets to be recorded. The recirculation flow rate was then increased in steps until stable conditions were reached. This entire procedure was then repeated at other power levels by adjusting sodium conditions.

5. EVAPORATOR THERMAL PERFORMANCE

The following subsections contain the bayonet tube evaporator test section thermal performance results. This includes the measured overall heat transfer coefficients for the boiling region and the sodium-side Nusselt number correlation derived from these measurements. The departure from nucleate boiling results are presented along with the steam-side heat transfer performance in the transition boiling regime. The available data on the steam side flow distribution are presented along with the sodium-side and steam-side pressure drops.

5.1 HEAT TRANSFER PERFORMANCE

The usual method used in evaluating the thermal performance of a heat exchanger device is to measure the inlet and outlet temperatures and the flow rates of the two fluids. If the fluid properties can be considered constant and the geometry is clean (i.e., a well-defined geometry), a convenient measure of the thermal performance of the heat exchanger device is the overall heat transfer coefficient calculated from the measured heat transfer rates and logarithmic mean temperature difference.

In liquid metal steam generators, the ideal conditions considered above rarely exist. In the present evaporator, the heat transfer rate has to be derived from measurements at the sodium-side only because the exit enthalpy of the steam-water mixture cannot be measured. The sodium-side geoemtry is rather complex and the sodium properties are changing to some degree. On the steam-side, there are two heat transfer regions where the heat transfer coefficient varies from a relatively low subcooled forced convection coefficient to a very high nucleate boiling coefficient near the exit. Nevertheless, the logarithmic mean temperature difference and the overall heat transfer coefficient are useful concepts if evaluated over certain sections with relatively clean geometry and within a well-defined boiling regime.

In the present investigation of the evaporator performance, the overall heat transfer coefficient in the boiling regime was evaluated using the above methods and by using the EVAP data reduction code. This procedure is based on the concept of matching analytic calculations of the axial sodium temperature distribution as obtained from EVAP to the measured axial sodium temperature distribution by varying parameters in assumed functional forms of the heat transfer correlations.

5.1.1 Data Reduction Procedure

A summary description of the EVAP code is given in Appendix A-1. Basically, the code performs a detailed thermal-hydraulic analysis of the evaporator test section using the best possible nodal mathematical model of the evaporator. This includes mathematical descriptions of the heat transfer coefficients and pressure drops throughout the unit. The heat transfer correlations governing the performance in the boiling region and used as models in the EVAP code are presented below.

For the sodium-side, the Nusselt number is given by:*

$$Nu = \frac{h_{Na} D_H}{k} = C_1 + C_2 (Pe)^{.8} \qquad \textbf{(5-1)}$$

where C_1 and C_2 are constants to be determined.

Selection of the right tube wall thermal conductivity is especially critical since the thermal resistance of the wall constitutes about 60% of the overall resistance. Available data on thermal conductivity of the heater tubes are summarized in Figure 3-6. The spread in the data is great and it is difficult to decide what value should be used. Since the actual value is likely to be somewhere between the extreme values, the data of Reference 32 were selected and used in all subsequent data reduction. These data can be described by:

$$k = 25 - 0.005\ \overline{T}\ (\text{Btu/h-ft-}^\circ\text{F}) \qquad \textbf{(5-2)}$$

* For notation see the nomenclature at the front.

The steam-side nucleate boiling heat transfer coefficient for the present swirl flow geometry is not known from previous experimental data. However, since the thermal resistance of the steam-side is generally a small fraction of the total, Chen's correlation[13] is believed to describe the steam-side nucleate boiling coefficient to a sufficient degree of accuracy. Chen's correlation is given by:

$$h = S\ 0.00122 \times \frac{k_f^{0.79} \times C_{pf}^{0.45} \times \rho_f^{0.49} \times g^{0.25}}{\sigma^{0.5} \times \mu_f^{0.29} \times H_{fg}^{0.24} \times \rho_g^{0.24}} \times \Delta T_{sat}^{0.24} \times \Delta P_{sat}^{0.75} + F\ 0.023 \times Re_f^{0.8} \times Pr_f^{0.4} \times \frac{k_f}{D_H} \quad (\text{Btu/h-ft-°F}) \tag{5-3}$$

Using these correlations, the measured inlet conditions of the sodium- and steam-sides, and the measured sodium and recirculation flow rates as input, the EVAP code was run for a few cases with different values of C_1 and C_2 in the sodium-side correlation until a reasonable agreement between measured and calculated axial sodium temperature distribution was achieved. A typical example of the match achieved for operation at approximately full load is shown in Figure 5-1 and a similar comparison is made for approximately half-load conditions in Figure 5-2. In these figures, the measured sodium temperatures at different axial locations are averages of the thermocouple readings in the edge channel and the center channel. Referring to Figure 5-3, the edge flow channel is here defined by the shell-side flow area between the flow shroud and an imaginary circle through the center of the edge tubes, while the center channel is defined by the shell-side flow area inside this circle. The locations of the sodium thermocouples used to measure the sodium temperature distribution are shown in Figure 4-13. The reason for using average thermocouple readings was that some temperature fluctuations were observed in the sodium in the upper portion of the unit; by taking averages, a better estimate of the real sodium temperature was obtained. (Details about these sodium temperature fluctuations are given in subsection 7.1.2.)

Once a trend in the performance was established, the remainder of the data was processed; a comparison between the measured and calculated sodium temperature distributions was made in each case. Only slight changes in the constants C_1 and C_2 in Equation 5-1 had to be made in a few subsequent cases, after which excellent agreement between measurement and analysis was consistently achieved. Due to temperature and heat flux variations along the evaporator, the individual conductanoos given by the previous correlations were found to vary considerably with axial position along the evaporator. The corresponding local values of the overall heat transfer coefficients varied by about 25% axially in the boiling region with the largest values occurring in the upper portion of the unit near the sodium inlet. An average value of the overall heat transfer coefficient was needed for comparison with design predictions. This average value was calculated from the following relation:

$$1/\bar{U}_{EVAP} = (1/\bar{h}_s)d_o/d_i + (d_o/2\bar{k})\ln(d_o/d_i) + 1/\bar{h}_{Na} \tag{5-4}$$

where the mean values of the individual conductances were calculated using the formula:

$$\bar{h} = \frac{1}{N} \sum_{i=1}^{N} h_i \tag{5-5}$$

where N is the total number of heat transfer coefficients used in the boiling region of the EVAP computer model. The heater tube mean thermal conductivity was calculated using the average of the steam temperature and the sodium inlet temperature.

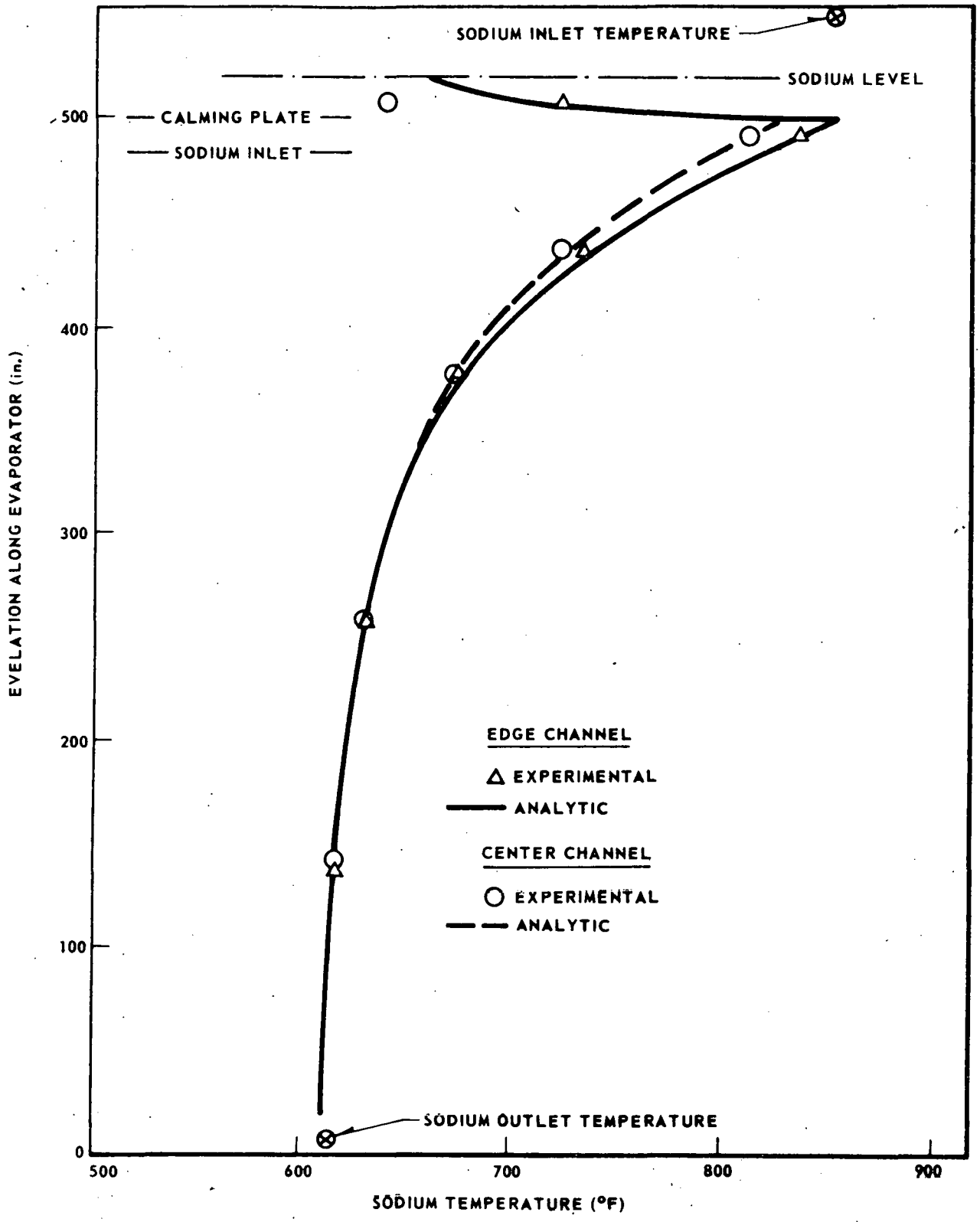

Figure 5-1. *Comparison of Measured Axial Sodium Temperature Profiles for the Evaporator at Approximately 1500 kWt*

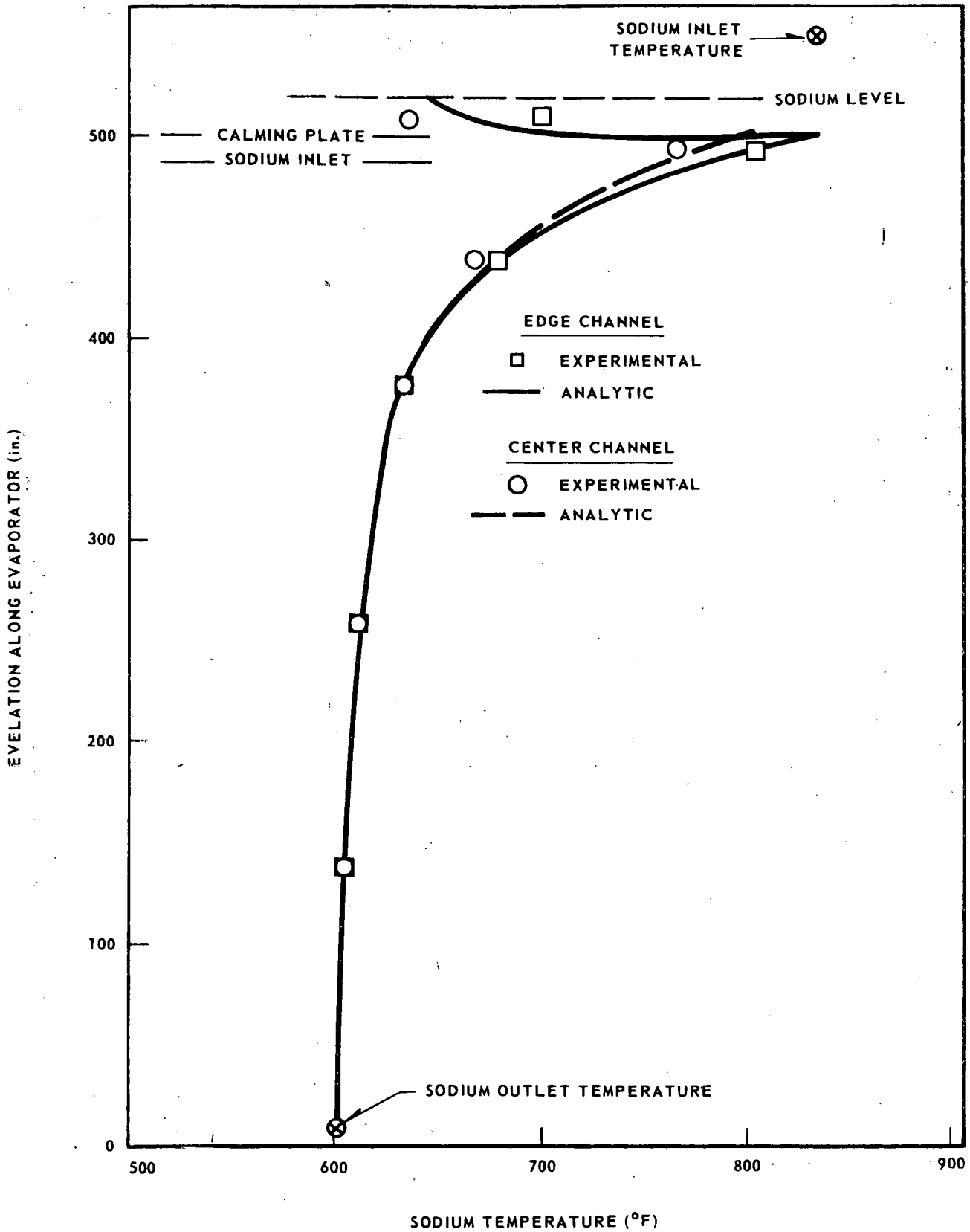

Figure 5-2. *Comparison of Measured Axial Sodium Temperature Profiles and Analytic Profiles for the Evaporator at Approximately 750 kWt*

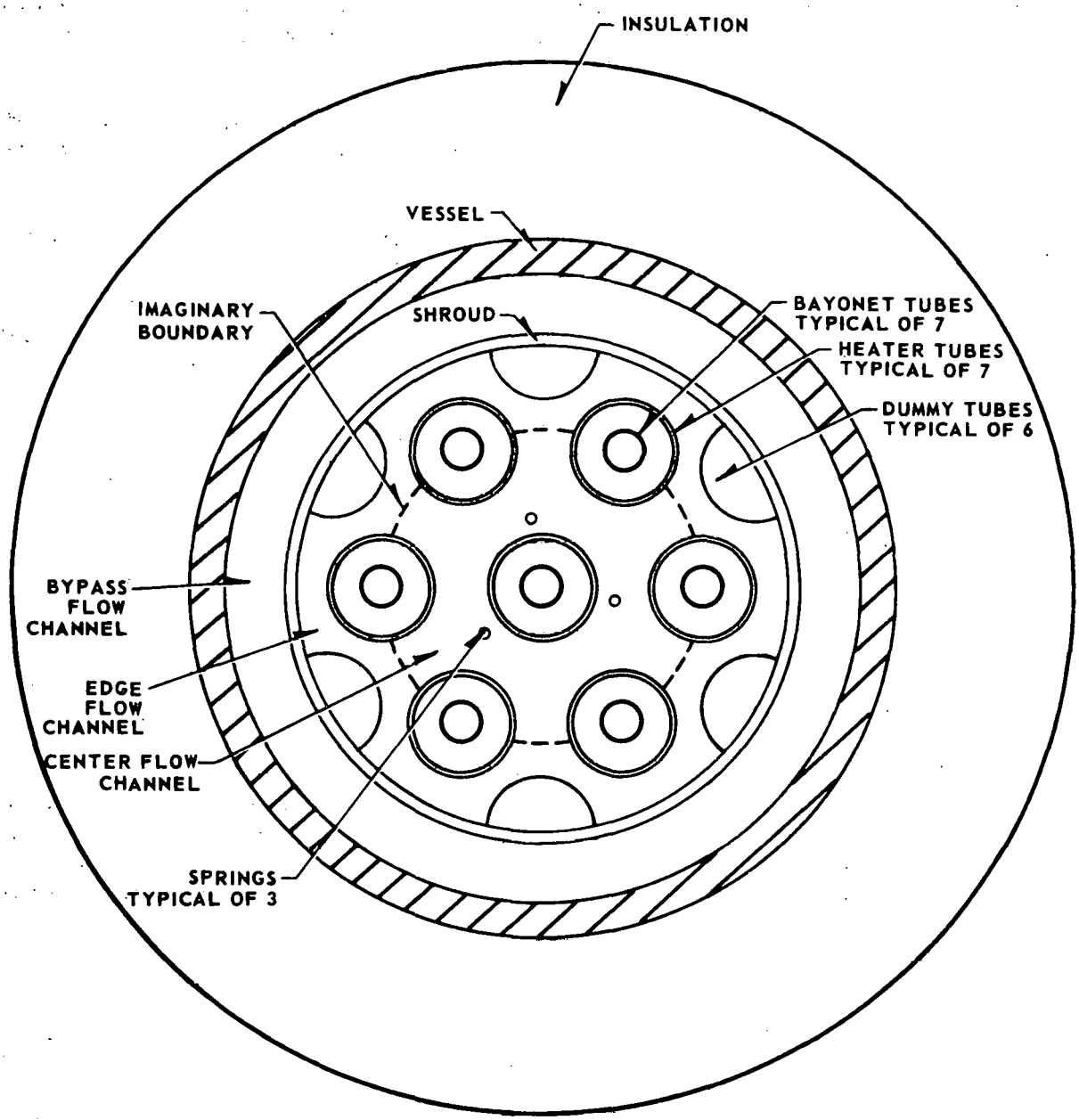

Figure 5-3. Schematic Diagram of a Typical Cross-Section in the Evaporator Test Section

In addition to the thermal performance evaluation procedure just described, the overall heat transfer coefficients over the boiling region were also evaluated using the standard logarithmic mean temperature difference procedure mentioned earlier. This was accomplished by assuming that the sodium temperature distribution in any one axial plane was uniform. The coefficients were evaluated between the plane at elevation 492.0 in. where six thermocouples are located (Figure 4-13), and the plane at elevation 257.5 in. generally above the start of the boiling region.

It is apparent from Figures 5-1 and 5-2 that considerable cross-sectional temperature variation exists near the upper measurement location. A mean temperature at elevation 492.0 in. was obtained by averaging all the thermocouple readings.

A schematic diagram of the system under consideration is shown in Figure 5-4. Neglecting heat losses, the rate of heat transfer in the boiling region on the sodium-side is:

$$Q_b = W(H_{in} - H_{out}) \quad \text{(Btu/h)} \tag{5-6}$$

The logarithmic mean temperature difference for the boiling region is:

$$LMTD_b = \left[T_{in} - t_{out} - (T_{out} - t_{in})\right] \Big/ \ell n \left[(T_{in} - t_{out})/(T_{out} - t_{in})\right] \quad (^\circ F) \tag{5-7}$$

The boiling region overall heat transfer coefficient is then:

$$\overline{U}_{LMTD} = Q_b/(A_b \times LMTD_b) \quad \text{(Btu/h-ft}^2\text{-}^\circ\text{F)} \tag{5-8}$$

The steam-water temperatures used in evaluating $LMTD_b$ were taken from the corresponding EVAP runs.

5.1.2 Boiling Region Overall Heat Transfer Coefficient

The overall heat transfer coefficient was evaluated for 116 runs, of which 16 were regular thermal performance runs of relatively low exit steam quality. The majority of the data, however, were taken during the departure from nucleate boiling tests at high exit steam quality corresponding to some partial film boiling near the upper portion of the unit. The ranges of conditions maintained for the evaporator during the tests were as follows:

- Sodium Inlet Temperature — 740 to 912°F (855)*
- Sodium Outlet Temperature — 595 to 621°F (632)
- Sodium Flow Rate — 39,293 to 94,962 lb/hr (75,000)
- Steam Drum Pressure — 1,555 to 1,674 psia (1,635)
- Steam-Water Flow Rate — 5,882 to 21,020 lb/hr (22,500)
- Water Inlet Temperature — 454 to 575°F (565)
- Steam-Water Exit Quality — 15 to 98% (31.5)
- Thermal Power — 740 to 1,516 kWt (1,500)

* The numbers in parentheses indicate rated or design values.

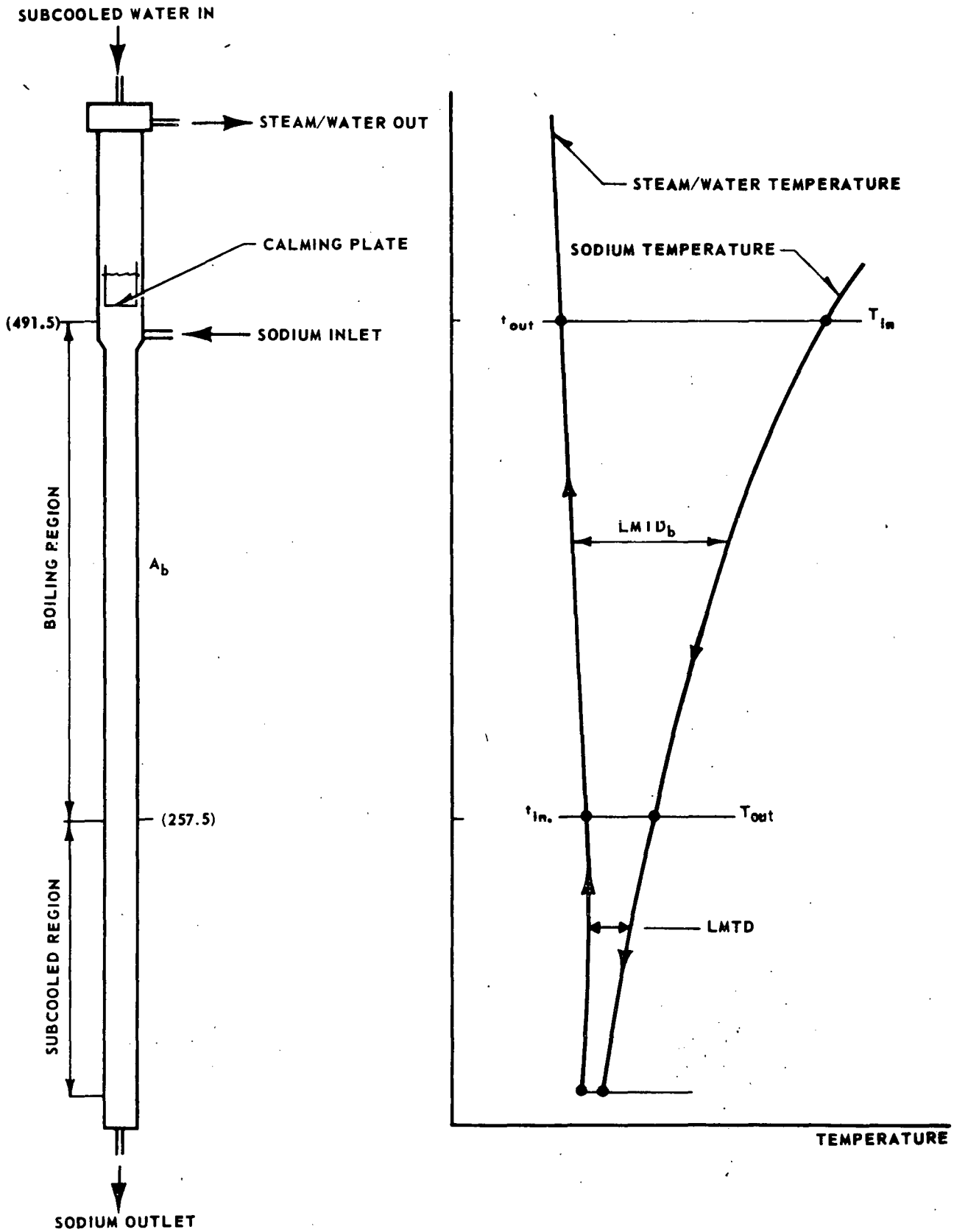

Figure 5-4. *Schematic Diagram of Thermocouple Measurements Used to Calculate the Log Mean Temperature Difference and the Overall Heat Transfer Coefficient*

The measured boiling region overall heat transfer coefficients are presented in Table B-1 in Appendix B-1 along with test parameters.

The overall heat transfer coefficients in the column denoted by $\overline{U}_{EVAP}$ were evaluated using Equation 5-4 with the mean values of the individual conductances from the EVAP code as explained in subsection 5.1.1. The second set of measured overall heat transfer coefficients was evaluated using the log mean temperature approach also explained previously. For comparison, the overall heat transfer coefficients predicted using design methods (no fouling effect) at actual test sodium flow rates but with the design wall thermal conductivity of 16.25 Btu/h-ft-°F and a steam-side heat transfer coefficient of 5102 Btu/h-ft²-°F for all cases* are also presented in Table B-1.

A more detailed comparison of the overall heat transfer coefficients based on the EVAP code results with the design prediction at near-rated conditions is shown in Table 5-1.

Table 5-1
SUMMARY OF EVAPORATOR THERMAL PERFORMANCE FOR THE BOILING REGION AT NEAR-RATED CONDITIONS

HEAT TRANSFER COEFFICIENTS (Btu/h-ft² °F)

Location	Predicted Coefficients	SGTR Experiment[(a)] Exit Steam Quality = 0.34
Overall $\overline{U}$	586	923
Steam Side, $\overline{h}_s$	(Chen's Correlation) 5105	8959
Equivalent Wall, $\overline{h}_w$	(Wall Thermal Conductivity 16.25) 1046	1376
Sodium Side, $\overline{h}_{Na}$	(Seban-Shimazaki Correlation) 1966	4713
Fouling Coefficient, h_f	No Fouling Effect	No Fouling Effect

(a) Run 3-29-71 (2010)
Thermal Power . . . . . 1517 kWt
Steam Drum Pressure . . . . . 1650 psia
Sodium Inlet Temperature . . . . . 856°F
Sodium Flow Rate . . . . . 69100 lb/h

It can be seen from Table B-1 that the measured overall heat transfer coefficients are considerably higher than the predicted values. The scatter in the log mean temperature based values is great, due mainly to the difficulty in determining the actual small temperature difference between the sodium-side and steam-side at the start of the boiling region in the lower part of the unit. A summary of the original data for all runs is given in Table B-2 in Appendix B-1.

The overall heat transfer coefficient was evaluated for the boiling region only since approximately 80% of all heat transfer takes place in this region. In the subcooled region (Figure 5-4), the heat transfer is small and the temperature differences are difficult to determine accurately; therefore, a direct experimental evaluation of the calculated overall heat transfer coefficient was impossible for this region.

The excellent performance of the evaporator compared to design predictions is postulated to be due to the following:

1. The sodium-side conductance is believed to be somewhat higher than one would normally find for parallel flow in rod bundles because the evaporator contains a baffle or support plate with

*This steam-side coefficient was calculated in the original design calculations[33] at a particular flow rate, exit steam quality and heat flux. Although the actual test conditions were generally somewhat different, this value was used for convenience to avoid extensive recalculations since it has small effect on the overall value.

an area ratio* of approximately 0.5 approximately every eight hydraulic diameters along the bundle (for details see Figure 4-6). The heater tubes are held against the support plates by three springs along the entire length of the tubes as indicated schematically in Figure 4-8. The net effect of this geometry is to introduce additional mixing effects as compared to a "clean" rod bundle, thus increasing the effective Reynolds number of the flow. Also, in the upper portion of the unit where the sodium flows across the six-edge tubes (Figure 4-7) and enters the tube bundle, there is a considerable cross-flow component; and, since the heat transfer rate is the largest here, this could have some effect on the overall performance. Finally, the sodium-side conductance was estimated using the Seban-Shimazaki[5] correlation which is believed to be very conservative for this geometry.

2. The heater tube wall thermal conductivity is probably higher than the value of 16.25 Btu/h-ft-°F used in the design prediction. The compilation of thermal conductivity data shown in Figure 3-6 support this assertion, since it falls on the very low side of the available data.

3. Finally, the steam-side heat transfer coefficient may be somewhat higher than predicted by the Chen's nucleate boiling correlation[13] due to the swirl flow in the annulus. However, this effect is believed to be small, since the steam-side contributes little to the overall heat transfer resistance.

The previous evaluation has yielded overall heat transfer coefficients for the boiling region based on matching of the calculated sodium temperature profile and based on measured sodium temperatures and log mean temperature differences. The EVAP calculations resulted in a heat transfer correlation for the sodium-side by the determination of C_1 and C_2 in Equation 5-1.

The object of the next subsection will be to separate the sodium-side conductances from the measured overall conductances by the Wilson-plot technique[34] and obtain a sodium-side heat transfer correlation that is based on direct measurements. Of course, one would expect to obtain near identical correlations by the two methods.

5.1.3 Boiling Region Sodium-Side Heat Transfer Coefficient

When the overall heat transfer coefficient is available from measurements, it is often possible to separate the individual conductances making up the overall conductance and obtain a correlation for one of the conductances by a method often referred to as the Wilson-plot technique.[34] The method is particularly useful when one of the heat transfer coefficients is known or has little effect on the overall heat transfer coefficient and the wall conductance can be specified accurately.

In the present investigation, it was desired to obtain a correlation for the sodium-side heat transfer coefficient in the boiling region of the evaporator. The average sodium-side heat transfer coefficient may be evaluated from the following equation obtained by rearranging Equation 5-4:

$$1/\bar{h}_{Na} = 1/\bar{U}_{LMTD} - (1/\bar{h}_s)\ d_o/d_i - (d_o/2\bar{k})\ \ell n\ (d_o/d_i) \qquad \textbf{(5-9)}$$

In this equation, the average overall heat transfer coefficient U is available from direct measurement based on the log mean temperature approach in Table B-1.

Two other quantities are needed for the evaluation: (1) the steam-side heat transfer coefficient $\bar{h}_s$ and (2) the mean thermal conductivity $\bar{k}$ of the heater tube wall. The steam-side conductance for the nucleate boiling regime is assumed to be given by Chen's correlation.[13] This is a reasonable assumption, since the overall heat transfer coefficient is influenced only slightly by the steam-side coefficient in the boiling regime. The heater tube wall, however, constitutes a significant heat transfer resistance and influences the overall heat transfer coefficient strongly (approximately 60% of total). The wall thermal conductivity used in Equation 5-9, therefore, must be selected with care. In this evaluation the data of Reference 32 given by Equation 5-2 were assumed to be correct. The effect of this assumption will be considered later.

The area ratio equals the sodium flow area through the plates/total sodium flow area in bundle.

In order to correlate the sodium-side heat transfer coefficient, a functional form of the correlation must be specified. In the present case, the form of the Seban-Shimazaki correlation given by Equation 5-1 is assumed where the exponent of 0.8 on the Peclet number is retained and the coefficients C_1 and C_2 are to be determined. Substitution of Equation 5-1 into Equation 5-9 and rearranging results in:

$$\frac{D_H/k}{1/\bar{U}_{LMTD} - (1/\bar{h}_s)\ d_o/d_i - (d_o/2\bar{k})\ \ell n\ (d_o/d_i)} = C_1 + C_2\ (Pe)^{0.8} \qquad \textbf{(5-10)}$$

This equation is of the linear form:

$$y = C_1 + C_2 x$$

where

$$y = Nu = \frac{\bar{h}_{Na}\ D_H}{k} = \frac{D_H/k}{1/\bar{U}_{LMTD} - (1/\bar{h}_s)\ d_o/d_i - (d_o/2\bar{k})\ \ell n\ (d_o/d_i)} \qquad \textbf{(5-11)}$$

and

$$x = (Pe)^{0.8} \qquad \textbf{(5-12)}$$

For each run, x and y can be calculated and the data points plotted. If the assumption of the functional form of the correlation is reasonable, the data points should fall on a straight line, the slope of the line being given by C_2 and the intercept with the y-axis (x = 0) given by C_1.

The available heat transfer data obtained from direct measurement were treated in this manner; the resulting Wilson-plot is shown in Figure 5-5. The scatter in the data is considerable, mainly because the scatter in the measured overall heat transfer coefficients is large as is evident from Table B-1. However, considering the complexity of this system, some scatter must be expected, and the results are probably reasonable. The line drawn through the data has the slope $C_2 = 0.1$, and the intercept with the y-axis is $C_1 = 5$. The resulting sodium-side correlation is then:

$$Nu = 5 + 0.1\ (Pe)^{0.8} \qquad \textbf{(5-13)}$$

This is in excellent agreement with the initial trial and error result using the EVAP code.

The extrapolation of the data to very small Peclet numbers is not valid and the selection of $C_1 = 5$ was guided by previous work in this area (e.g., that by Seban-Shimazaki[5]). However, more recent experiments[4] have shown that the Nusselt number is about twice the value given by Equation 5-13 for Peclet numbers less than approximately 200. Therefore, the range of validity of Equation 5-13 is approximately:

$$200 < Pe < 1200$$

Equation 5-13 is valid for this particular geometry (i.e., tube bundles with triangular array configuration with a P/D ratio of 1.5 and with similar tube support geometry). In general, the type of heating is specified to be approximately constant heat flux as in electrically heated rods and nuclear-heated fuel pins or approximately constant wall temperature. The present system is somewhere between the two cases and probably is closer to the constant wall temperature case; this imposes an additional limitation on Equation 5-13 for application to other systems.

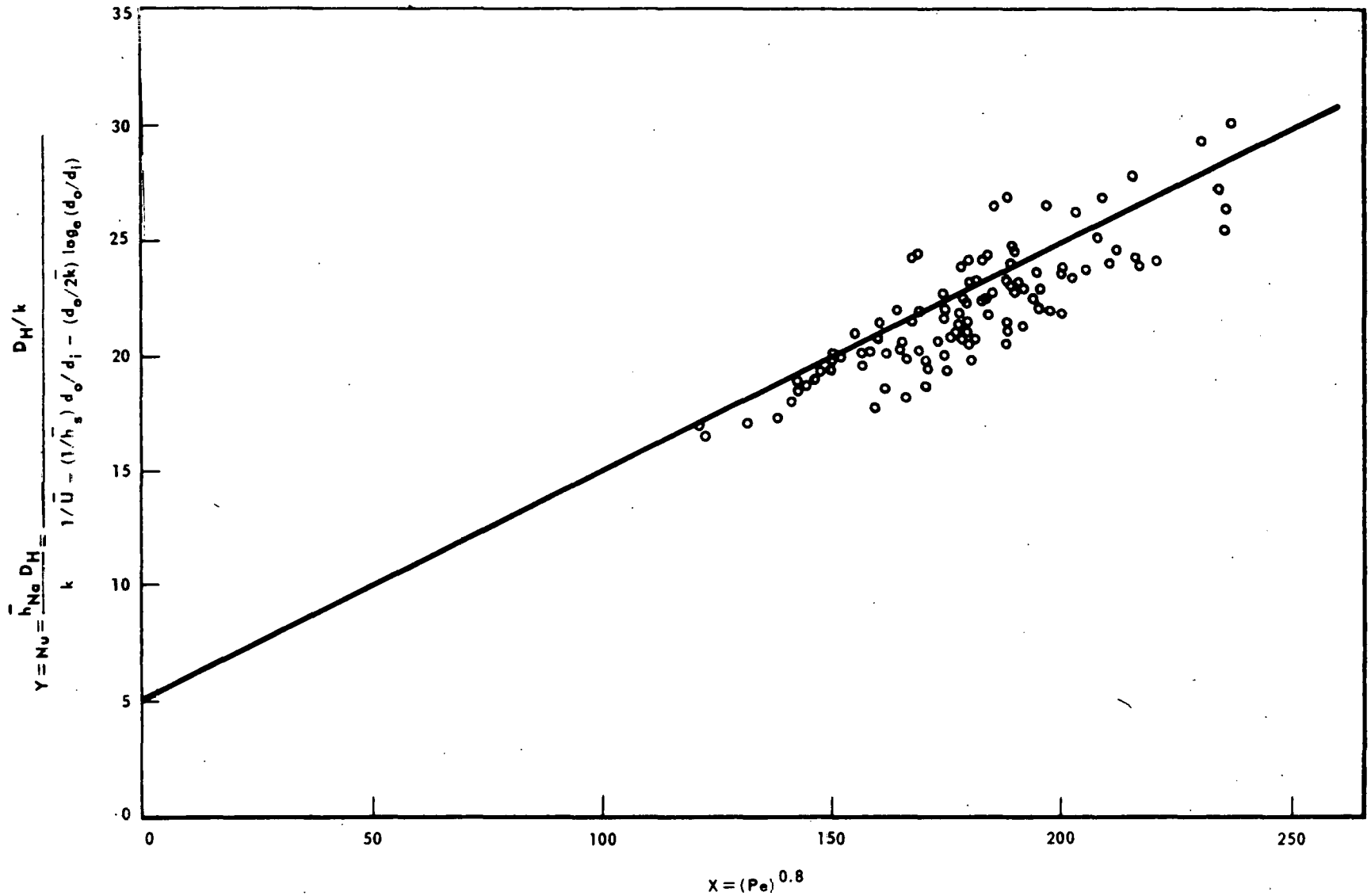

Figure 5-5. *Wilson-Plot of the Average Sodium Side Heat Transfer Coefficient Deduced from Measurements in the Boiling Region of the Evaporator*

A comparison of the present results with two other correlations is made in Figure 5-6, where Nusselt number is plotted vs Peclet number. Curve 1 is Equation 5-13 and Curve 2 is the Borishanskii correlation[4] for the same P/D ratio. The Seban-Shimazaki[5] correlation which was used for the design prediction is shown as Curve 3. The present correlation is approximately 50% higher than the Borishanskii data which is considered to be the most recent available for straight tube bundle geometry without spacers. There is no question that the present geometry has higher sodium-side heat transfer than the corresponding "clean" tube bundle geometry; rather, the question is how much higher? In that connection, it is interesting to look at the key assumption made, the heater tube wall thermal conductivity. If the very low conductivity values of the data on Figure 3-6 had been assumed. the Nusselt number would have been somewhat higher than indicated in Figure 5-6. On the other hand, if the highest thermal conductivity value had been used, the resulting correlation would have been close to Curve 2. The question raised above cannot be answered fully at this time, but it should be pointed out that the equations for the steam-side, wall, and sodium-side conductances given by Equations 5-3, 5-2, and 5-13, respectively, together predict the evaporator performance in the boiling region; therefore, the absolute values of the individual conductances are unimportant for the design of similar systems. The breakdown into individual conductances is only important when the general validity of Equation 5-13 is to be established.

5.2 DETERMINATION OF SODIUM BYPASS FLOW IN THE EVAPORATOR

The evaporator test model was designed to allow some of the hot sodium entering at the top to flow downward in the bypass flow channel between the vessel and the flow shroud and exit through a piston type seal at the lower end of the tube bundle. The general arrangement can be seen from Figure 5-3. Details of the seal are shown in Figure 4-6.

The prediction of the bypass flow rate through the 0.010-in. radial clearance gap is complicated by several factors. First, the prediction of the pressure drop across the seal is uncertain because it is approximately the same as the frictional pressure drop through the tube bundle. This is so because the sodium heads are approximately equal and the friction pressure drop in the bypass channel is close to zero. Additionally, the eccentricity of the seal is now known (i.e., it is not known if the radial gap adjusts itself to be close to zero on one side and approximately 0.020 in. on the other, etc.). Finally, it is not known whether the flow in the gap is laminar or turbulent, or some combination of both.

It was the intent in designing the seal to select the radial clearance in the hot operating condition so that approximately 95% of the flow would pass through the tube bundle and the balance through the bypass channel. Significantly higher bypass flow rates would hurt the thermal performance; too small a gap and corresponding bypass flow rate would increase the risk for self-welding, etc., preventing relative thermal expansion between the flow shroud and the vessel.

An indirect experimental method of evaluating the approximate bypass flow rate through the seal was used. The temperature profiles in the bypass channel at various bypass flow rates were calculated using the EVAP code. The results were compared to temperature measurements from the external thermocouples along the vessel shown in Figure 4-13. These thermocouples did not read the sodium temperature directly, but were calibrated to yield the bypass channel sodium temperature distribution by applying correction factors to the thermocouple readings obtained during the isothermal thermocouple calibration described in subsection 4.6.1.

The results of such a parametric study are shown in Figure 5-4, where the analytic axial and cross-sectional temperature distributions are compared to measurements for bypass flow rates of 6, 7.5, and 12%. In this figure, the predicted results for the center and edge channels are for the 6% bypass flow rate case. (For the higher bypass flow rates, the temperature unbalance between the center and edge channel is somewhat larger, but it is not included on the figure due to obvious space limitations.)

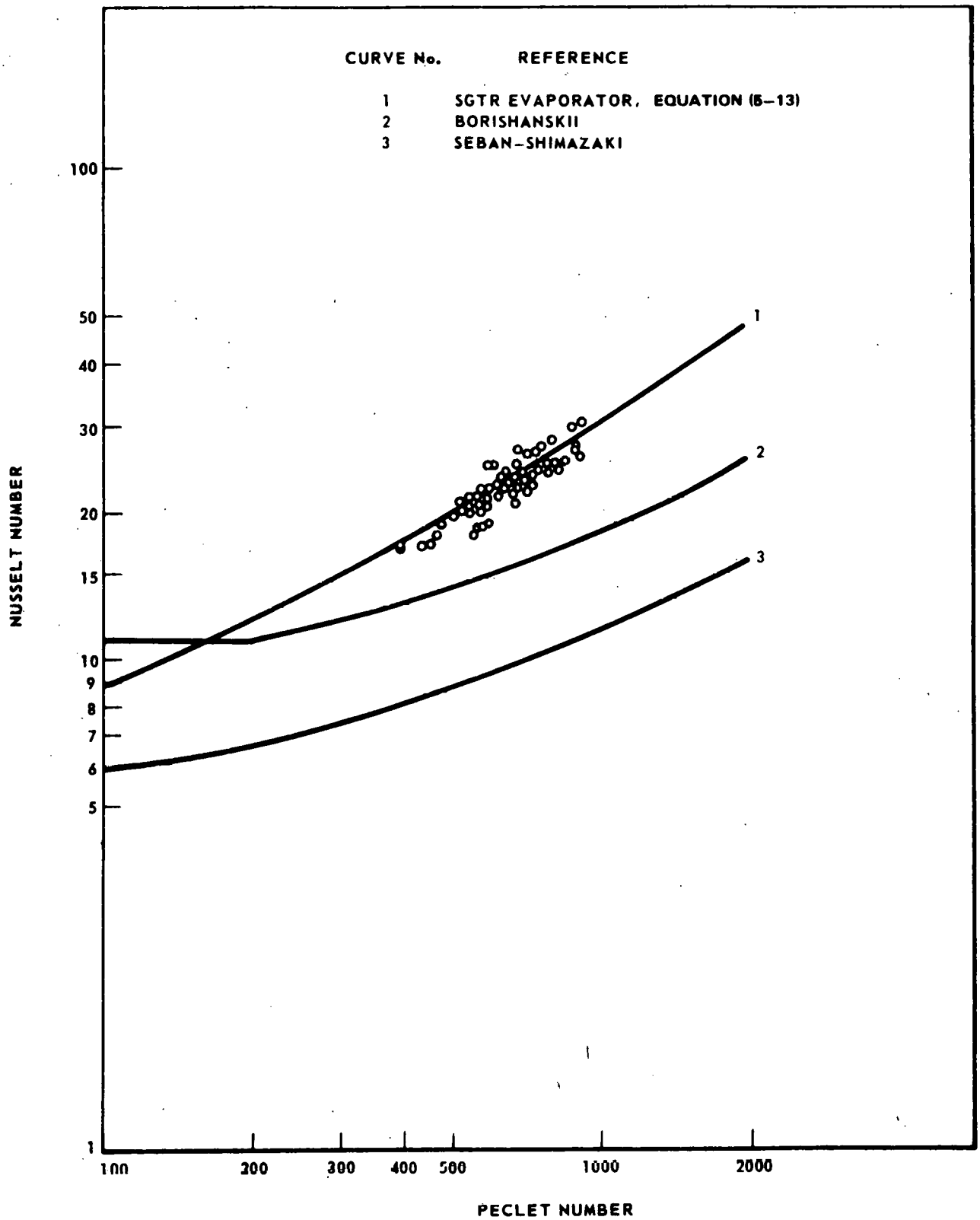

Figure 5-6. Comparison of Measured Sodium Side Nusselt Number to Existing Correlations

From Figure 5-7, it can be seen that the actual bypass flow rate is approximately 6% of the total flow. The same process was repeated for a different case with higher inlet temperature and lower sodium flow rate; this also resulted in a bypass flow rate of approximately 6%. These results are in general agreement with the 5% design prediction. The only major assumption involved in arriving at the above results is the prediction of the heat transfer through the flow shroud. The thermal conductivity of the shroud was calculated from Equation 5-2, the same as for the tubes, and the heat transfer coefficients were calculated from Equation 5-13.

It is interesting to note from Figure 5-7 that relatively large bypass flow rates (e.g., 12%) do not hurt the thermal performance noticeably, since most of the heat is transferred through the flow shroud into the tube bundle anyway. However, it should be noted that the temperature unbalance between the edge channels and the remaining channels is increased by the higher bypass flow rates, due to more heat transfer from the bypass channel. Increasing the bypass flow rate much above 12% would hurt the thermal performance, since the sodium-side conductance would decrease and the bypass channel sodium would not be able to transfer all its heat through the flow shroud. Also, the power unbalance between the seven tubes would increase.

5.3 DEPARTURE FROM NUCLEATE BOILING MEASUREMENTS

Presented below are the departure from nucleate boiling test results and associated analytical evaluations. The nature of the departure from nucleate boiling phenomenon and the importance of knowing when it occurs were discussed in subsection 3.3.

In general, for most geometries and types of systems, a criterion for the onset of DNB can readily be found. For the present swirl flow geometry, however, it appears that the onset of DNB is not a very distinct phenomenon; but rather it appears to happen more gradually than in some of the more common systems. This required the establishment of a rather arbitrary criterion in establishing the actual onset of DNB for all of the data points for use in this study.

In order to evaluate the local steam quality at the DNB measurement location, data on the overall heat transfer coefficient of the bayonet tube were needed, since there is a reduction in steam quality along the tube due to regenerative cooling by the colder inlet water inside the bayonet tube. This presented no problem with the P/D = 6 insert, since the bayonet tubes used with these inserts were noninsulated. However, the insulation characteristics of the double wall bayonet tubes employed with the P/D = 3 inserts were unknown and had to be evaluated before the overall coefficient could be determined. This evaluation is described below.

5.3.1 Evaluation of Bayonet Tube Insulation Characteristics

Details of the double wall bayonet tubes are shown in Figure 4-9; a schematic diagram is shown in Figure 5-8. The approximately 10 ft of double wall section at the top have lower heat transfer conductance than the single wall section. This reduces the regenerative effect (i.e., heat transfer from the steam-water mixture to the subcooled water entering the bayonet tubes at temperatures approximately 100°F or more lower than the saturation temperature).

The insulation characteristics of the double wall tube will depend on the media present between the two concentric tubes (e.g., air or steam vs water), and also on the degree of fluid movement in the gap. In the present case, small holes were drilled in the inner tube (Figure 4-9) which allowed water to enter the gap. Since there was some clearance between the enlarged portions of the inner tube and the bayonet tube, some small flow of water in the gap is to be expected due to pressure gradients in the main stream.

The evaluation of the insulation characteristics was accomplished by using two long thermocouples lowered into the bayonet tubes and positioned immediately above the end of the double wall, as indicated in Figure 5-8. The thermocouple leads were taken through the evaporator head by Conax fittings along with five wires of the same diameter as the thermocouples lowered into the remaining tubes to avoid flow unbalance on the steam-side. The temperature gradient in the subcooled water is relatively small in the insulated section, but becomes larger immediately below, as indicated in Figure 5-8. Therefore, the thermocouples had to be positioned carefully just above this point.

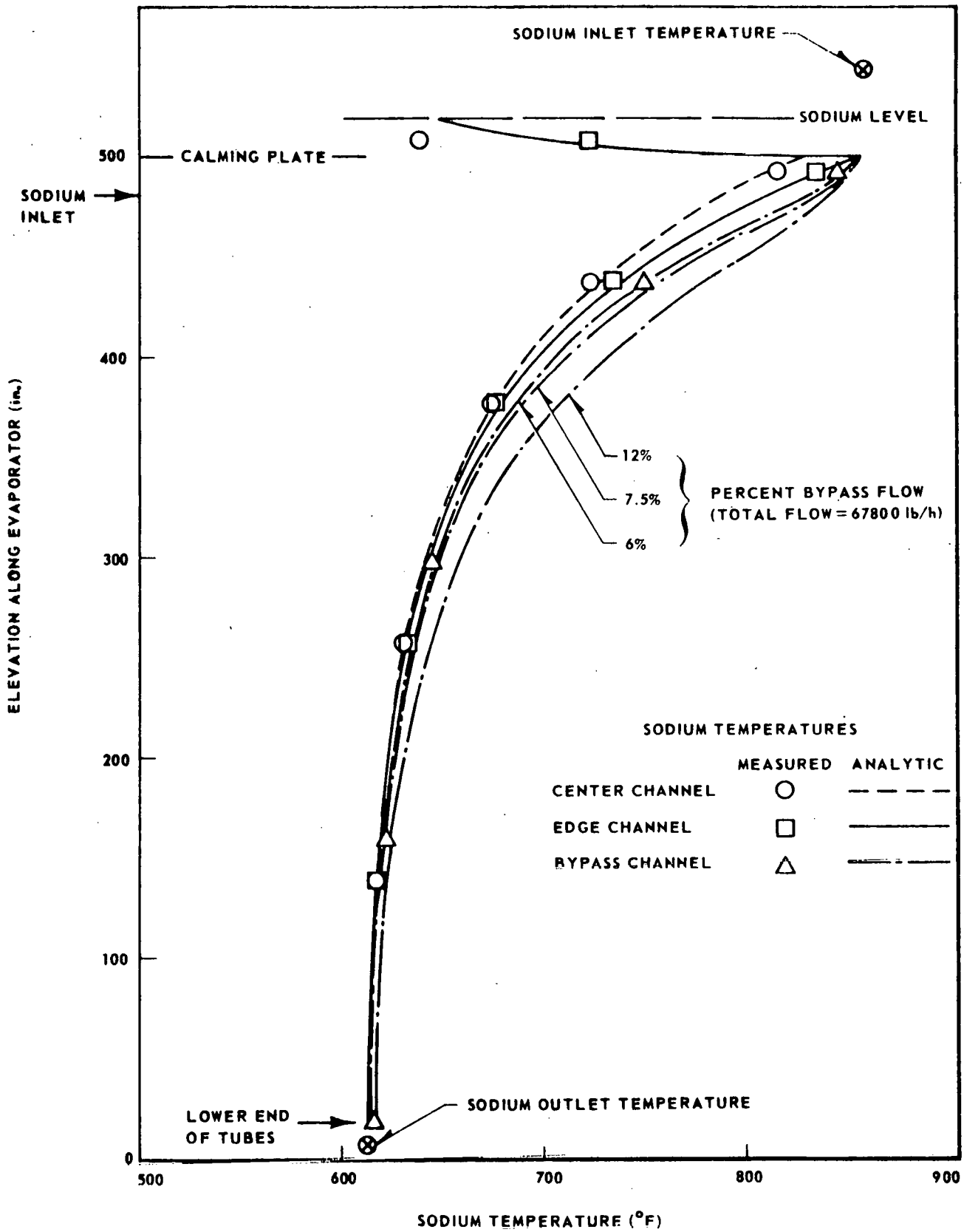

Figure 5-7. *Measured Axial Sodium Temperature Profiles in the Bypass Channel Compared to Analytic Predictions with Various Bypass Flow Rates*

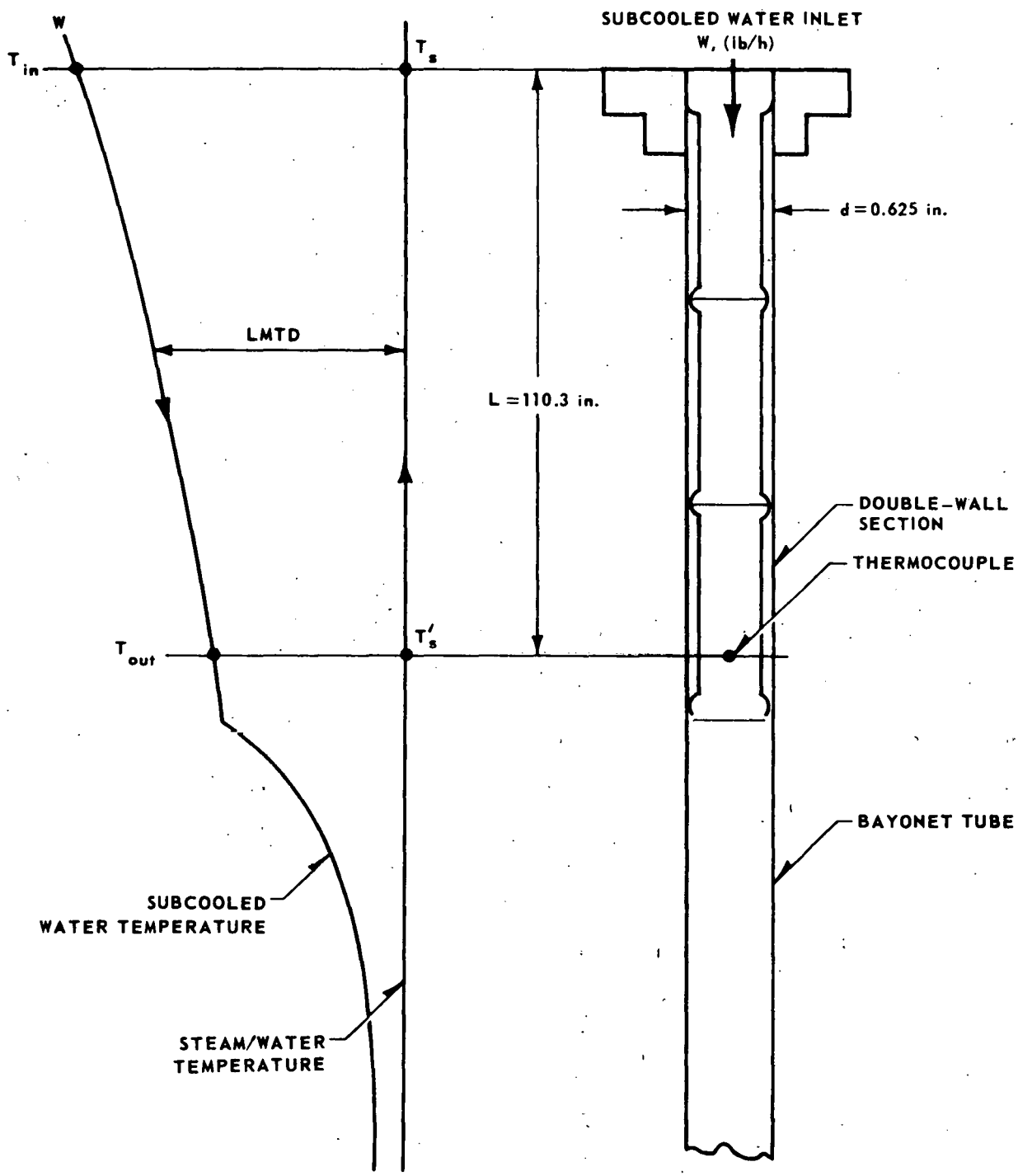

Figure 5-8. Schematic Diagram of the Double Wall Section of the Bayonet Tubes Used with the P/D = 3 Swirl Generator Insert and Corresponding Temperature Profiles

The calculation of the overall heat transfer coefficient for the double wall portion of bayonet tube B was accomplished by calculating a log mean temperature difference from the measured temperatures T_{in}, T_{out}, T_s, and T_s' (Figure 5-8). The total heat transfer in the region was calculated from the flow rate and the temperature increase of the subcooled water, after which the overall heat transfer coefficient can be calculated using Equation 5-8 where the area is based on the outside diameter of the bayonet tube and the length is as given in Figure 5-8.

The available data and the results of these calculations are shown in Table 5-2. Also shown in the table is the estimated steam quality which was different for each case. The corresponding water inlet temperature and the log mean temperature difference were also different for each case.

Table 5-2
INSULATED (DOUBLE WALL) BAYONET TUBE HEAT TRANSFER DATA AND THE DEDUCED OVERALL HEAT TRANSFER COEFFICIENTS

Date	Time	Inlet Temperature T_{in} (°F)	Outlet Temperature T_{out} (°F)	Steam/Water Temperature T_s(=T_s') (°F)	Log Mean Temperature Difference LMTD (°F)	Water Flow Rate W (lb/h)	Heat Transfer Q (Btu/h)	Heat Transfer Area A (ft²)	Overall Heat Transfer Coefficient U (Btu/h-ft² °F)	Steam Exit Quality X (%)
11-30-71	0012	504.7	517.2	556.4	45.2	1481	22210	1.5	325.8	28
11-30-71	0112	513.8	528.8	574.2	52.5	1366	24804	1.5	312.7	32
11-30-71	0212	525.1	541.7	596.7	62.9	1349	27394	1.5	288.4	41
11-30-71	0312	508.5	528.5	598.0	79.1	1356	32757	1.5	274.4	47
11-30-71	0412	506.4	527.1	603.0	85.8	1300	32456	1.5	250.5	52
11-30-71	0512	499.9	522.8	603.8	92.0	1319	36252	1.5	261.1	65
11-30-71	0612	505.9	527.6	605.7	88.5	1353	35402	1.5	265.0	68
11-30-71	0712	410.5	469.0	603.0	161.5	655	43354	1.5	177.9	94
11-30-71	0915	410.4	486.9	600.1	148.2	622	54249	1.5	242.6	98
11-30-71	0945	411.6	473.4	608.4	164.0	695	48716	1.5	196.8	92

The deduced overall heat transfer coefficients are plotted in Figure 5-9 vs the log mean temperature difference. The behavior shown in Figure 5-9 is surprising, since one would think that larger temperature differences between the two tubes would enhance natural convection in the gap which would result in increasing the overall heat transfer coefficient, rather than the reverse indicated behavior. On the other hand, the pressure gradients in the tube are smaller at the higher temperature differences (Table 5-2), because the flow is generally lower; this could possibly result in lower flow through the gap and thus more than offset the increased natural convection effects. Since the thermal resistance is mainly in the gap between the two tubes, the effect of changing coefficients on the outside surfaces is not considered to be significant.

It is interesting to compare the experimental results with the overall heat transfer coefficient calculated assuming stagnant water in the gap. This coefficient is lower than the experimental by a factor of approximately 4. It was thought initially that the assumption of stagnant water in the gap was reasonable. The present evaluation stresses the need for careful selection and testing of a bayonet tube insulation arrangement for the demonstration plant evaporator.

In the reduction of the DNB data to be described next, a value of 280 Btu/h-ft²-°F was used for the double wall section of the bayonet tubes. From Figure 5-9 it can be seen that this is the approximate mean value of all data points.

5.3.2 Data Collection and Data Reduction Procedure

The basic instrumentation used to study the departure from nucleate boiling characteristics of the annular swirl flow geometry were thermocouples located on the outside heater tube walls. Details of the method by which the thermocouples were attached to the wall are shown in Figure 4-15; locations of the DNB thermocouples are shown in Figure 4-13. Due to the considerably better than expected thermal performance, only the thermocouples at elevation 490.5 in. were used, because the heat flux at the lower elevation was much smaller than at the top elevation in the region of which the departure from nucleate boiling is of greatest importance.

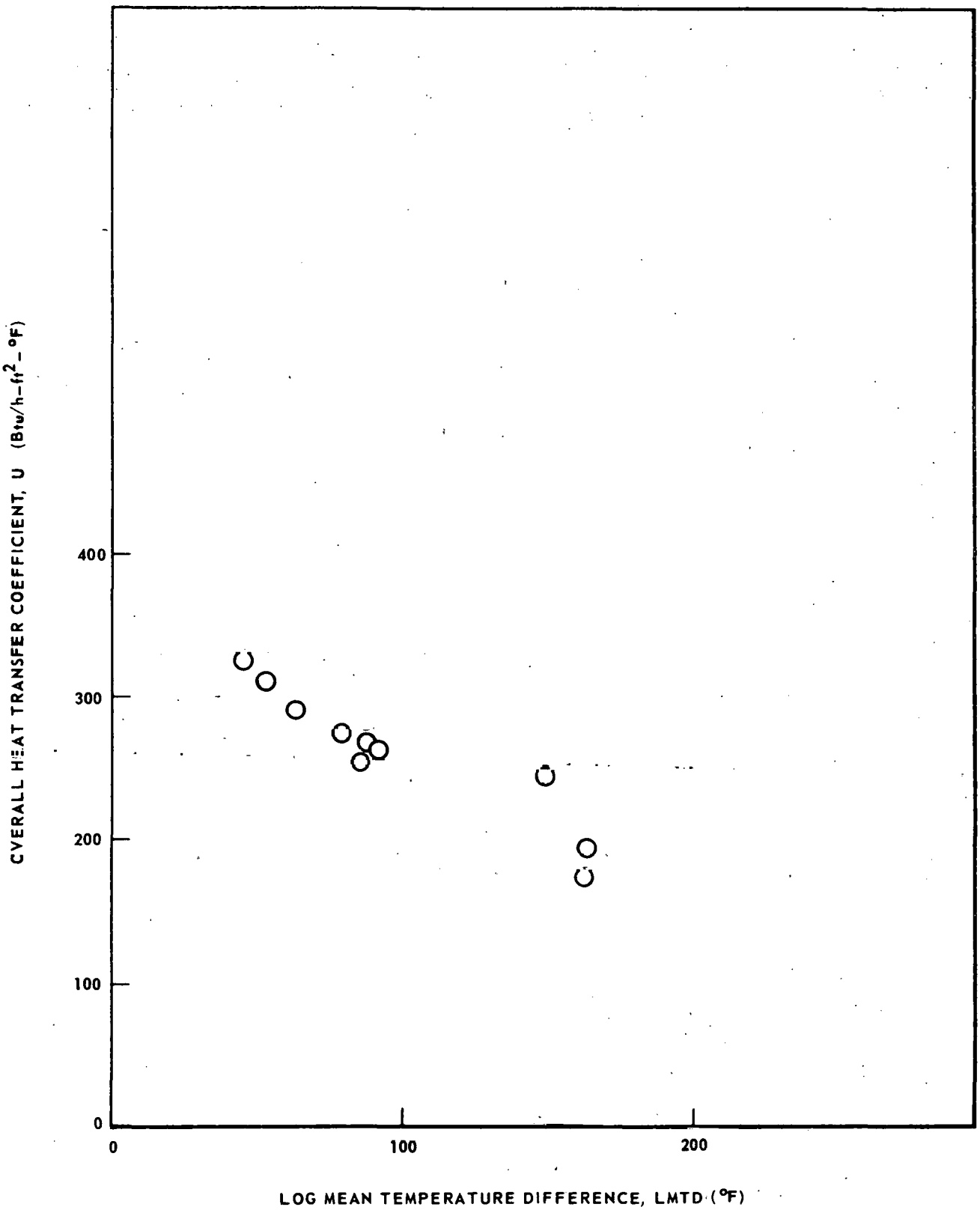

Figure 5-9. Measured Overall Heat Transfer Coefficients of the Insulated (Double Wall) Bayonet Tubes vs. the Log Mean Temperature Difference

The swirl generators were carefully positioned equidistant relative to the DNB thermocouples as indicated in Figure 5-10 for both P/D swirl generator inserts tested. However, in tube F, the swirl generator was rotated 135 degrees counterclockwise for the P/D = 3 insert to position one thermocouple 180 and the other 90 degrees away from the swirl generator in order to get some feel for local circumferential effects. The symbols "W" and "D" associated with the DNB thermocouples stand for "wet" and "dry," respectively, and originated from the idea that the water would tend to pile up on the upstream surface of the swirl generator (wet) while the downstream surface would have more steam around it (dry).

The thermocouples were connected directly to two Sanborn oscillograph recorders along with other parameters important to the test. Typical Sanborn traces of the DNB thermocouples and other pertinent parameters are shown in Figure 5-11 for the P/D = 6 insert and in Figure 5-12 for the P/D = 3 insert taken during DNB runs.

The test procedure followed is described in subection 4.7.2. In general, the procedure consisted of establishing steady-state conditions at relatively low steam quality and fully nucleate boiling conditions. The recirculation flow rate was then reduced in steps, thus increasing the local steam quality at the measurement points until the DNB thermocouples indicated some change (e.g., an increasing temperature level or showed increased fluctuations,* both of which are evident from Figures 5-11 and 5-12). A complete set of data was then recorded using the data acquisition system. The increased activity of the DNB thermocouples and/or temperature level change is evidence of a breakdown in the nucleate boiling process and the beginning of the partial film boiling regime at the measurement location.

The recirculation flow rate was then reduced further until a distinct jump in the wall temperature was noted. This increase in the wall temperature indicates a definite change in the local steam-side heat transfer conductance from an intermediate partial film boiling coefficient to a local film boiling coefficient. The recirculation flow rate was then increased in steps approximately to the starting point of fully nucleate boiling conditions and new test conditions were established. During any one of these tests, it was difficult to keep the system pressure constant and the pressure could increase by approximately 20 to 30 psi. A familiar problem in any test system is that changing one parameter inevitably is accompanied by small perturbations of other parameters. In the present system, however, the changes occurred mainly in the pressure, while the total heat transferred remained essentially constant.

It is apparent from Figures 5-11 and 5-12 that each thermocouple behaves differently compared to the others with respect to temperature level and temperature fluctuations near the DNB point. Also, there was some variation from run to run due to slightly different steps taken in the reduction of the recirculation flow rate. Some variation between the characteristics of the Sanborn traces for the two different swirl generator inserts tested was noted. This is apparent from Table B-3, where the mean values of the temperature rise for the four DNB thermocouples from the state of fully nucleate boiling to the time of data acquisition are tabulated. In order to compare the performance of the two swirl generator inserts on the same basis, a criterion that could be applied uniformly to all data had to be defined.

The DNB criterion arrived at is basically that the average temperature rise of the four DNB thermocouples should be identical for all runs. This criterion was arrived at mainly from practical considerations in that a mathematical linear expression for the recirculation flow rate near the DNB point in terms of a standard DNB thermocouple rise to be applied for all runs, and the actual average temperature rise for the particular run could be obtained. This model is illustrated in Figure 5-13, where the assumed relationship between the recirculation flow rate is plotted vs the average temperature rise of the DNB thermocouples. The point "1" is given from the data collected near the DNB point (e.g., as shown in Figures 5-11 and 5-12). The point "0" can be found from the Sanborn traces of the recirculation flow at the point just before the DNB thermocouples start to indicate a transition, or where the average rise of the DNB thermocouples is zero. The slope of the line through these two points can be found and an equation written for the recirculation flow rate as:

$$W_{DNB} = W - S \times W \times (\Delta T_s - \Delta T) \qquad \textbf{(5-14)}$$

* The fluctuations shown by the DNB thermocouples, even in the nucleate boiling mode, are due to outside sodium temperature fluctuations, also indicated by the sodium thermocouple (T/C 1) in Figures 5-11 and 5-12, and will be discussed separately later.

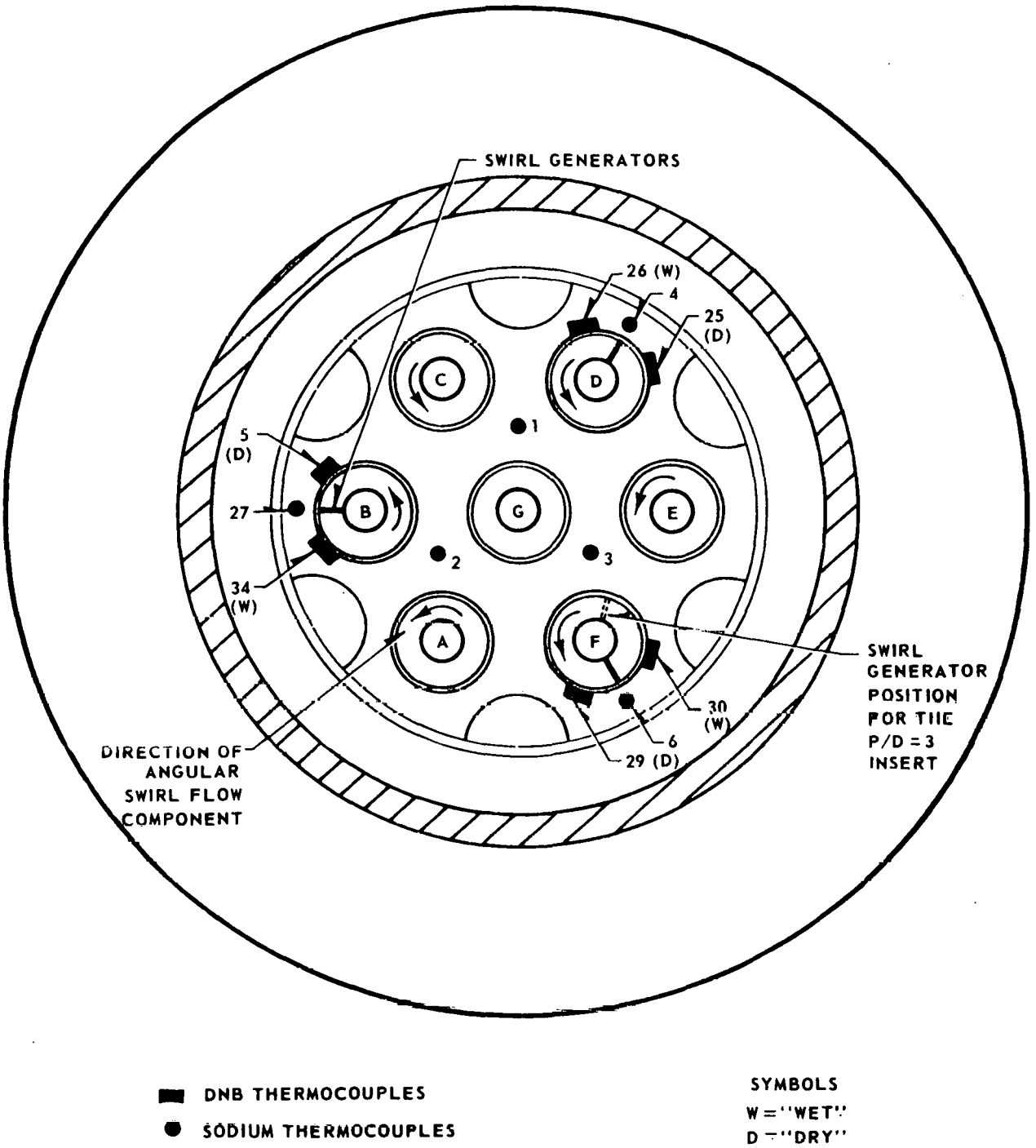

Figure 5-10. Details of Departure from Nucleate Boiling Thermocouple Locations Relative to Swirl Generator

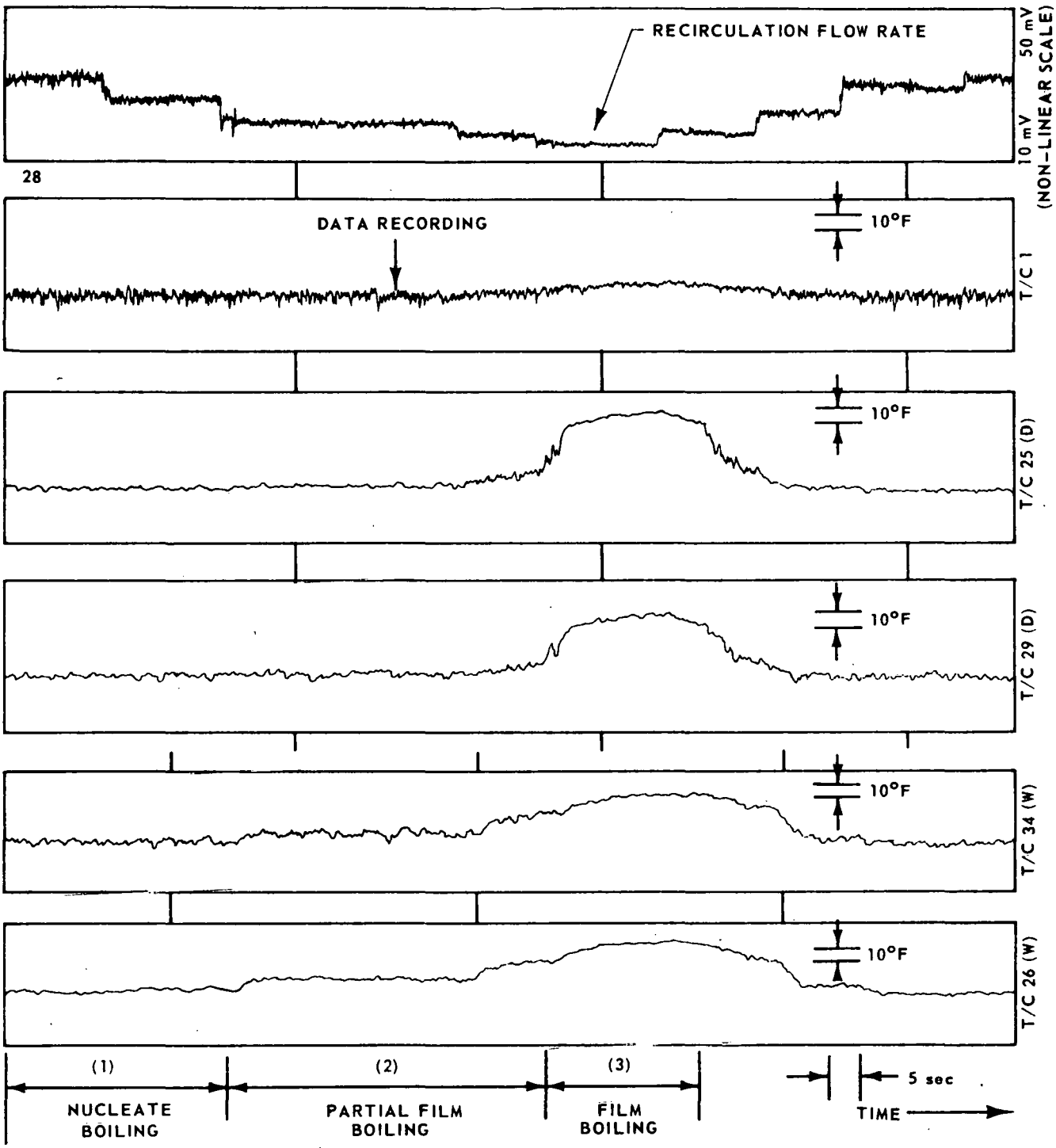

Figure 5-11. Typical Sanborn Traces of the DNB Thermocouples during a DNB Run with the P/D = 6 Insert

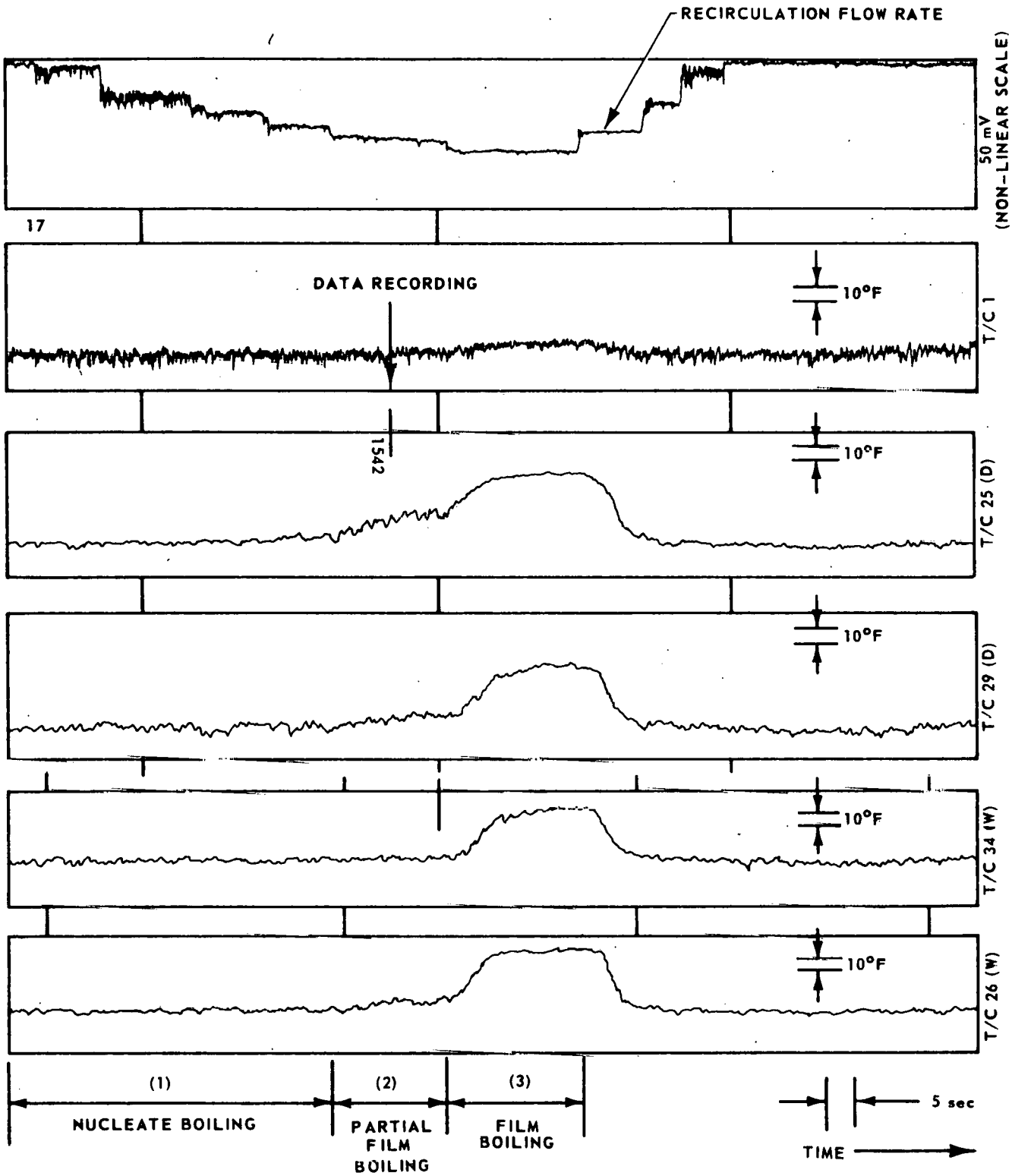

Figure 5-12. Typical Sanborn Traces of the DNB Thermocouples during a DNB Run with the P/D = 3 Insert

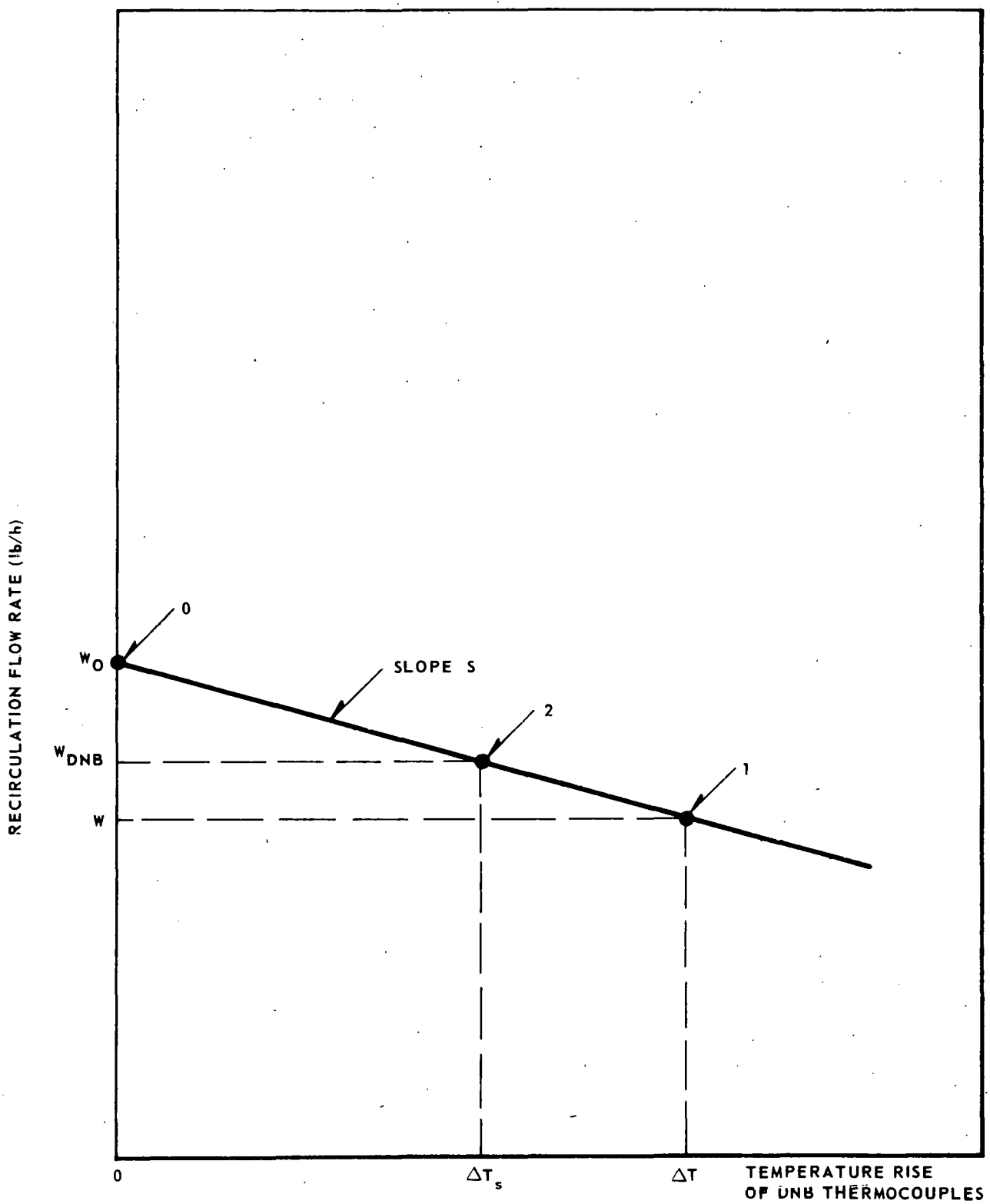

Figure 5-13. Schematic Diagram of Assumed Relationship between Recirculation Flow Rate and the Average Temperature Rise of the Heater Tube Wall in the DNB Criterion

The slope S was evaluated for all DNB runs using the data from the W and W_o columns in Table B-3 for both P/D ratio inserts. It was found that the slope varied from run to run; to ensure uniformity, the average value of the slope, $\bar{S}$, was evaluated for both sets of data. The value of ΔT_s, the standard average temperature rise of the DNB thermocouples to be applied for all runs, was arbitrarily selected to be 5.091°F, since this was the mean ΔT for all the P/D = 6 DNB runs as indicated in Table B-3. Also, the mean value of the slope, $\bar{S}$, was selected from the P/D = 6 data to be 0.0235. The choice of these two standard parameters will affect the results to some degree, but this particular choice is believed to be reasonable.

Once the recirculation flow rate at DNB had been determined (given in the W_{DNB} column in Table B-3), the data were processed in the EVAP code as for the thermal performance runs and the local steam quality at the DNB measurement point determined. The heat flux just prior to the onset of DNB can be evaluated from the local temperature difference and the local overall heat transfer coefficient corresponding to nucleate boiling obtained from the thermal performance evaluation. However, at the DNB point, the overall heat transfer coefficient no longer corresponds to the fully nucleate case, since a small wall temperature rise did occur, corresponding to a slight change in the average steam-side coefficient. This was accounted for by evaluating the local steam-side coefficient as described in subsection 5-4. The local heat fluxes calculated this way were in general only slightly different from the fully nucleate boiling heat fluxes.

5.3.3 Departure from Nucleate Boiling Results

The departure from nucleate boiling data obtained consisted of 57 points for the first swirl generator insert tested (P/D = 6) and 43 points for the second insert tested (P/D = 3). (For definitions of the pitch and the diameter used in the P/D ratio, see Figure 3-2.) Approximately 10 of these runs were disregarded in the final DNB evaluation, because the corresponding Sanborn traces were not well defined (i.e., they did not include the full range of possible boiling modes or the traces were recorded during a much longer time period and thus made the interpretation difficult). The range of system conditions experienced during the tests are given in subsection 5.1.

The sodium-side data used as input to the EVAP code are shown in Table B-2. The heater tube wall temperature data are shown in Table B-3, along with measured recirculation flow rates and the recirculation flow at DNB deduced from the temperature data according to the DNB criterion defined in the previous subsection. The output from the EVAP code yielded the local nucleate boiling heat flux and the steam quality at the DNB point. The nucleate boiling heat fluxes were adjusted according to the procedure outlined in the previous subsection to account for the change in steam-side heat transfer coefficient. These heat fluxes were then multiplied by a correlation factor given by:

$$C = (D_H/D_O)^{0.7} \; (G/G_O)^{0.45}/(1 + A_R)^{0.25} \qquad \textbf{(5-15)}$$

where A_R is the radial acceleration in "g's" experienced by the fluid due to the swirling motion imposed by the swirl generator. This correlation factor was proposed by Tippets[35] in the early stages of the ESADA project for this particular geometry. The radial acceleration A_R is a function of the mass flux, the steam quality; the P/D ratio of the swirl generator and a mathematical expression for it is given in Appendix C-3. The value of the correlation factor is plotted in Figures C-3 and C-4 vs the local steam quality with the mass flow rate, G, as a parameter.

A summary of the reduced nucleate boiling data is given in Table B-4 in Appendix B-1. The local critical heat fluxes multiplied by the correlation factor are plotted in Figure 5-14 vs the local steam quality at the DNB measurement point. The local steam qualities at which DNB occurred range between 70 and 95% for this particular range of heat flux. It would have been desirable to extend the range of heat fluxes to higher values, but the maximum heat flux was limited by the maximum sodium inlet temperature which was approximately 900°F.

It is apparent from Figure 5-14 that the P/D = 3 data tend to fall slightly below the P/D = 6 data. This is an indication that the exponent of 0.25 in the correlation factor, Equation 5-14, is too high and an adjustment might have been desirable. However, it is felt that a detailed investigation of the effect of swirl generators with various P/D ratios on the DNB characteristics in the laboratory is needed and that a detailed examination of correlation properties should be made then.

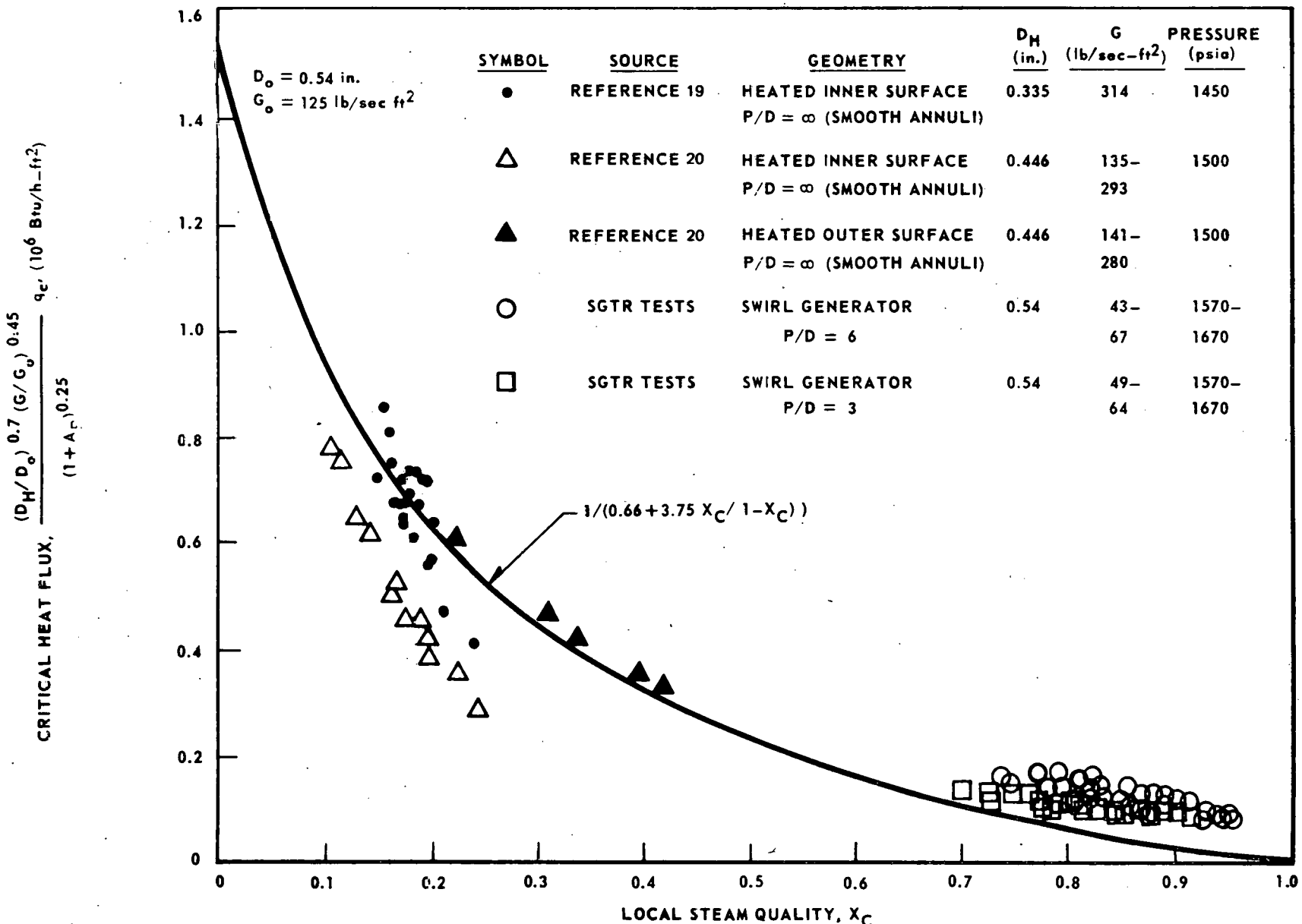

Figure 5-14. Critical Heat Flux with Correlation Factor Applied vs. Local Steam Quality for the SGTR Bayonet Tube Evaporator Test Model with the P/D = 6 and P/D = 3 Swirl Generator Inserts

By considering the data on Figure 5-14, it appears that the DNB steam quality for the P/D = 3 swirl generator insert is generally lower than for the P/D = 6 insert (i.e., the data appear to be shifted to the left by about 3%). This is inconsistent with the idea that increasing the P/D ratio would delay the onset of DNB and requires some discussion. The explanation may be that more of the water phase is tied up on the bayonet tube surface and the swirl generator with the P/D = 3 insert than with the P/D = 6 insert. To explain this further, consider Figures 5-15, 5-16, and 5-17, which show the results of air/water tests at NSP* for a similar geometry to the present. It can be seen that the water clings to the bayonet tube surface and the swirl generator surface even after the heater tube surface is completely dried out. With the P/D = 3 insert, there is twice as much swirl generator surface for the remaining water to cling to; a corresponding earlier dry-out of the heater tube surface might be expected.

The main conclusion that can be drawn at this point is that there does not seem to be any advantage with the P/D = 3 insert vs the P/D = 6 insert as far as onset of DNB is concerned.

Since the departure from nucleate boiling could only be detected immediately after the transition boiling regime had started corresponding to an average wall temperature rise of approximately 5°F, a design limit must be drawn below all data. The curve drawn in Figure 5-14 has the equation:

$$1/[0.66 + 3.75X_c/(1 - X_c)] \qquad \textbf{(5-16)}$$

The functional form of Equation 5-16 was established by Tippets[21] and has been used successfully in previous work.[37] The critical heat flux design limit is then given by the relation:

$$Cq_c = 1/[0.66 + 3.75X_c/(1 - X_c)] \qquad \textbf{(5-17)}$$

when C is the correlation factor given by Equation 5-15. The value of q_c calculated above for the "hottest" tube (i.e., the tube with the largest local steam quality should be greater or equal to the actual maximum heat flux at this point). For the present system, the local critical steam quality is estimated to be between 60 and 70% for the hottest tube. The original design was based on a maximum critical steam quality of 38% as estimated from Tippets' design criterion.[35]

5.4 HEAT TRANSFER PERFORMANCE BEYOND DNB

It was pointed out earlier while considering the Sanborn traces of the two typical DNB runs shown in Figures 5-11 and 5-12 that thermocouple traces were taken over three different boiling regimes. Region 1 in these figures represents fully nucleate boiling conditions, while Region 2 represents the partial film boiling regime which is an intermediate transition condition before the pure film boiling condition starts; this condition is denoted by Region 3. The information contained in these traces, along with the complete data recordings at the approximate DNB point and at fully nucleate boiling conditions, will be used to estimate the local steam-side heat transfer coefficients and the local inside wall temperature at the DNB point as a function of the local steam quality.

5.4.1 Measurement of Steam-Side Heat Transfer Coefficient Beyond DNB

In Region 1 of Figures 5-11 and 5-12, the boiling is fully nucleate; therefore, the steam-side heat transfer coefficient can be estimated. As described previously in subsection 4.7.2, complete data sets were normally recorded twice for each DNB run, once near the DNB point and once approximately 20 min prior to this. This corresponds to a point in time to the left on the traces in Figures 5-11 and 5-12. The average DNB and sodium thermocouple data for this recording are shown in Table B-5-1 in Appendix B-1. The average values of the thermocouple data can be used to estimate the effective overall heat transfer coefficient of the DNB thermocouple insulation shown schematically in Figure 5-18.

* These results were made available from Nuclear Systems Programs of General Electric Company, Cincinnati.

NOTE: PHOTOGRAPH COURTESY OF GENERAL ELECTRIC MISSILE AND SPACE DIVISION, CINCINNATI, OHIO.

W_{H_2O}	=0.00685 lb/sec	TUBE i.d.	=0.875 in.
W_{Air}	=0.0323 lb/sec	C.B.	=0.25 in.
X	=0.8250	P/D	=3.0

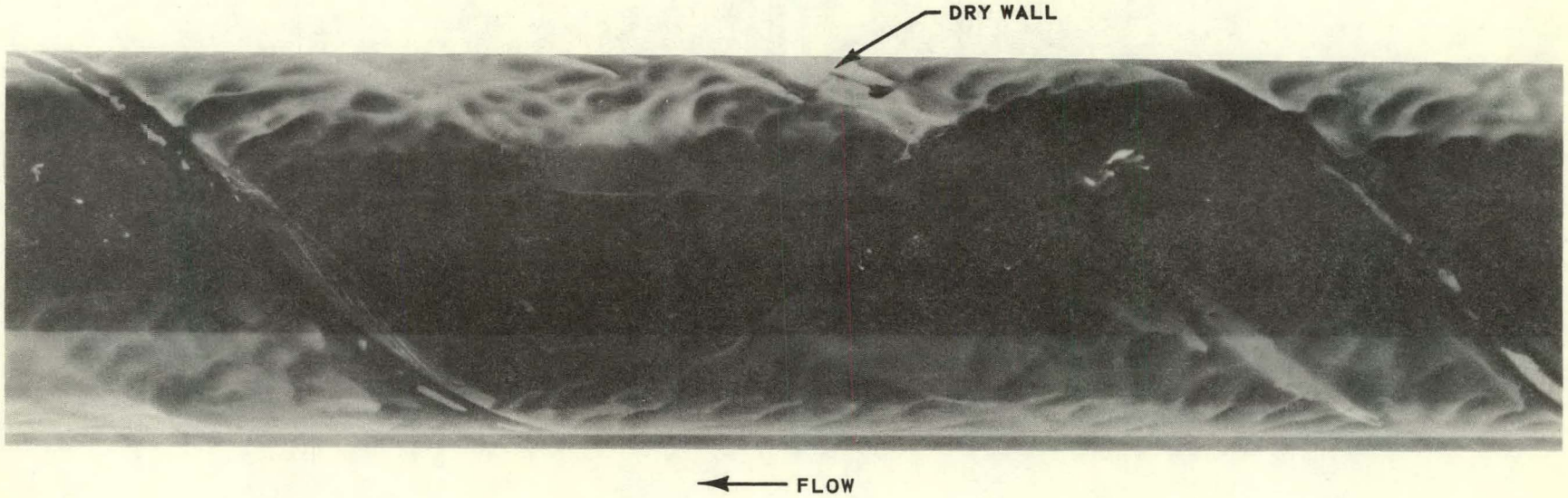

Figure 5-15. Phase Distribution of Air/Water Mixture in Annular Swirl Flow Geometry at Approximately 82 Percent Quality (Photograph Courtesy of General Electric Missile and Space Division, Cincinnati, Ohio)

NOTE: PHOTOGRAPH COURTESY OF GENERAL ELECTRIC MISSILE AND SPACE DIVISION, CINCINNATI, OHIO.

W_{H_2O}	= 0.0033 lb/sec	TUBE i.d.	=0.875 in.
W_{Air}	= 0.04 lb/sec	C.B.	=0.25 in.
X	=0.9238	P/D	=3.0

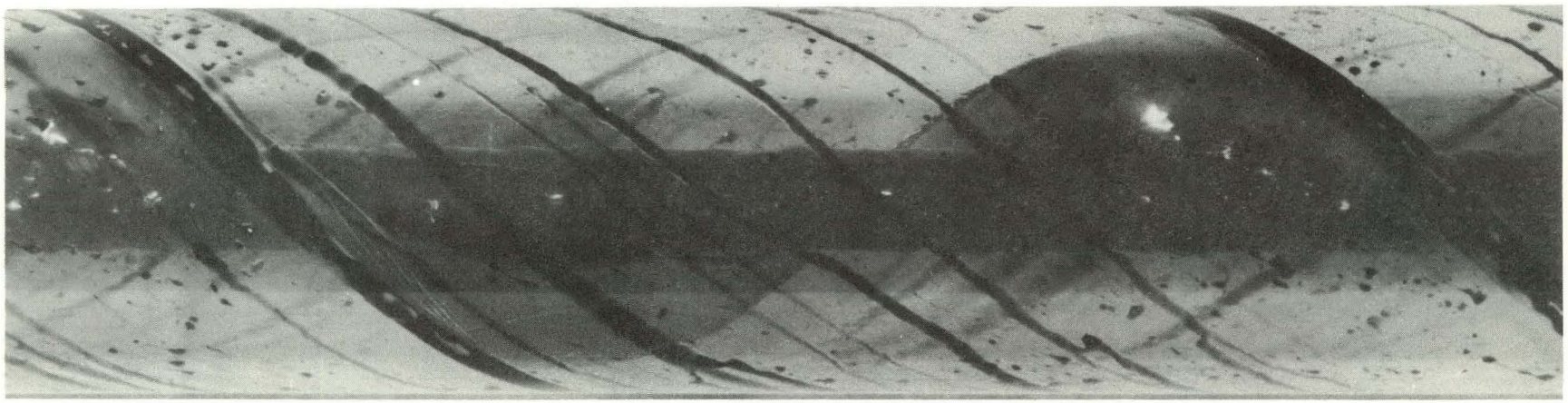

FLOW

Figure 5-16. Phase Distribution of Air/Water Mixture in Annular Swirl Flow Geometry at Approximately 92 Percent Quality Showing the Presence of Rivulets (Photograph Courtesy of General Electric Missile and Space Division, Cincinnati, Ohio)

NOTE: PHOTOGRAPH COURTESY OF GENERAL ELECTRIC MISSILE AND SPACE DIVISION, CINCINNATI, OHIO.

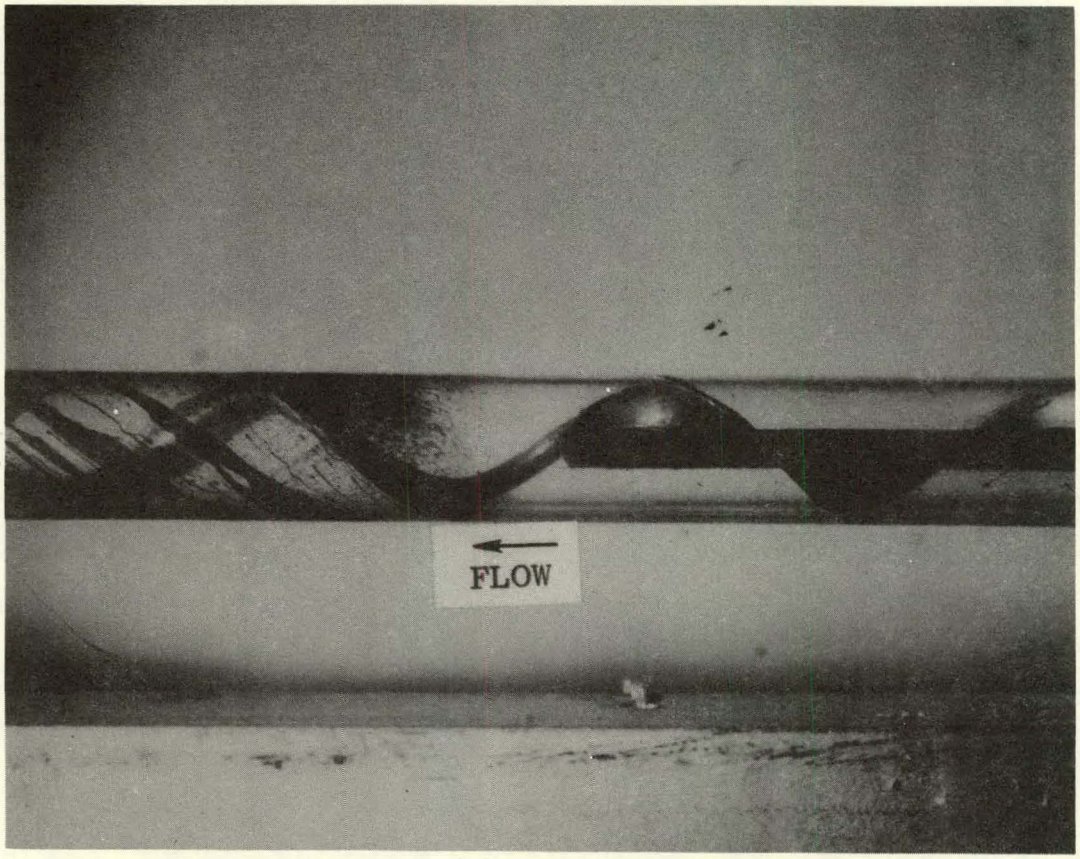

Figure 5-17. Phase Distribution of Air/Water Mixture in Annular Swirl Flow Geometry at Approximately 95 Percent Quality Showing Water Flow along the Center Body (Photograph Courtesy of General Electric Missile and Space Division, Cincinnati, Ohio)

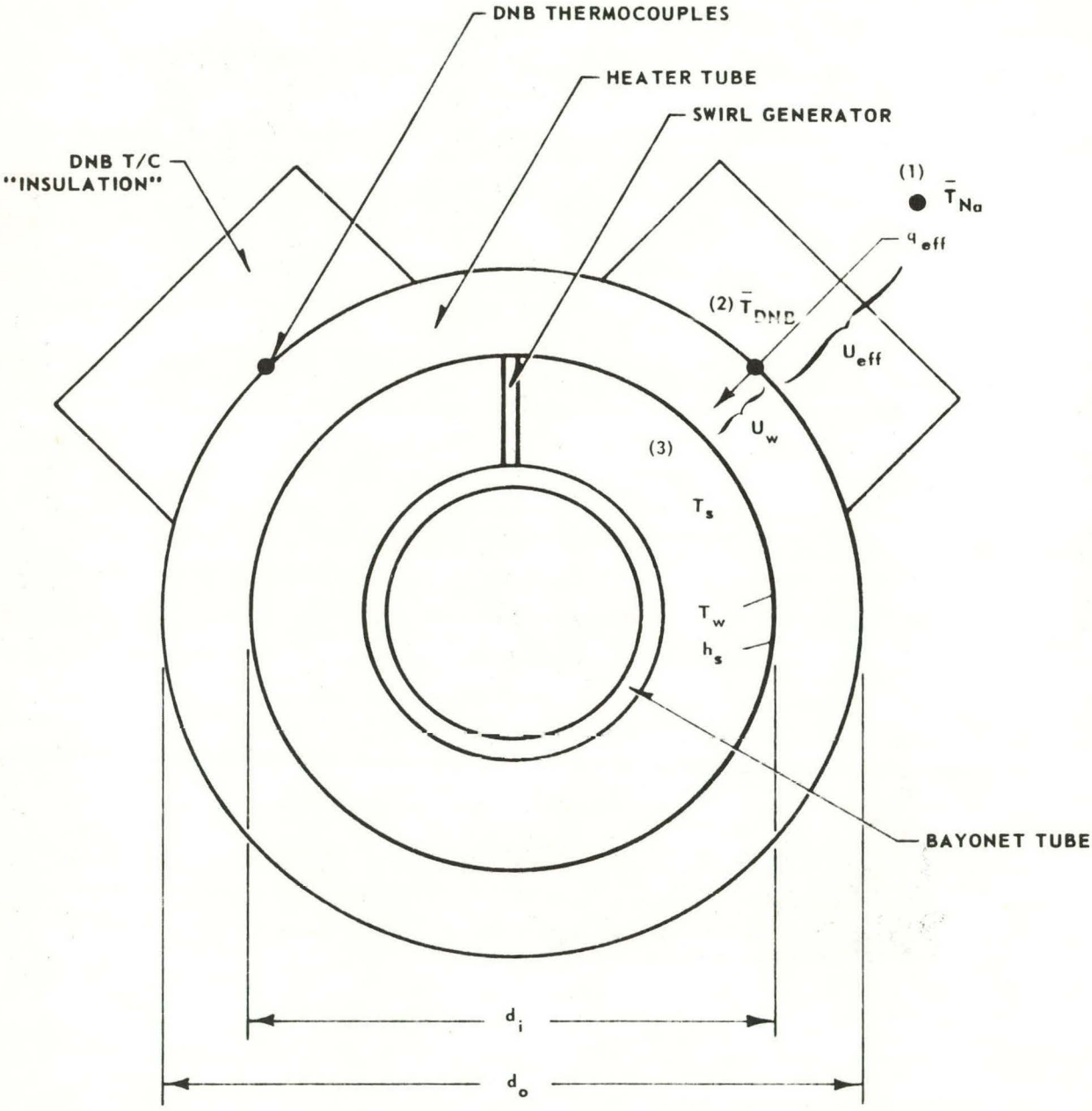

Figure 5-18. Diagram of Bayonet Tube at the DNB Thermocouples

The steam-side heat transfer coefficient is large compared to that of the wall and, therefore, for fully nucleate boiling conditions, can be selected to be approximately 10,000 Btu/h-ft²-°F. Then the effective overall heat transfer coefficient from point 2 to point 3 (Figure 5-18) can be calculated from the relation:

$$1/U_w = (1/h_s)\frac{d_o}{d_i} + (d_o/2k)\ \ln\ (d_o/d_i) \qquad \textbf{(5-18)}$$

where k is given by Equation 5-2. The effective heat flux from 2 to 3 can then be calculated by using the above value for U_w and the measured temperature difference as follows:

$$q_{eff} = U_w\ (\overline{T}_{DNB} - T_s) \quad (\text{Btu/h-ft}^2) \qquad \textbf{(5-19)}$$

The effective heat flux from 2 to 3 is also the effective heat flux from 1 to 2 and, together with the measured outside sodium temperature, the effective overall heat transfer coefficient for the DNB thermocouple insulation can be calculated as follows:

$$U_{eff} = q_{eff}/(\overline{T}_{Na} - \overline{T}_{DNB}) \qquad \textbf{(5-20)}$$

This evaluation was made for the DNB runs where data were available; the data, along with calculated results, are shown in Table B-5-1. Some scatter in the value of U_{eff} is observed and is believed to be due to uncertainty in the value of T_{Na}. This quantity was obtained from individual sodium temperature measurements at Elevation 492.0 in., and these thermocouples did show considerable fluctuations as will be shown later. Physically, U_{eff} cannot vary much for the sodium flow and temperature range tested; therefore, a mean value of U_{eff} is believed to be representative for the actual situation. Averaging of $\overline{U}_{eff}$ approximately 2900 for the P/D = 6 data and $\overline{U}_{eff}$ approximately 2700 for the P/D = 3 data. These values were used in subsequent data analysis to obtain the local steam-side heat transfer coefficient.

At the point near DNB where data were recorded, the average temperatures $\overline{T}_{Na}$ and $\overline{T}_{DNB}$ are available, and since $\overline{U}_{eff}$ is available from the previous evaluation, the effective heat flux from 1 to 2 which is the same as from 2 to 3 can be found from:

$$\overline{q}_{eff} = \overline{U}_{eff}(\overline{T}_{Na} - \overline{T}_{DNB}) \qquad \textbf{(5-21)}$$

From this, the average overall heat transfer coefficient from 2 to 3 can be calculated from:

$$\overline{U}_w = \overline{q}_{eff}/(\overline{T}_{DNB} - T_s) \qquad \textbf{(5-22)}$$

and finally, the steam-side coefficient can be evaluated by rearranging Equation 5-18 to:

$$1/\overline{h}_s = (d_i/d_o)(1/\overline{U}_w - (d_o/2k)\ \ln\ (d_o/d_i) \qquad \textbf{(5-23)}$$

The average temperature data and the results of this calculation are given in Table B-5-2, along with the tube inside wall temperature calculated from.

$$\overline{T}_w = T_s + \overline{q}_{eff}/\overline{h}_s \quad (°F) \qquad \textbf{(5-24)}$$

The local steam quality at this recording was obtained from the EVAP output of the corresponding thermal performance runs; these are also included in Table B-5-2.

In the region denoted by 3 in Figures 5-11 and 5-12, film boiling prevails locally in the tubes near the DNB measurement point. This is the general case; however, for some runs, the recirculation flow rate was not decreased as low as in most cases resulting in boiling conditions between partial film and film boiling, as will be evident later. In Region 3, no complete data set was available; however, the average sodium temperature and average DNB thermocouple reading could be read from the Sanborn traces; (e.g., the reading from T/C 1 in Figures 5-11 and 5-12) by adding the average differences to the previous data. These data, along with the calculated local film boiling calculations, are shown in Table B-5-3. Also shown in the table is the local steam quality for each run that was evaluated from the trace of the recirculation flow rate and an energy balance assuming no change in the total heat transfer rate.

5.4.2 Partial and Film Boiling Results

The available data were treated as outlined above and the results are summarized in Tables B-5-2 and B-5-3, along with the local steam qualities. For each DNB run, two sets of steam-side heat transfer coefficients and the corresponding local steam qualities are available and these data points are plotted on Figure 5-19 for both P/D ratio inserts. The general trend in the data is as expected. At steam qualities larger than about 70%, a decrease in the steam-side heat transfer coefficient is noted. At approximately 100% local steam quality, the local heat transfer coefficient has dropped from a fully nucleate boiling coefficient to approximately 1500 Btu/h-ft² and continues to decrease as the steam becomes superheated. The theoretical asymptotic value of $\bar{h}_s$ for fully developed film boiling for the range of conditions tested is approximately 500 Btu/h-ft² and this is approached for high steam qualities.

The steam-side heat transfer coefficient in Figure 5-19 is a local value at the DNB thermocouple location. Quinn[31] studied the general behavior of the partial film coefficient as a function of steam quality for rod bundles and found that its local value depends on the development of the thermal and hydrodynamic boundary layers and on bulk superheat effects. The heat transfer coefficient is generally higher for developing flows than for fully developed flows. The development length is the approximate distance from the axial location in the tube where the steam-water mixture consists essentially of steam only. Thus, the high value of $\bar{h}_s$ at approximately 100% and larger steam quality can be explained partially as being due to a developing boundary layer effect. Furthermore, there will always be water droplets mixed in with the steam due to nonequilibrium effects even at steam qualities >100%. These will hit the wall and partially evaporate, thus resulting in an apparent higher heat transfer coefficient than with the steam alone.

The apparent scatter in the data is large. This is believed to be due in part to the fluctuating behavior of the thermocouple readings the averages of which may still be off a few degrees. However, the DNB tests were run over a large range of conditions as stated in connection with the DNB evaluation (in particular, the heat flux) and, of course, this will influence the partial film boiling coefficient if not to as large a degree as it does for the fully nucleate boiling coefficient. The steam-side heat transfer coefficient is also affected by the mass flux, but since the mass flux did not vary much, this effect is probably smaller than the heat flux effect.

An analysis to predict the transition region behavior is outside the scope of this work, but an empirical fit through the average of the data on Figure 5-19 is given by the following formula valid for the local quality range of $0.70 < X < 1.05$

$$\overline{Nu}_s = \frac{\bar{h}_s D_H}{k_f} = Ae^{-bx^2} \qquad \textbf{(5-25)}$$

where

$$A = 200.000$$
$$b = 4.539$$

This formula was used in adjusting the nucleate boiling heat fluxes at DNB as described in subsection 5.3.3.

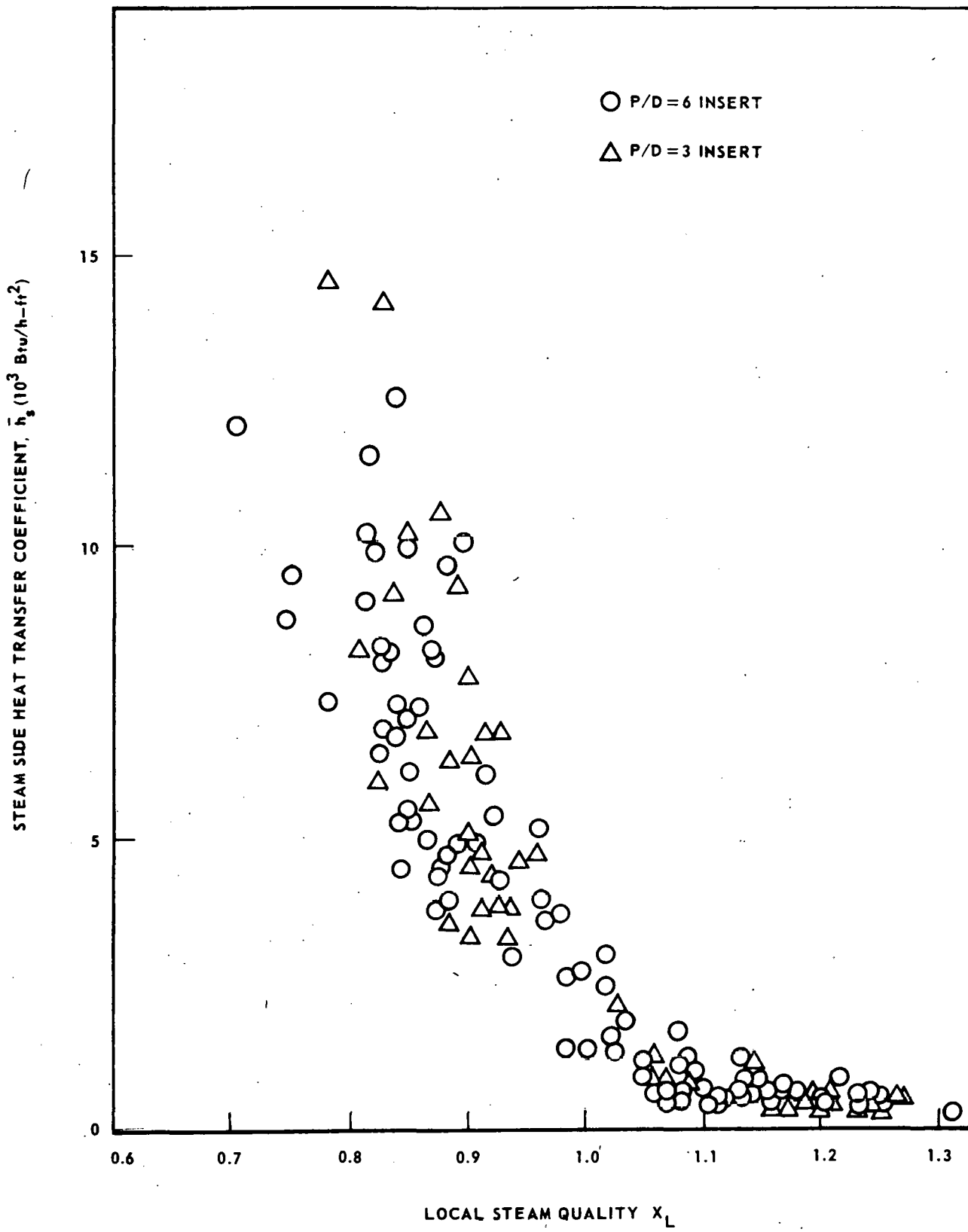

Figure 5-19. Local Steam Side Heater Tube Heat Transfer Coefficient at the Upper DNB Thermocouple Location vs. Local Steam Quality for Both the P/D = 6 and P/D = 3 Swirl Geherator Inserts

The heater tube inside wall temperature calculated from Equation 5-24 is plotted in Figure 5-20 vs the local steam quality for the two P/D ratios tested. Since the temperatures are calculated from average quantities, they are also average values and do not contain any wall temperature fluctuation component. In Figure 5-20, the effect of heat flux is more apparent than in Figure 5-19, especially at large X, in that the points corresponding to the P/D = 3 insert are generally higher than the P/D = 6 points. The reason for this is that the average heat flux for the P/D = 3 insert tests was higher as indicated in Figure 5-20 where the maximum values of the sodium temperature for each data set are given.

The S-shaped behavior of the wall temperature data is reminiscent of the trend observed by Carver, et al.,[30] for boiling in coiled tubes shown in Figure 3-5* (modified form of Figure 24 in Reference 30). Carver found that the breakdown of the nucleate boiling process was a gradual process occurring over a range of steam qualities and not uniformly around the tube (i.e., the breakdown in the nucleate boiling process started at a lower average local steam quality at some angular positions than at others). This resulted in a gradual transition as opposed to the corresponding behavior for straight channel flow also indicated in Figure 3-5.

The results in Figure 5-20 show that the departure from nucleate boiling in the present swirl flow geometry occurs gradually by some mechanism similar to that for boiling in coiled tubes. In Reference 30, however, the circumferential effect was carefully studied using a number of circumferentially located thermocouples at different axial locations. In the present tests, some feel for angular effects can be obtained from the DNB thermocouples. As noted earlier and seen in Figures 5-11 and 5-12, it appears that some thermocouples respond earlier than others or have a consistently larger temperature rise than others. This is also apparent from Table B-3, which lists all DNB thermocouple ΔT's. In particular (Figure 5-10), it is noted that DNB T/C 26, which is a "wet" thermocouple, almost consistently has higher ΔT's than the other thermocouples for the P/D = 6 tests. A similar trend is noted with DNB T/C 34 which is also "wet," but not to as large a degree as with T/C 26. On the other hand, for the P/D = 3 tests, the DNB T/C 25, which is "dry," has the largest response followed by T/C 26 which is located in the same tube and is "wet." Also, in the P/D = 3 tests, T/C 29 did not show any unexpected behavior even though it was located 180 degrees from the swirl generator (see Figure 5-10). The previous observations indicate that there is an angular effect in the present geometry; however, the evidence is insufficient to draw any conclusions of exactly what the angular effect is.

The present experiments have shown that the DNB point is difficult to define because it appears to occur gradually, and the inside wall temperature behavior vs local steam quality appears to be similar to that observed for coiled tubes. The angular effect observed for coils is there, but more experiments have to be performed in order to get a better understanding of how the gradual transition process occurs. This could be done in conjunction with experiments to investigate wall temperature fluctuation behavior associated with the transition in detail. Analytic efforts in this direction will be considered next.

5.4.3 Transient Analysis of the Heater Tube Wall

The temperature fluctuations experienced by the heater tube in the transition region is of vital importance to the design of once-through steam generators. For the present bayonet tube evaporator, certain economic advantages can be gained if operated with exit steam qualities of ~100%. This, of course, implies operating with DNB somewhere in the tubes which, according to present thinking, is not acceptable.

The wall temperature fluctuations are caused by a changing steam-side heat transfer coefficient associated with the drying out and rewetting of the steam-side surface. Intuitively, one might expect that the magnitude of the wall fluctuation is a maximum for a very low frequency change in the steam-side heat transfer coefficient and approach zero for very high frequency changes due to thermal inertia effects.

* Note that this is for a constant heat flux system.

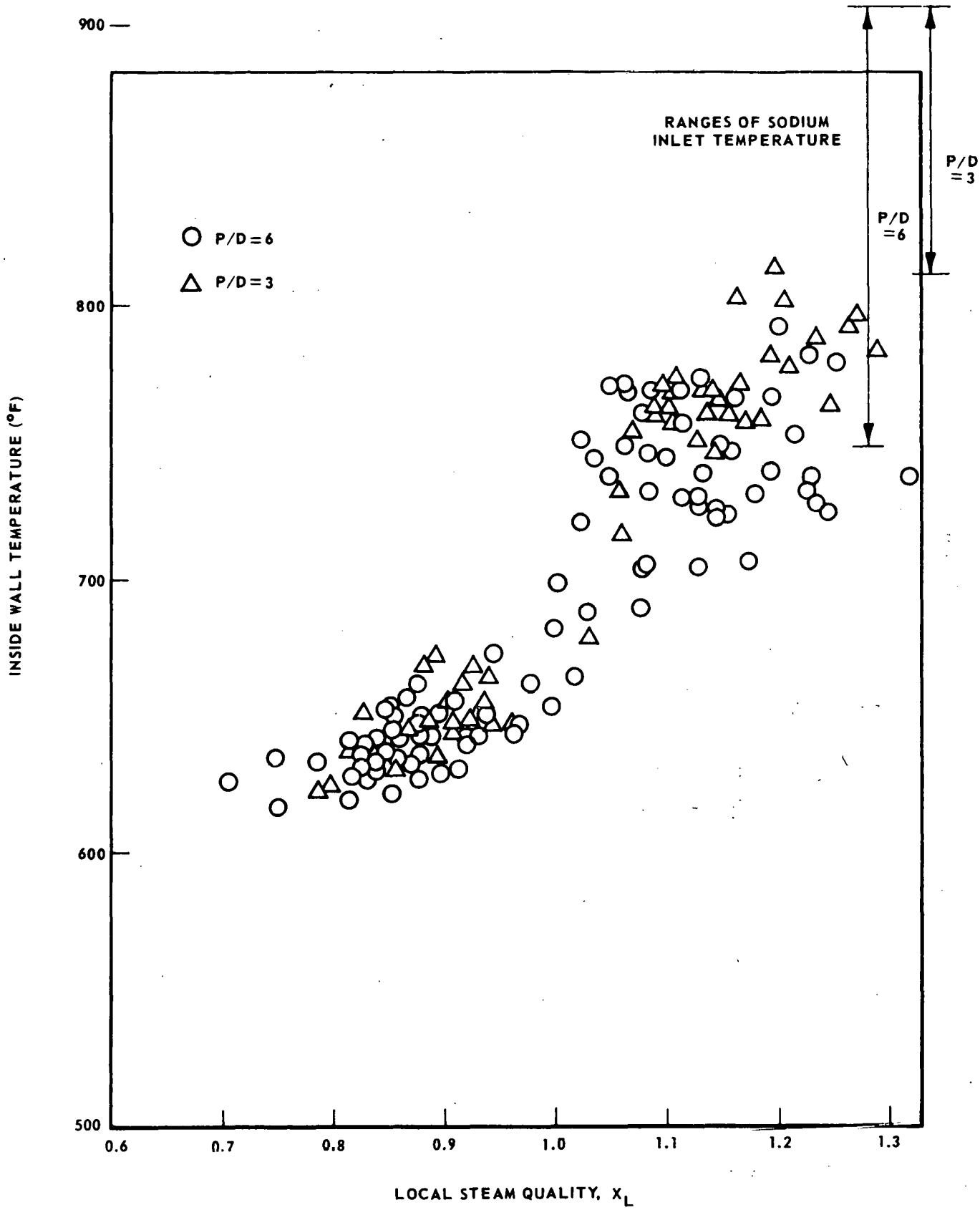

Figure 5-20. Inside Heater Tube Wall Temperature at the Upper DNB Thermocouple Location vs. Local Steam Quality for Both the P/D = 6 and P/D = 3 Swirl Generator Inserts

In order to study the above effects, a transient analysis of the tube wall was made using a finite difference approach on the computer. The transient model is described in Appendix C-1 and consisted of a 2-D, 91-point grid of the half-section of the tube to the left of the swirl generator (Figure C-1), since a line through the swirl generator is a line of symmetry.

The presence of the DNB thermocouple "insulation" was simulated by using the effective mean overall heat transfer coefficient of 2900 Btu/h-ft² evaluated earlier as a boundary condition on the surface covered by the "insulation." The sodium-side heat transfer coefficient on the remainder of the surface was kept at 4000 Btu/h-ft²-°F, which is a typical value. The total steam-side surface was subjected to a periodic varying heat transfer coefficient of different forms including the sine wave, the saw-tooth wave and the square wave. These fluctuations were constructed so that the maximum steam-side heat transfer coefficient was ~12,000, which corresponds to fully nucleate boiling conditions and a minimum value of 500, which is an average value for film boiling. The sodium temperature was held constant at the current prototypical value of 855°F, and the steam temperature was fixed at 605°F.

5.4.4 Comparison of Maximum Heater Tube Wall Temperature Fluctuations to Experiment

The effect of the functional form of the steam-side heat transfer coefficient variation was first investigated. The results for saw-tooth, sine-wave, and square-wave functions are shown in Figure 5-21, where the maximum inside and outside wall temperature fluctuations are plotted vs the cycling frequency of the steam-side heat transfer coefficient. At high frequency, the maximum wall temperature fluctuation is small and the effect of the surface cycling is not felt throughout the wall due to thermal inertia effects as indicated on the plot of percent wall penetration. The inside wall temperature fluctuation and the wall penetration depth increase with decreasing cycling frequency, and at about 5 Hz the inside variation is felt on the outside surface as well. At low frequencies the thermal inertia effect is less important and the constant value that one would calculate by the slide rule corresponding to the two extreme values of the steam-side coefficient is approached.

Even though the maximum and minimum values of the steam-side coefficient (equal to 12,000 and 500 Btu/h-ft²-°F, respectively) were the same for all functions, the square-wave variation is the most severe and results in the largest temperature variation throughout the tube wall. The analysis revealed that, in this respect, the determining factor was the fraction of the total cycle for which the heat transfer coefficient was at or near its lowest value (i.e., the longer the tube was dried out momentarily, the more severe the fluctuation).

The results in Figure 5-21 apply for the total steam-side surface subjected to film blanketing, and at an angular location of 90 degrees (Figure C-1) away from the swirl generator. If a smaller portion of the surface is film blanketed, the resulting local fluctuation is somewhat smaller; however, the decrease is not as great as one might expect due to relatively small circumferential temperature gradients. The maximum temperature fluctuation at an angular location of 45 degrees (Figure C-1), or the DNB thermocouple location, is, in general, 5 to 10% lower than at 90 degrees due to a reduced heat flux at this point, caused by the presence of the DNB T/C "insulation."

It is apparent from the previous analysis that the frequency of the varying steam-side coefficient is a determining factor in surface temperature fluctuation behavior as well as the functional form. The Sanborn traces of the DNB thermocouples, such as shown in Figures 5-11 and 5-12, contain information about the frequency of the wall temperature fluctuations actually occurring in this system as well as the magnitude of the **outside** wall temperature variation in the transition region. However, most of the DNB runs did not show any definite signs of outside wall temperature fluctuation, but rather a shift or rise of the wall temperature at the beginning of the transition region. For some runs, and in particular for T/C 25, the wall temperature fluctuation (due to transition boiling) could be clearly distinguished from that due to outside sodium temperature variation. In addition, the rms value of the peak-to-peak fluctuation and the mean frequency could be obtained. An example of such a DNB run is shown in Figure 5-22 from the P/D = 6 insert tests. The available data on the wall temperature fluctuation are shown in Table 5-3.

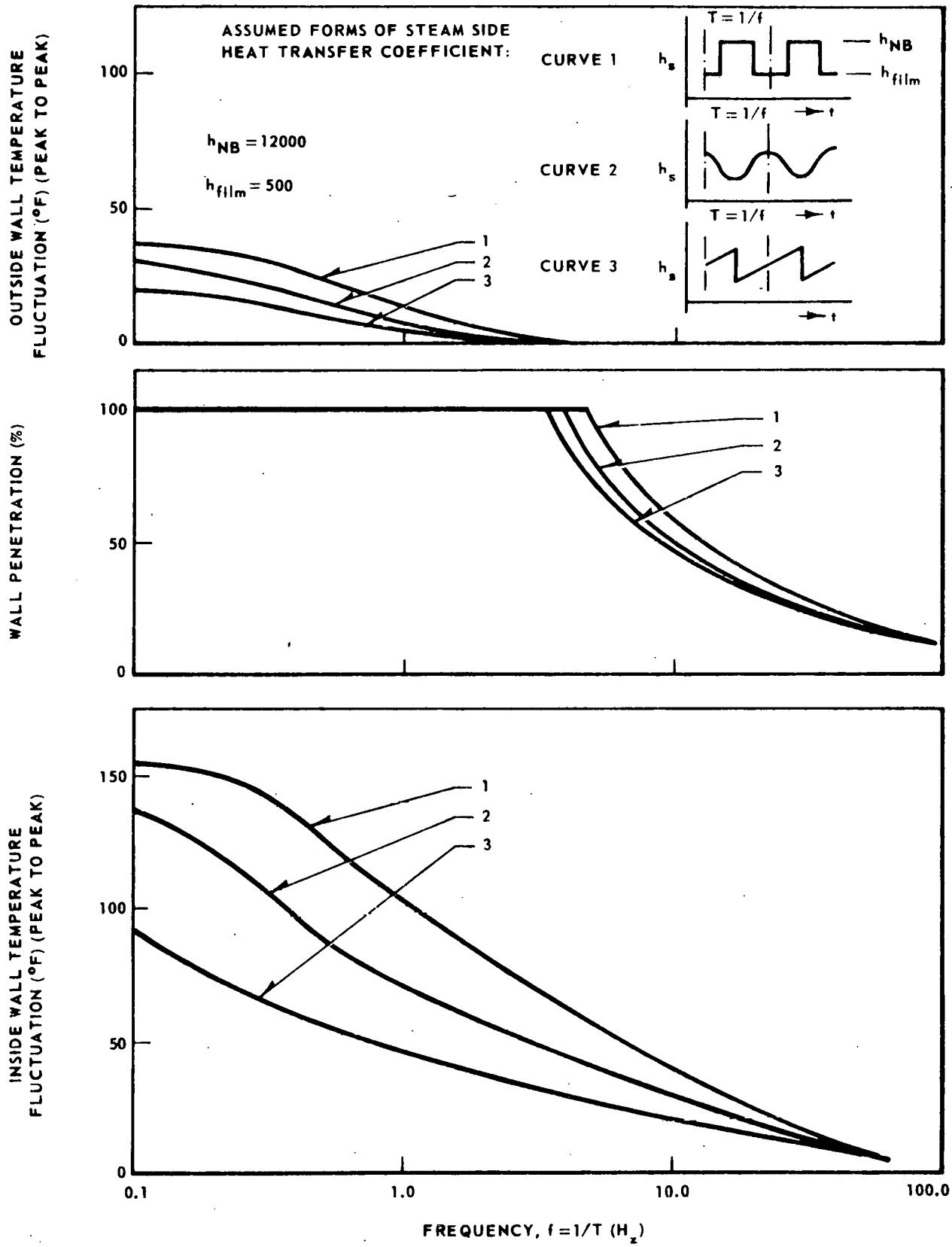

Figure 5-21. Theoretical Maximum Heater Tube Wall Temperature Fluctuation vs. Frequency at an Angular Location of 90° away from the Swirl Generator for the Total Steam Side Surface Subjected to Various Periodic Cycling of the Steam Side Heat Transfer Coefficient

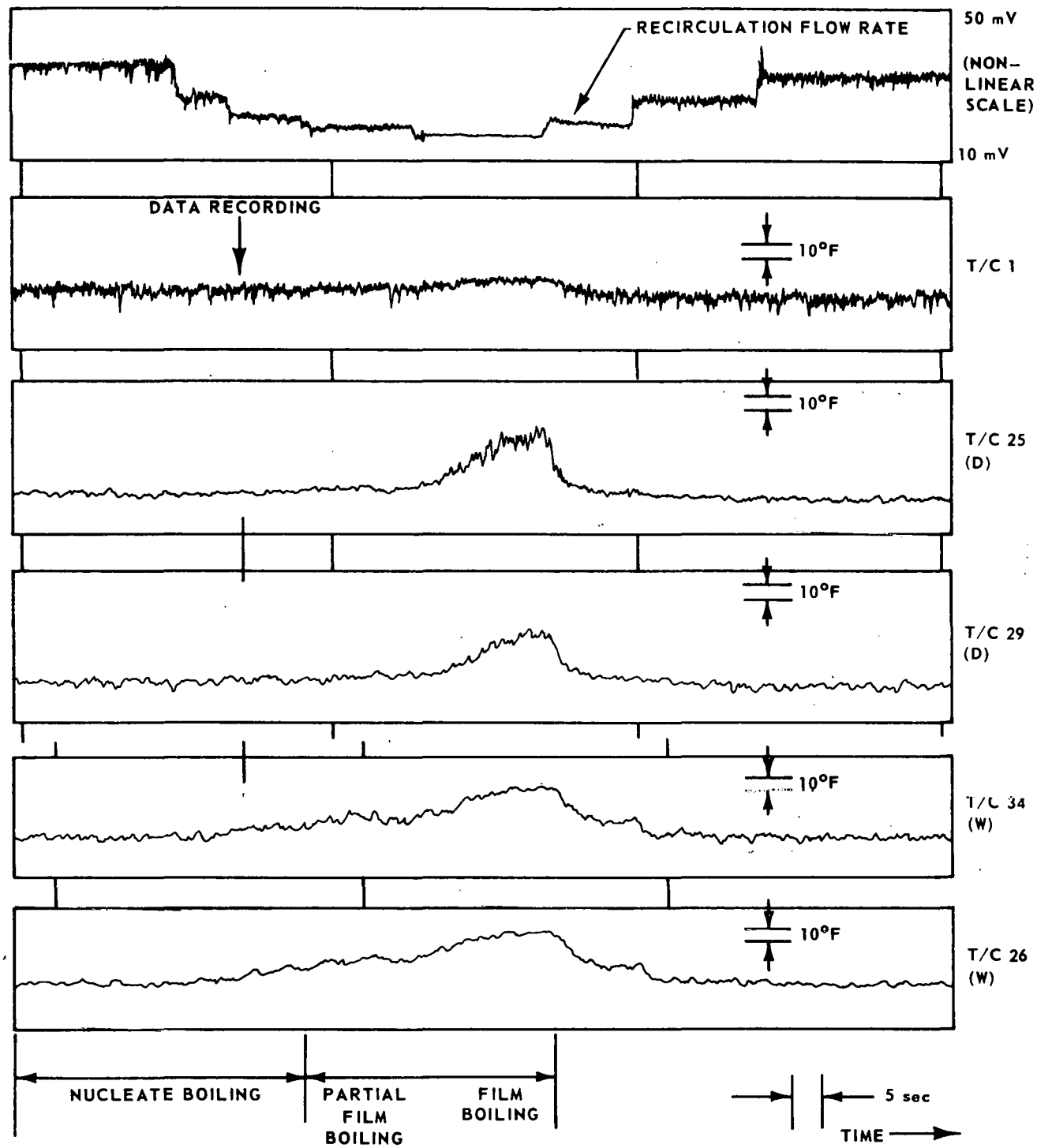

Figure 5-22. Sanborn Traces of the DNB Thermocouples during a DNB Run with P/D = 6 Swirl Generator Insert

Table 5-3
OUTSIDE WALL TEMPERATURE FLUCTUATION AND FREQUENCY DATA IN THE TRANSITION REGIME FROM SANBORN TRACES OF THE DNB THERMOCOUPLES

	Date	Time	DNB T/C	Peak-to-Peak Amplitude (°F)	Frequency (1/sec)
P/D = 6 Swirl Generator Inserts	8-17-71	1435	25	8.5	0.31
	8-17-71	1435	29	4.5	0.27
	8-17-71	1543	25	4.0	0.32
	8-19-71	0856	25	4.0	0.36
	8-19-71	1020	25	3.5	0.32
	8-19-71	1128	25	3.0	0.33
	8-19-71	1128	26	2.5	0.24
	8-09-71	1602	25	6.0	0.28
	8-09-71	1057	25	5.0	0.30
	8-09-71	1057	29	4.0	0.22
	8-06-71	1508	25	7.0	0.36
	8-06-71	1508	29	6.0	0.20
P/D = 3 Swirl Generator Inserts	10-19-71	1129	25	6.0	0.22
	10-19-71	1317	25	3.5	0.20
	10-19-71	1753	25	4.0	0.26
	10-19-71	1429	25	5.0	0.28
	10-19-71	1506	25	6.0	0.28
	10-19-71	1542	25	4.0	0.24

The observed **outside** wall temperature fluctuations correspond to certain fluctuations on the inside surface. The computer program used to generate Figure 5-21 was used again assuming the square-wave behavior for the steam-side heat transfer coefficient over the total surface. The minimum value of the steam-side coefficient had to be raised from 500 to 3300 Btu/h-ft² °F for the calculated inside wall temperature fluctuation to fall above the experimental data. The calculated results for both values of the steam-side coefficient are shown in Figure 5-23 along with the experimental data from Table 5-3. The calculated outside wall temperature fluctuation denoted by "2" in Figure 5-23 is above all measured data for this value of the steam-side coefficient; thus, the corresponding inside wall temperature fluctuation represents an upper bound on the wall temperature fluctuation that did occur in the present system. The severity of the actual fluctuations is believed to be less than implied here because, as noted earlier from the Sanborn traces, only part of the surface appears to experience fluctuations of these magnitudes.

It is interesting to note the range of frequencies of the observed fluctuations is ~0.20 to 0.35 Hz, which is comparable to the results of Hench,[23] which reported ~0.5 Hz for transition boiling in rod bundles. The frequency may depend on the mass flux on the steam side; however, no such effect could be noted here because of the narrow range of mass flux rates tested. It appears from Figure 5-23 that the average frequency is smaller for the P/D = 3 than for the P/D = 6 data. This effect may be a real one; however, more tests are needed before definite conclusions can be drawn on this point.

The above results show that there is reason to believe that a once-through bayonet tube steam generator may be feasible. A development program to optimize the swirl generator with respect to minimizing the wall temperature fluctuations is recommended.

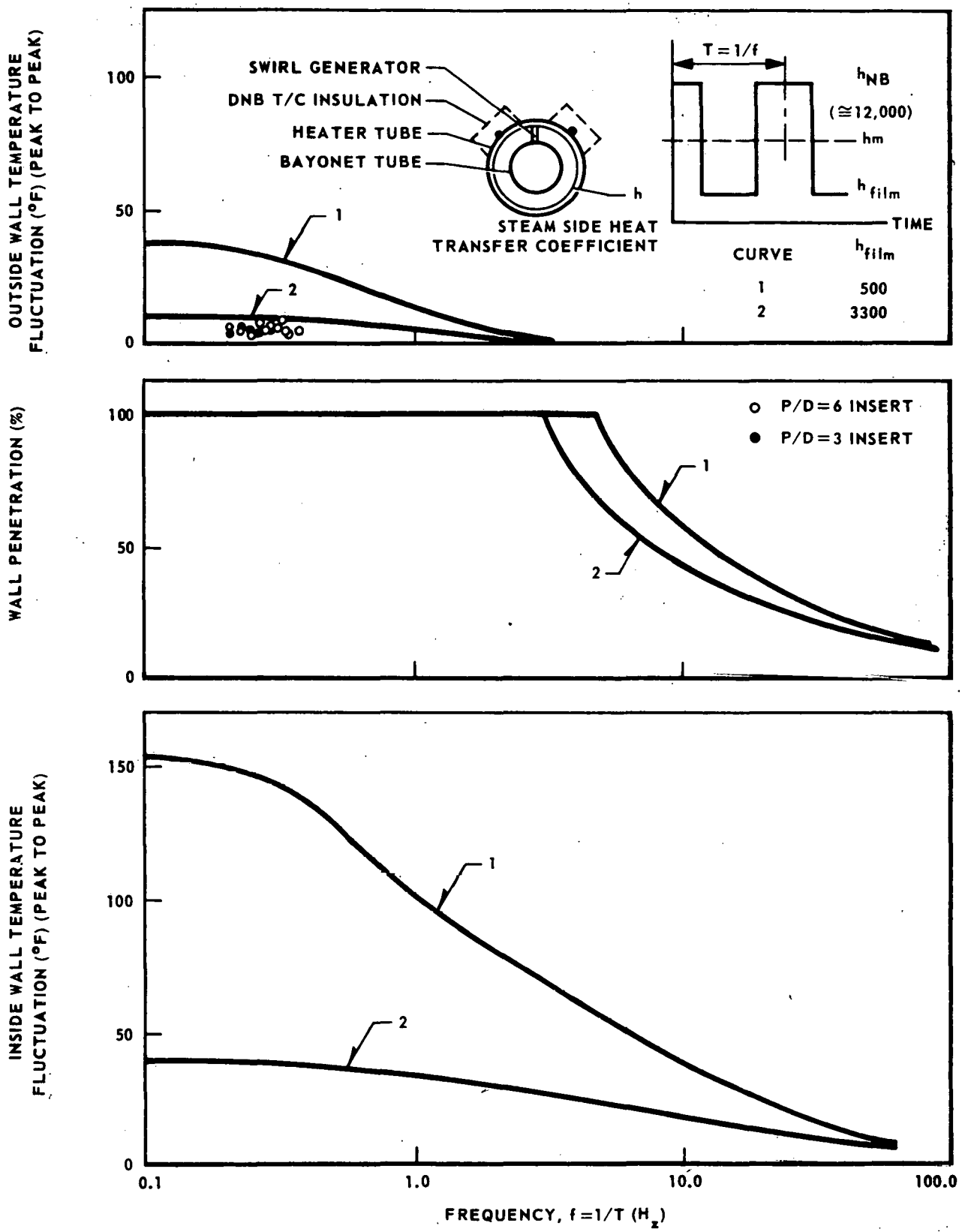

Figure 5-23. *Comparison of Theoretical Maximum Heater Tube Wall Temperature Fluctuations Compared to Measured Wall Temperature Fluctuations*

5.5 STEAM-SIDE FLOW DISTRIBUTION

A limited amount of steam-side flow distribution data for the evaporator is available. The flow in each tube was measured by orifices located at the top end of the bayonet tubes (Figure 4-6), and a diagram of the orifice arrangement is shown in Figure 5-24. The orifices were manufactured and calibrated with water by Foster Wheeler Corporation before being installed in the evaporator with the P/D = 6 swirl generator inserts.[36]

The pressure drop across the orifices was measured as the difference between the inlet plenum pressure and the pressure tap. The impulse lines from the pressure taps were taken out through the head by Conax fittings and fed directly to a Barton differential pressure transmitter. Each of the seven tubes, denoted arbitrarily by A through G, had to be valved in separately, and, thus, only one reading could be obtained at a time. It was thus imperative that the recirculation flow rate was held constant during the time period necessary for the pressure drop across each tube to be recorded in sequential order on the Sanborn recorder; however, no problems were experienced in this respect.

The Sanborn trace from the first test made is shown in Figure 5-25 for a relatively low flow rate. At higher flow rates, difficulties were experienced with the reading from Tube E, the impulse line of which appeared to have become partially blocked up after the recirculation flow rate had been approximately doubled. That partial blocking had occurred, was inferred from the fact that the trace went far off scale and did not show any similarity to the traces from the other tubes and to the previous trace at low flow rate. Further confirmation that something had happened to the impulse line was gathered when the flow was decreased again to about the same level as with the first run, and the problem still existed for Tube E. The problem was not pursued any further due to time limitations.

The pressure drop data are shown in Table 5-4, along with actual water flow rates and percent deviation from the mean flow rate. The water flow rates were obtained from the calibration curves supplied by Foster Wheeler Corporation.[36]

Table 5-4
STEAM SIDE FLOW DISTRIBUTION DATA FOR THE EVAPORATOR OPERATING AT NEAR RATED CONDITIONS[(a)]

Run		Bayonet Tube A	B	C	D	E	F	G	Average Flow (lb/h)
	ΔP (psi)	0.65	0.69	0.66	0.66	0.65	0.65	0.64	
1	W (lb/h)	1100	1120	1110	1100	1080	1105	1090	1100.71
	% Deviation	0.00	1.75	0.84	0.00	-1.82	0.39	-0.91	
	ΔP	2.31	2.40	2.35	2.35	(b)	2.35	2.22	
2	W	2030	2000	2020	2010		2050	1930	2006.67
	%	1.16	-0.33	0.66	0.17		2.16	-3.82	
	ΔP	2.15	2.25	2.20	2.22		2.23	2.07	
3	W	1960	1940	1955	1950		2000	1860	1944.17
	%	0.81	-0.21	0.56	0.30		2.87	-4.33	
	ΔP	1.90	2.00	1.98	1.97		1.96	1.87	
4	W	1850	1840	1860	1850		1880	1775	1842.50
	%	0.41	-0.14	0.95	0.41		2.04	-3.66	

(a) Exit steam quality was in the range of approximately 30% to 60%.
(b) Value not given due to instrument problems.

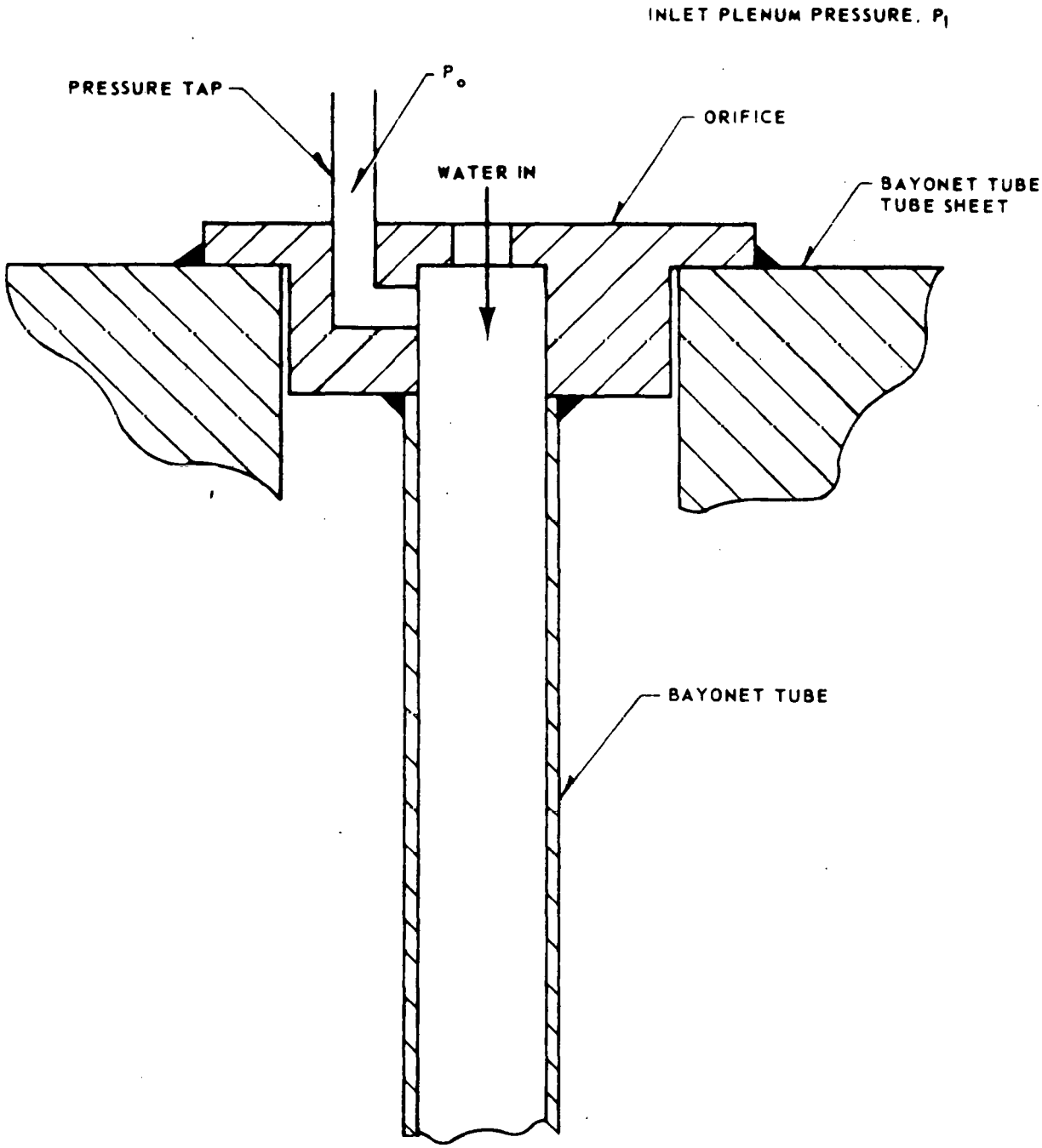

Figure 5-24. *Diagram of Orifices Installed on the Bayonet Tubes and Used to Measure the Steam Side Flow Distributions with the P/D = 6 Inserts*

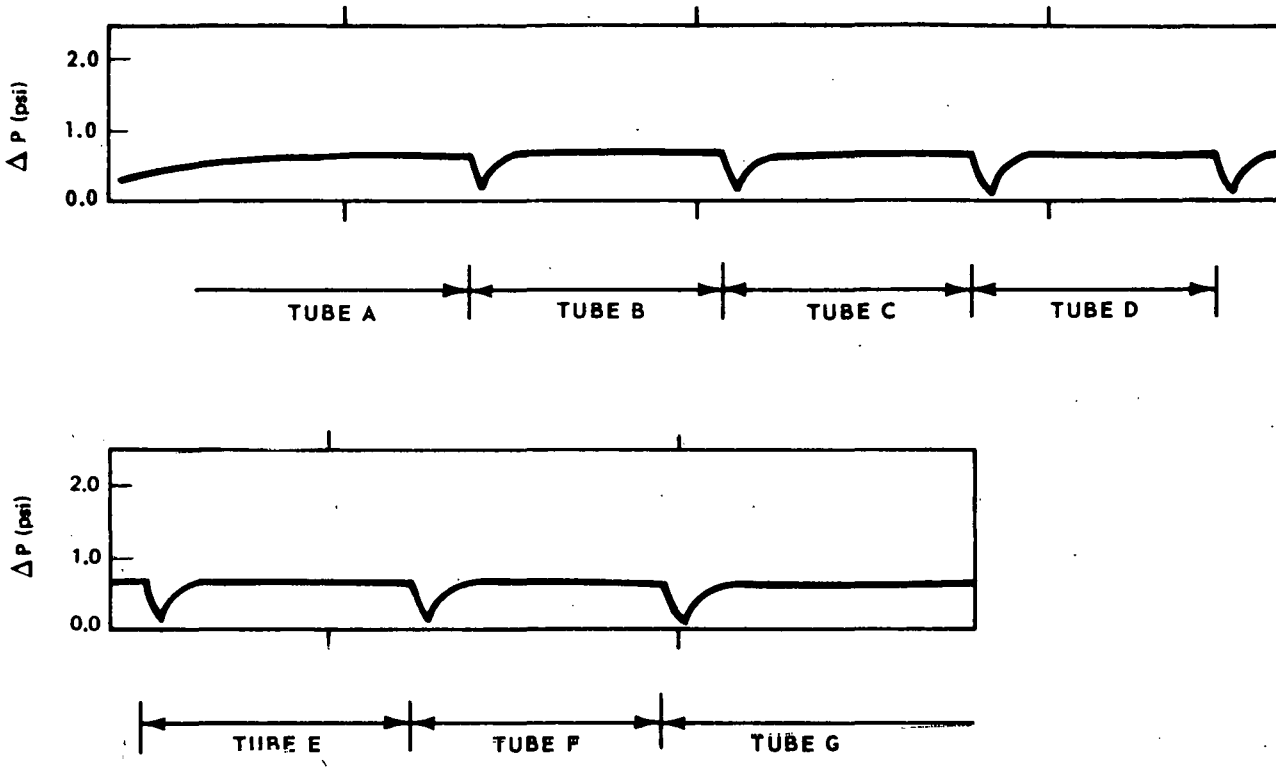

Figure 5-25. Sanborn Trace of Pressure Drops across the Bayonet Tube Orifices with the P/D = 6 Insert

It is apparent from Table 5-4 that the flow distribution is quite uniform with the center tube having about 4% less flow than the average tube for the higher flow rates. There seems to be no reason why the center tube should have less flow than the edge tubes. It was noted in Figures 5-2 and 5-3 that the average sodium temperature in the center channel was less than in the edge channel. Thus, the center tube runs "cooler" or receives less heat than the others; this was predicted by the EVAP code to be approximately 1 to 2%. This results in a lower average steam quality and thus a lower friction pressure drop. Thus, with a constant plenum-to-plenum driving pressure, the flow should be higher in the center tube than in the edge tubes. One other factor that might influence the flow distribution is dimensional tolerances. In Reference 36 it was found that the center tube orifice had slightly higher pressure drop than the others and this might have caused the indicated flow unbalance.

From the previous discussion, it can be concluded that the flow distribution is very uniform. It is believed that the relatively large fraction of the pressure drop occurring in the bayonet tubes contributes greatly to this result.

5.6 PRESSURE DROPS

The measured sodium- and steam-side pressure drops for the evaporator are compared to calculated results in this subsection. This subject will not be treated extensively because the pressure drop data are not considered to be very accurate. The approach here will be to present the various pressure drop measurements for 25 runs selected over as wide a range of flow rates as possible and compare to calculated results using the prediction methods used by Foster Wheeler Corporation for the original design.[32]

5.6.1 Sodium-Side Pressure Drops

Absolute pressure measurements at the inlet and outlet of the evaporator were recorded automatically by the data acquisition system. The pressure difference was formed by summation in an electronic summer and this reading was also recorded. Locations of the pressure drop transmitters and instrument connection details are shown on Figures 4-2 and 4-3, respectively.

The pressure difference as recorded by this instrumentation does not represent the friction drop directly due to the static head of sodium involved. The friction pressure drop on the sodium side is obtained by subtracting the measured pressure difference between outlet and inlet from the static head. The pressure drop reading, as obtained by subtraction of absolute readings between the outlet and inlet, did not check the reading obtained from the ΔP instrument as can be seen from Table 5-5. By comparing the static head to the ΔP instrument reading, it is clear that there is something wrong since the friction pressure drop given by the difference between the static head and the ΔP reading is often negative. On the other hand, the difference between the static head and the ΔP reading, based on absolute pressures, shows reasonable numbers and are also given in the next to last column in the table. Also shown for comparison are the pressure drops which were derived by the procedures used in the Foster Wheeler design calculations.[33] The measured and calculated pressure drops are plotted vs the sodium Peclet number in Figure 5-26. The solid line in this figure represents the predicted friction pressure drop from the last column in Table 5-5. The points in Figure 5-26 are those given in the next to the last column in Table 5-5 and probably represent the most accurate data available. In view of the uncertainty in the data, no definite conclusions can be drawn; however, it appears that the sodium-side pressure drop may have been over-predicted aprpoximately by a factor of two. The reason for this is difficult to assess but must be due to over-prediction of the effect of the baffle plates since this is where the majority of the pressure drop occurs.

5.6.2 Steam-Side Pressure Drops

Absolute pressure measurements were made at the inlet and outlet of the evaporator and at the steam drum. The steam drum pressure and the evaporator exit pressure should read close to the same pressures under most conditions which provided a check on these readings. In addition to these absolute readings, the difference between the steam-side inlet and the outlet was measured by summation of absolute pressures in an electronic summer. The pressure data were recorded automatically by the data acquisition system. Pressure instrumentation connection details are shown in Figure 4-3, and the measurement points are shown in Figure 4-2.

Pressure drop data for 25 runs are shown in Table 5-6, along with recirculation flow rate and exit steam quality. The runs were selected over as wide a range of these two quantities as practical. From the table it is clear that the steam drum pressure and the evaporator pressure are in reasonable agreement, except for the last few runs and the corresponding pressure drops are shown in the table. The differential pressure drop measured by the summer is also shown for comparison and the agreement is reasonable except for the first 5 runs.

The three columns of pressure drops do not represent the friction pressure drop directly. The net static head of water/steam in the bayonet tube and annulus must be added to these. This was done using the Foster Wheeler design methods,[33] making the simplification that the subcooled length was the same for all cases, and the results are shown in the two columns next to the last column in Table 5-6 for the pressure drops based on absolute readings. The last column shown in the table is the predicted friction pressure drops, using the methods of Reference 33, except that the swirl flow friction was predicted using the methods of Reference 11.

The numbers in the last two columns are plotted in Figure 5-27 vs the Reynold's number in the bayonet tube. The bayonet tube Reynold's number was used in the plot because most of the pressure drop is in the bayonet tubes. The predicted pressure drop is represented approximately by the solid line in Figure 5-27. The agreement between prediction and the particular data set used is very good except at low bayonet tube Reynold's numbers where the pressure drop is small and the accuracy of the measurement poor. Although no definite conclusions can be drawn, the results are encouraging, and it appears that the steam-side pressure drop can be predicted with considerable confidence.

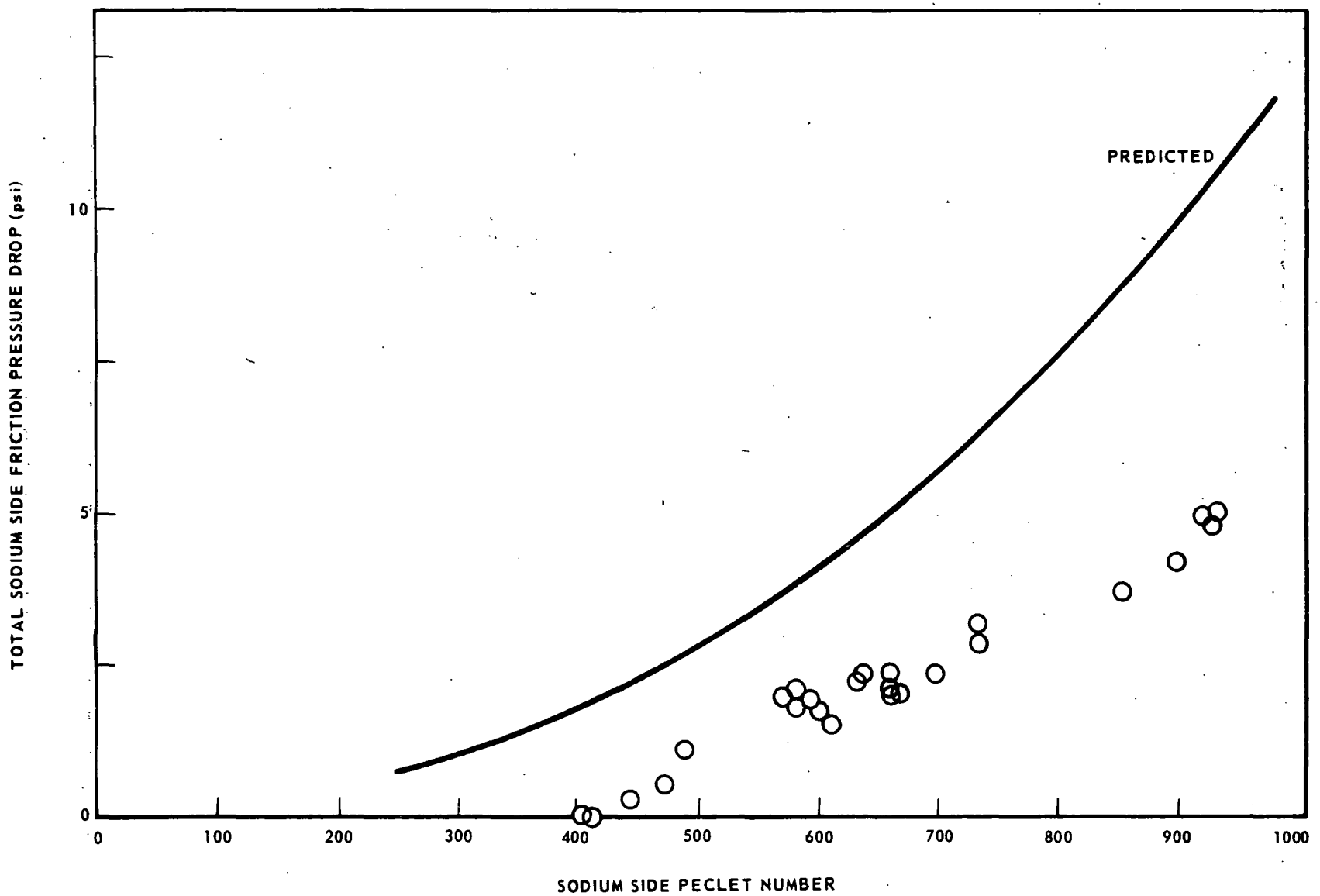

Figure 5-26. *Comparison of Predicted Sodium Side Friction Pressure Drop to Measured Friction Pressure Drop for the Evaporator vs. the Sodium Average Peclet Number*

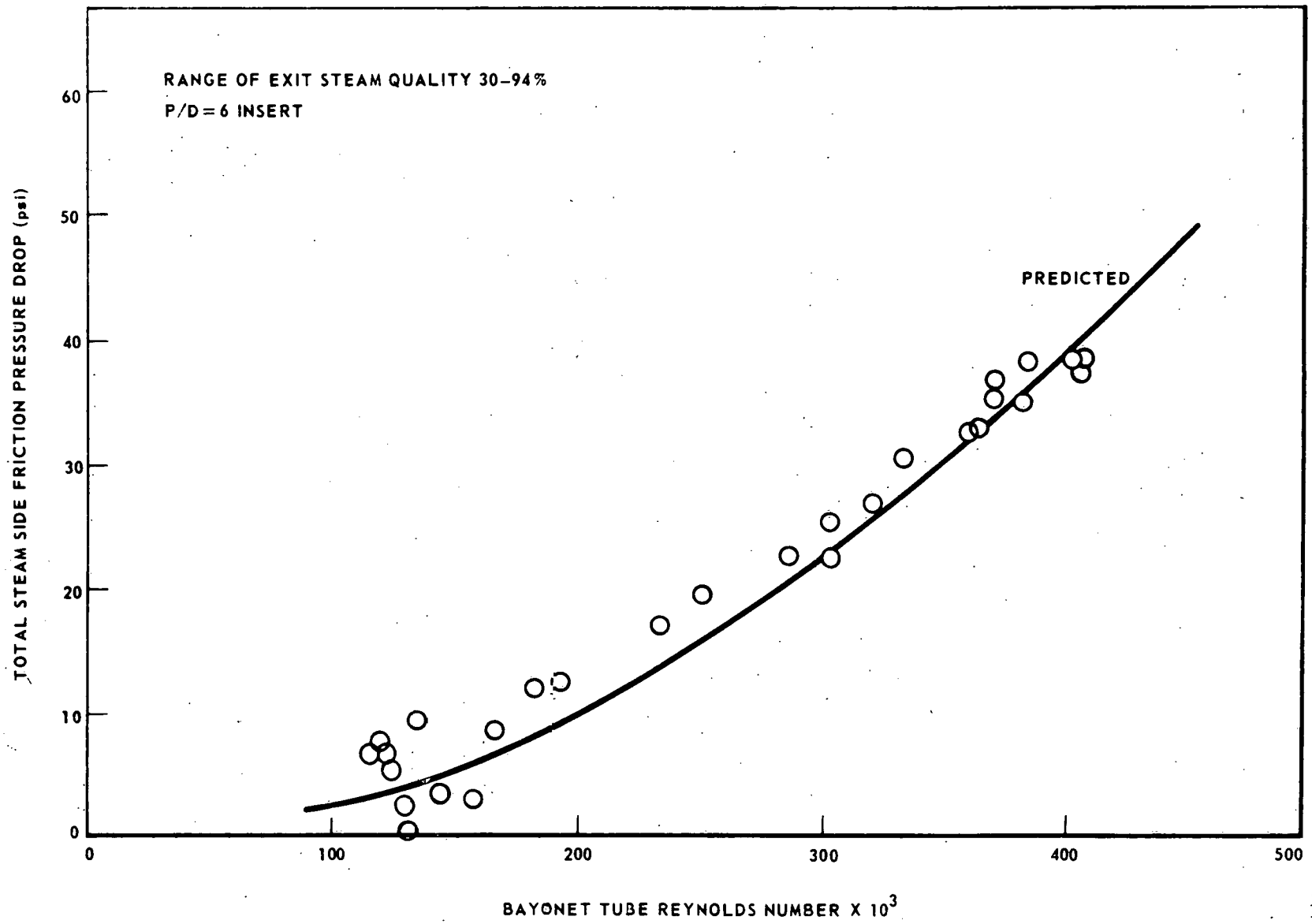

Figure 5-27. Comparison of Predicted Total Steam Side Friction Pressure Drop to Measured Friction Pressure Drop for the Evaporator vs. the Bayonet Tube Reynolds Number and for Exit Steam Qualities in the Range of Approximately 30 - 94 Percent

Table 5-5
SODIUM-SIDE PRESSURE DROP DATA FOR THE EVAPORATOR

Date	Time	Peclet Number	Sodium Flow Rate (lb/h)	Static Head (Inches of Sodium)	Static Head (psi)	Sodium Inlet (psig)	Sodium Outlet (psig)	Outlet-Inlet (psi)	ΔP From Instrument (psi)	Measured Friction Pressure Drops (psi)	Predicted Friction Pressure Drops (psi)
3-29-71	2010	695	69100	521	16.37	33.7	47.6	13.9	15.8	2.47	5.75
3-29-71	2125	657	65100	521	16.37	42.9	57.0	14.1	16.0	2.47	5.10
3-29-71	2155	656	65100	522	16.40	42.2	56.4	14.2	16.1	2.20	5.10
3-30-71	0530	610	60300	522	16.40	33.1	47.9	14.8	16.9	1.60	4.38
3-30-71	1133	599	59000	520	16.34	17.8	32.3	14.5	16.8	1.84	4.19
5-20-71	1647	734	73400	519	16.31	21.6	34.7	13.1	15.1	3.21	6.49
5-20-71	1848	735	75200	515	16.18	27.0	40.2	13.2	15.0	2.98	6.81
5-21-71	1334	634	62800	509	15.99	22.4	36.0	13.6	16.0	2.39	4.75
5-21-71	1349	632	62100	511	16.05	22.0	35.7	13.7	16.2	2.35	4.64
5-21-71	1419	665	63100	513	16.12	20.7	34.7	14.0	16.4	2.12	4.80
5-21-71	1434	663	62800	515	16.18	20.7	34.7	14.0	16.3	2.18	4.75
5-28-71	1131	588	58100	517	16.24	25.8	40.0	14.2	16.8	2.04	4.07
5-28-71	1201	575	57800	518	16.27	24.5	38.7	14.2	16.8	2.07	4.02
5-28-71	1231	579	58000	517	16.24	25.7	39.9	14.2	16.7	2.04	4.05
5-28-71	1301	576	56800	517	16.24	24.6	38.7	14.1	16.7	2.14	3.89
8-6-71	1109	897	91053	520	16.34	30.1	42.2	12.1	13.8	4.24	9.98
8-6-71	1228	926	94962	517	16.24	33.4	44.6	11.2	12.8	5.04	10.86
8-6-71	1432	918	93700	517	16.24	28.1	39.3	11.2	13.0	5.04	10.57
8-6-71	1546	926	94632	520	16.34	25.7	37.2	11.5	12.9	4.84	10.78
8-9-71	1057	851	85909	518	16.27	20.1	32.6	12.5	14.4	3.77	8.89
8-13-71	1009	402	39243	516	16.21	25.0	41.2	16.2	18.7	0.01	1.85
8-13-71	1042	406	39749	516	16.21	23.2	39.4	16.2	18.7	0.01	1.90
8-13-71	1115	442	43293	517	16.24	21.9	37.8	15.9	18.5	0.34	2.26
8-13-71	1206	471	46239	518	16.27	20.4	36.1	15.7	18.3	0.57	2.57
8-13-71	1346	489	48015	517	16.24	27.8	42.9	15.1	17.6	1.14	2.78

Table 5-6
STEAM-SIDE PRESSURE DROP DATA FOR THE EVAPORATOR

Date	Time	Recirculation Flow Rate (lb/h)	Exit Steam Quality (%)	Bayonet Tube Reynolds Number $X10^{-3}$	Steam Drum Pressure, P_d (psig)	Outlet Pressure P_{out} (psig)	Inlet Pressure P_{in} (psig)	Difference $P_{in}-P_d$ (psi)	Difference $P_{in}-P_{out}$ (psi)	ΔP From Instrument (psi)	Friction Pressure Drop Based on $P_{in}-P_d$ (psi)	Friction Pressure Drop Based on $P_{in}-P_{out}$ (psi)	Calculated Friction Pressure Drop (psi)
3-29-71	2010	20967	34	404	1635.7	1634.0	1665.5	29.8	31.5	6.5	36.1	37.8	40.1
3-29-71	2125	15762	46	304	1594.3	1591.7	1610.3	16.0	18.6	3.5	23.1	25.7	23.1
3-29-71	2155	16523	43	318	1577.2	1574.0	1594.3	17.1	20.3	4.0	24.0	27.2	25.2
3-30-71	0530	21020	30	405	1569.7	1565.1	1597.8	28.1	32.7	7.0	34.1	38.7	40.2
3-30-71	1133	20663	35	398	1623.6	1620.7	1653.6	30.0	32.9	7.2	36.3	39.2	38.9
5-20-71	1647	19109	35	368	1587.2	1584.6	1613.8	26.6	29.2	28.8	32.9	35.5	33.5
5-20-71	1848	19086	36	368	1572.8	1567.3	1597.9	25.1	30.6	31.3	31.5	37.0	33.4
5-21-71	1334	19819	31	382	1603.7	1598.3	1630.9	27.2	32.6	32.5	33.3	38.7	35.8
5-21-71	1349	17064	37	329	1579.1	1574.0	1598.4	19.3	24.4	24.5	25.8	30.9	26.9
5-21-71	1419	12915	47	249	1555.8	1550.3	1562.9	7.1	12.6	11.7	14.3	19.8	15.7
5-21-71	1434	9249	48	178	1591.8	1585.5	1590.5	-1.3	5.0	3.4	5.9	12.2	8.2
5-28-71	1131	19775	30	381	1578.6	1574.5	1604.1	25.5	29.6	30.2	31.5	35.6	35.7
5-28-71	1201	14832	39	286	1589.5	1585.4	1601.4	11.9	16.0	15.3	18.5	22.6	20.4
5-28-71	1231	12078	49	233	1572.6	1568.4	1578.4	5.8	10.0	9.0	13.1	17.3	13.7
5-28-71	1301	9907	51	191	1607.2	1603.2	1608.5	1.3	5.3	3.4	8.7	12.7	9.3
8-6-71	1109	7403	94	143	1646.8	1643.4	1638.3	-8.5	-5.1	1.34	0.4	3.8	5.3
8-6-71	1228	6651	83	128	1657.5	1656.1	1650.1	-7.4	-6.0	1.19	1.2	2.6	4.3
8-6-71	1432	6803	87	131	1637.5	1637.5	1629.2	-8.3	-8.3	0.95	0.4	0.4	4.4
8-6-71	1546	8182	87	158	1652.6	1653.7	1647.8	-4.8	-5.9	11.16	3.9	2.8	6.4
8-9-71	1057	8612	81	166	1620.2	1619.0	1619.1	-1.1	0.1	2.14	7.4	8.6	7.1
8-13-71	1009	6105	82	118	1572.9	1560.8	1560.2	-12.7	-0.6	2.15	-4.2	7.9	3.6
8-13-71	1042	6125	80	118	1557.3	1545.3	1544.2	-13.1	-1.1	2.05	-4.6	7.4	3.6
8-13-71	1115	6019	80	116	1627.9	1616.9	1615.7	-12.2	-1.2	1.97	-3.7	7.3	3.5
8-13-71	1206	6998	68	135	1599.8	1589.1	1590.1	-9.7	1.0	2.46	-1.5	9.2	4.7
8-13-71	1346	6396	76	123	1634.3	1626.5	1623.6	-10.7	-2.9	1.69	-2.3	5.51	3.9

6. SUPERHEATER THERMAL PERFORMANCE

6.1 HEAT TRANSFER PERFORMANCE

The thermal performance results of the helical coil superheater are given in this section. The results include the overall heat transfer coefficients evaluated for the coil region and the steam-side pressure drop. The sodium-side pressure drop will be discussed only briefly because the pressure drop was very small, as expected, which made an evaluation difficult. The data reduction procedure used to obtain the overall heat transfer coefficients is discussed in the following subsection.

6.1.1 Data Reduction Procedure

The complex geometry of the helical coil superheater makes it difficult to measure the overall heat transfer coefficient directly. The approach taken, therefore, was to use an indirect method based on matching of calculated sodium temperature profiles with measured sodium temperature profiles. The locations of the sodium thermocouples used to measure the sodium temperature profiles are shown in Figure 4-14. A circumferential sodium temperature profile at the lower end of the coil region is obtained from thermocouples 1 through 9, and an axial sodium temperature profile is obtained from thermocouples 9 through 12. The sodium temperature distribution was calculated from measured inlet test conditions by using the SUPER data reduction code developed for this purpose. This code works much the same way as the EVAP code developed for the evaporator. A summary description of the SUPER code is given in Appendix A-2.

The SUPER code is based on a nodal model of the superheater. Given the inlet conditions of the steam and sodium along with the flow rates, the temperature and pressure distribution of the steam in the tubes and the sodium temperature distribution are calculated. Approximately 60% of all heat transfer is in the helical coils and evaluation of the overall heat transfer coefficient was made for this region. The overall heat transfer coefficients used in the code were calculated from the following correlations:

The sodium-side heat transfer coefficient was calculated for cross flow using the Rickard[6] correlation given by

$$Nu = \frac{h_{Na} D_H}{k} = 4.02 + 0.028 \, Pe_{max}^{0.67} \tag{6-1}$$

For the wall thermal conductivity, the data from Reference 36 given by Equation 5-2 were used. The steam-side heat transfer coefficient for the coil is[16]

$$Nu = \frac{h_s D_H}{k} = 0.0133 \, (Re)_f^{0.84} \, (Pe)_f^{1/3} \, C_3 \tag{6-2}$$

Since the steam-side heat transfer coefficient is the controlling conductance in the superheater, the constant miltiplier C_3 was introduced; this was the parameter varied to achieve matching of the calculated and measured sodium temperature profiles. This choice was guided by the observation that, in general, the heat transfer in curved tubes or coils is higher than in straight tubes approximately as the ratio of the friction factors for the coiled and straight tube.[18] This ratio is given by Ito's correlation:[17]

$$f_c/f = (Re(r/R)^2)^{0.05} \tag{6-3}$$

A comparison of the axial sodium temperature profile obtained with the SUPER code for one run is shown in Figure 6-1 and the corresponding circumferential temperature distribution near the lower end of the coils is shown in Figure 6-2. The value of C_3 in this case was 1.4 and was found after several trials; this resulted in the best fit for most of the data considered.

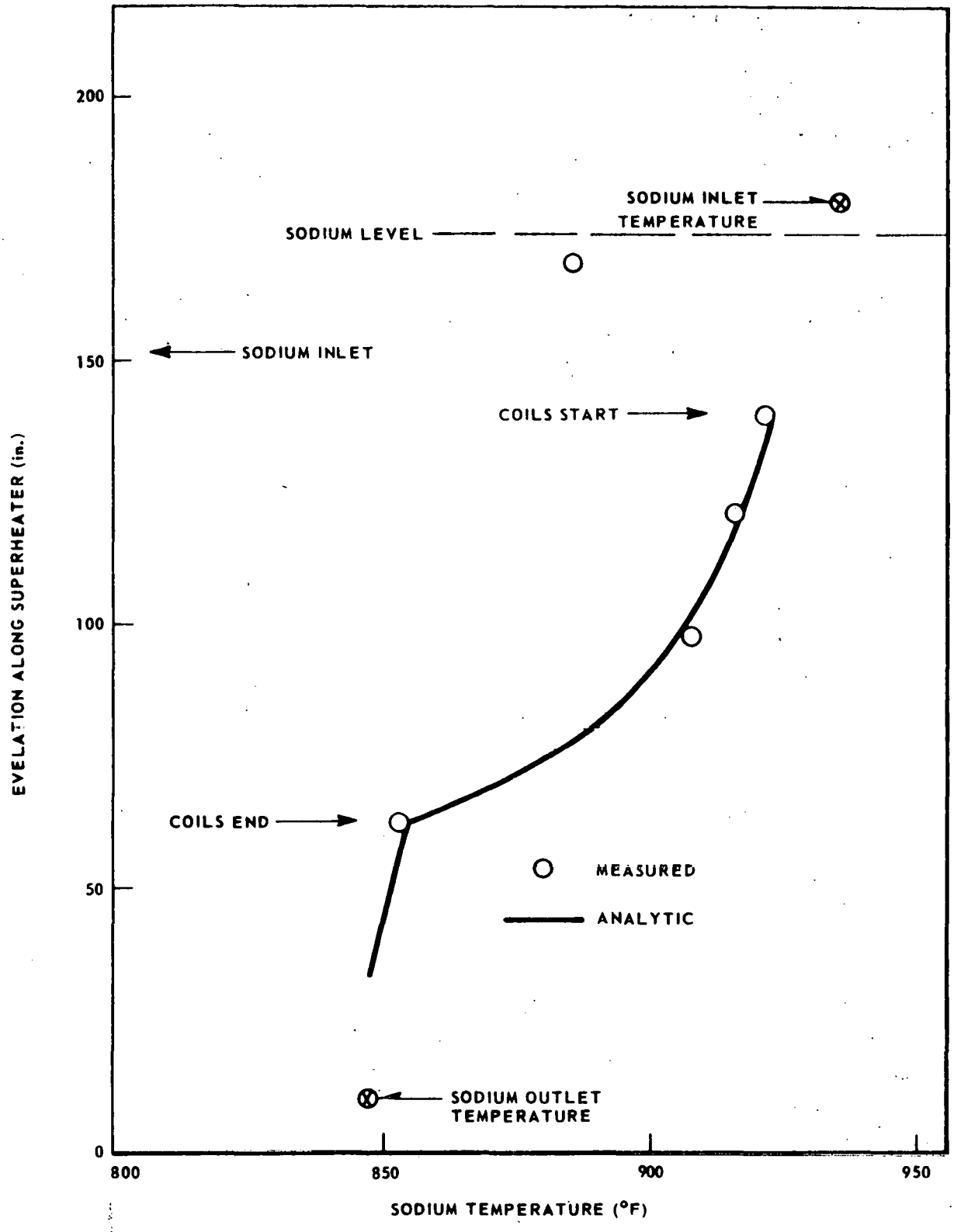

Figure 6-1. Comparison of Measured and Calculated Axial Sodium Temperature Profile In Segment No. 2 of the Superheater

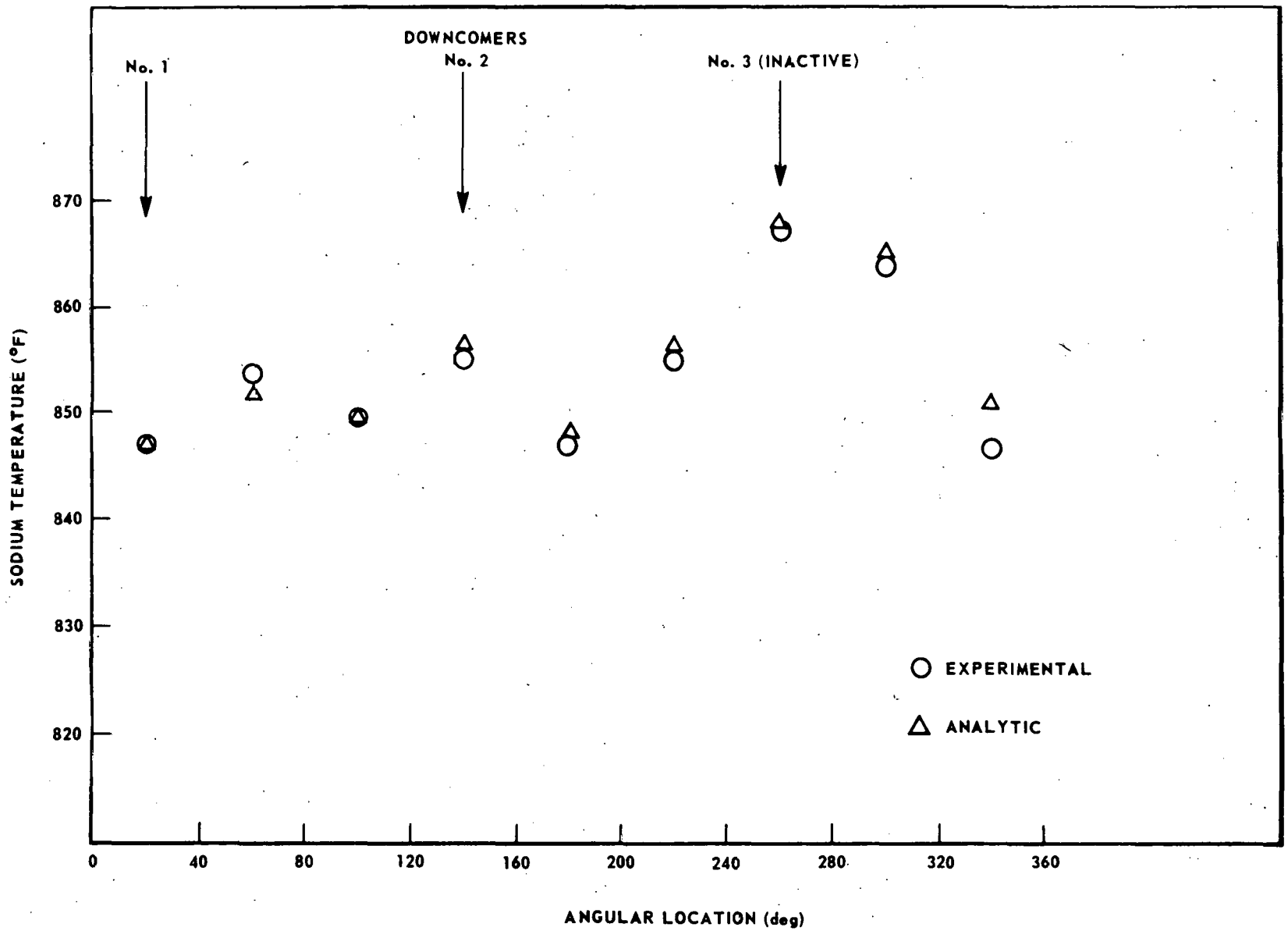

Figure 6-2. *Comparison of Experimental and Analytic Circumferential Sodium Temperature Variations near the Lower End of the Coiled Section in the Superheater*

The local heat transfer coefficients given by Equations 6-1 and 6-2 varied considerably, especially on the steam-side, because the thermal properties of superheated steam are changing strongly. It is convenient for comparison purposes to calculate an average overall heat transfer coefficient for the coil region. The approach used for the evaporator boiling region was used here also (i.e., first the average surface coefficients and the mean thermal conductivity were calculated, and these were used in Equation 5-4 to yield the mean overall heat transfer coefficient).

6.1.2 Coil Region Overall Heat Transfer Coefficient

A limited amount of the available thermal performance data was reduced. The range of operating conditions maintained during these runs is given below:

- Sodium Inlet Temperature — 907 to 959°F (935)*
- Sodium Outlet Temperature — 834 to 858°F (855)
- Steam Inlet Temperature — 600 to 611°F (607)
- Steam Outlet Temperature — 882 to 936°F (905)
- Thermal Power — 335 to 487 kW (500)
- Steam Drum Pressure — 1555 to 1693 psia (1635)

* The numbers in parentheses indicate design or rated conditions.

The measured mean overall heat transfer coefficients for the 25 runs considered are given in Table B-6, along with some test parameters. Also given in the table are the predicted mean overall heat transfer coefficients using the same prediction methods as were used in the original design calculations.[38] In calculating these coefficients, the actual test sodium and steam flow rates and a wall thermal conductivity of 16.25 Btu/h-ft-°F (the same as in the original design calculations) were used. The overall heat transfer coefficients given in the table have no fouling effect included and they can therefore be compared directly.

It is apparent that the thermal performance in the coil region is considerably better than predicted. A tabulation of the individual average conductances and the overall conductance is given in Table 6-1 below.

Table 6-1
SUMMARY OF SUPERHEATER THERMAL PERFORMANCE FOR THE COIL REGION AT NEAR-RATED CONDITIONS

Location	Heat Transfer Coefficients (Btu/h-ft^2 °F)		
	Predicted Coefficients		SGTR Experiment
Overall $\bar{U}$	–	280	383
Steam Side, $\bar{h}_s$	(Heinemann Correlation)	594	883
Equivalent Wall, $\bar{h}_w$	(Wall Thermal Conductivity = 16.25)	1015	1287
Sodium Side, $\bar{h}_{Na}$	(Rickard Correlation)	3251	3396
Fouling, $\bar{h}_f$	No Fouling Effect		No Fouling Effect

The main reason for the better-than-predicted performance is believed to be that the steam-side heat transfer coefficient is larger in the coils due to the curvature than in a straight tube. Although this is in agreement with observations,[18] there is no way to establish the validity of the assumed split between the individual conductances arrived at in Table 6-1. However, the overall heat transfer coefficients calculated using the above methods (i.e., the steam-side heat transfer coefficient given by Equation 6-2 with C_3 equal to 1.4, the wall conductivity given by Equation 5-2, and the sodium-side coefficient given by Equation 6-1) predict the performance in the coil region. The complexity of the geometry made it impossible to evaluate a meaningful logarithmic temperature difference and evaluate an overall heat transfer coefficient directly from measurements. If this had been possible, the Wilson plot technique used for the evaporator boiling region might have been used here also to correlate the steam-side heat transfer coefficient.

Comparisons between the measured axial and circumferential sodium temperature profiles are shown in Figures 6-1 and 6-2 for a typical run. The sodium temperature in the calming region (Figure 4-10) near the sodium level is lower than the sodium inlet temperature as shown in Figure 6-1 and measured by thermocouples 13 and 14 (Figure 4-14). Although insufficient data are available to show what the sodium temperature profile was like in this region, the measured temperatures are given in Table B-7, along with other thermocouple data. The steep temperature gradients noted in the evaporator near the calming region area are not present in the superheater. The main reason for this is the much lower heat transfer rates to the tubes in this region due to the film coefficient on the steam-side.

The temperature distribution at the outlet of the coil region is shown in Figure 6-2. It is worthwhile to note the relatively high sodium exit temperature in the region near the inactive downcomer tube (Tube 3). The maximum spread in the measured exit temperatures is about 30°F as compared to a total temperature drop of about 90°F. This is a significant temperature unbalance and gives rise to some thermal stresses in the flow shrouds. These problems should be kept in mind when leaky tubes are plugged in any steam generator. The points denoted "analytic" in Figure 6-2 were the temperatures calculated by the SUPER code using the standard circumferential flow distribution arrived at based on these temperature measurements from the early runs (more on this in Appendix A-2). The main lesson to be learned from these results is that extreme care must be taken by the designer to ensure good flow distribution and avoid temperature maldistributions as the ones measured here.

6.2 STEAM-SIDE FLOW AND TEMPERATURE DISTRIBUTION IN THE SUPERHEATER

In order to measure the exit steam temperatures from the two active helical coils, thermocouples were installed in the tube-sheet near Nozzle N-2 (Figure 4-10). The thermocouples were inserted into holes drilled perpendicular to the flow direction and attached by appropriate fittings.

Temperature data recorded at near-rated conditions for a few runs are given in Table 6-2 below.

Table 6-2
STEAM EXIT TEMPERATURE DATA FOR THE SUPERHEATER

		Temperatures (°F)	
Date	Time	Tube 1	Tube 2
11-20-71	1752	904.3	907.0
11-21-71	1054	928.3	929.4
11-23-71	1927	917.4	920.8
12-4-71	0115	912.7	915.5
12-10-71	0243	913.1	916.4

The steam exiting Tube 2 appears to be consistently 3°F higher than in Tube 1, which is within the accuracy of the thermocouples. However, if the measured temperatures had been substantially different from each other, one reason could have been poor flow distribution. This is unlikely since each tube is of the same length, has the same number of bends, etc., and thus has the same hydraulic resistance. The other possibility would have been temperature maldistribution due to different heat rates to the tubes.

The present results indicate that the steam-side flow and temperature distribution in the tubes is good. In view of the substantial sodium-side temperature maldistribution indicated in Figure 6-2, this is encouraging.

6.3 PRESSURE DROPS

6.3.1 Sodium-Side Pressure Drops

The absolute pressures of the sodium at the inlet and outlet of the superheater were measured (Figure 4-2). The signals from the corrrsponding pressure transmitters were connected to an electronic summer to get the differential pressure drop across the sodium-side of the superheater.

Some of the recorded data are shown in Table 6-3, along with the average sodium Peclet number and the static head of sodium between the two measurement locations. Comparison of the ΔP reading from the instrument and the differential pressure drop obtained by subtracting the absolute pressure drop readings shows some discrepancy between the two. The frictional pressure drop is obtained by subtracting these ΔP values from the static head of sodium and the corresponding frictional pressure drops are shown in the last two columns of Table 6-3.

Table 6-3
SODIUM-SIDE PRESSURE DROPS FOR THE SUPERHEATER

Date	Time	Sodium Peclet Number	Static Head h_{Na} (psi)	Inlet Pressure P_I (psig)	Outlet Pressure P_U (psig)	$P_O - P_I = P_{OI}$ (psi)	ΔP From Instrument (psi)	Friction Pressure Drop $h_{Na} - \Delta P_{OI}$ (psi)	Friction Pressure Drop $h_{Na} - \Delta P$ (psi)
3-30-71	1728	77	5.52	41.59	46.79	5.20	8.23	0.32	-2.71
3-31-71	0430	76	5.42	31.81	37.79	5.98	9.07	-0.56	-3.65
3-31-71	1536	69	5.70	22.76	27.96	5.20	8.03	0.50	-2.33
3-31-71	1551	72	5.69	22.68	27.77	5.09	7.87	0.60	-2.18
3-31-71	1606	72	5.72	22.65	27.88	5.23	7.75	0.49	-2.03
3-31-71	1635	86	5.79	22.82	27.51	4.69	7.41	1.10	-1.62

From these two columns, it is evident that the measurements are not going to be of much value. The basic problems involved in attempting to measure the pressure drop are (1) small magnitudes of the pressure drops from which static heads have to be subtracted, and (2) instruments that are not accurate enough. The frictional pressure drop for the superheater was estimated to be less than 0.1 psi in the original design calculations.[38] The major conclusion that can be drawn from this evaluation is that a measurement of a pressure drop of this magnitude should not be attempted.

As for the actual frictional pressure drop in the superheater, there is no reason to believe that it deviates substantially from the prediction. This very small pressure drop is believed to play a major role in the sodium side hydraulic instability observed during these tests. This will be discussed in Section 7.

6.3.2 Steam-Side Pressure Drops

Steam-side absolute pressures were measured at the steam drum, at the inlet to the superheater, and at the superheater outlet (Figure 4-2). The steam-side pressure drop was obtained by electronic summation of the transmitter signals from the absolute pressure readings at the inlet and outlet.

During this evaluation, it was noted that the absolute pressure reading at the superheater inlet showed an inconsistent behavior and will be substituted by the steam drum pressure reading, which is measured upstream of the superheater inlet (Figure 4-2). Presure drop data for the 25 runs considered in the thermal performance evaluation are given in Table 6-4, along with the mean steam-side Reynolds number. The two columns giving the measured steam-side pressure drops (the first based on subtraction of absolute values and the other the instrument reading) differ by a substantial amount. These same values are plotted in Figure 6-3 vs the Reynolds number.

The predicted friction, momentum, and total pressure drops are listed in the last three columns in Table 6-4, and the last column is represented by the solid line in Figure 6-3. The method of Reference 38 was used in predicting the frictional pressure drop. The predicted pressure drops fall between the two sets of measured pressure drops and it is impossible to decide which measurement to believe. The results of this evaluation are largely inconclusive as to the exact magnitude of the actual steam-side pressure drop; however, evaluation serves to illustrate the need for careful selection and calibration of instrumentation if reliable results are to be expected.

Table 6-4
STEAM-SIDE PRESSURE DROPS FOR THE SUPERHEATER

Date	Time	Mean Reynolds Number X 10^{-3}	Steam Drum Pressure P_D (psig)	Superheater Outlet Pressure P_C (psig)	Pressure Difference P_D-P_O (psi)	ΔP From Instrument (psi)	Calculated Friction Pressure Drop (psi)	Calculated Momentum Pressure Drop (psi)	Calculated Total Pressure Drop (psi)
3-30-71	1728	672	1572	1557	12.5	42.0	32.7	1.11	33.8
3-31-71	0430	651	1540	1524	16.3	42.0	30.7	1.04	31.7
3-31-71	1536	652	1586	1574	12.4	37.6	30.8	1.04	31.8
3-31-71	1551	669	1606	1593	13.0	42.5	32.4	1.10	33.5
3-31-71	1606	686	1629	1617	12.4	48.7	34.1	1.15	35.3
3-31-71	1635	733	1678	1665	12.6	59.8	39.0	1.31	40.3
5-20-71	1327	555	1597	1583	14.1	41.6	22.2	0.75	22.9
5-20-71	1458	649	1604	1589	14.9	42.6	30.5	1.03	31.5
6-8-71	1153	691	1633	1620	12.6	47.8	34.6	1.17	35.8
6-8-71	1524	752	1640	1627	13.8	48.1	41.2	1.39	42.6
6-8-71	1908	764	1645	1631	13.5	49.1	42.5	1.43	43.9
7-24-71	2056	709	1636	1621	14.5	49.2	36.5	1.23	37.8
7-25-71	0352	722	1642	1625	17.0	48.9	37.9	1.28	39.2
7-25-71	1228	679	1615	1600	15.3	44.4	33.4	1.13	34.5
7-12-71	1932	698	1635	1623	12.1	49.9	35.4	1.19	36.6
7-22-71	0540	675	1609	1593	16.5	42.5	33.1	1.12	34.2
7-23-71	0856	692	1643	1627	15.4	51.0	34.8	1.17	35.9
7-24-71	0625	722	1637	1621	16.0	49.0	37.9	1.28	39.2
7-31-71	0251	765	1602	1580	22.1	35.6	42.6	1.43	44.1
7-31-71	2221	686	1633	1618	14.7	47.3	34.2	1.15	35.3
8-2-71	2324	729	1601	1583	17.2	40.9	38.6	1.30	40.0
11-3-71	0815	717	1617	1600	16.9	42.5	37.3	1.26	38.6
7-31-71	0120	712	1640	1623	17.3	47.9	36.8	1.24	38.1
12-4-71	0115	647	1643	1628	14.6	51.8	30.3	1.03	31.3
12-10-71	0243	632	1610	1596	14.7	43.0	28.9	0.98	29.8

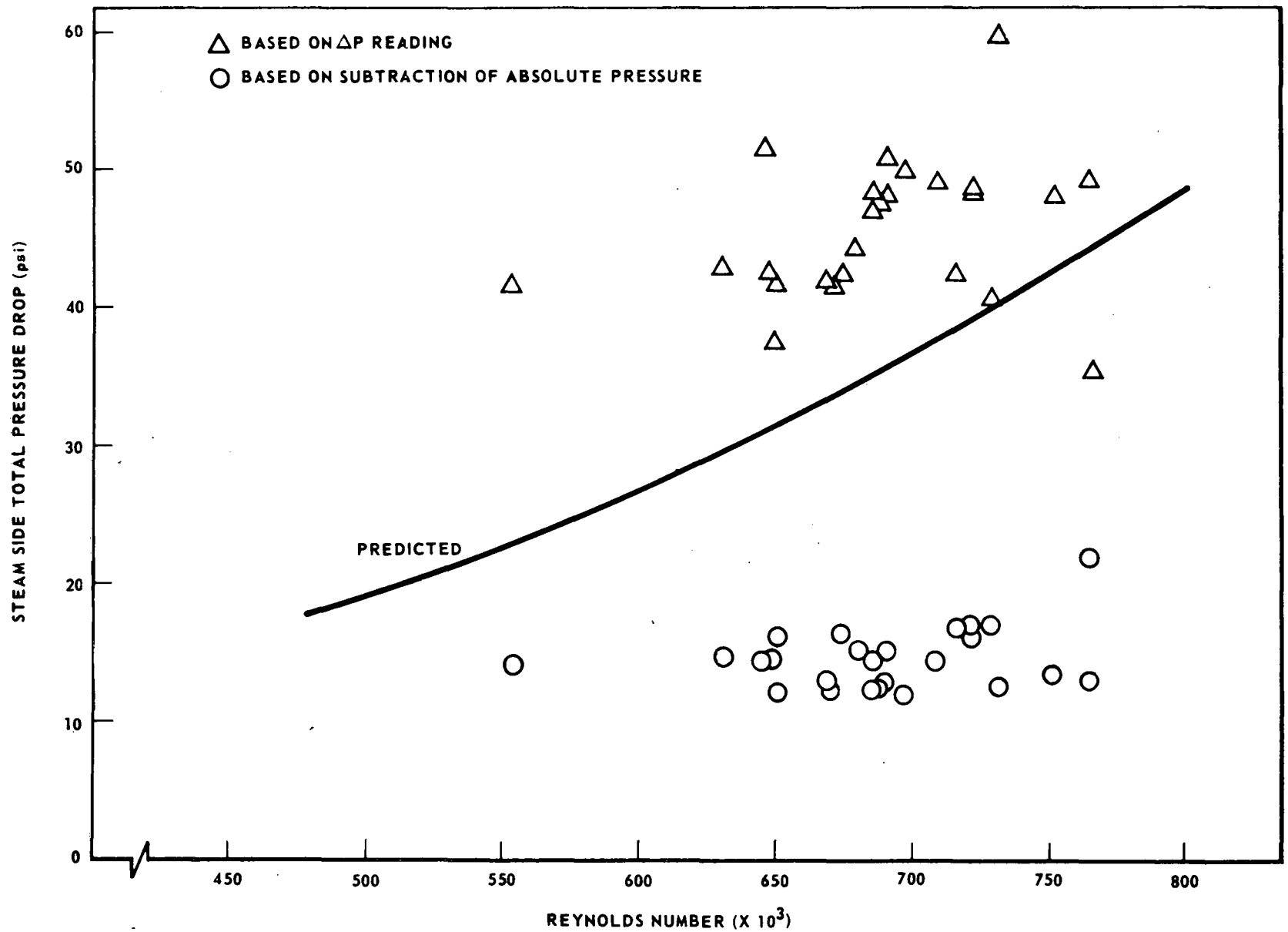

Figure 6-3. Comparison of Measured and Predicted Steam Side Pressure Drop In the Superheater

7. SYSTEM STABILITY

The observations regarding sodium-side and steam-side stability are presented in this section. The stability of boiling systems has been studied extensively[39,40,41] for various geometries and boiling conditions. Sodium-side instabilities, on the other hand, do not seem to have been reported in the literature. The main feature of the present sodium-side instability is a sudden change in the sodium flow rate between the two units, accompanied by level changes in the superheater and evaporator. This general level shift, along with a smaller amplitude periodic level variation observed in the evaporator, are believed to contribute to large sodium temperature fluctuations in the evaporator in and near the calming region area.

The steam-side of the evaporator was found to be stable for the range of operating conditions considered for the reference demonstration plant evaporator design; however, when the steam exit quality was increased to about 120%, or net superheated conditions of approximately 100°F, the boiling system was unstable. These observations will now be considered in more detail.

7.1 SODIUM-SIDE STABILITY

A diagram showing details of the part of the sodium system of interest with regard to stability is shown in Figure 7-1. For more details, see the flow diagram on Figure 4-2 and the evaporator and superheater details on Figures 4-7 and 4-10, respectively.As can be seen from Figure 7-1, there are three different electromagnetic flowmeters; flowmeter F1 is located between the superheater and evaporator; flowmeters F2 and F3 are located near the evaporator exit and after the electromagnetic pump, respectively.

If the sodium levels in the superheater and evaporator, as well as in the expansion tanks, are not changing, all three flowmeters should read the same. Variations in sodium levels, however, will cause temporary changes in the flow rates. It was noted initially that the mV signals from the flowmeters, in particular flowmeter F1, seemed to have a considerable amount of what was thought initially to be "noise" when connected to a Sanborn recorder. Closer examination of the "noise," however, showed that the signals were real. This prompted a more detailed study of the phenomenon by connecting more instrumentation to the Sanborn recorders. This included the cover gas pressures of the superheater and evaporator which are essentially the sodium inlet pressures in the two units. Also, the sodium levels in the two units were recorded, along with thermocouples in and immediately below the calming regions of the two units. The thermocouples were included in both units because large temperature fluctuations had been observed just below the calming region in the evaporator.

By using the isolation valves denoted by V1, V2, etc., in Figure 7-1, it was possible to have sodium flow through both models or through either one of the units. The models could also be bypassed altogether with flow of isothermal sodium through the lines only. The steam-sides of the two units could also be valved off and sodium-circulated at near isothermal conditions through the system.

7.1.1 Sodium Flow and Level Fluctuations

A systematic study of the observed sodium flow and level fluctuations was made in order to identify the parameters causing the problem. It was observed initially that the magnitude of the flow variations was a function of the sodium flow rate and this parameter was therefore varied over as wide a range as possible.

The tests were conducted with the steam-sides of both the superheater and evaporator isolated, or at near isothermal sodium conditions. Tests were also run with both models operating at near-rated conditions, but the sodium flow rate could not be varied over as wide a range under nonisothermal conditions. Also, tests were run for isothermal sodium conditions with sodium flow through the evaporator or superheater alone and with both units isolated.

The results of these tests with the superheater and evaporator on line are shown in Figures 7-2 through 7-5. These figures are the Sanborn traces of the three electromagnetic flowmeters, the superheater sodium level and cover gas pressure, and the evaporator level and cover gas pressure. The mV signals have been converted to the equivalent engineering units. The symbol appearing along each measurement corresponds to the symbols on Figure 7-1.

3

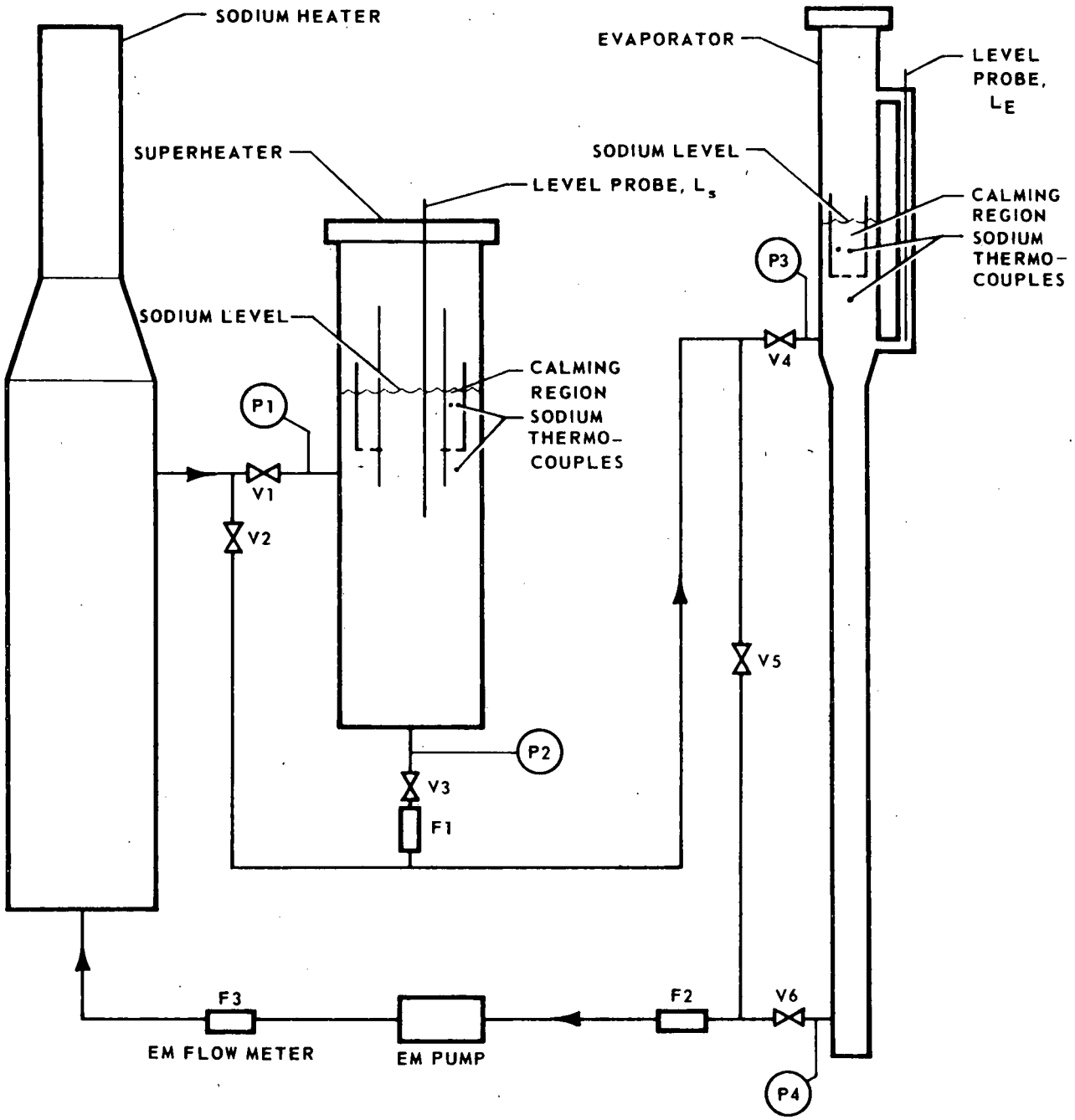

Figure 7-1. Schematic Diagram of Sodium System

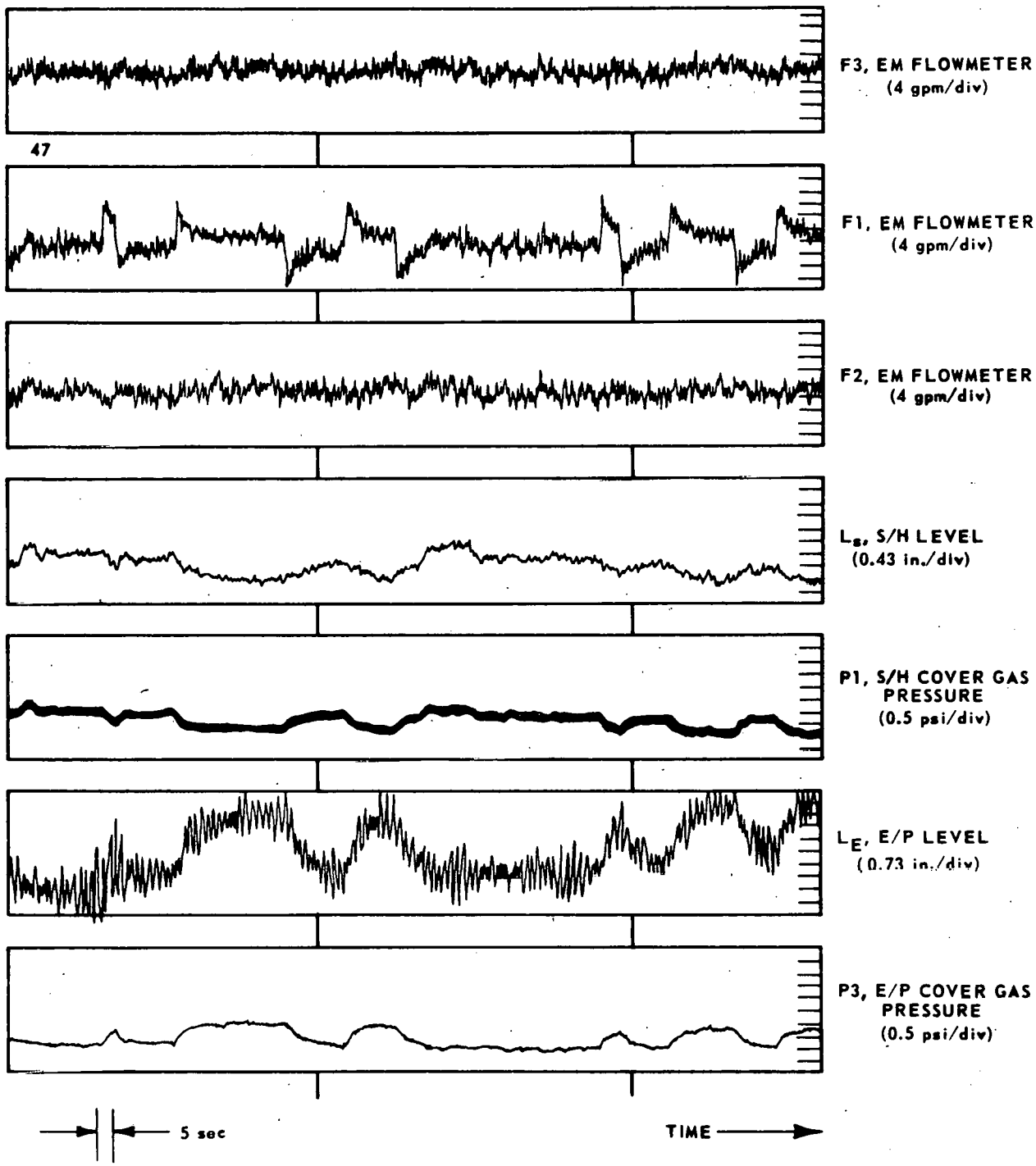

Figure 7-2. *Sanborn Traces of Sodium Flow and Level Variations in the SGTR at Isothermal Conditions and Sodium Flow Rate of 205 gpm, Superheater and Evaporator on Line*

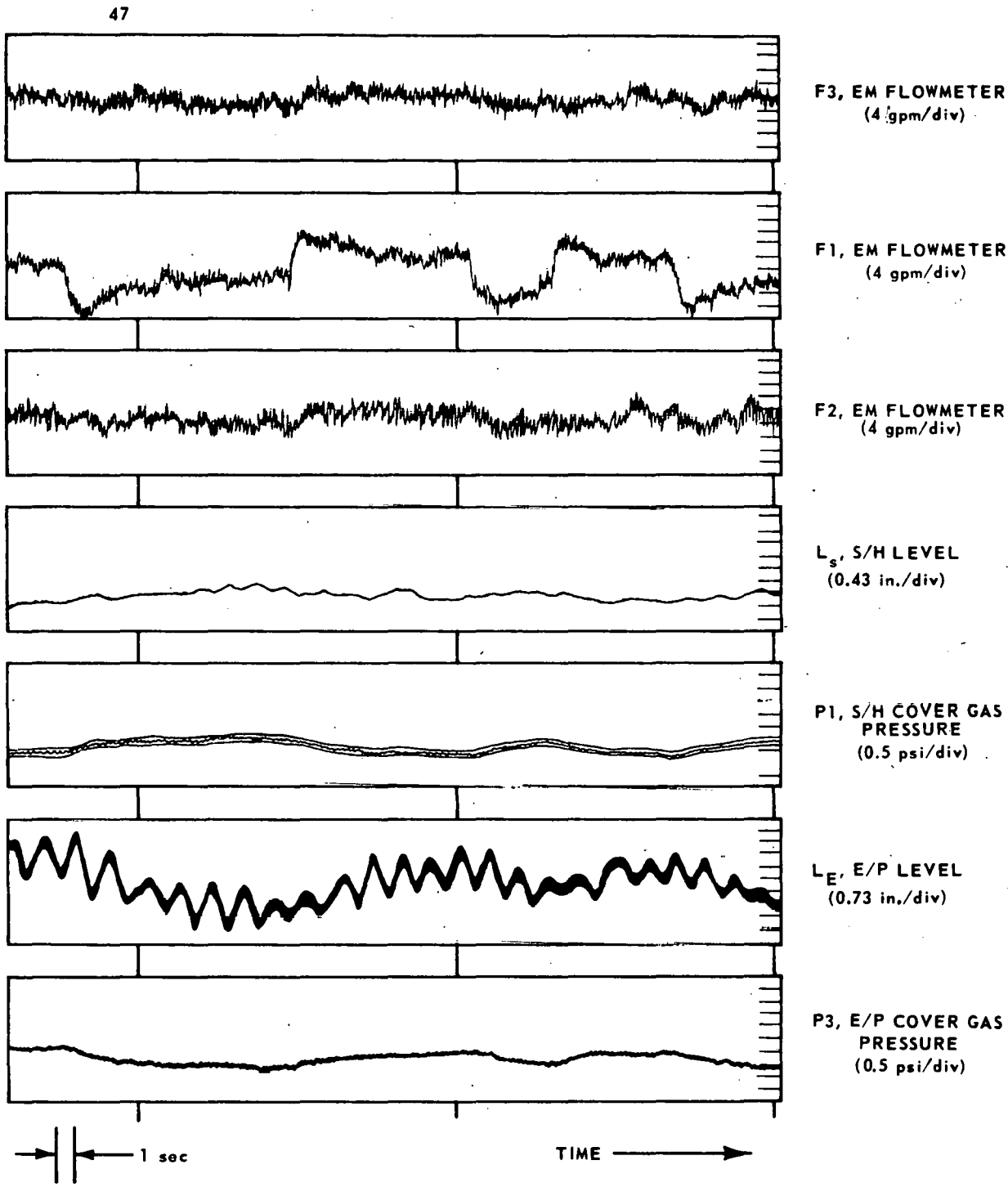

Figure 7-3. Sanborn Traces of Sodium Flow and Level Variations in the SGTR at Isothermal Conditions and Sodium Flow Rate of 205 gpm, Superheater and Evaporator on Line (Same Conditions as in Figure 7-2, but at Higher Chart Speed)

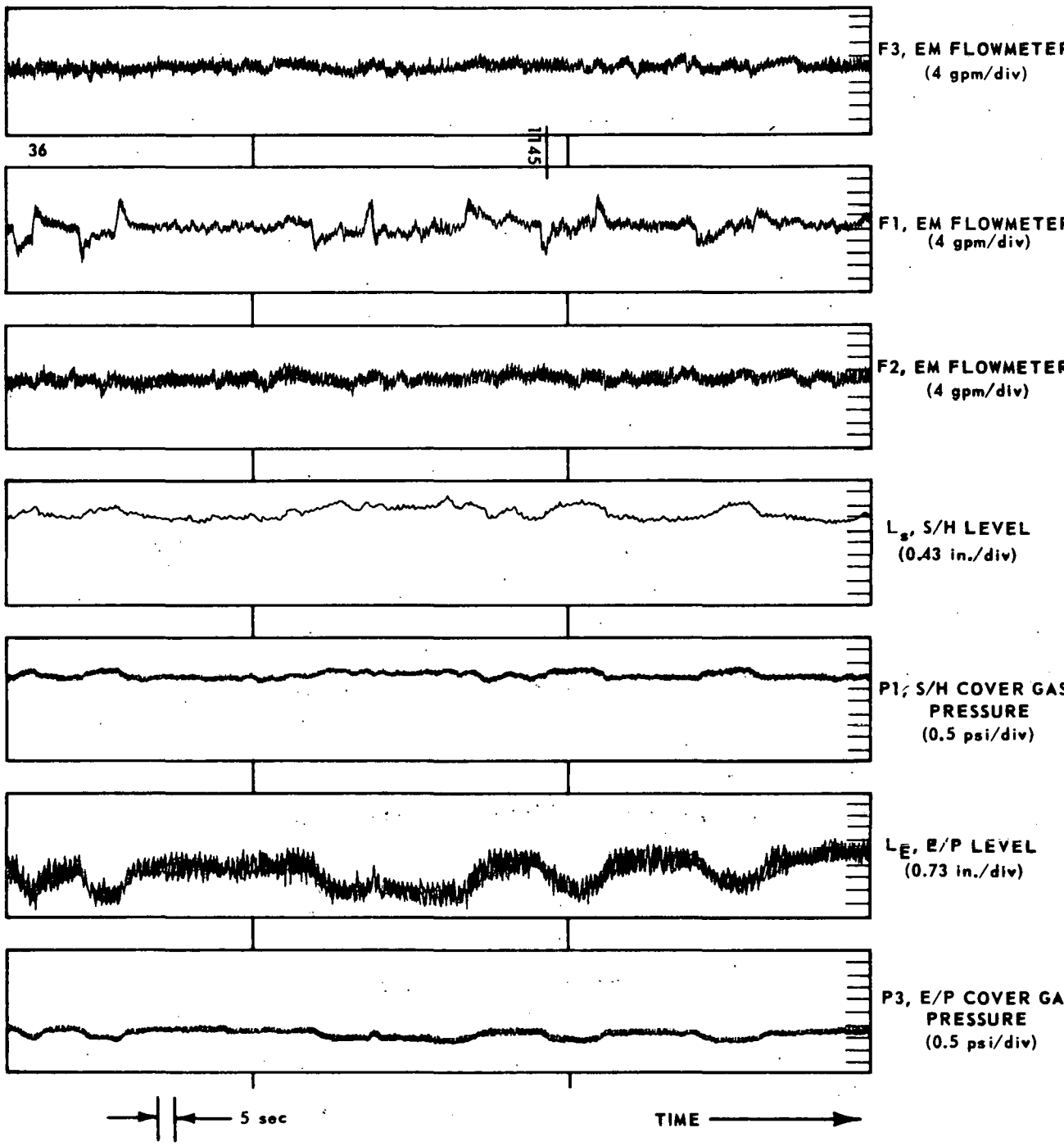

Figure 7-4. *Sanborn Traces of Sodium Flow and Level Variations in the SGTR at Non-Isothermal Conditions and Sodium Flow Rate of 120 gpm, Superheater and Evaporator on Line*

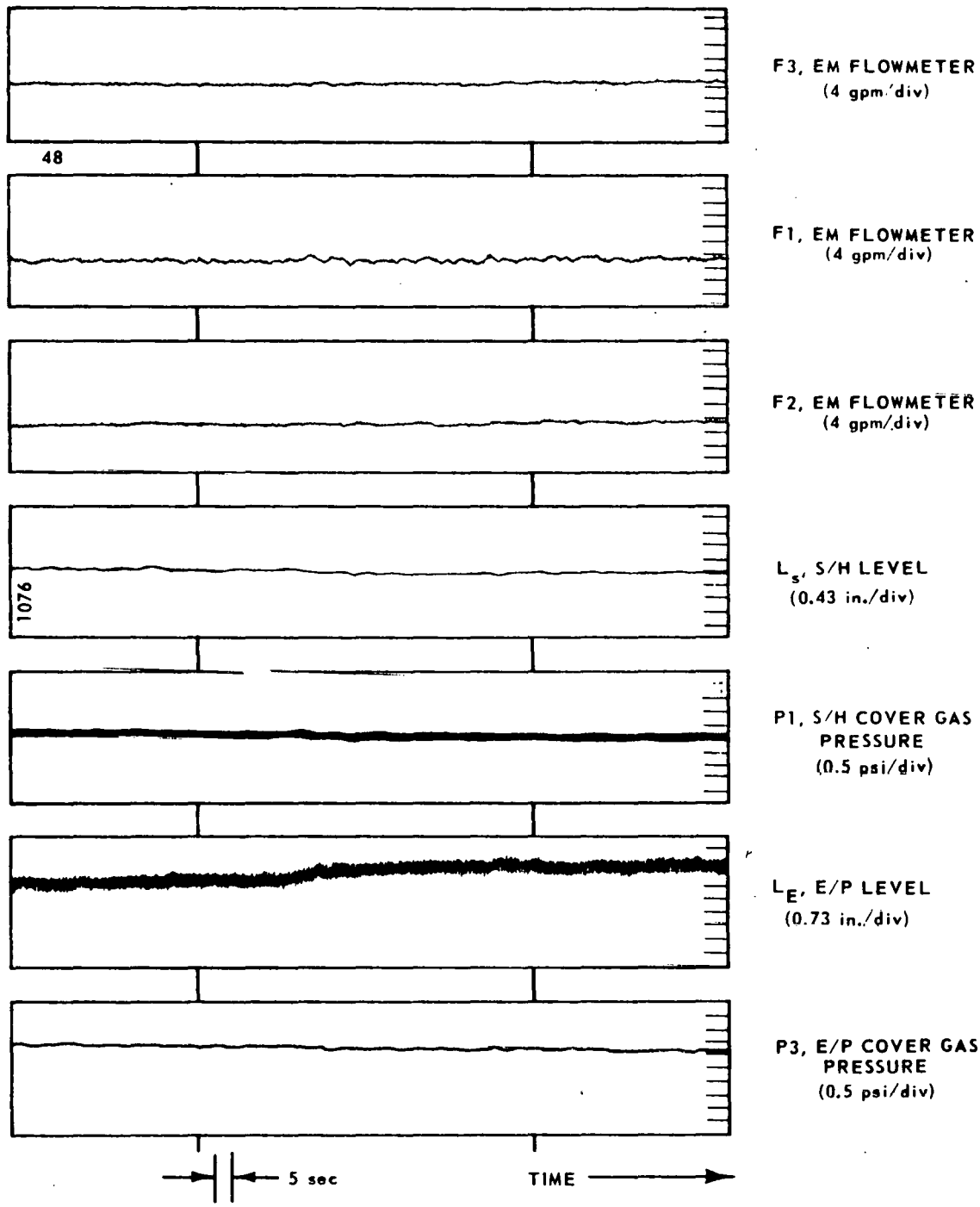

Figure 7-5. *Sanborn Traces of Sodium Flow and Level Variations in the SGTR at Isothermal Conditions and Sodium Flow Rate of 34 gpm, Superheater and Evaporator on Line*

The results for a large sodium flow rate are shown in Figure 7-2. The sodium flow rates as measured by flowmeters F1, F2, and F3 have high-frequency signals superimposed on general low-frequency flow variations. The high-frequency signals might, at first, appear to be electronic noise, but a look at Figure 7-5 reveals that the signals almost disappear at a low flow rate; therefore, it is a real signal. It is not clear what is causing the high-frequency signal, but it may be due to larger turbulence intensity in the sodium or some other flow- or vibration-induced problem. (Another theory is that the electromagnetic pump is introducing the high-frequency fluctuation, but this is doubtful because the high-frequency component would be damped out in the cover gas regions.)

The main concern of the tests, however, is the low-frequency, erratic fluctuation in the sodium flow between the superheater and the evaporator given by F1. It is apparent that this flow rate either drops or increases rapidly and is gradually restored to some mean value if not interrupted by another sudden drop or increase. Corresponding to a sudden increase in the flow rate, there is a drop in the sodium level in the superheater and an increase in the evaporator sodium level and vice versa. When the sodium levels change, the pressures change due to volume changes; thus, a level increase results in higher pressure and vice versa.

By comparing Figure 7-2 to Figures 7-4 and 7-5, which are for sodium flow rates of 120 and 34 gpm, respectively, it is apparent that the magnitude of the erratic sodium flow fluctuations between the superheater and evaporator is decreasing with decreasing flow and the fluctuations are almost absent for the 34 gpm run. The corresponding level and pressure variations are, of course, also decreasing with decreasing flow. It was found that the nature of the flow fluctuations was independent of the sodium conditions (i.e., whether the sodium system was isothermal or not), thus ruling out the possibility that density gradients in the units due to temperature gradients could cause the problem.

It is apparent that there must be some kind of triggering mechanism that initiates the flow perturbation. A suspect in this respect is the cover gas pressure. It is obvious that a sudden, rapid change in a cover gas pressure in the superheater or evaporator would result in a problem like this. However, by considering Figure 7-3 with the same sodium conditions as in Figure 7-2, but recorded at five times the chart speed, it is apparent that the pressure change in the superheater and evaporator is a **result** of the flow change and not the opposite, since the pressure change appears to occur a short but finite time after the flow rate change has started. Also, it is difficult to visualize any mechanisms by which the cover gas pressures can change in this irregular manner.

Returning now to Figures 7-2 and 7-3, it is apparent that, in addition to the general low-frequency level change, there is a higher frequency, periodic variation superposed, especially in the evaporator. In the evaporator, this component exhibits a beating effect. A look at Figures 7-4 and 7-5 reveals that the magnitude of the high-frequency component decreases with decreasing flow rate. Note that the P1, L_E, and P3 signals have some 60-cycle noise superposed because high-sensitivity settings of the amplifiers had to be used.

With regard to the evaporator sodium level measurement, it is worthwhile to note that the level probe is located in a side arm on the vessel (Figure 7-1), while the superheater level probe measures the level directly. Thus, one cannot say with certainty whether the sodium level in the evaporator itself varies with the magnitudes indicated by the probe; the cover gas pressure reading should have shown a corresponding variation which is not evident from Figure 7-3. Therefore, the indicated high-frequency variation in the evaporator level may not be real. The superheater has a much larger cross section than the evaporator and, therefore, the magnitude of the level and pressure variations is generally smaller.

An attempt was now made to identify the cause of the instability problem. The superheater was isolated and the sodium was flowing through the evaporator alone. The results of this test are shown in Figure 7-6 for a large flow rate and in Figure 7-7 for a low flow rate. The traces of F2 and F3 are similar to those of Figure 7-2. The superheater level is, of course, constant and the low-frequency general level change is absent for both flow rates. However, the high-frequency level variation in the evaporator is the same as with the superheater on line. Thus, the high-frequency periodic level change does not depend on the superheater; but the low-frequency erratic flow and level changes are associated with the superheater.

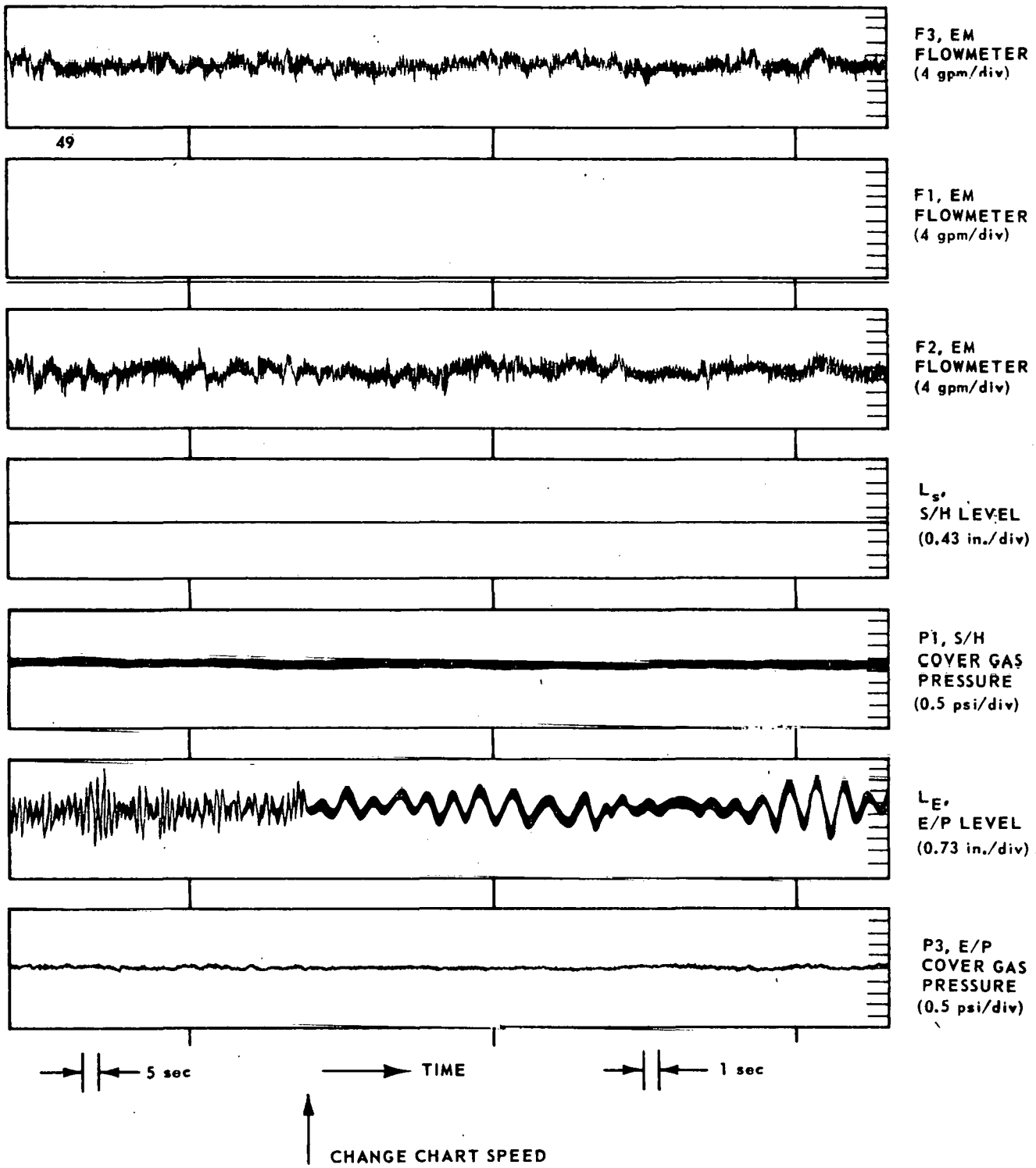

Figure 7-6. *Sanborn Traces of Sodium Flow and Level Variations in the SGTR at Isothermal Conditions and Sodium Flow Rate of 205 gpm, Superheater Isolated, Evaporator on Line*

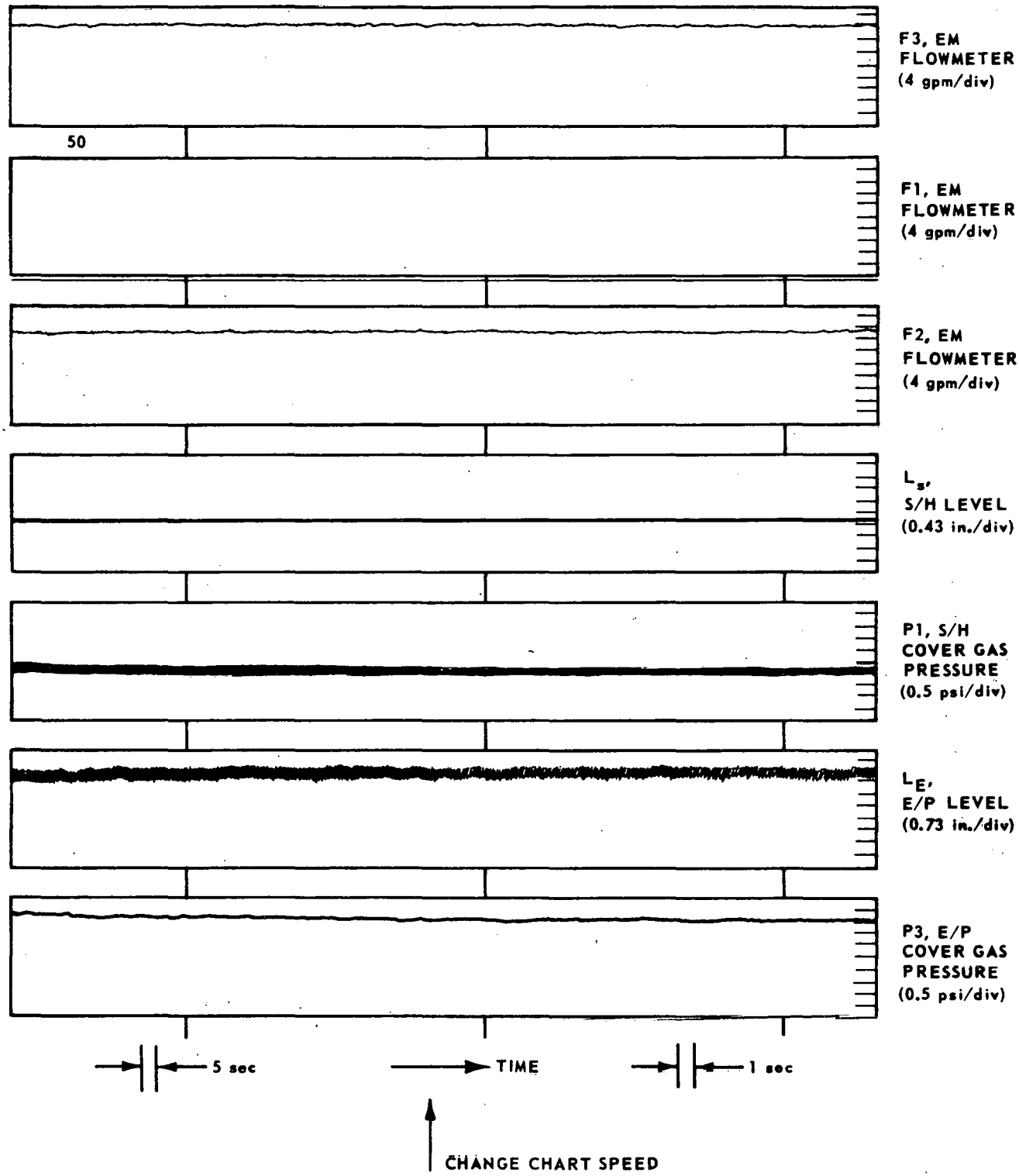

Figure 7-7. *Sanborn Traces of Sodium Flow and Level Variations in the SGTR at Isothermal Conditions and Sodium Flow Rate of 34 gpm, Superheater Isolated, Evaporator on Line*

The traces obtained with the superheater on line and the evaporator isolated are shown in Figures 7-8 and 7-9 for high and low flow rates, respectively; the traces obtained with both the superheater and evaporator isolated are shown in Figure 7-10 for high and low flow rates. The low-frequency erratic variation in the superheater flow rate, indicated by F1, is now absent. It is clear that there is a coupling effect between the superheater and evaporator, since the low-frequency erratic flow and level fluctuation only occur with series operation of the two units. It was felt that the coupling effect could be due to the low pressure drop in the superheater. To test this hypothesis, hydraulic flow resistance was introduced near the superheater exit by throttling the isolation valve V3. The results of this are shown in Figure 7-11 for a high sodium flow rate and in Figure 7-12 for a lower flow rate. From these figures, it is apparent that by introducing the hydraulic flow resistance corresponding to 50 to 60% closure of V3, the superheater and the evaporator became decoupled and the instability problem disappears.

This finding is the answer to the design problem but does not give any clue to what type of hydraulic instability or what mechanisms are involved to trigger the flow and level shift. It has been suggested that there is a U-tube manometer type effect, the superheater constituting one leg, and the connecting sodium line and upper portion of the evaporator the other. Thus, with the elevations of the levels in the two units being different, there could be an equilibrium problem involved which may be triggered by small flow and corresponding pressure drop changes in the units and connecting piping. In general, very little can be said about the problem at this time. An investigation using water flow model tests should be conducted to define the instability in greater detail, since it is believed that whenever series operation of units with cover gas spaces is involved, this type of instability may occur.

7.1.2 Sodium Temperature Fluctuations

Sodium thermocouples in and below the calming region were recorded on the Sanborns at near-rated operating conditions. Sanborn traces of these thermocouples are shown in Figures 7-13 and 7-14. The locations of the sodium thermocouples are indicated in Figure 7-1 and shown in more detail in Figures 4-13 and 4-14. Thermocouples 13 and 14 in the superheater have a considerable amount of noise, but the edge of the traces represent approximately the variations in these temperatures.

It is clear from Figures 7-13 and 7-14 that there is little sodium temperature fluctuation in the superheater; however, the temperature fluctuations in the evaporator are extensive, particularly immediately below the calming plate, where approximately ±50°F was recorded for the worst conditions. The maximum fluctuation appears to be a function of the sodium level or amount of sodium above the calming plate. This is evident from Figure 7-13, where the sodium level was approximately 25 in. above the calming plate, while the sodium level for the conditions of Figure 7-14 was only 11 in. above the calming plate. This reduced the magnitude of the temperature fluctuation by a factor of about two. However, it is clear from these figures that the temperature fluctuation in the calming region itself increased when the sodium level was decreased.

It is difficult to explain fully why these large amplitude, high-frequency temperature fluctuations occur. It is believed that one factor is the radial flow of sodium across the six-edge tubes near the top of the flow shroud to reach the flow area around the center tube (for details of the geometry, see Figure 4-7). The heat transfer rate for nucleate boiling on the steam-side is large here, and intermittent mixing with hotter sodium arriving from some other direction could cause some temperature variation; however, it is not likely that this large magnitude could result. The major contributor, therefore, is believed to be cooler sodium from the calming region mixing in with the hotter entering sodium. This is possible through holes in the calming plate, and it is believed that the previously described sodium level fluctuation tends to "pump" sodium in and out of the calming region through these holes. Also, the cooler sodium contained in the calming region has a higher density than the hotter entering sodium and a natural circulation effect may result.

Whatever mechanisms are involved in removing cold sodium from the calming region and replenishing it with hotter sodium, it appears that the large temperature fluctuation could be explained by mixing from the calming region. It is apparent from Figures 5-1 and 5-2 that the average sodium temperature in the

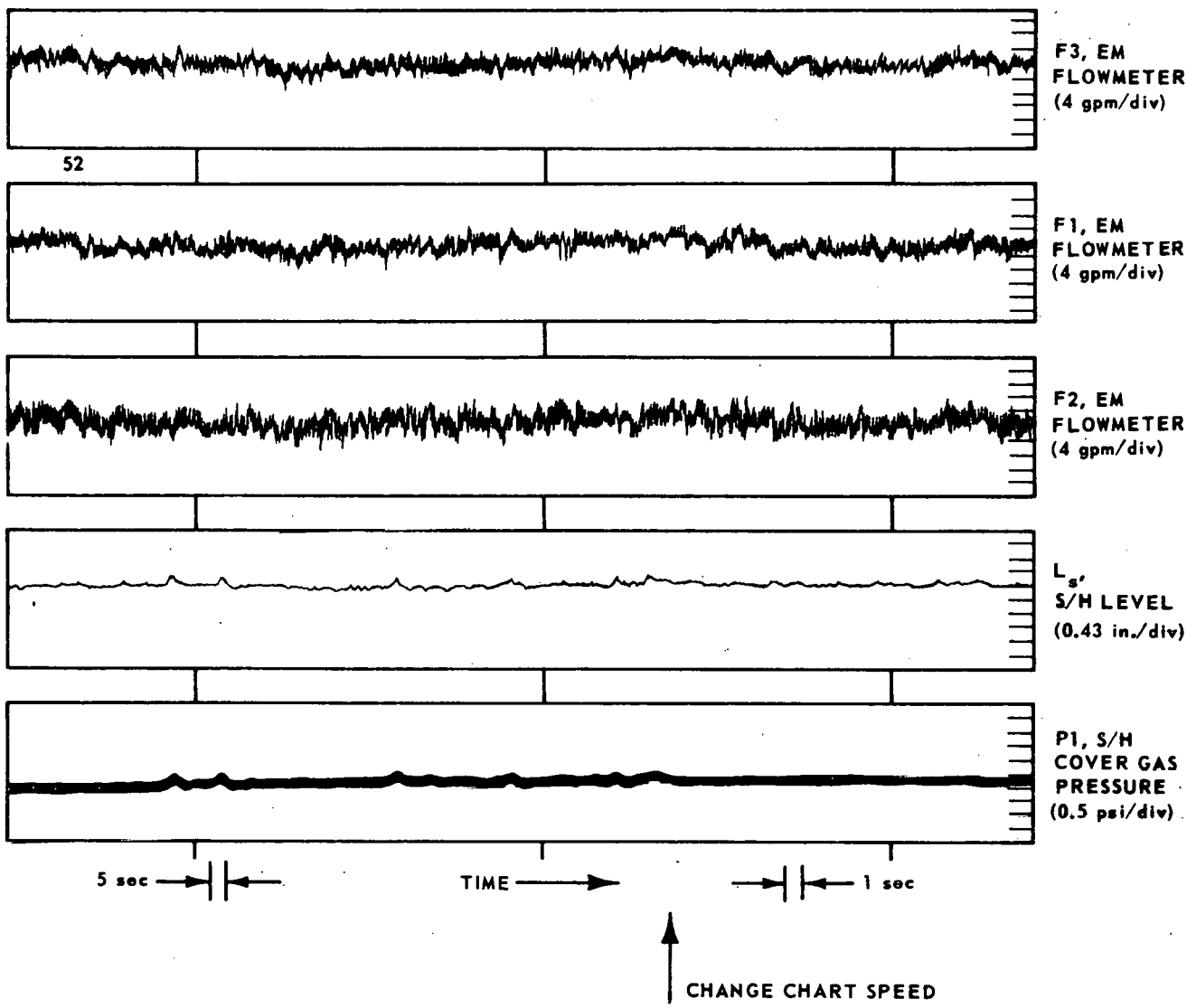

Figure 7-8. *Sanborn Traces of Sodium Flow and Level Variations in the SGTR at Isothermal Conditions and Sodium Flow Rate of 180 gpm, Superheater on Line, Evaporator Isolated*

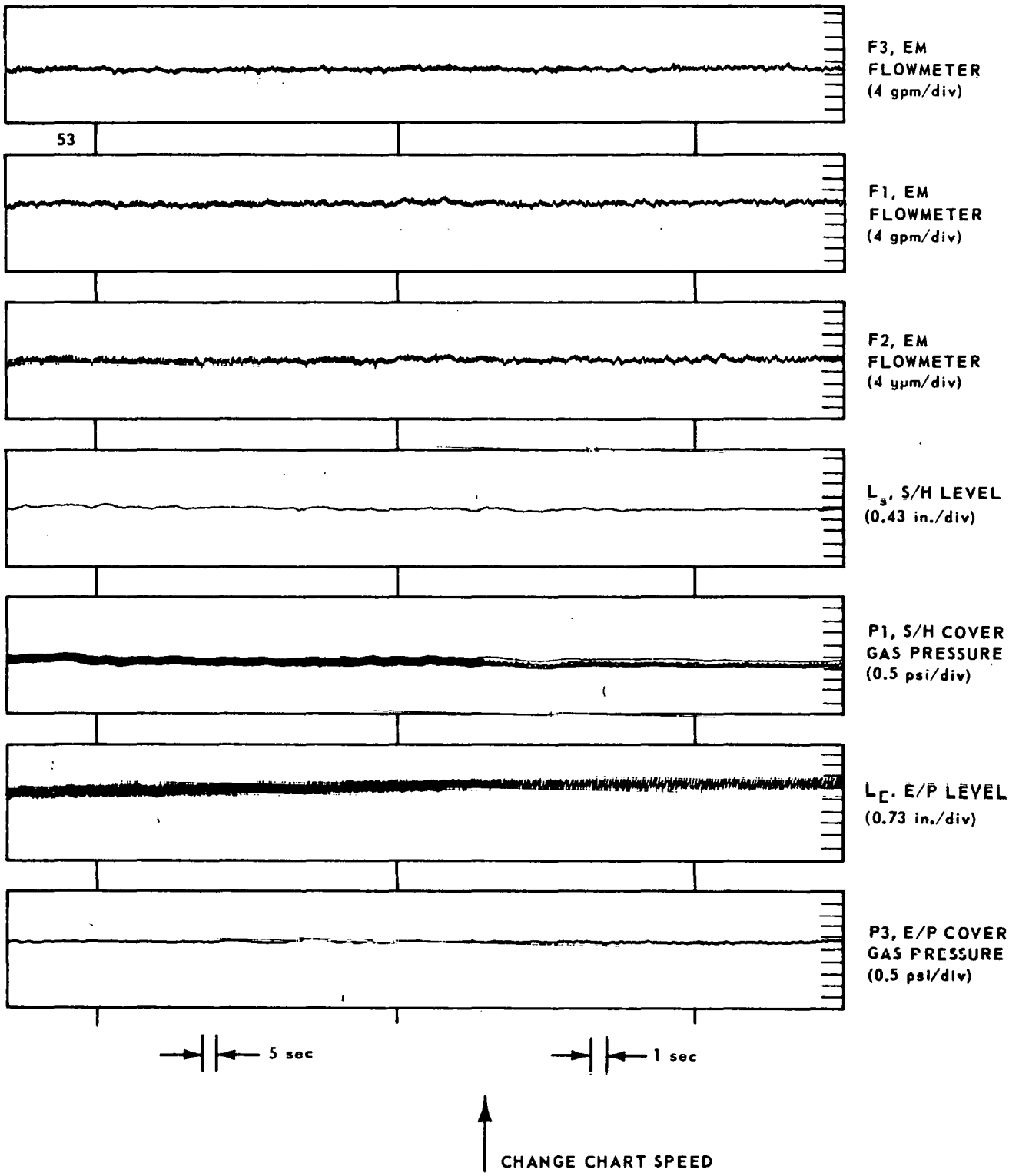

Figure 7-9. *Sanborn Traces of Sodium Flow and Level Variations in the SGTR at Isothermal Conditions and Sodium Flow Rate of 70 gpm, Superheater on Line, Evaporator Isolated*

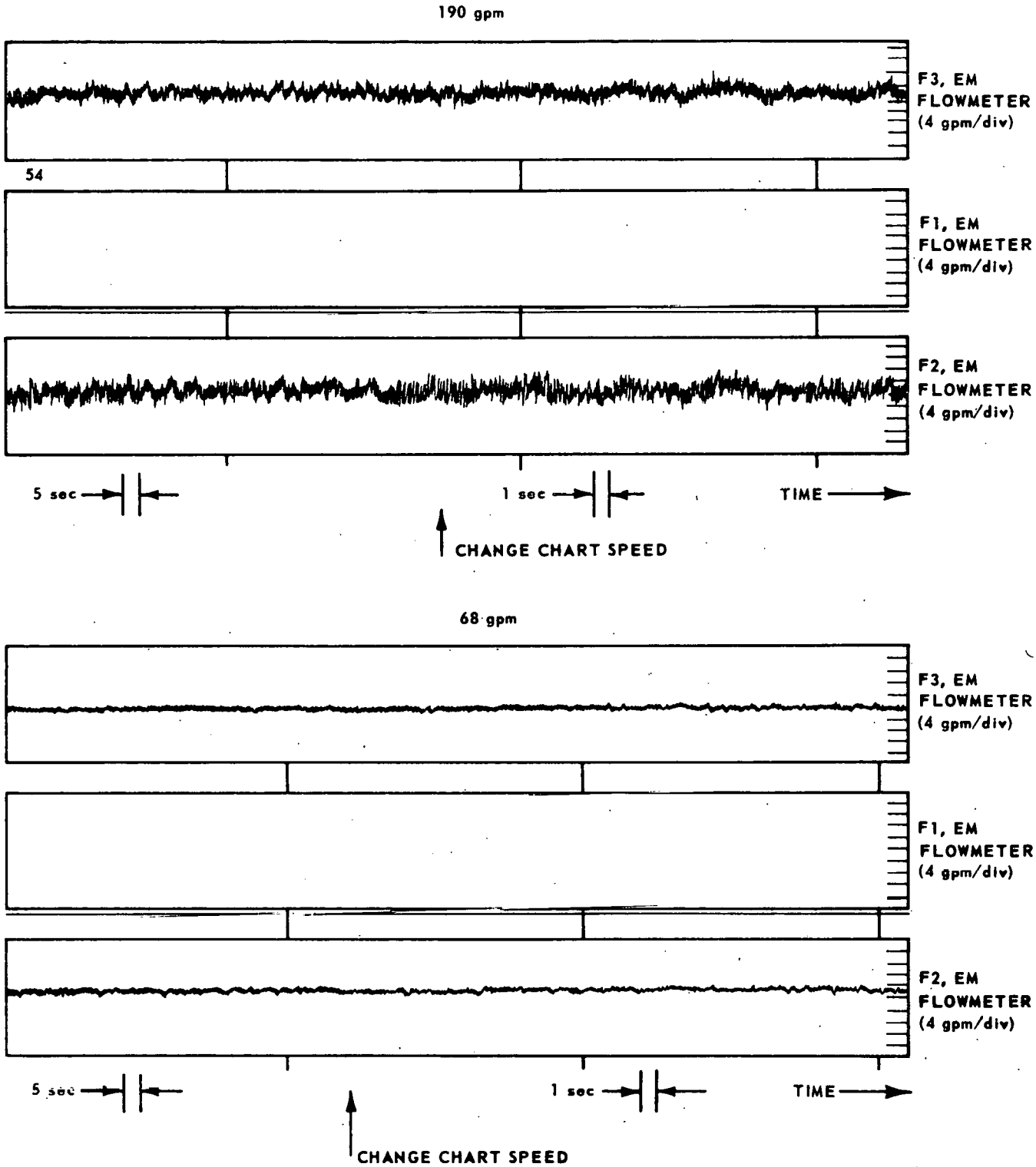

Figure 7-10. Sanborn Traces of Flow and Level Variations in the SGTR at Isothermal Conditions and Sodium Flow Rates of 190 and 68 gpm, Superheater and Evaporator Isolated

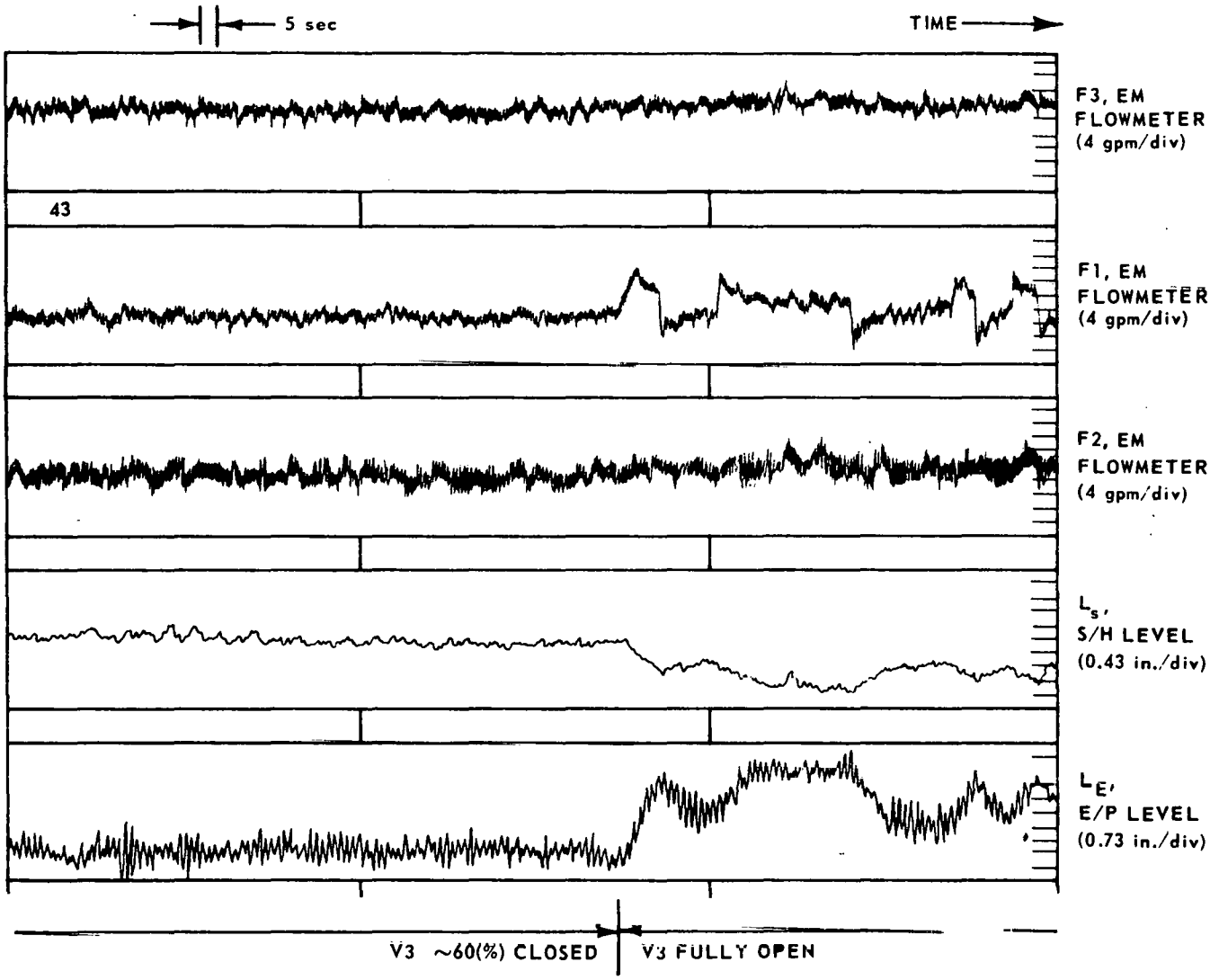

Figure 7-11. *Sanborn Traces of Sodium Flow and Level Variations in the SGTR at Isothermal Conditions and Showing Effect of Introducing Flow Resistance in the Line between the Superheater and Evaporator Test Sections, Sodium Flow Rate 175 gpm*

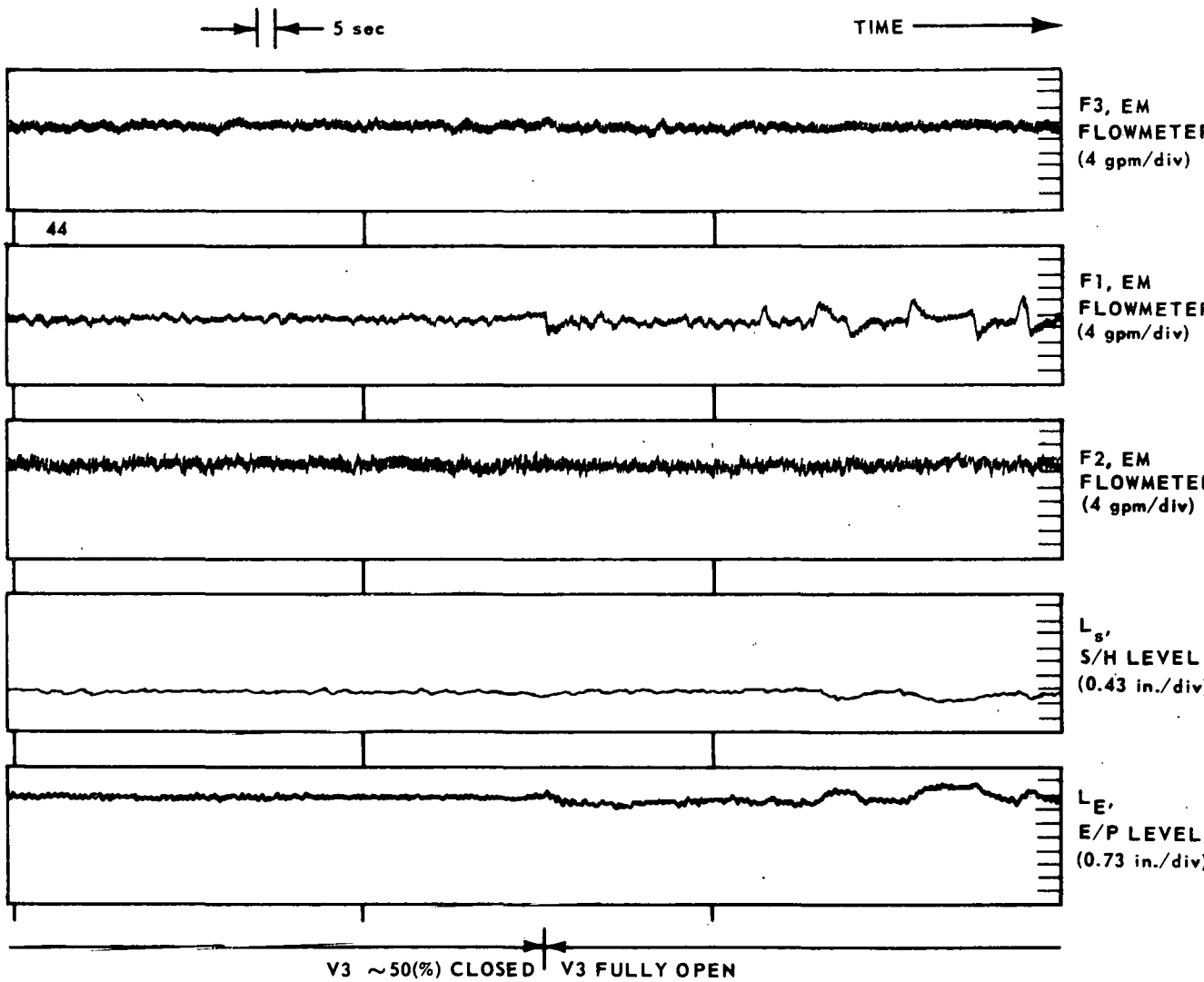

Figure 7-12. ***Sanborn Traces of Sodium Flow and Level Variations in the SGTR at Isothermal Conditions*** *Showing Effect of Introducing Flow Resistance in the Line between the Superheater and* ***Evaporator Test Sections, Sodium Flow Rate 90 gpm***

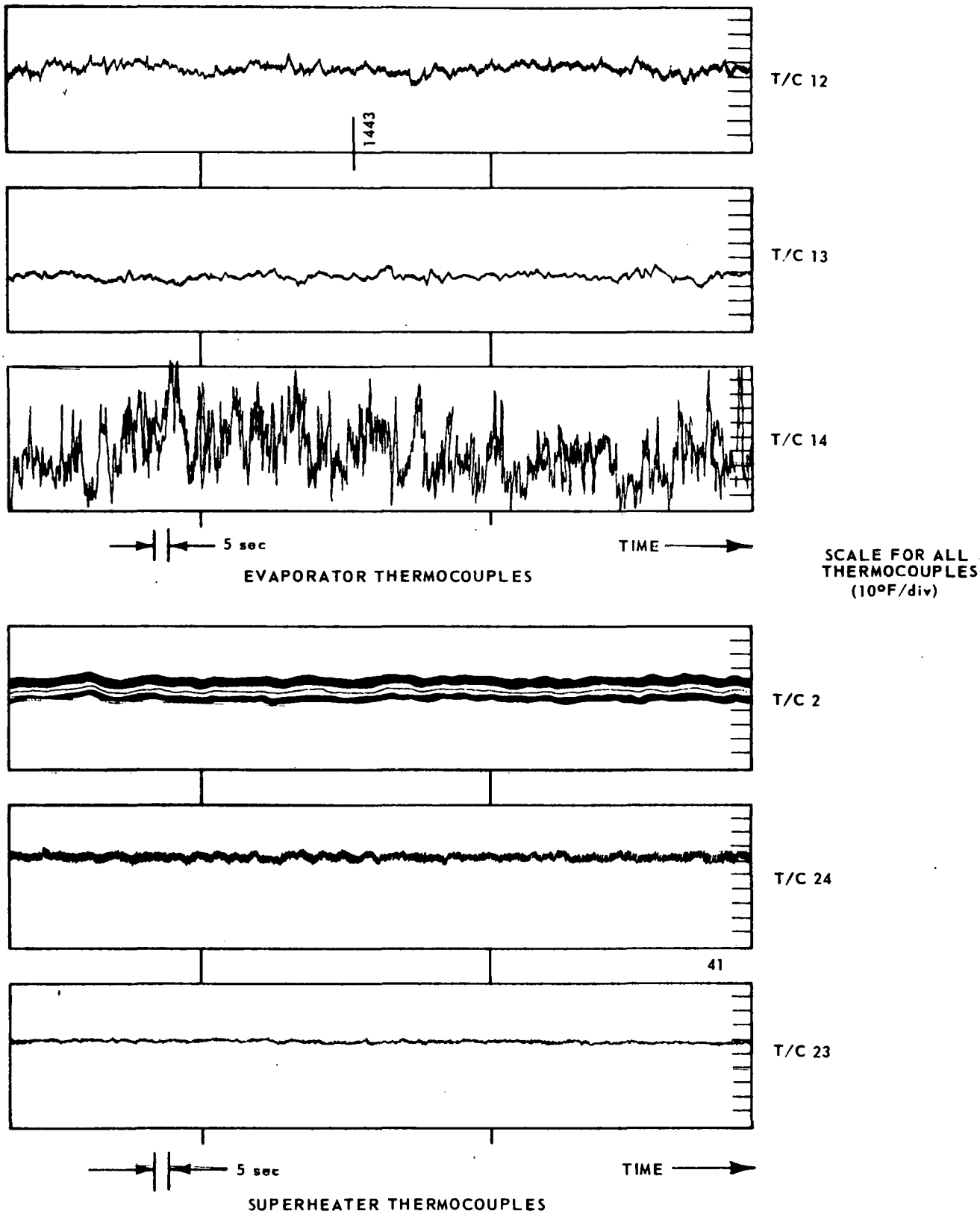

Figure 7-13. *Sanborn Traces of Temperature Variations in the Sodium below and above the Calming Plates in the Superheater and Evaporator Models Operating at Near-Rated Conditions, Sodium Level in the Superheater Nine Inches above the Calming Plate, Sodium Level in Evaporator 25 Inches above the Calming Plate*

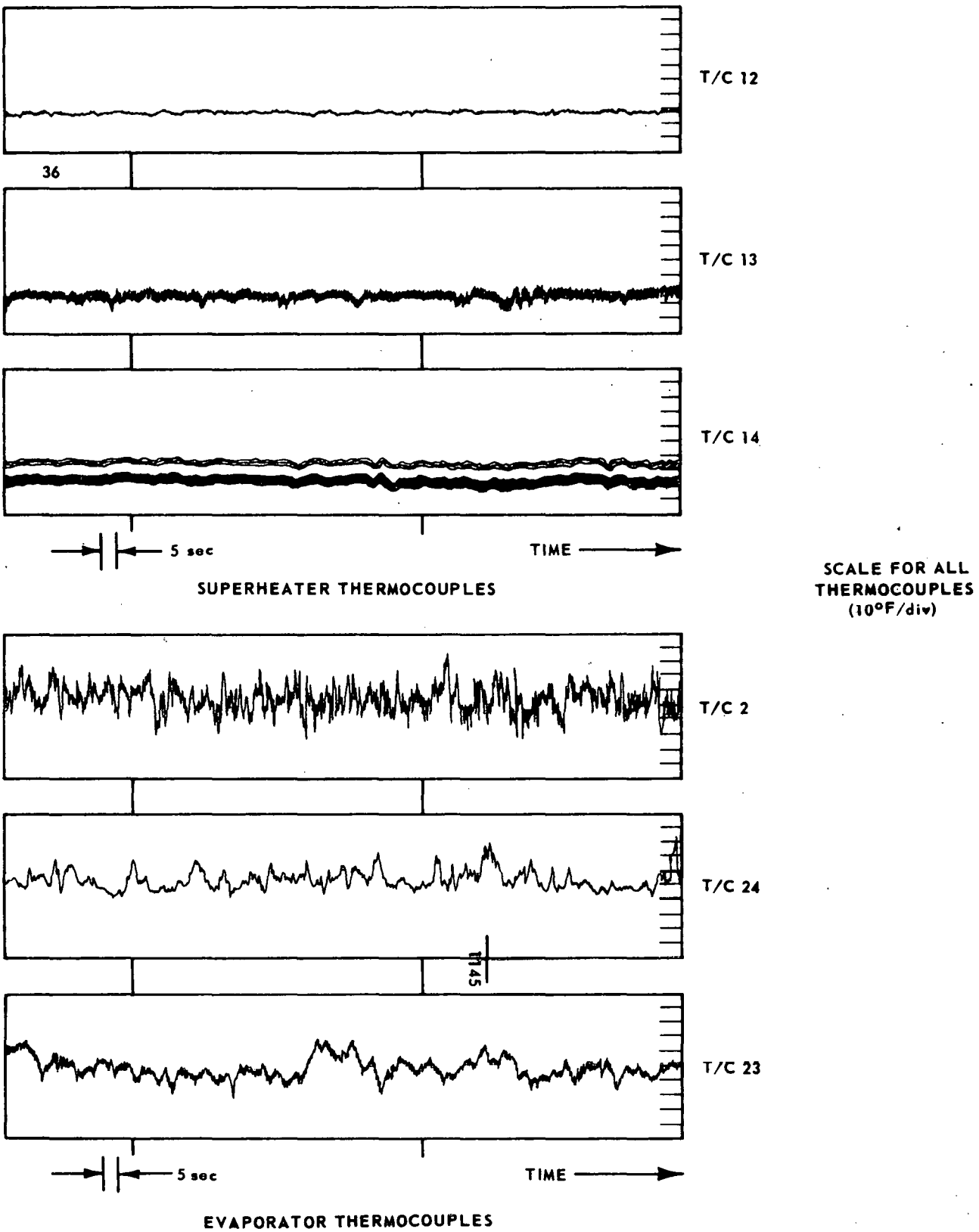

Figure 7-14. *Sanborn Traces of Temperature Variations in the Sodium below and above the Calming Plates in the Superheater and Evaporator Models Operating at Near-Rated Conditions, Sodium Level in Superheater 12 Inches above Calming Plate, Sodium Level in Evaporator 11 Inches above Calming Plate*

calming region is approximately 100 to 150°F less than the sodium entering the evaporator. With high sodium level, the amount of cool sodium present above the calming plate is larger; thus, the potential for getting a larger burst of cool sodium mixed in with the hot sodium below the calming region is present due to the larger natural circulation potential.

It appears then that the problem can be solved at least in part by making the volume of sodium above the calming plate as small as possible and limiting the flow to and from the calming region. Water flow model tests may be useful to investigate the problem further. It should be noted that sodium thermocouple 2 showed the largest fluctuation, but all thermocouples at elevation 492 in. showed considerable fluctuation and followed the same general trends as thermocouple 2. At lower elevations, no temperature fluctuations were observed.

7.2 STEAM-SIDE STABILITY

One of the objectives of the testing of the Steam Generator Test Rig (SGTR) bayonet tube evaporator was to verify the ability of the evaporator to operate stable over the range of boiling conditions experienced in practice. The consequences of boiling instabilities occurring in the evaporator may be unpredictable performance, unnecessary thermal cycling of the tubes, and the possibility for vibration of the tubes and support structure.

The potential for boiling instabilities exists, in general, when the pressure drop from the inlet plenum to the outlet plenum is small and the heating rate is high. A slight change in the heat rate can then cause a change in the two-phase flow pattern with corresponding change in the two-phase pressure drop; thus, a different fluid flow rate may result. The interaction between the heat input and fluid dynamics can thus result in periodic flow oscillations or "chugging" in a boiling channel.

The instability characteristics of a boiling system can often be improved by introducing flow resistance at the boiling channel inlets. In the present bayonet tube geometry, the pressure drop occurring in the bayonet tube is generally a large fraction of the total pressure drop, and thus the bayonet tube geometry is inherently stable. This was indeed verified during the present tests; however, under the very special conditions of once-through operation with considerable superheat at the exit, it was found that boiling may occur in the bayonet tubes and a very unstable system resulted.

Operation at conditions even approaching the unstable range is of no interest at the present time, but the results obtained will be reported here for later reference, and may be of general interest to people working with stability problems of boiling systems. The particular instability problem of boiling in the bayonet tubes was analyzed using a simple single bayonet tube model. The observed boiling in the bayonet tubes was predicted by this model; however, by insulating the bayonet tubes along the total length, the analysis showed that boiling in the bayonet tubes would not occur, and this particular type of instability would not be a problem, even at the off design, once-through operation conditions.

7.2.1 Experimental Results

In a boiling system where several boiling channels operate in parallel, the pressure drop across each channel, as well as the pressure drop from the common inlet and outlet plenums, are constant when the system is operating stable. However, with instable operation, the plenum pressure drop and the pressure drop across each boiling channel will vary while the total flow rate may be constant. This principle was utilized to verify the stability characteristics of the bayonet tube evaporator.

In order to measure the pressure drop across the tubes, holes were drilled in the tube-sheet into the annular space between the bayonet tube and the tube-sheet for Tubes B, D, and F near the steam/water exit nozzle as indicated in Figure 4-6. The holes served as pressure taps and impulse lines from these points and from the inlet plenum were connected to a Barton differential pressure transmitter. Since only one transmitter was available, each tube had to be valved in separately. In the tests that will be described subsequently, Tube B was connected to the transmitter.

A schematic diagram of the steam system showing most of the quantities recorded during the stability tests is given in Figure 7-15. The steam drum pressure and the inlet and outlet plenum pressures, along with the difference between the plenum pressures, were connected to the Sanborn recorders. In addition to these measurements, the recirculation flow rate and the steam flow rate leaving the steam drum were recorded. A number of temperatures were also recorded. These included the water temperatures near the lower end of the bayonet tube double wall insulation in Tube B and the center tube, Tube G. In order to get an indication of superheat at the exit, a thermocouple was inserted into the pressure tap in the tube-sheet for Tube D. The Tube B outside wall temperature was recorded at two elevations by utilizing DNB thermocouples 34 and 20 (Figure 4-13).

The test procedure generally followed for the stability tests was to establish steady-state conditions at various power levels with sodium-side and steam-side conditions near prototypical. The Sanborn traces of the stability instrumentation were observed; and, if there were no signs of instabilities (e.g., a periodic variation of the Tube B pressure drop could be detected), the recirculation flow rate was decreased slightly after a complete data recording by the data acquisition system had been made. Decreasing the recirculation flow rate results in lower plenum-to-plenum pressure drops and higher exit steam quality; the potential for instabilities is increased. This process was continued until instabilities were detected, even if this meant decreasing the recirculation flow rate to the point where superheated conditions at the exit were reached and the evaporator was operating as a once-through forced circulation boiler.

During the process of decreasing the recirculation flow rate, many changes occurred in other loop parameters (e.g., the system pressure and sodium exit temperature were changing and often did not have time to come to equilibrium before a complete data recording was made). Therefore, quantities calculated from these data recordings (e.g., the steam exit quality) have a considerable amount of uncertainty associated with them, and this unsteadiness should be kept in mind when the results given in the following are interpreted.

The stability tests were run near the end of the test program with the P/D = 3 swirl generator inserts and the bayonet tubes were partially insulated for the top 10 ft (Figure 4-9). The three stability runs to be described in the following were at approximately 900, 1100, and 1500 kWt (1500 rated). The steam system pressure was in the range 1550 to 1650 psia and the sodium inlet temperature was in the range of approximately 830 to 890°F during the tests.

The Sanborn traces of the stability instrumentation during a stability run at approximately 1100 kWt are shown in Figures 7-16 through 7-21 and summaries of the data recordings by the data acquisition system taken during the run are shown in Table B-8-1. These figures and tables give the conditions for normal stable operation, approximate conditions immediately before initiation of instabilities and during unstable operation, as well as transition to stable conditions.

From Figure 7-16 it can be seen that there are no periodic oscillations. In particular, the pressure drop across Tube B, denoted by ΔP_B and the differential pressure instrumentation, do respond to a decrease in the recirculation flow rate. At this point, it should be noted that the plenum-to-plenum ΔP reading is not very accurate because this reading is a result of electronic summation of the plenum pressure readings, and with small pressure differences, this is not a satisfactory arrangement. In Figure 7-17, the departure from nucleate boiling point is passed as indicated by a rise in the tube surface temperature (readings T_1 and T_2). The pressure drop is now very low and the flow sustained mostly by natural circulation; the steam exit quality is approximately 100%.

Decreasing the water flow rate still further results in complete natural circulation flow as indicated in Figure 7-18* and considerable superheated steam exit conditions. As indicated before, however, the steam exit conditions at this point cannot be determined very accurately due to the changing sodium conditions and water inlet conditions.

* The difference between the static pressures at the inlet and outlet is zero. The head developed by the recirculation pump, which is still running, is dissipated in the flow control valve downstream of the pump.

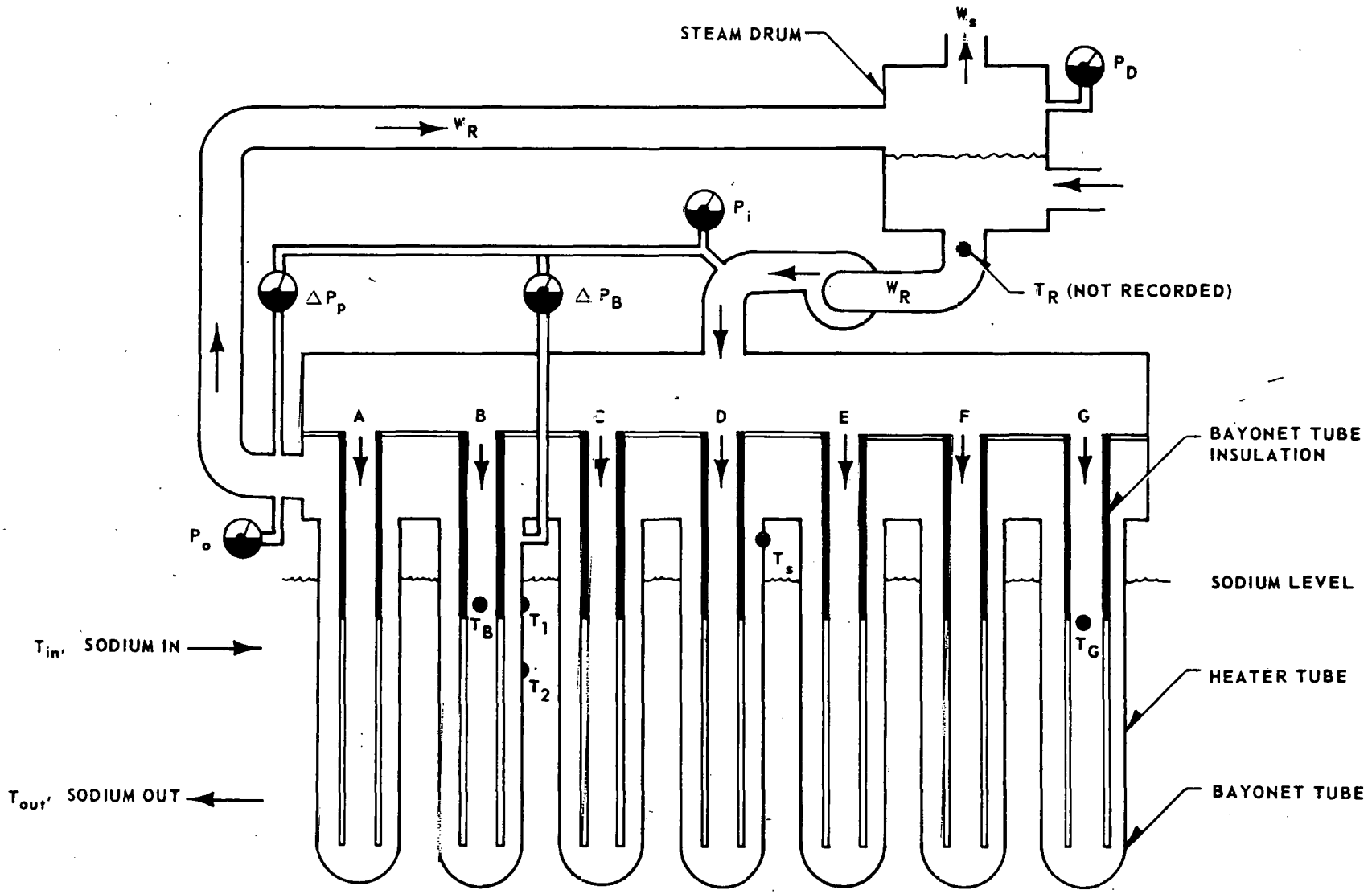

Figure 7-15. Schematic Diagram of the Evaporator Steam System Showing Locations of Stability Instrumentation Recorded on the Sanborns

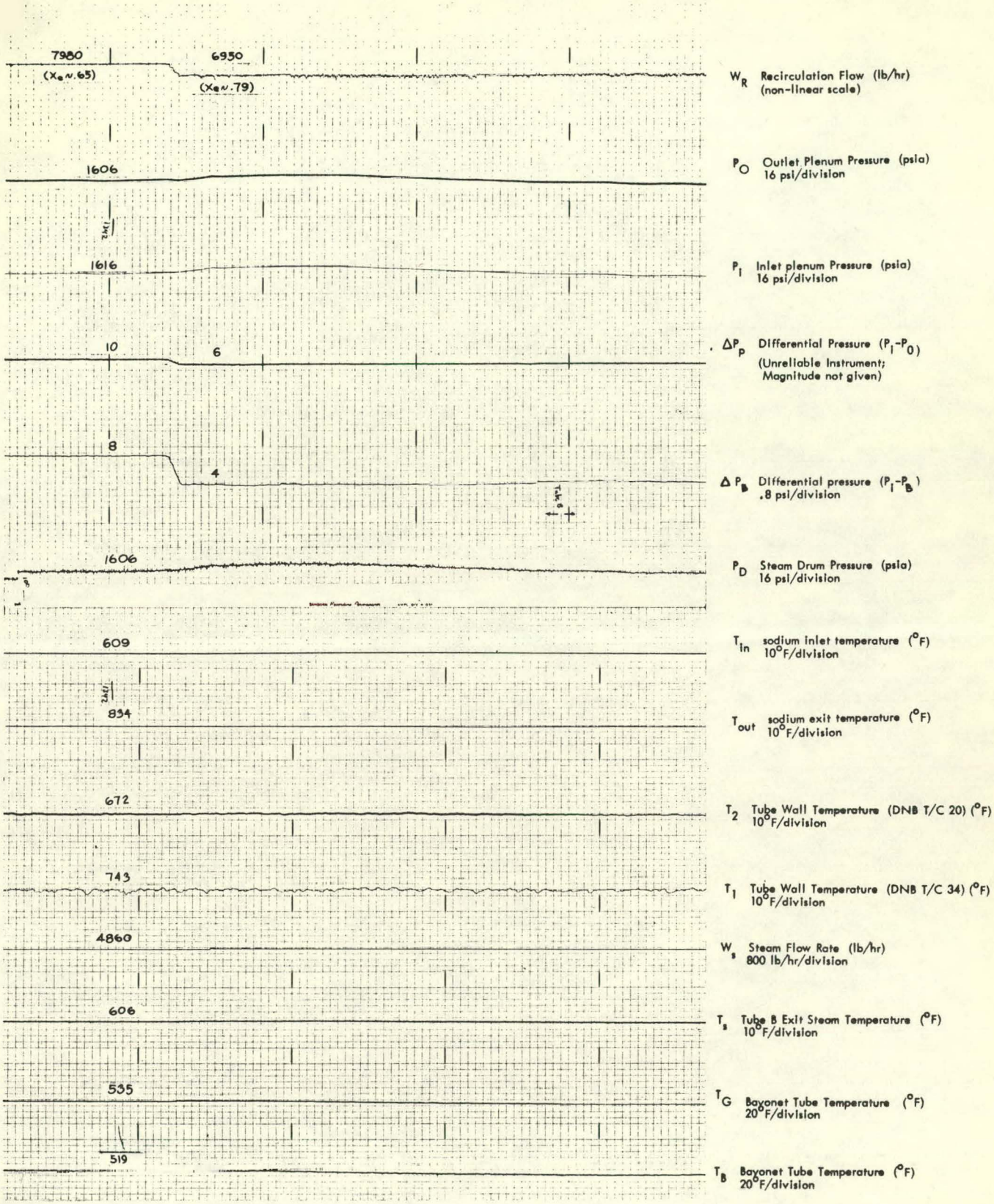

Figure 7-16. Sanborn Traces of Selected Stability Instrumentation on the Evaporator During Stable Operation at Approximately 1100 kWt and 65 Percent Exit Steam Quality, Time Approximately 1342 Hours

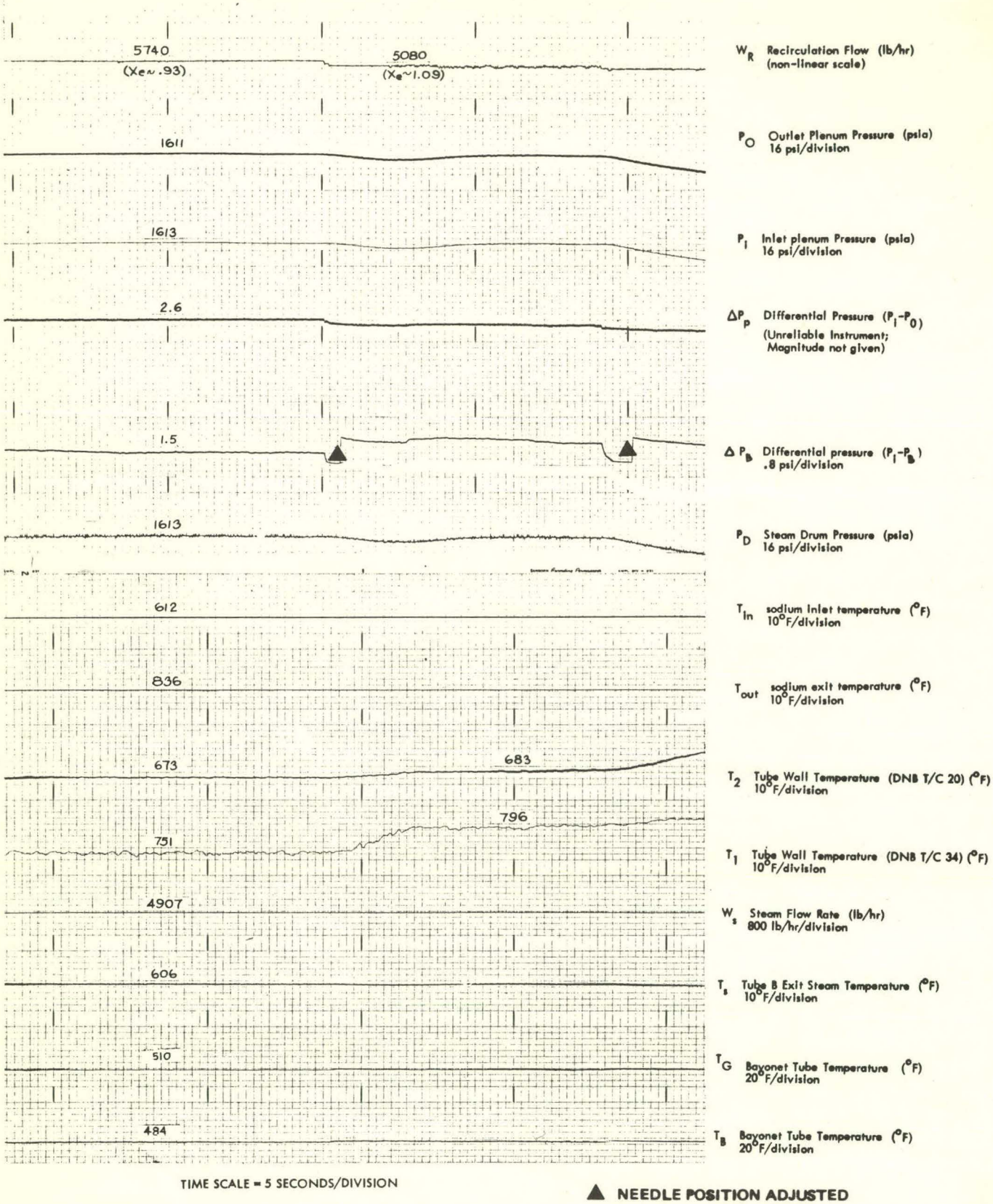

Figure 7-17. ***Sanborn Traces of Selected Stability Instrumentation on the Evaporator during Stable Operation at Approximately 1100 kWt Showing Transition to Partial and Film Boiling at the DNB Thermocouple Locations, Time between 1421 and 1441 Hours***

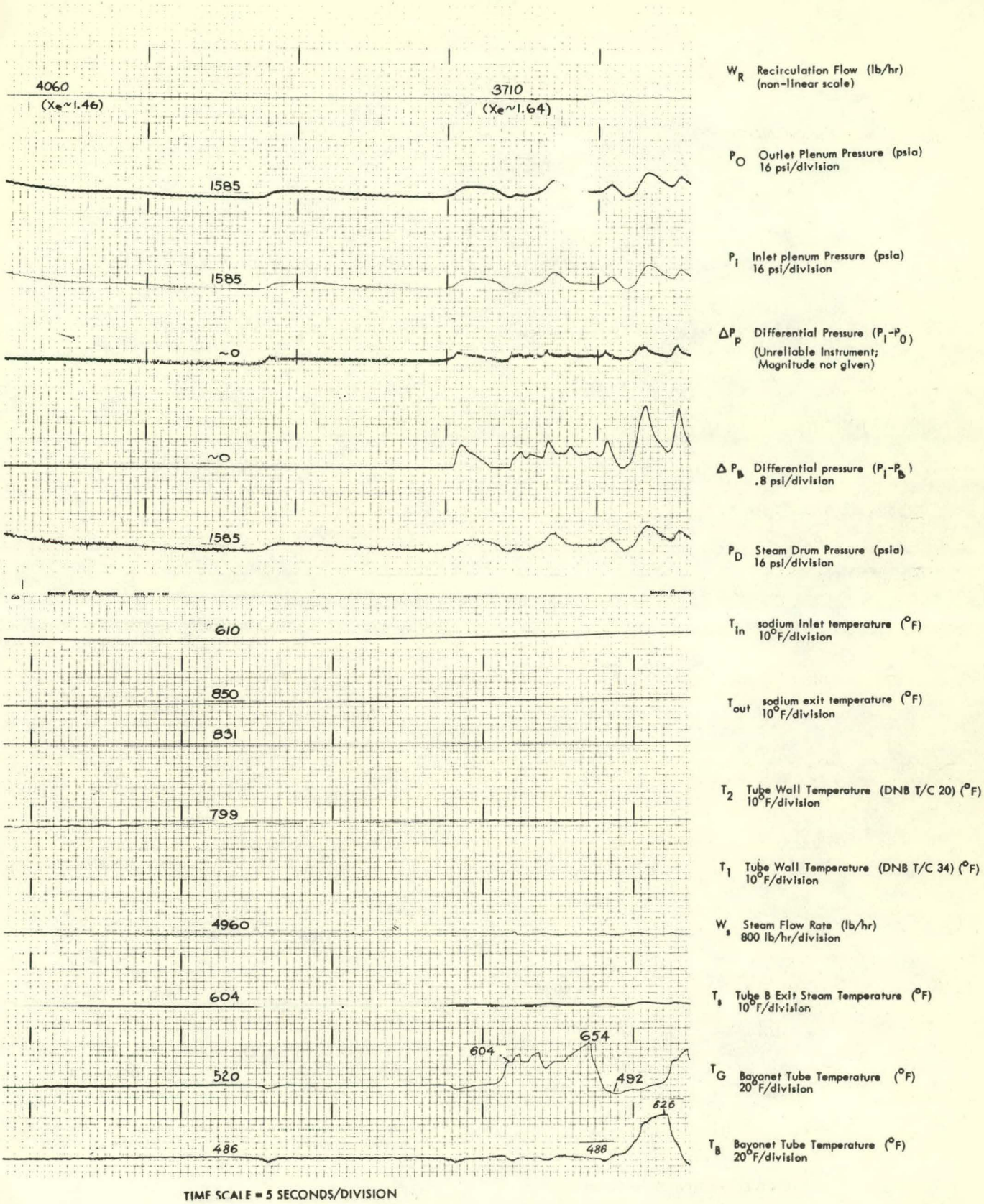

Figure 7-18. Sanborn Traces of Selected Stability Instrumentation on the Evaporator Operating at Approximately 1100 kWt Showing Initiation of Instabilities in the Center Tube at Net Superheat Conditions, Time Between 1501 and 1521 Hours

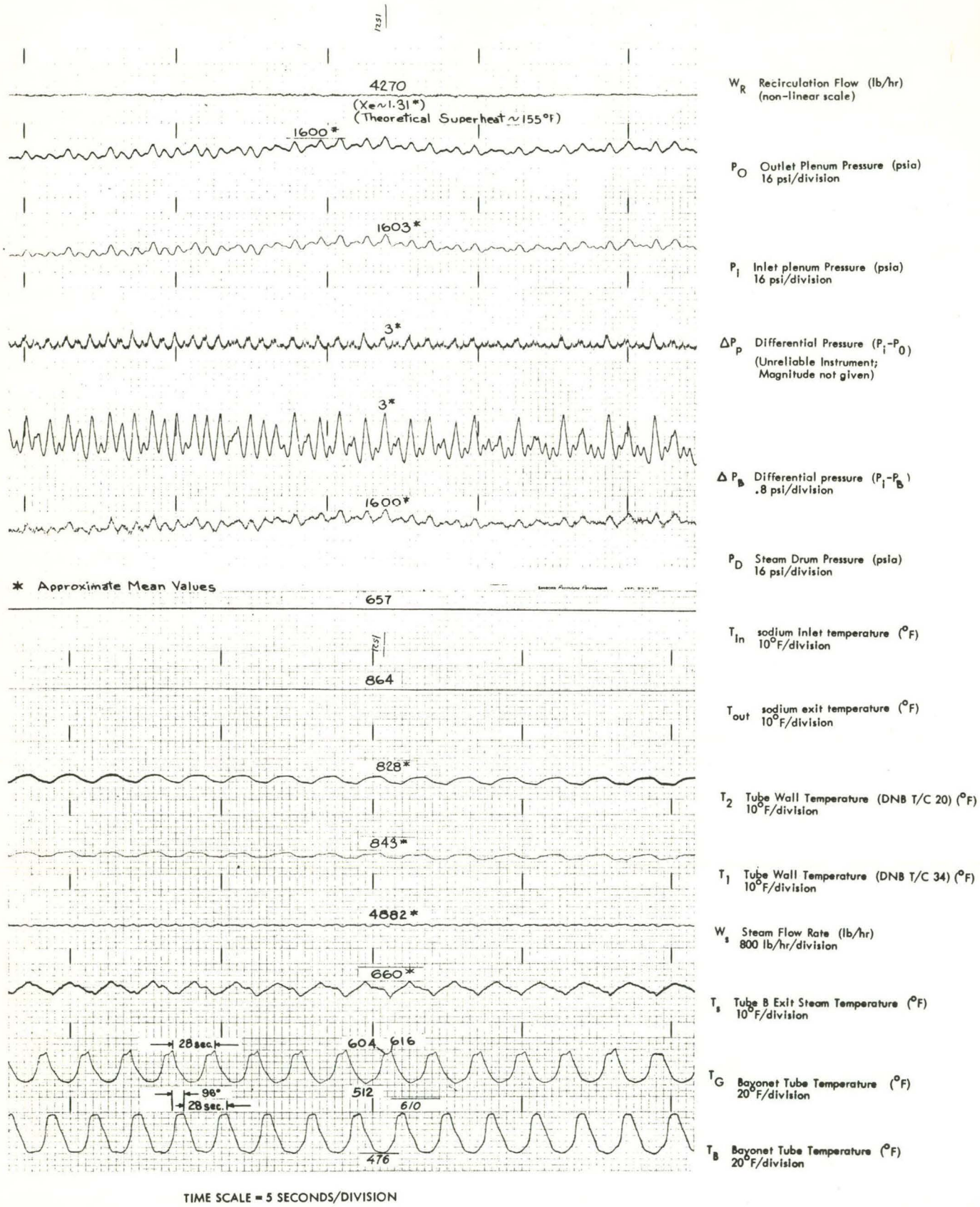

Figure 7-19. Sanborn Traces of Selected Stability Instrumentation on the Evaporator During Unstable Operation at Approximately 1100 kWt and Net Superheat Conditions, Time Approximately 1521 Hours

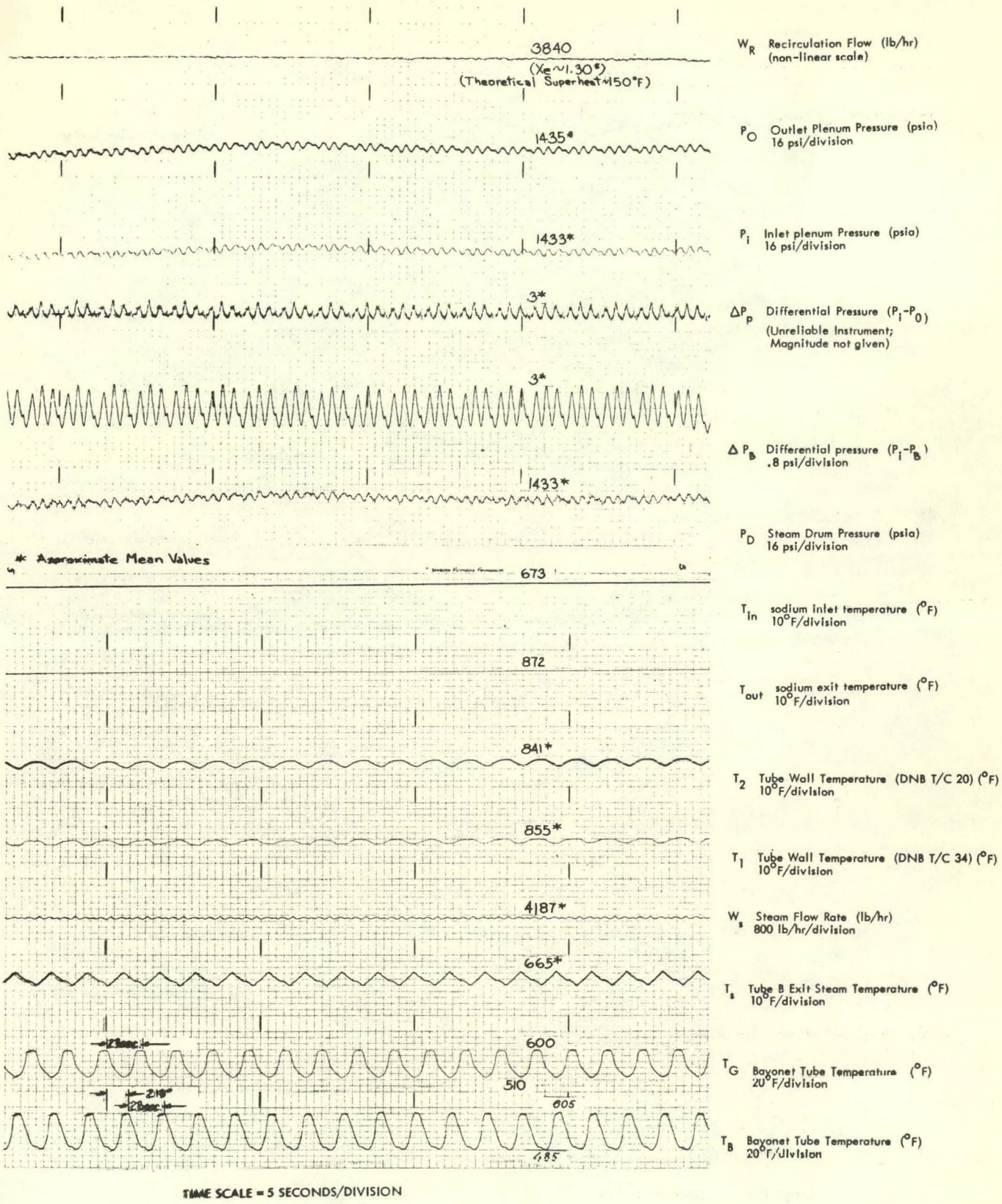

Figure 7-20. Sanborn Traces of Selected Stability Instrumentation on the Evaporator During Unstable Operation at Approximately 1100 kWt and Net Superheat Conditions, Time Approximately 1541 Hours

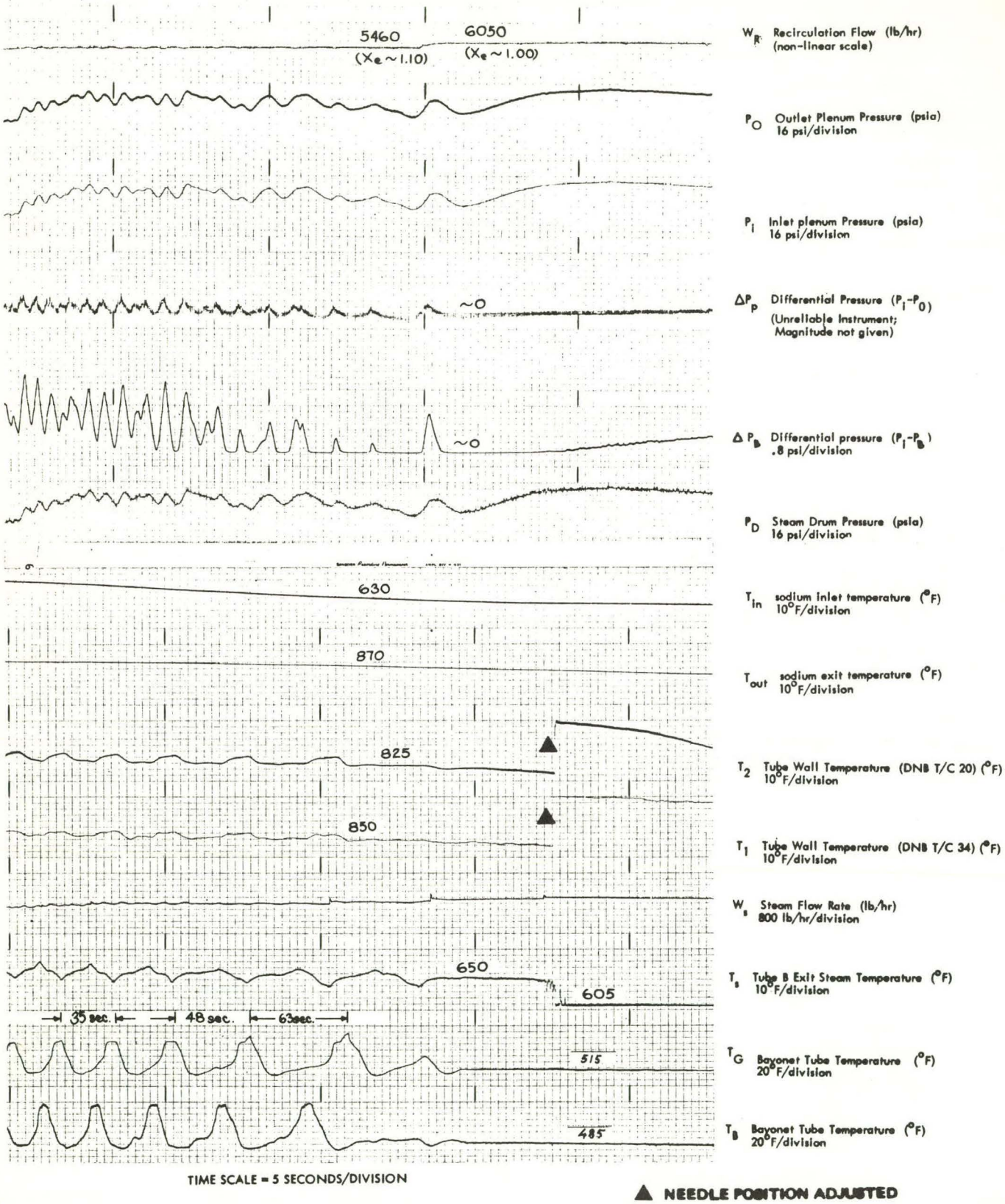

Figure 7-21. Sanborn Traces of Selected Stability Instrumentation on the Evaporator Operating at Approximately 1100 kWt Showing Transition to Stable Boiling Conditions, Time Between 1541 and 1601 Hours

Things start to happen very rapidly now. By considering Figure 7-18, it is observed that there is a dip in the system pressure (indicated by P_I, P_O, P_D), and also in the water temperature in the bayonet tubes as given by T_B and T_G, followed by a small rise in the system pressure (no manual controls were made at this time). A short while after, there is a repeat of this occurrence, but this time there is a rise in the pressure drop across Tube B, denoted by ΔP_B, and the water temperature in the center tube starts to increase and reaches a saturation temperature of approximately 604°F corresponding to the existing system pressure. This temperature stays constant for a short while and then makes a few ups and downs before a temperature of approximately 654°F is reached. After this, the temperature T_G drops down to a very low value, but now the water temperature in Tube B starts to increase and the system pressure as well as the pressure drops have started to oscillate. This is more apparent from Figure 7-19, where it is seen that everything except the recirculation flow rate and sodium inlet and outlet temperatures show a periodic oscillatory behavior. At this point, it is worthwhile to mention that the thermocouple (denoted by T_S on the figures) did not show any sign of superheat when the steam exit conditions should be superheated according to heat balances based on the sodium-side measurements. Additionally, this thermocouple shows only approximately 60°F superheat on Figure 7-19, which does not agree with calculations. However, it was verified later that this thermocouple was not inserted far enough into the pressure tap hole in the tube-sheet to see the steam directly. Therefore, the thermocouple was surrounded by water in the cavity until the tube-sheet had been heated sufficiently to boil off all the water in the cavity; under these circumstances, the magnitude of the reading cannot be relied upon.

It is interesting at this time to take a look at Figure 7-22, which shows the average sodium temperature profiles measured in the evaporator during this test run at normal stable operation, just before initiation of instabilities, and at unstable conditions. This figure tends to verify that the exit steam conditions were indeed superheated, since the slope of the profile indicates the rate of heat transfer in the various regions of the unit; for film boiling, the heat rate is generally very low compared to nucleate boiling.

It will take too much space to describe what happens further in detail; therefore, attempts to concentrate on important characteristics will be made. First, by considering Figures 7-19 and 7-20, it is observed that the period of the temperature oscillations in the bayonet tubes changes, and so does the phase shift; the characteristics of the various traces change slightly. By increasing the water flow rate, transition to stable conditions occurs as shown in Figure 7-21.

The Sanborn recordings for the approximately 1500 kWt run are shown in Figures 7-23 through 7-26, the corresponding summaries of the data are shown in Table B-8-2. Essentially, the same behavior is observed at this power level. The evaporator is stable at normal operating conditions, but becomes unstable when a considerable amount of superheat is reached at the exit; however, in this case, there is some net pressure drop across Tube B when the instability starts.

The Sanborn recordings for the approximately 900 kWt run are shown in Figures 7-27 through 7-30; summaries of the data are shown in Table B-8-3. The conclusions reached for the two previous runs can be reached here too, and the general characteristics of the observed instability are similar to the previous runs. The detailed study of all traces, however, is left to the reader.

The previous results have shown that the boiling system tends to get unstable when the exit conditions become superheated. When considerable superheat at the exit has been reached, it just happens that the imposed driving pressure drop on the evaporator is small or nonexistent due to the low water flow rates (approximately 3000 lb/h to 5000 lb/h while the design flow rate was 22,500 lb/h). It is then easy to draw the conclusion that the low pressure drop is the main reason for the instability; however, it is clear from the previous traces, particularly from the traces of the water temperatures in the bayonet tubes T_G and T_B, that there is boiling occurring in the bayonet tubes. This is evidenced from the fact that the temperatures often increased rapidly to the saturation temperature, then remained constant, while all water locally evaporated, and then often increased again to temperatures higher than the saturation temperature, indicating superheated conditions. This is only possible if the steam in the annulus is superheated, because the pressure in the bayonet tube is always higher than in the annulus.

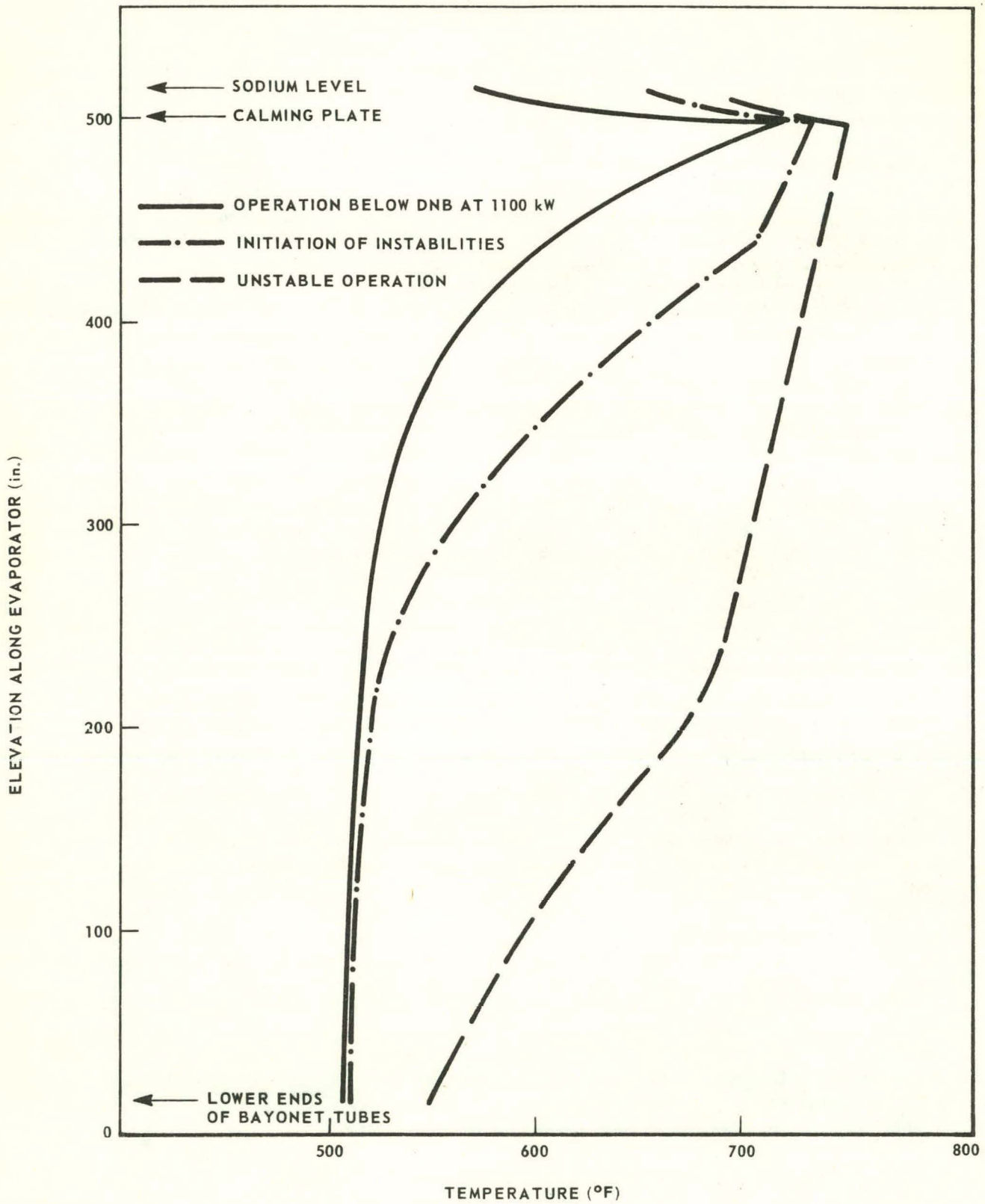

Figure 7-22. Measured Sodium Temperature Profiles in the Evaporator Test Model during Different Modes of Operation

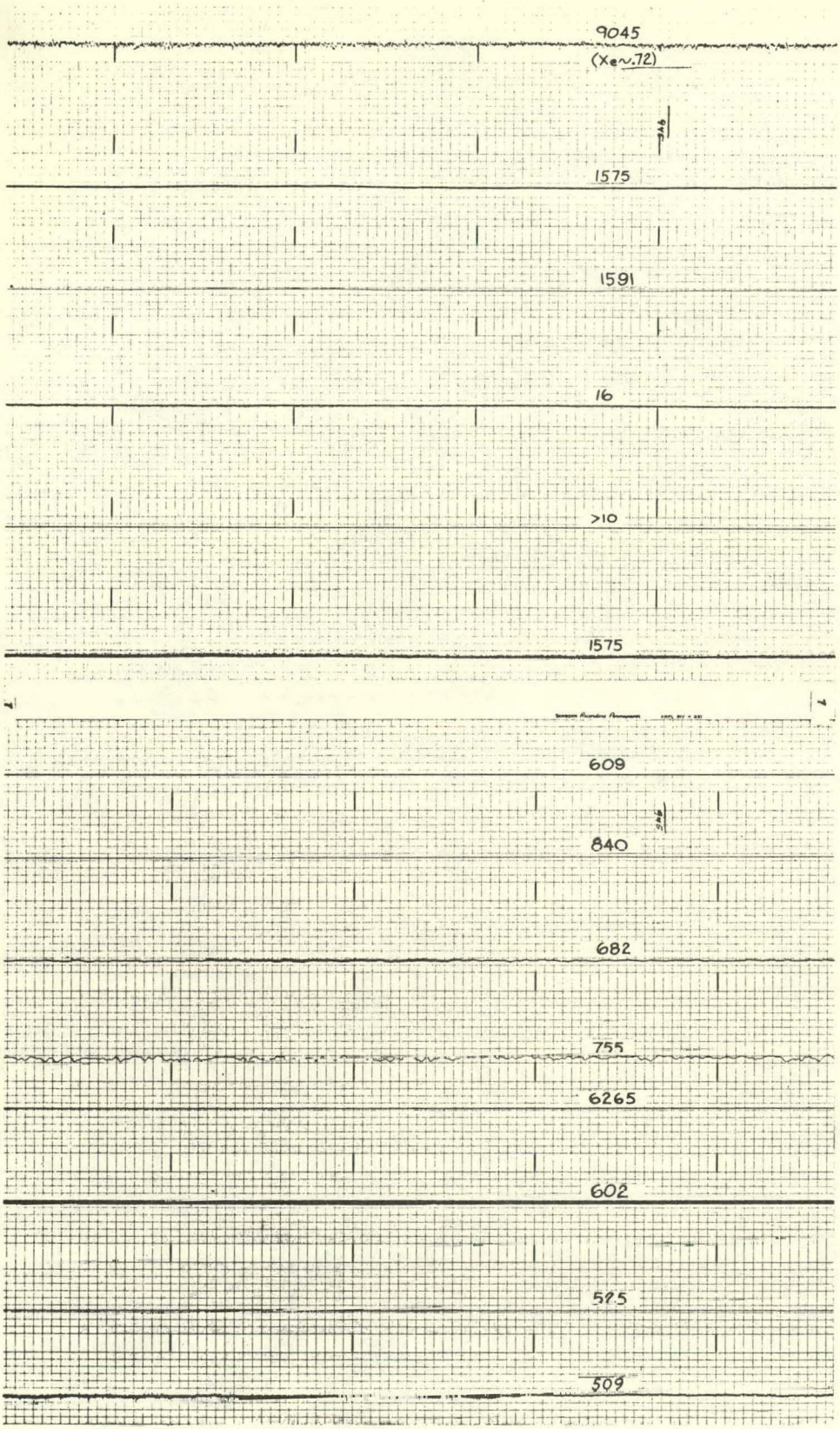

W_R Recirculation Flow (lb/hr) (non-linear scale)

P_O Outlet Plenum Pressure (psia) 16 psi/division

P_I Inlet plenum Pressure (psia) 16 psi/division

ΔP_p Differential Pressure (P_i-P_0) (Unreliable Instrument; Magnitude not given)

ΔP_B Differential pressure (P_i-P_B) .8 psi/division

P_D Steam Drum Pressure (psia) 16 psi/division

T_{in} sodium inlet temperature (°F) 10°F/division

T_{out} sodium exit temperature (°F) 10°F/division

T_2 Tube Wall Temperature (DNB T/C 20) (°F) 10°F/division

T_1 Tube Wall Temperature (DNB T/C 34) (°F) 10°F/division

W_s Steam Flow Rate (lb/hr) 800 lb/hr/division

T_s Tube B Exit Steam Temperature (°F) 10°F/division

T_G Bayonet Tube Temperature (°F) 20°F/division

T_B Bayonet Tube Temperature (°F) 20°F/division

TIME SCALE = 5 SECONDS/DIVISION

Figure 7-23. Sanborn Traces of Selected Stability Instrumentation on the Evaporator During Stable Operation at Approximately 1500 kWt and 72 Percent Exit Steam Quality, Time Approximately 945 Hours

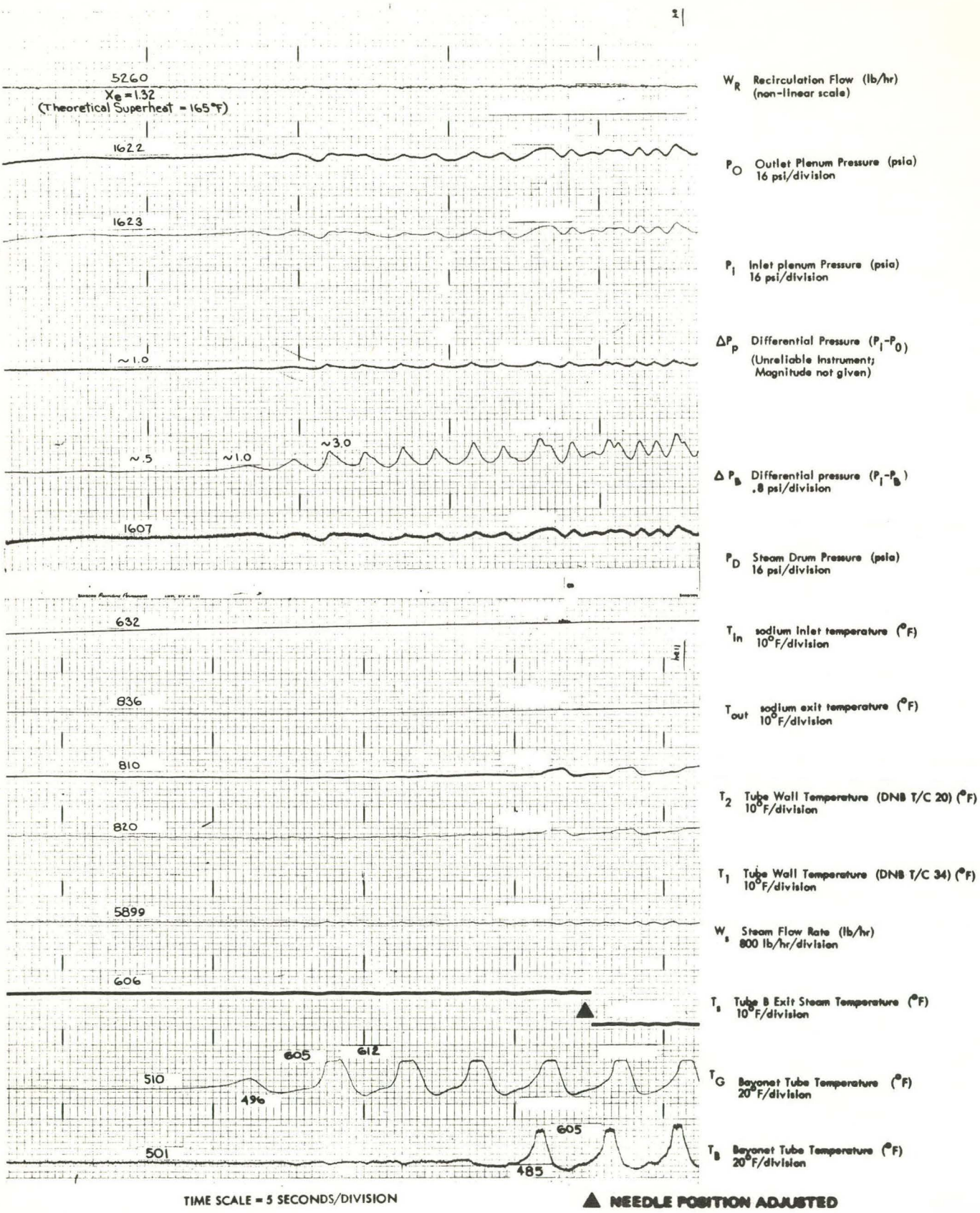

Figure 7-24. Sanborn Traces of Selected Stability Instrumentation on the Evaporator Operating at Approximately 1500 kWt Showing Initiation of Instabilities in the Center Tube at Net Superheat Conditions, Time Approximately 1104 Hours

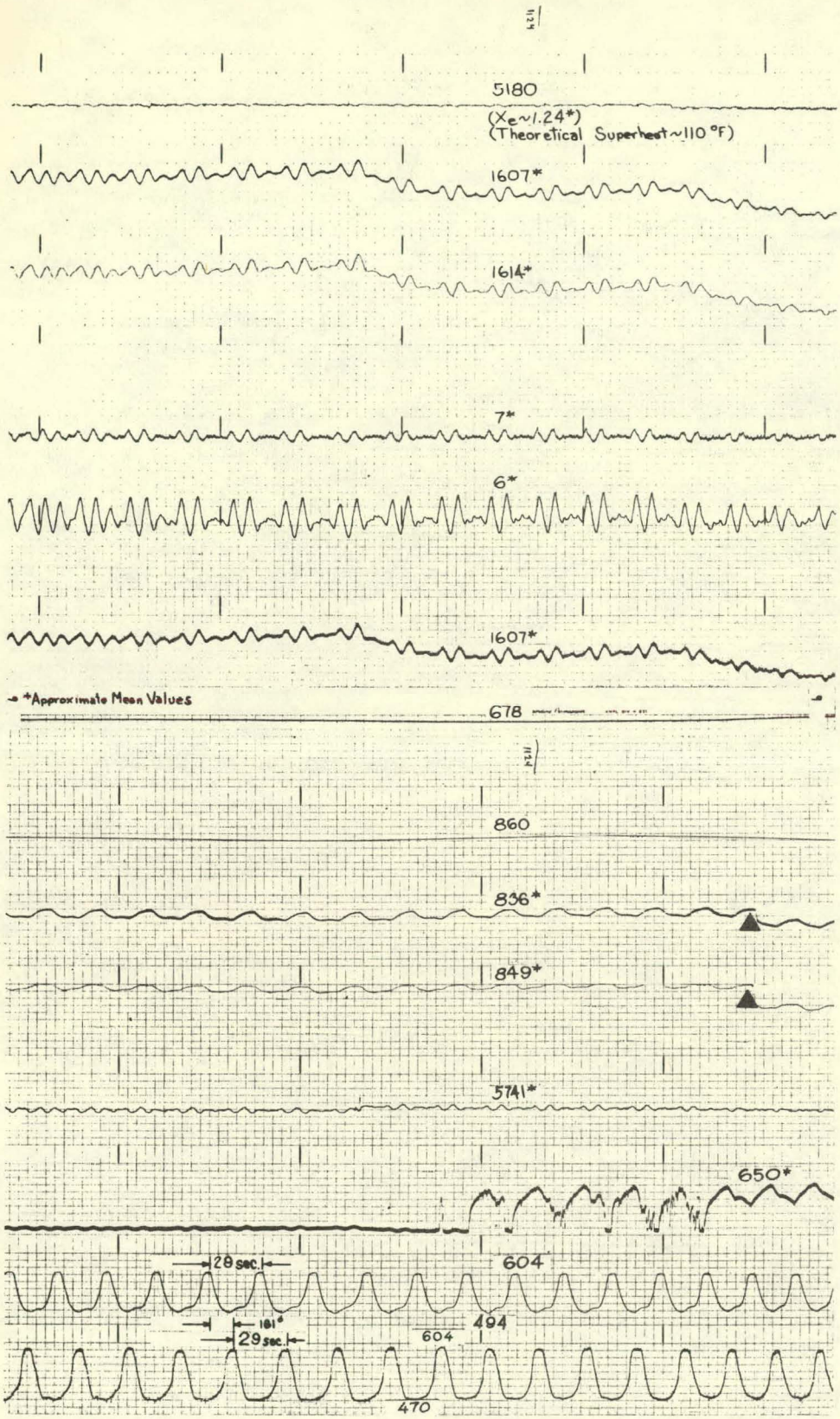

W_R Recirculation Flow (lb/hr) (non-linear scale)

P_O Outlet Plenum Pressure (psia) 16 psi/division

P_I Inlet plenum Pressure (psia) 16 psi/division

ΔP_P Differential Pressure (P_I-P_O) (Unreliable Instrument; Magnitude not given)

ΔP_B Differential pressure (P_I-P_B) .8 psi/division

P_D Steam Drum Pressure (psia) 16 psi/division

T_{in} sodium inlet temperature (°F) 10°F/division

T_{out} sodium exit temperature (°F) 10°F/division

T_2 Tube Wall Temperature (DNB T/C 20) (°F) 10°F/division

T_1 Tube Wall Temperature (DNB T/C 34) (°F) 10°F/division

W_s Steam Flow Rate (lb/hr) 800 lb/hr/division

T_s Tube B Exit Steam Temperature (°F) 10°F/division

T_G Bayonet Tube Temperature (°F) 20°F/division

T_B Bayonet Tube Temperature (°F) 20°F/division

TIME SCALE = 5 SECONDS/DIVISION

▲ NEEDLE POSITION ADJUSTED

Figure 7-25. Sanborn Traces of Selected Stability Instrumentation on the Evaporator During Unstable Operation at Approximately 1500 kWt and Net Superheat Conditions, Time Approximately 1124 Hours

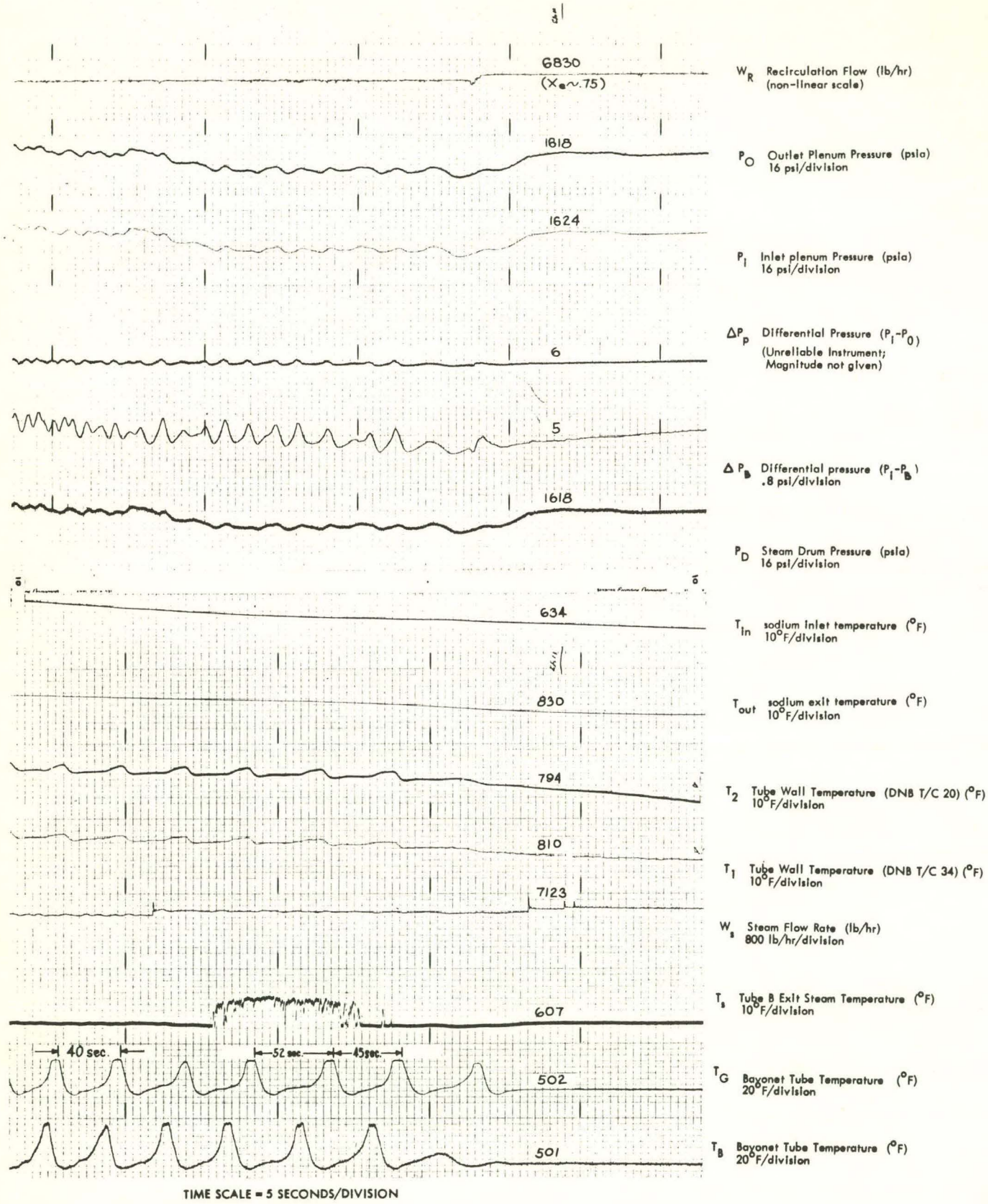

Figure 7-26. Sanborn Traces of Selected Stability Instrumentation on the Evaporator Operating at Approximately 1500 kWt Showing Transition to Stable Boiling Conditions, Time Approximately 1143 Hours

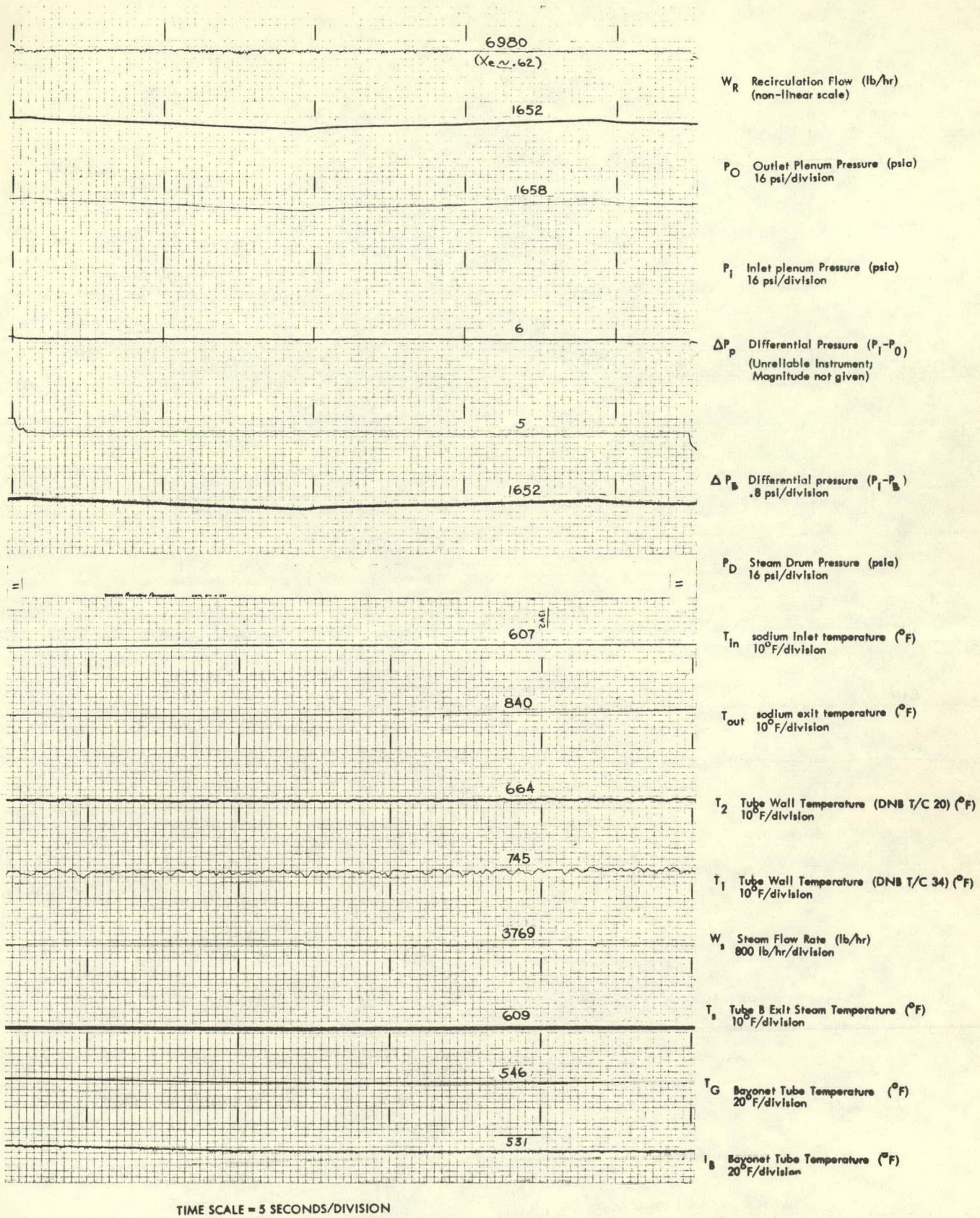

TIME SCALE = 5 SECONDS/DIVISION

Figure 7-27. Sanborn Traces of Selected Stability Instrumentation on the Evaporator During Stable Operation at Approximately 900 kWt and 62 Percent Exit Steam Quality, Time Approximately 1242 Hours

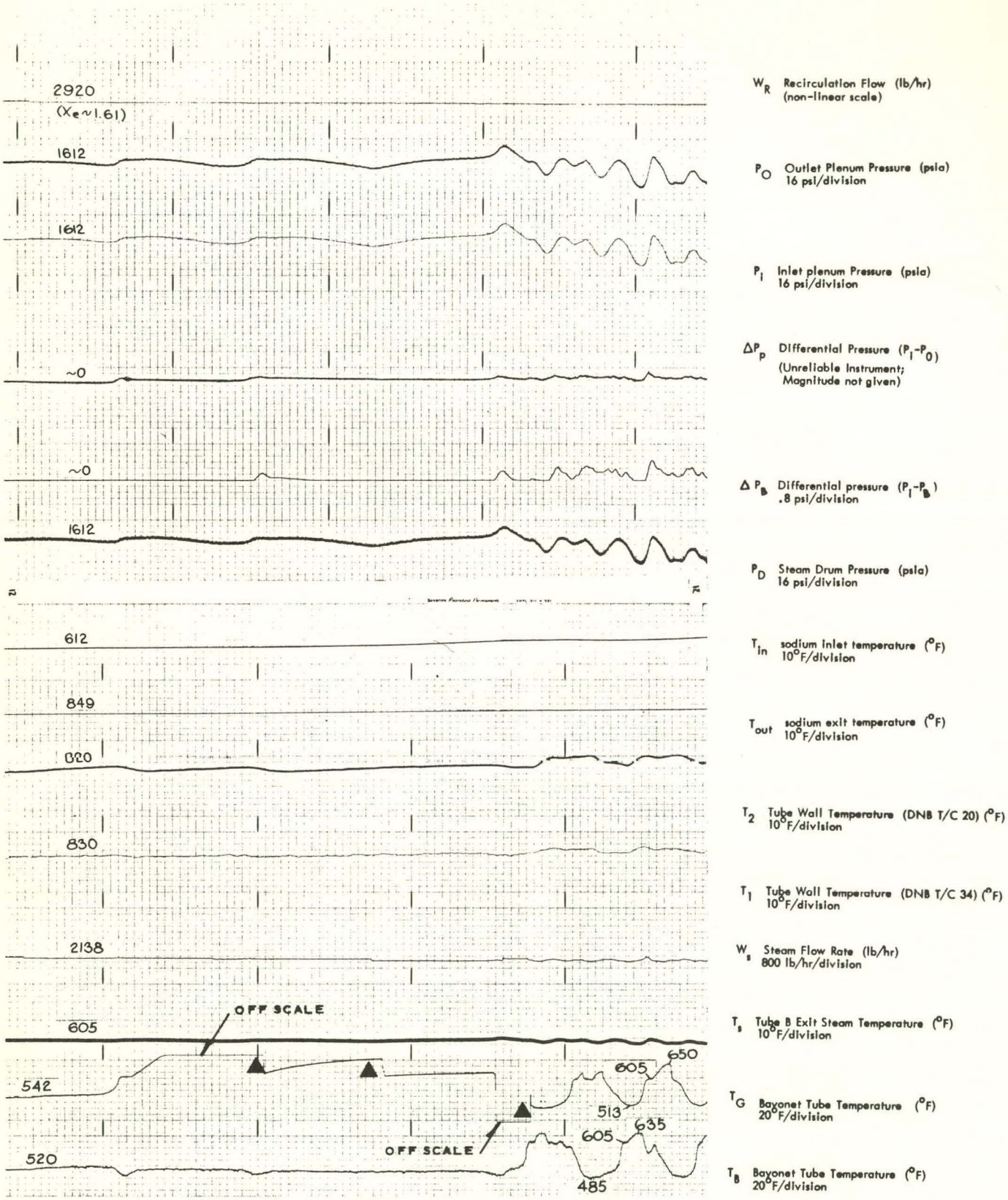

Figure 7-28. Sanborn Traces of Selected Stability Instrumentation on the Evaporator Operating at Approximately 900 kWt Showing Initiation of Instabilities in the Center Tube at Net Superheat Conditions, Time between 1402 and 1422 Hours

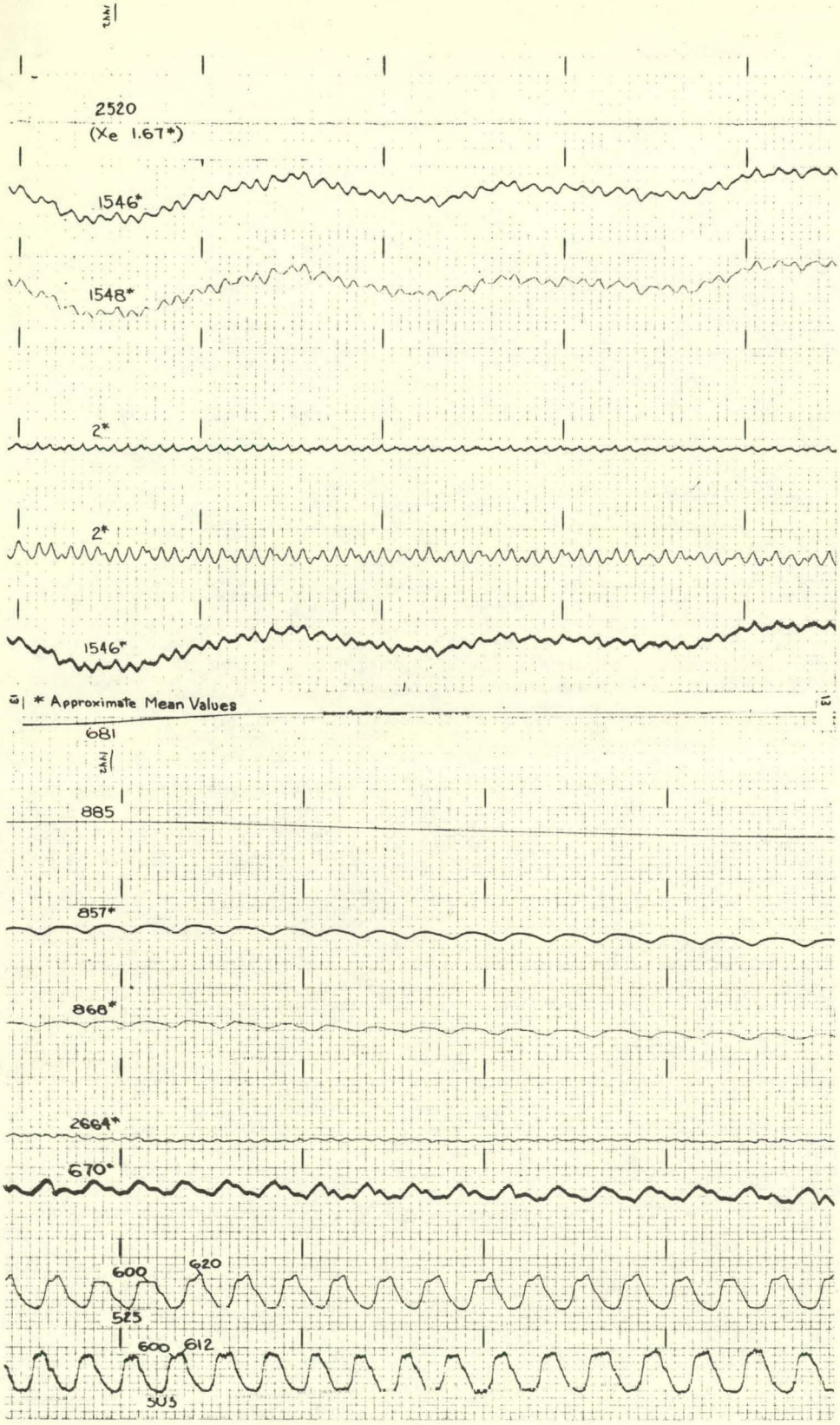

W_R Recirculation Flow (lb/hr) (non-linear scale)

P_O Outlet Plenum Pressure (psia) 16 psi/division

P_I Inlet plenum Pressure (psia) 16 psi/division

ΔP_P Differential Pressure ($P_I - P_O$) (Unreliable Instrument; Magnitude not given)

ΔP_B Differential pressure ($P_I - P_B$) .8 psi/division

P_D Steam Drum Pressure (psia) 16 psi/division

T_{in} sodium inlet temperature (°F) 10°F/division

T_{out} sodium exit temperature (°F) 10°F/division

T_2 Tube Wall Temperature (DNB T/C 20) (°F) 10°F/division

T_1 Tube Wall Temperature (DNB T/C 34) (°F) 10°F/division

W_s Steam Flow Rate (lb/hr) 800 lb/hr/division

T_s Tube B Exit Steam Temperature (°F) 10°F/division

T_G Bayonet Tube Temperature (°F) 20°F/division

T_B Bayonet Tube Temperature (°F) 20°F/division

TIME SCALE = 5 SECONDS/DIVISION

Figure 7-29. Sanborn Traces of Selected Stability Instrumentation on the Evaporator During Stable Operation at Approximately 1100 kWt and 65 Percent Exit Steam Quality, Time Approximately 1342 Hours

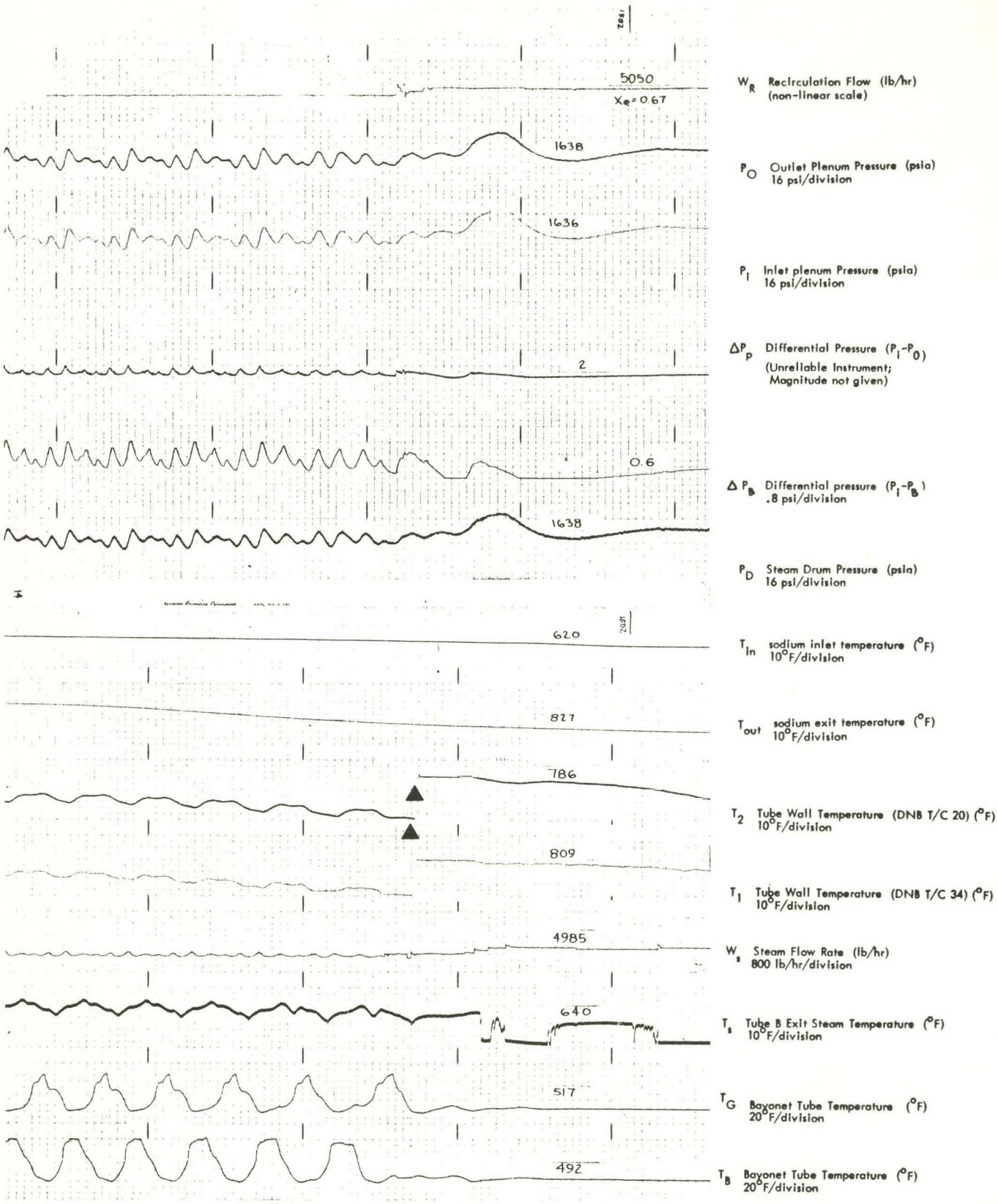

Figure 7-30. Sanborn Traces of Selected Stability Instrumentation on the Evaporator Operating at Approximately 900 kWt Showing Transition to Stable Boiling Conditions, Time Approximately 1502 Hours

This type of boiling instability may not have been encountered before. A simple analysis of a single bayonet tube will be made to see if the observed behavior can be predicted.

7.2.2 Analysis of Single Bayonet Tube

In an attempt to explain the observed boiling instability, a simple model of the bayonet tube assembly as shown in Figure 7-31 may be used. In this figure, the bayonet tube assembly is thought of as being a U-tube, where the left leg is the bayonet tube and the right leg the annulus between the bayonet tube and the heater tube.

On the left-hand portion of Figure 7-31, normal operation of the bayonet tube assembly is pictured. The inlet pressure is larger than at the outlet and the water/steam temperature profile as is shown in the sketch. In the right-hand portion of Figure 7-31, unstable operation in the early stages is pictured. The static pressure at the inlet is approximately equal to the static pressure at the outlet, as observed in the tests. Thus, the flow is sustained mainly by natural circulation. The steam in the annulus is superheated also according to observations, and there is a high heat transfer rate through the bayonet tube wall to the fluid in the bayonet tube immediately below the insulated portion. This high heat transfer rate may heat the water in the bayonet tube until steam bubble or void formation starts.

This is believed to be the point where the instability starts. The void results in higher pressure drop due to the two-phase multiplier involved; thus, the flow rate must drop because the applied pressure difference is negligible. Additionally, the natural circulation head is diminished when the void is introduced in the bayonet tube; this also tends to decrease the flow rate. With the lower flow rate, the potential for more void formation is there, and eventually flow stoppage and expulsion of the mixture in both directions may occur. However, when this occurs, the superheated region in the annulus will be pushed out and the high heat transfer rate across the bayonet tube is no longer there. The void formation in the bayonet ceases and the flow is restored.

At this time, interaction between the other tubes, the increased plenum-to-plenum pressure drop due to more total void in the system, and changing system pressure and corresponding flashing must be taken into account. It is worthwhile to note that the total flow rate is constant; therefore, the periodic void formation, etc., in each tube must be out of phase and must happen in some sequential order.

As a first attempt to analyze the problem, a single bayonet tube was considered. The one-dimensional conservation equations were written in finite difference form and a calculation technique similar to that used by Meyer and Rose[40] was employed. The major assumptions involved were that the static pressure drop across the tube was constant and the effect of flashing was neglected. A more complete description of the problem formulation and the model is given in Appendix C-2.

The predicted water temperature profiles in the bayonet tube corresponding approximately to the conditions of instability run 1 are shown in Figure 7-32. The temperature profile for $t = 0$ corresponds to the steady-state profile reached with boundary condition 1, pictured in the adjoining sketch, corresponding to a saturated condition in the annulus. At $t = 0$, a change to boundary condition 2, also corresponding approximately to the observed steam temperature profile for this run, was made. Of course, in the real system, the steam temperature change was not a step change, and the adapted behavior is an idealization.

From Figure 7-32 it is apparent that after a short time interval, the water in the bayonet tubes becomes saturated and void formation starts. This is indicated more clearly in Figure 7-33, where the void fraction, the water temperature, and the mass flow rate are plotted vs time for the point in the bayonet tube where the saturation condition is first reached. The water temperatures show a more rapid increase than in the experiments, due to the idealized boundary condition behavior. As soon as saturation conditions have been reached and void formation occurs, the expected decreasing trend in the mass flow rate does occur.

This simple analysis predicts that boiling does occur in the bayonet tube in agreement with experimental evidence. More could be learned about the phenomenon by introducing a time-varying steam boundary condition and perhaps a time-varying pressure drop behavior using the same analysis techniques. It is

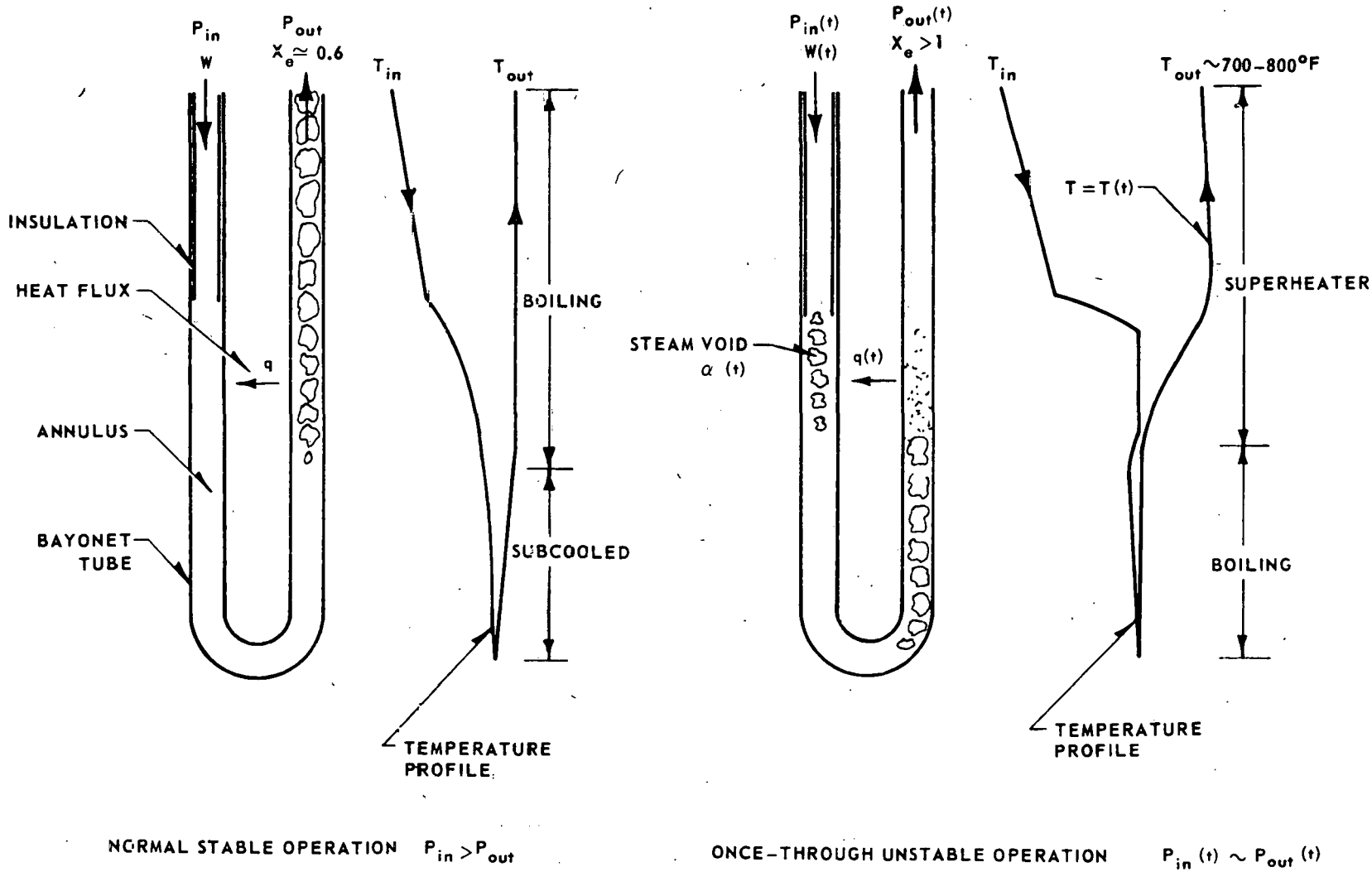

Figure 7-31. Diagram of Stable and Unstable Mode of Operation for One Bayonet Tube Assembly Idealized as a U-Tube

This type of boiling instability may not have been encountered before. A simple analysis of a single bayonet tube will be made to see if the observed behavior can be predicted.

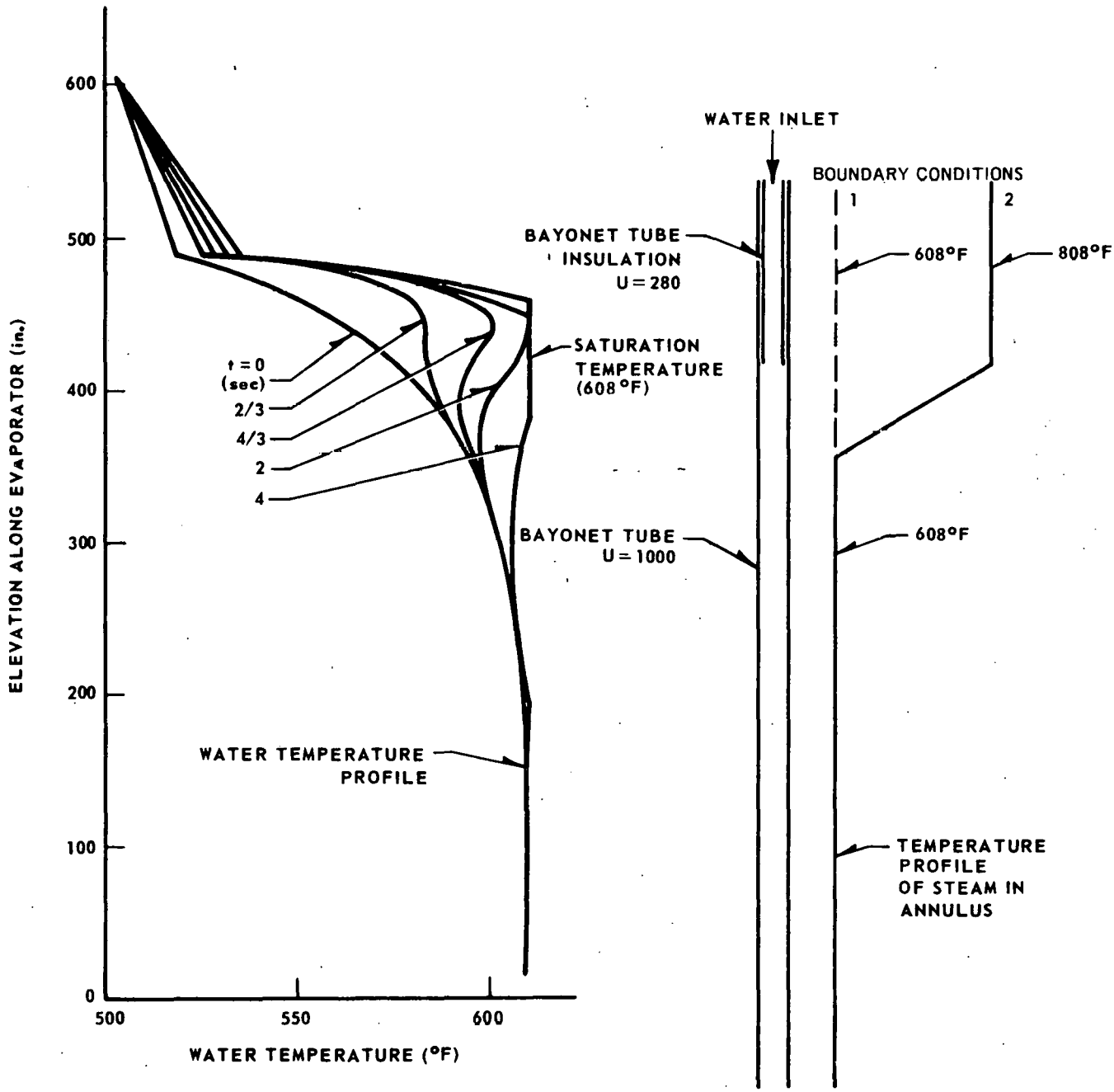

Figure 7-32. Results of Transient Analysis of Single Bayonet Tube with Boundary Condition 1 for $t < 0$ and Boundary Condition 2 for $t > 0$

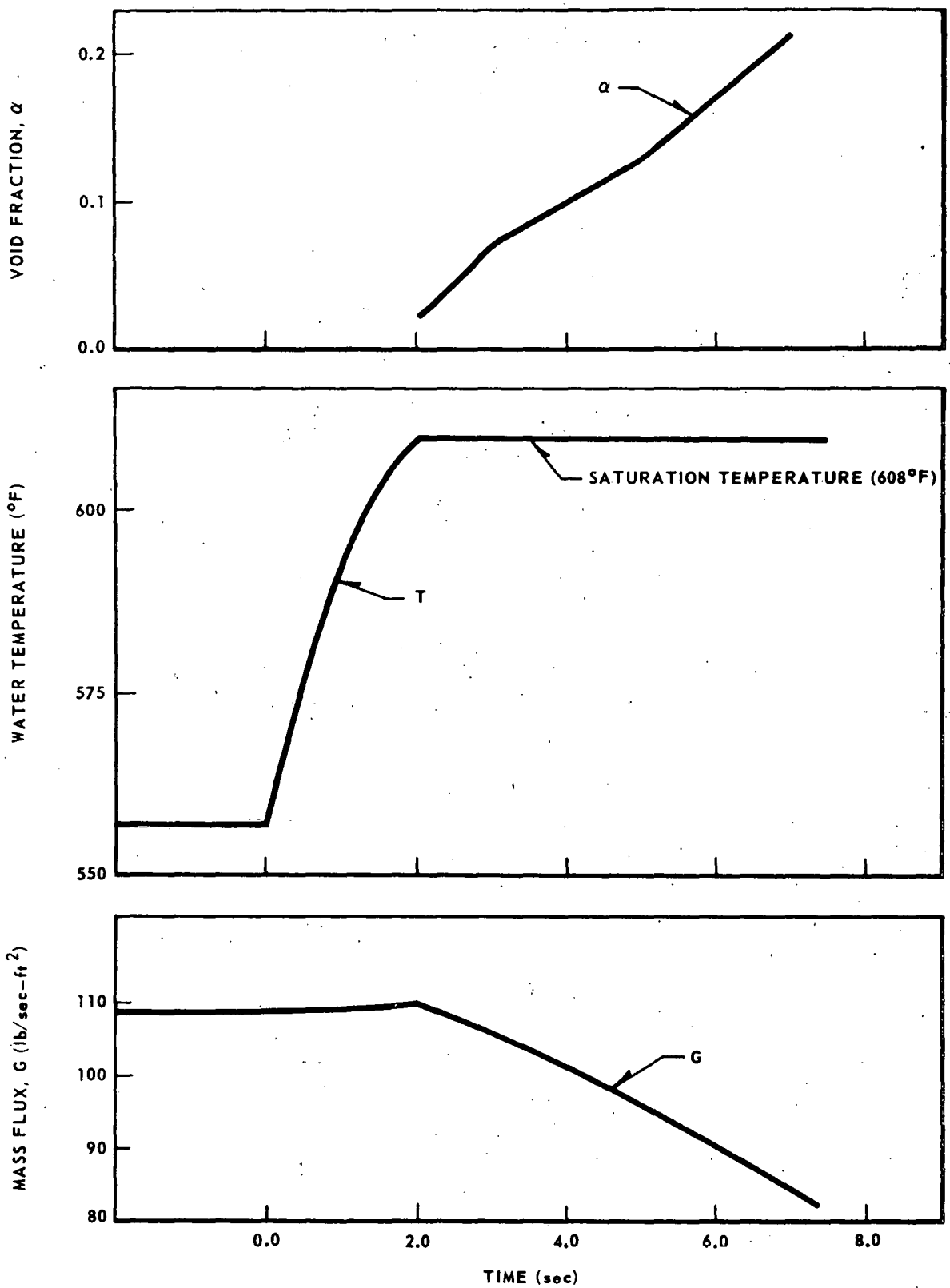

Figure 7-33. Transient Analysis of Single Bayonet Tube Showing Variation of the Mass Flow Rate, Water Temperature, and Steam Void Fraction at Elevation 450.5 Inches Using the Boundary Conditions in Figure 7-32

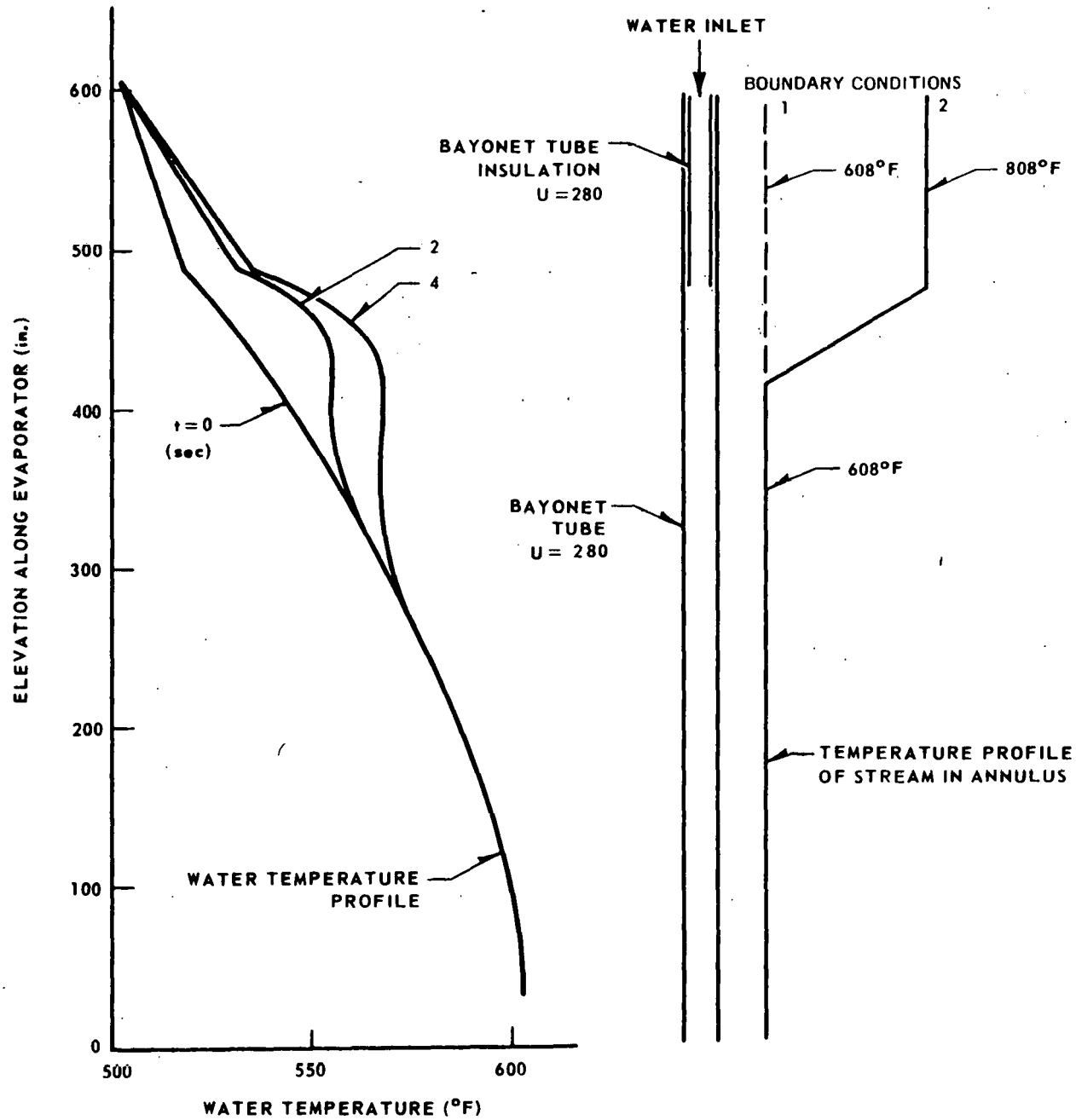

Figure 7-34. *Results of Transient Analysis of Single Bayonet Tube with Boundary Condition 1 for $t < 0$ and Boundary Condition 2 for $t > 0$ Using Bayonet Tube Overall Heat Transfer Coefficient of $U = 280$ for the Entire Length*

interesting to see how this boiling instability can be prevented. The first idea that comes to mind is to insulate the bayonet tube along its total length. This was accomplished by changing the overall heat transfer coefficient U from 1000 to 280, the approximate value for the insulated portion of the bayonet tube. The result is shown in Figure 7-30, where the water temperature profile is shown at different times. The profile at t = 4 sec is approximately the steady-state profile, and it can be seen that boiling is not predicted to occur.

It is apparent that boiling in the bayonet tubes can be avoided to the degree needed by an appropriate choice of bayonet tube design. Another method to avoid boiling may be to decrease the diameter of the bayonet tubes and thus obtain higher pressure drop and flow velocity; however, the effect of this was not studied.

As mentioned before, the instability problem observed is of little interest to the present steam generator design because it occurs far outside the planned operating range; therefore, it is questionable whether any more analytic efforts should be applied. The problem, however, is of academic interest and appears to be an extremely difficult problem to analyze in its full glory. In a complete description of the problem, the coupling between boiling in the bayonet tubes and in the annuli, as well as the interaction between the steam/water mixture and the tube walls, must be taken into account. Additionally, the sodium temperature profile must be accounted for and the system pressure variation in the tubes and in the external system must be considered. The problem then becomes so difficult that a solution is probably impossible. However, a useful case to analyze would be the case of completely insulated bayonet tube walls, which, in a way, uncouples the water in the bayonet tubes from the steam/water in the annuli. Another limiting case would be an extension of the analysis that was performed here to include all seven tubes with more realistic boundary conditions.

ACKNOWLEDGMENTS

The principal technical contribution to the work in this report, within General Electric Company, was provided by the following individuals:

Project Engineer (ESADA Program) ..... F. E. Tippets

Task Leader (ESADA Program) ..... J. M. Roberts

Facilities and Test Support ..... J. M. Scott
J. J. Damon
G. J. Rittenmyer

Instrument Support ..... D. A. Greene
W. H. Hayward
N. R. McBurney

Data Reduction and Analysis ..... A. Hunsbedt
D. E. Naaf

The conscientious efforts of D. M. Miller, who did most of the tedious work involved in reducing the data and who prepared the figures and tables, and Sharon Snave, who typed the report, are gratefully acknowledged.

REFERENCES

1. Cho, S. M., Auge, L. J., Fenton, R. E., and Gardner, K. A., *Performance Changes of a Sodium-Heated Steam Generator*, ASME Paper 71-HT-15, August 1971.

2. Armijo, J. S., and Scott, J. M., *Sodium Heated Steam Generator Model Tests at the SGTR–Volume 1, Test Rig Operating Experience and Cleaning, Disassembly, and Inspection of the Steam Generator Test Model*, July 1972 (GEAP-10580).

3. Rogers, J. T., et al., *Heat Transfer in Rod Bundles*, presented at the annual meeting of the ASME, New York, December 3, 1968.

4. Borishanskii, V. M., Gotovskiim, M. E., and Firsova, E. V., "Heat Transfer to Liquid Metals in Longitudinally Wetted Bundles of Rods," *Atomnaya Energiya, 27*, pp. 549-552, December, 1969.

5. Seban, R. A., and Shimazaki, T., "Heat Transfer to a Fluid in a Smooth Pipe with Walls at Constant Temperature," *Trans, ASME*, **73**, Series C, p. 803, 1951.

6. Rickard, C. L., Dwyer, O. E., and Dropkin, D., *Heat Transfer Rates to Cross-Flowing Mercury in a Staggered Tube Bank–II*, ASME 57-HTII.

7. Gunter, A. Y., and Shaw, W. A., *A General Correlation of Friction Factor for Various Types of Surfaces in Cross Flow*, ASME Trans., 1945.

8. Roberts, J. M., *Task VI Final Report, Volume 1, Steam Generator Development, Steam Generator Design Analysis, and Model Tests*, January 1971 (NEDC-13689).

9. Dittus, F. W., and Boelter, L. M. H., "Heat Transfer in Automobile Radiators of the Tubular Type," *Univ. of Calif. Press,* **2**, No. 13, p. 443, 1930.

10. Moody, L. F., *Friction Factor for Pipe Flow*, Trans. ASME, 1944.

11. Seban, R. A., and Hunsbedt, A., *Friction and Heat Transfer in the Swirl Flow of Water in an Annulus*, submitted for consideration of publication in Int. H. of Heat Mass Transfer, January 1972.

12. Jens, W. H., and Lottes, P. A., *Analysis and Heat Transfer Burnout, Pressure Drop, and Density Data for High Pressure Water*, May 1, 1951 (ANL-4627).

13. Chen, J. C., *Correlation for Boiling Heat Transfer to Saturated Fluids in Convective Flow*, ASME Paper 63-HT-34.

14. Peterson, J. R., Converse, G. L., and Gutstein, M. U., *An Experimental Study of Pressure Loss and Phase Distribution for Air-Water Flow in a Tube Containing Swirl Generators*, presented at the Fifth International Energy Convention Engineering Conference, Las Vegas, Nevada, September 21-25, 1970.

15. Martinelli, R. C., and Nelson, D. B., *Prediction of Pressure Drop during Forced Circulation Boiling of Water*, ASME Trans., August 1948, 695-700.

16. Heineman, J. B., *An Experimental Investigation of Heat Transfer to Superheated Steam in Round and Rectangular Channels*, 1960 (ANL-6213).

17. Ito, H., "Friction Factors for Turbulent Flow in Curved Pipes," *Journal of Basic Engineering*, ASME, June 1959, pp. 133-134.

18. Seban, R. A., and McLaughlin, E. F., "Heat Transfer in Tube Coils with Laminar and Turbulent Flow," *Int. J. of Heat Mass Transfer,* **6**, pp. 387-395.

19. Janssen, E., and Kervinen, J., *Burnout Conditions for Single Rod in Annular Geometry, Water at 600 to 1400 psia*, February 1963 (GEAP-3899).

20. "Nonuniform Heat Generation Experimental Program—Final Report," *Babcock and Wilcox*, April 1967 (BAW-3238-13).

21. Tippets, F. E., "Analysis of the Critical Heat Flux Condition in High-Pressure Boiling Water Flows," *Trans. ASME J. of Heat Transfer*, 1964.

22. Tippets, F. E., *Proposed Critical Heat Flux Design Limits for Boiling Water Reactors*, February 1964 (APED-4551, Class II).

23. Hench, J. E., *Forced-Flow Transition Boiling Experiments in a Two-Rod Test Section at High Pressures*, ASME Paper, 64-WA/HT-44.

24. Hench, J. E., *Transition and Film Boiling Data at 600, 1000, and 1400 psia in Forced Convection Heat Transfer to Water*, 1964 (GEAP-4492/EURAEC 1983).

25. Quinn, E. P., *Single Rod, Forced Flow, Transition Boiling Heat Transfer from Smooth and Finned Surfaces*, 1965 (GEAP-4786).

26. Kunsemiller, D. F., *Multirod, Forced Flow, Transition, and Film Boiling Measurements*, 1965 (GEAP-5073).

27. Quinn, E. P., and Swan, C. L., *Visual Observations of Fluid Behavior in High-Pressure Transition Boiling Flows*, 1964 (GEAP-4636/EURAEC 1258).

28. Cumo, M., Farello, G. E., and Ferrari, G., "Notes on Droplet Heat Transfer," *Chemical Engineering Progress Symposium Series No. 92,* **65**.

29. Brevi, R., et al., "Measurement of the Effect of Twisted Tapes on the Forced-Convection Heat Transfer and Burnout in Heat Exchangers," *Nuclear Science and Engineering,* **46**, pp. 131-139, 1971.

30. Carver, J. R., Kakarala, C. R., Slotnik, J. S., *Heat Transfer in Coiled Tubes with Two-Phase Flow*, Babcock and Wilcox Research Report 4438, July 1964.

31. Quinn, E. P., *Physical Model of Heat Transfer beyond the Critical Heat Flux*, 1966 (GEAP-5093/EURAEC 1603).

32. *Standards of Tubular Exchanger Manufacturers Association*, Fifth Edition, 1968.

33. Dawson, B., *Performance Calculations on the ESADA Steam Generator Model*, 0-59-1163, Foster Wheeler Corporation, April 1, 1969.

34. Wilson, E. E., *A Basis for Rational Design of Heat Transfer Apparatus*, ASME Paper 1477, June 1915.

35. Tippets, F. E., *Critical Heat Flux Design Limit for Bayonet-Tube Steam Generator at 1600 psi*, unpublished work at GE-BRD, completed April 28, 1969.

36. Encke, R., *Appendix A, Orifice Calibrations for the ESADA Steam Generator Model*, 0-59-1163, Foster Wheeler Corporation, May 6, 1969.

37. Peterson, J. R., *High Performance 'Once-Through' Boiling of Potassium in Single Tubes at Vapor Temperatures from 1500°F to 1750°F*, NASA Report R66 SD 3020, 1966.

38. Dawson, B., *Performance Calculations on the ESADA Superheater Model*, Foster Wheeler Corporation, July 11, 1969.

39. Quandt, E. R., "Analysis and Measurement of Flow Oscillations," 1961, Chemical Engineering Progress Symposium Series, **57**, No. 32.

40. Meyer, J. E., and Rose, R. P., "Application of a Momentum Integral Model to the Study of Parallel Channel Boiling Flow Oscillations," *Journal of Heat Transfer, Trans. ASME,* **85**, Series C, 1963.

41. Neal, L. G., and Zivi, S. M., *Hydrodynamic Stability of Natural Circulation Boiling Systems*, TRW Systems, June 30, 1965 STL-372-14(1).

42. Golden, G. H., Tokar, V. T., and Miller, D., "Thermocouple Properties of Sodium-Recommended Values," *Reactor and Fuel Processing Technology,* **11**, No. 1, Winter, 1967-68.

43. *Thermodynamic and Transport Properties of Steam*, ASME Steam Tables, 1967.

44. Ozisik, M. N., "Boundary Value Problems of Heat Conduction," *International Textbook Company*, 1968.

APPENDIX A
DATA REDUCTION CODES

A-1 SUMMARY DESCRIPTION OF EVAP CODE

One aspect of the steam generator testing in the Steam Generator Test Rig (SGTR) is to evaluate the steady-state thermal performance at different power levels of the evaporator test section. The EVAP computer code is a tool to be used in this evaluation. The main idea is to make a complete analysis corresponding to a particular operating condition using measured inlet conditions and compare the results to the corresponding outlet and axial temperature distribution data. After adjusting constants and factors in the correlations used in the analysis and the analytic results match the corresponding measured data, a lot more detailed information than could be obtained by direct measurement becomes available. The code can also be used to study in depth the effect a particular parameter has on the operation of the evaporator test section.

The EVAP code solves the energy equation in a plane for a small axial portion or cut of the evaporator at a time in the steady-state. The solution is accomplished by finite difference techniques for a number of axial sequential planes along the evaporator starting at the top.

The EVAP code can, at the present time, handle steam with exit qualities in the range of approximately 50 to 100%. However, the code can be extended to handle superheated steam. With this modification, the analytic portion of the EVAP code could become a useful tool in designing a once-through bayonet tube steam generator.

Analytic Approach

There are three different geometries and corresponding heat transfer problems to be considered along the evaporator. In the cover gas region (the space between the sodium level and the tube-sheets), the main heat transfer occurring is between the steam/water in the annuli to the subcooled water in the bayonet tubes (Figures 4-6 and 4-7). However, some heat is transferred from the hot cover gas by convection and there is some radiation from the vessel wall and the sodium surface to the heater tubes.

In the calming region (the space between the calming plate and the sodium surface), heat is transferred from the steam/water to the subcooled water in the bayonet tubes. Approximately 5% of the total heat transfer from sodium through the heater tubes is transferred in the calming region. This heat transfer is assumed to be by natural convection.

In the long section between the calming plate and the lower end of the bayonet tubes, the geometry is fairly regular. This section is divided into a number of axial sections referred to as shroud regions. The length of each region can be varied in the analysis, but was normally about 20 in.; this resulted in about 20 axial nodes. In the shroud regions, heat is transferred by forced convection from the sodium to the steam/water in the annuli. Also, there is heat transfer from the steam/water to the subcooled water in the bayonet tubes.

Each of the regions mentioned above is treated as a separate heat transfer problem. Detailed description of the heat transfer models, heat transfer and pressure drop correlations, and solutions used in the different regions will not be given here; however, the nodal model used for the shroud regions where most of the heat is transferred is shown in Figure A-1. The model consists of 22 nodes, of which 14 are on the steam-side and the balance on the sodium-side. The nodal description of the sodium-side is somewhat arbitrary but is thought to represent the physical mechanisms involved, excluding the presence of the support plates and springs which are accounted for by a higher sodium-side conductance. The sodium-side flow distribution inside the flow shroud was based on pressure drop considerations and on a cross-flow model at the top of the unit arrived at from sodium temperature measurements. The complete solution is obtained by solving each problem separately in sequential order, starting at the top of the evaporator.

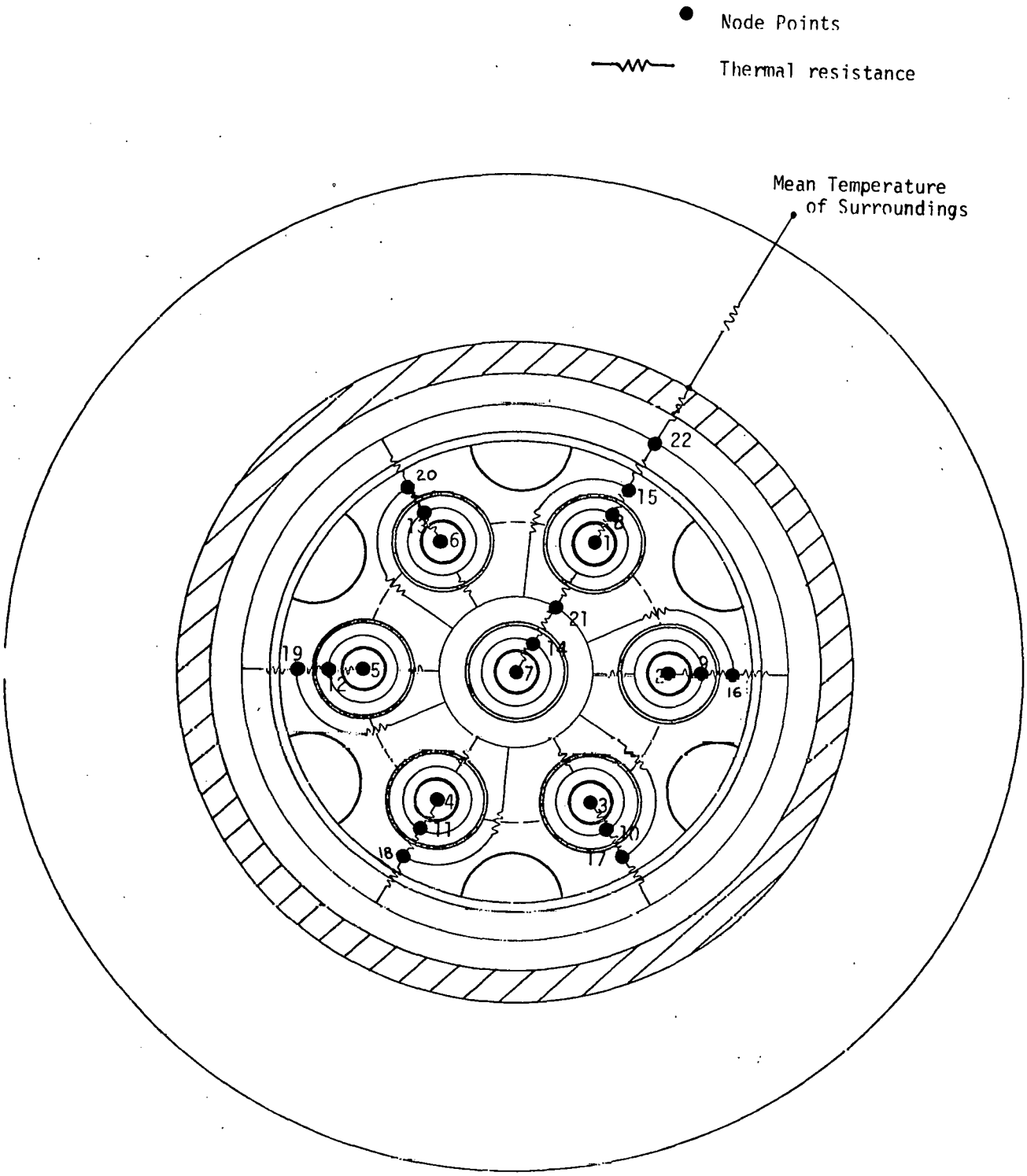

Figure A-1. Cross-Section of Evaporator Test Section Showing Basic Nodal Structure Used in the EVAP Code

To start the solution, boundary conditions must be specified for the subcooled water entering the bayonet tubes and the steam/water exiting the annuli. Since the steam/water exit condition is an independent variable in this analysis, an initial guess is made by performing a heat balance using measured loop temperatures, flow rates, etc. The condition of the subcooled water entering the bayonet tubes is set equal to the corresponding measured conditions and is held fixed throughout the calculations. Also, the sodium inlet temperature, sodium flow rate, measured recirculation flow rate, and individual bayonet flow rates are held fixed.

The solution proceeds downward through each region using the outlet conditions from the previous node or region as inlet or boundary conditions for the next node. At the lower end of the bayonet tube where the flow reverses, the enthalpy and pressure of the subcooled water in the bayonet tube must equal the enthalpy and pressure of the subcooled water in the annulus for all seven tubes. If this criterion is not met, the assumed steam/water outlet condition is changed using the discrepancies found at the lower end of the bayonet tubes as a basis for the correction. The process is then repeated until convergence is achieved. Normally, two to four iterations are necessary for satisfactory convergence.

Once a solution has been obtained that matches sodium-side measurements, detailed circumferential and axial sodium temperature distributions are available along with the steam-side enthalpy, temperature, and pressure distribution in each tube. Additionally, the variations of the individual heat transfer conductances, as well as the local overall heat transfer coefficients and heat fluxes, are given.

The heat transfer and pressure drop correlations were programmed on the computer and evaluated for each node. The sodium properties using the recommendation of Reference 42, and the steam properties from the ASME steam tables,[43] were also programmed on the computer.

A-2 SUMMARY DESCRIPTION OF SUPER CODE

The purpose and the basic functional operation of the SUPER code developed for the superheater model are the same as the EVAP code for the evaporator model. The geometry is more complex and is basically different from the evaporator; therefore, a slightly different approach has to be used.

The SUPER code solves the energy equation in a "coil plane" for a small axial portion of the superheater at a time in the steady-state. The solution is accomplished by finite difference techniques for a number of axial sequential coil planes along the superheater starting at the top. The SUPER code can handle steam with inlet moisture contents in the range of approximately 0 to 1%. It is also possible to extend the analysis so that then it could handle once-through operation.

Analytic Approach

There are four different geometries and corresponding heat transfer problems to be considered along the superheater. In the cover gas region (the space between the sodium level and the steam inlet/outlet nozzles), the heat transfer is small but is included for completeness. However, some heat is transferred from the hot cover gas by free convection and there is some radiation from the vessel wall and the sodium surface, especially to the downcomer steam tubes.

In the inlet region (the annular space between the coil banks and the sodium surface), heat is transferred to the steam mainly in the downcomers. Approximately 10% of total heat transfer from the sodium to the steam tubes is transferred in the inlet region. This heat transfer is assumed to be by natural convection since the flow velocity is low in the upper portion of the superheater.

In the coil region, the geometry is fairly irregular. This region is divided into a number of axial planes called "coil planes." Each coil plane has a thickness corresponding to the pitch between the coils. In the coil planes, heat is transferred by forced convection cross-flow from the sodium to the steam in the coils and by forced convection parallel flow to the downcomers. The heat transfer problem in the bottom loop region is similar to the one in the inlet region.

Each of the regions mentioneo above is treated as a separate heat transfer problem. Detailed description of the heat transfer models and solutions used in different regions will not be given here; however, the nodal model used in the "coil plane" is shown in Figure A-2. The kinds of nodes existing in this plane showing flow directions, etc., are shown in Figure A-3. The division of the shell-side into nine segments is somewhat arbitrary, but the presence of the tube supports form natural boundaries and nine thermocouples were located near the lower end of the coil bank to check the analysis (Figure 4-14). The complete solution is obtained by solving each problem separately in sequential order starting at the top of the superheater.

The sodium flow in each segment was first based on pressure drop considerations alone; however, early measurements revealed poor agreement between the calculated circumferential sodium temperature distribution near the lower end of the coil region and measurements. The sodium flow distribution was therefore adjusted by trial and error until a standard flow distribution was arrived at that resulted in close agreement between measurements and analysis in subsequent runs.

To start the solution, boundary conditions must be specified for the saturated steam entering and the steam exiting the superheater. The conditions of the steam entering and exiting the steam tubes are set equal to the corresponding measured conditions and the inlet steam conditions are held fixed throughout the calculations. Also, the sodium inlet temperature, measured steam flow rate, and sodium flow rate are held fixed.

The solution proceeds downward through each region using the outlet conditions from the previous node or region as inlet or boundary conditions for the next node. At the lower end of the bottom loop where the flow reverses, the enthalpy and pressure of the steam in the downcomer tube must equal the enthalpy and pressure of the steam in the upcomer tube for both active steam tubes. This is the main convergence criterion. In case the criterion is not met within certain limits, a second iteration with modified steam exit conditions is made and the process continued until convergence occurs. The measured outlet conditions of the steam and sodium as well as the measured axial and circumferential temperature profile are then checked to see if they match the calculations. If they do not check within certain limits, adjustments must be made to heat transfer correlations, pressure drop calculations, etc., and the program run again. When the analytical solution matches the measured results, detailed information is available on temperature distributions, pressure distributions, heat fluxes, surface and overall conductances, etc.

The heat transfer correlations, steam properties, and sodium properties were programmed the same way as for the evaporator.

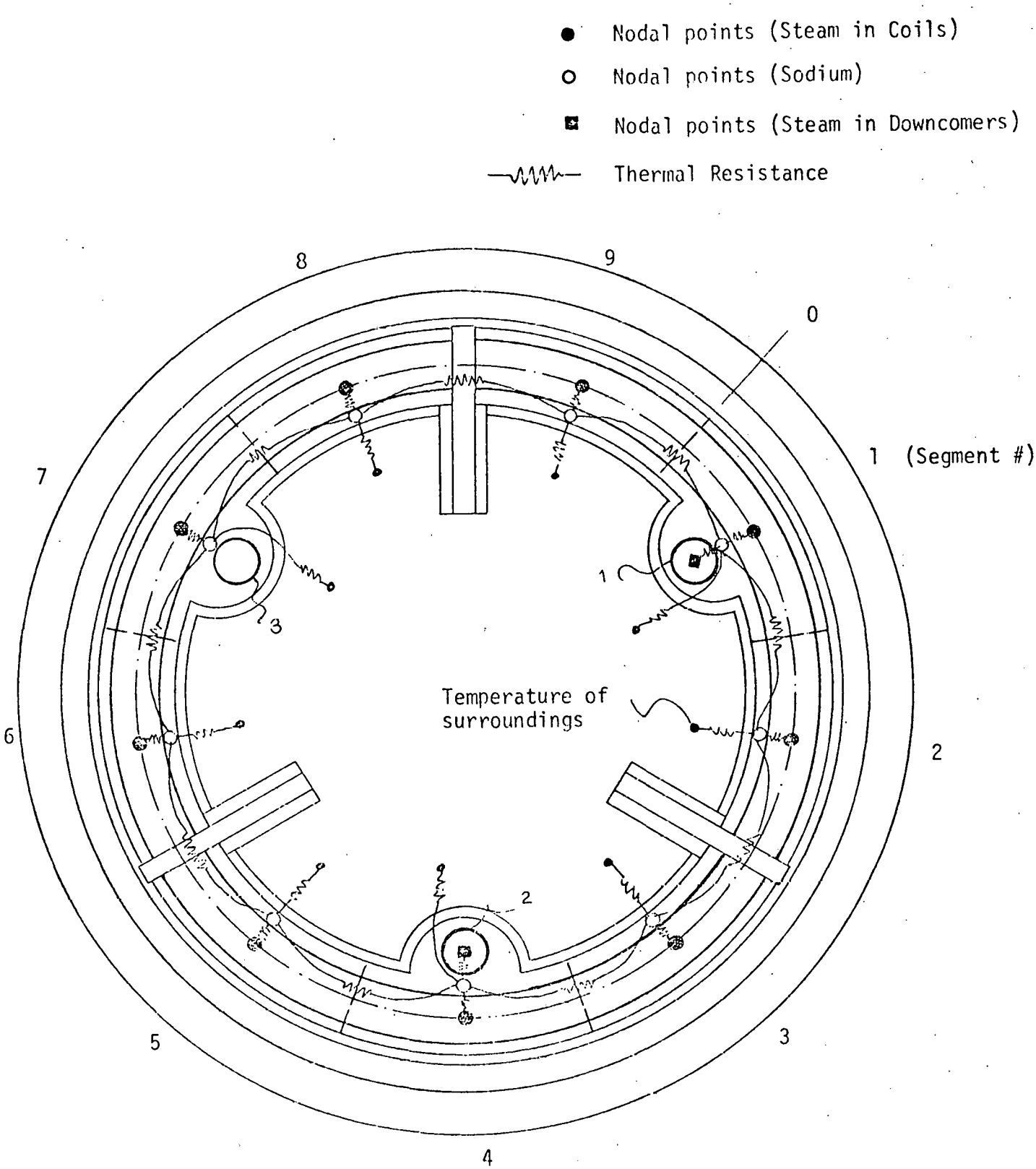

Figure A-2. Cross-Section of Superheater Test Section Showing Basic Nodal Structure Used in the SUPER Code

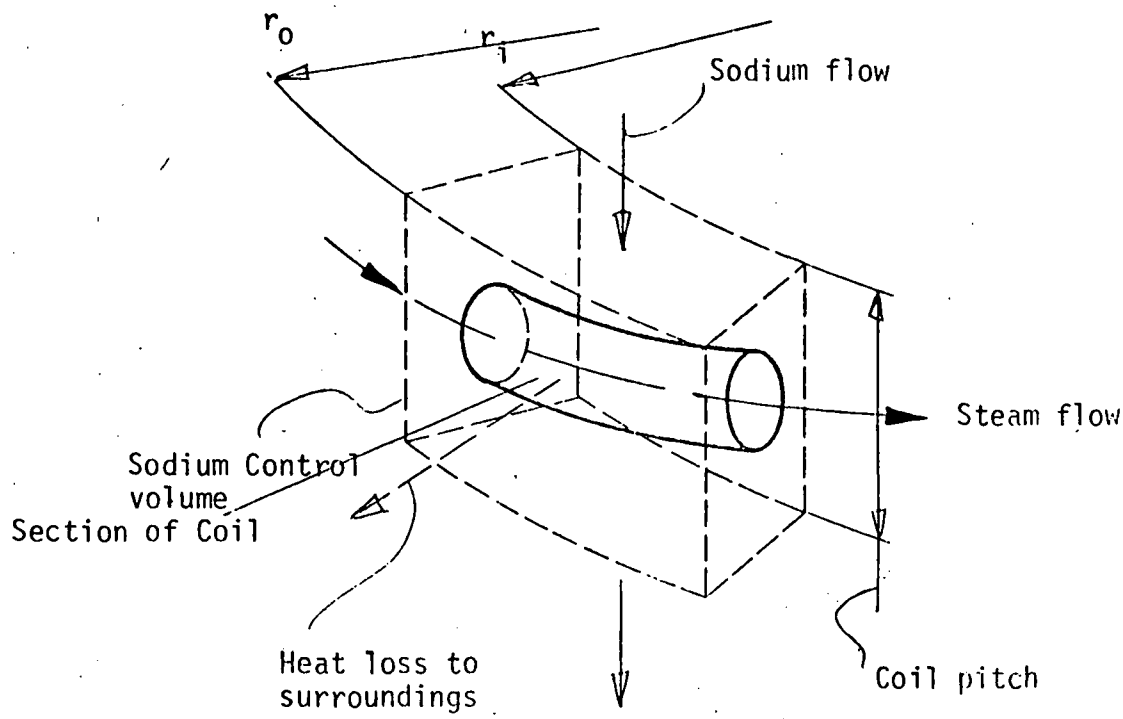

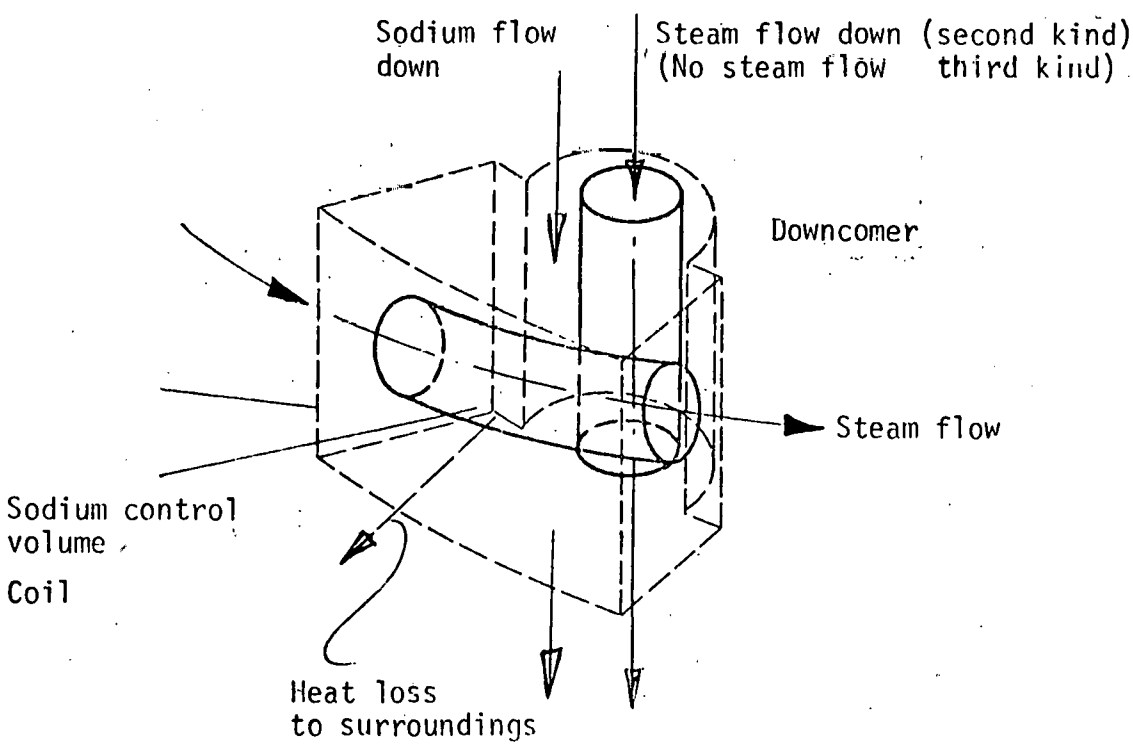

Figure A-3. Diagram of the Three Different Kinds of Nodes Used in the SUPER Code

APPENDIX B
EXPERIMENTAL DATA

APPENDIX B-1
EVAPORATOR PERFORMANCE DATA

Table B-1
OVERALL HEAT TRANSFER COEFFICIENTS

Test Date	Time	Predicted $\overline{U}$	Experimental $\overline{U}$ $\overline{U}_{EVAP}$	$\overline{U}_{LMTD}$	Sodium Inlet Temperature °F	Thermal Power kW	Exit Steam Quality %	Steam Drum Pressure psia
3-29-71	1740	541	756	707	835	740	15	1606
3-29-71	2010	583	923	937	856	1516	34	1635
3-29-71	2125	579	928	922	867	1509	46	1594
3-29-71	2155	579	926	928	864	1504	43	1577
3-30-71	0530	574	920	932	864	1406	30	1565
3-30-71	1133	572	922	935	893	1503	35	1623
5-20-71	1647	587	947	957	832	1472	35	1587
5-20-71	1848	589	941	911	830	1497	36	1572
5-21-71	1334	577	938	926	855	1393	31	1603
5-21-71	1349	576	933	922	859	1409	37	1579
5-21-71	1419	577	923	914	951	1392	47	1555
5-21-71	1434	577	916	899	853	1380	48	1591
5-28-71	1131	571	917	913	866	1366	30	1578
5-28-71	1201	571	914	903	865	1338	39	1589
5-28-71	1231	571	907	900	863	1336	49	1572
5-28-71	1301	570	904	869	865	1308	51	1607
8-05-71	1022	584	900	871	847	1400	64	1619
8-05-71	1340	572	875	834	892	1388	91	1659
8-05-71	1519	577	894	875	869	1344	87	1688
8-06-71	1910	583	866	833	826	1383	77	1667
8-06-71	1030	592	909	897	804	1319	86	1657
8-06-71	1109	602	897	892	785	1336	75	1661
8-06-71	1228	605	909	906	741	1381	74	1672
8-06-71	1336	605	908	890	755	1076	86	1637
8-06-71	1432	605	922	908	762	1188	87	1652
8-06-71	1508	605	937	910	779	1237	81	1610
8-06-71	1546	605	898	897	790	1402	84	1653
8-09-71	0851	588	907	877	836	1480	85	1652

Table B-1 (Continued)

Test Date	Time	Predicted $\overline{U}$	Experimental $\overline{U}$ $\overline{U}_{EVAP}$	$\overline{U}_{LMTD}$	Sodium Inlet Temperature °F	Thermal Power kW	Exit Steam Quality %	Steam Drum Pressure psia
8-09-71	0927	593	883	863	825	1484	83	1666
8-09-71	1020	595	885	864	813	1512	92	1633
8-09-71	1057	598	917	890	803	1481	88	1652
8-09-71	1338	581	856	856	839	1449	82	1617
8-09-71	1415	581	866	866	849	1373	78	1666
8-09-71	1451	580	853	852	857	1420	84	1668
8-09-71	1526	576	877	855	868	1437	83	1636
8-09-71	1602	578	889	874	866	1428	82	1665
8-10-71	0827	559	858	845	912	1444	77	1674
8-10-71	0901	562	863	850	900	1277	79	1649
8-10-71	0935	565	864	853	890	1293	80	1609
8-10-71	1008	567	870	857	883	1321	75	1649
8-10-71	1042	567	870	851	870	1316	81	1647
8-10-71	1116	567	869	855	859	1267	82	1649
8-10-71	1149	570	869	852	836	1212	89	1665
8-10-71	1313	573	876	867	845	1130	85	1639
8-10-71	1527	577	881	868	822	1242	83	1658
8-10-71	1601	582	891	877	813	1192	80	1632
8-13-71	1009	547	833	829	093	1226	83	1588
8-13-71	1042	548	833	813	885	1047	80	1572
8-13-71	1115	553	839	817	878	1000	73	1643
8-13-71	1206	557	839	813	864	1037	75	1639
8-13-71	1346	559	838	827	856	1051	72	1649
8-13-71	1420	559	842	820	840	1055	72	1670
8-13-71	1510	561	851	833	834	893	77	1603
8-13-71	1635	572	871	854	823	993	79	1664
8-17-71	1328	572	866	841	815	1102	75	1627
8-17-71	1401	575	867	839	801	1086	79	1566

Table B-1 (Continued)

Test Date	Time	Predicted $\overline{U}$	Experimental $\overline{U}$ $\overline{U}_{EVAP}$	$\overline{U}_{LMTD}$	Sodium Inlet Temperature °F	Thermal Power kW	Exit Steam Quality %	Steam Drum Pressure psia
8-17-71	1435	575	869	840	806	1073	77	1580
8-17-71	1509	574	863	849	786	1098	81	1517
8-17-71	1543	580	880	850	789	1007	78	1590
8-18-71	0903	569	872	850	898	1075	79	1602
8-18-71	0937	571	880	862	885	1455	87	1618
8-18-71	1010	574	882	860	874	1418	71	1614
8-18-71	1151	581	886	864	797	1433	81	1604
8-18-71	1225	591	909	888	797	1136	75	1625
8-18-71	1315	596	914	888	774	1296	78	1580
8-18-71	1349	596	897	896	783	1250	88	1606
8-18-71	1423	595	917	898	789	1286	79	1654
8-18-71	1530	578	892	865	842	1282	81	1612
8-19-71	0856	587	893	872	782	1350	84	1597
8-19-71	0946	584	890	859	781	1141	81	1620
8-19-71	1020	584	891	876	778	1081	76	1583
8-19-71	1128	590	886	865	749	1081	77	1534
8-20-71	1028	579	891	854	854	1008	76	1660
10-13-71	1234	576	902	873	862	1413	84	1635
10-13-71	1328	574	873	834	868	1493	98	1630
10-13-71	1432	568	885	843	880	1471	93	1615
10-13-71	1532	578	896	874	852	1452	97	1620
10-14-71	0917	576	892	871	850	1325	89	1630
10-14-71	1002	580	899	884	840	1357	91	1630
10-14-71	1026	583	904	901	830	1368	83	1615
10-14-71	1101	590	913	912	825	1449	87	1630
10-14-71	1147	592	921	924	817	1450	87	1625
10-14-71	1306	591	918	917	828	1488	85	1627
10-14-71	1345	589	916	899	833	1478	92	1642

Table B-1 (Continued)

Test Date	Time	Predicted $\overline{U}$	Experimental $\overline{U}$ $\overline{U}_{EVAP}$	Experimental $\overline{U}$ $\overline{U}_{LMTD}$	Sodium Inlet Temperature °F	Thermal Power kW	Exit Steam Quality %	Steam Drum Pressure psia
10-14-71	1424	584	911	894	859	1549	89	1637
10-14-71	1504	583	895	870	856	1462	97	1612
10-14-71	1604	589	915	898	836	1494	98	1640
10-15-71	0843	583	904	891	848	1467	94	1638
10-15-71	0922	584	909	902	850	1481	94	1640
10-15-71	1002	583	905	905	859	1535	99	1632
10-15-71	1042	584	912	896	868	1594	85	1645
10-15-71	1102	580	903	889	878	1577	92	1648
10-15-71	1142	578	903	892	885	1572	86	1649
10-19-71	0942	576	890	868	857	1382	98	1599
10-19-71	1018	579	895	876	836	1297	80	1647
10-19-71	1053	579	895	870	842	1338	91	1632
10-19-71	1129	578	899	889	851	1378	75	1640
10-19-71	1317	583	896	885	828	1351	75	1600
10-19-71	1353	586	895	872	803	1229	92	1654
10-19-71	1429	586	903	878	828	1585	90	1648
10-19-71	1506	586	907	893	819	1328	79	1660
10-19-71	1542	586	905	885	815	1310	88	1633
10-20-71	0857	577	897	875	864	1418	96	1643
10-20-71	0936	574	898	892	874	1422	75	1630
10-20-71	1015	568	879	869	883	1373	77	1587
10-20-71	1055	564	884	877	894	1311	86	1640
10-20-71	1135	559	870	853	912	1280	86	1666
10-20-71	1154	561	875	861	907	1314	91	1649
10-20-71	1314	563	878	869	910	1361	96	1631
10-20-71	1353	563	878	863	906	1359	86	1621
10-20-71	1433	566	912	883	895	1375	77	1630
10-20-71	1512	571	889	871	891	1432	91	1650
10-20-71	1552	576	901	887	875	1468	85	1652
10-21-71	0913	577	891	853	857	1380	93	1651
10-21-71	1032	578	877	874	855	1406	96	1636
10-21-71	1152	584	901	887	856	1522	90	1644

Table B-2
SUMMARY OF EVAPORATOR THERMAL PERFORMANCE DATA FOR P/D = 6

Test Date Time	Na Inlet Temp. (°F)	Na Outlet Temp. (°F)	Na Flow (lb/hr)	SODIUM TEMPERATURES Elev.: 508" Temp., (°F) edge*	cent.	Elev.: 492" Temp., (°F) cent.	edge	Elev.: 437" Temp., (°F) cent.	edge	Elev.: 377" Temp., (°F) cent.	edge	Elev.: 257" Temp., (°F) cent.	edge	Elev.: 137" Temp., (°F) cent.	edge	Evap. Inlet H_2O Temp. (°F)	Evap. Recirc. Flow, (lb/hr)	Steam Drum Press. (psia)
3-29-71 (1740)	835	601	35000	699.3	634.2	766.4	805.0	670.0	685.8	628.1	630.0	605.9	606.9	599.4	599.7	575	20596	1605
3-29-71 (2010)	856	613	69100	721.6	638.2	836.8	847.0	732.2	734.0	670.8	673.6	629.3	631.7	617.3	616.5	564	20976	1635
3-29-71 (2125)	867	610	65100	707.5	648.0	835.1	846.9	777.7	732.4	664.7	669.2	623.6	625.7	612.6	612.1	549	15763	1594
3-29-71 (2155)	864	608	65100	725.8	638.9	844.3	845.2	716.6	729.3	662.4	664.8	621.9	624.0	611.1	610.9	549	16523	1577
3-30-71 (0530)	864	605	60300	716.4	648.0	834.5	842.9	711.0	723.3	656.3	661.3	618.6	620.5	607.3	606.6	558	21020	1565
3-30-71 (1133)	893	610	59000	741.0	652.4	856.6	871.2	726.7	738.3	665.3	670.2	624.0	627.2	612.5	611.5	564	20663	1623
5-20-71 (1647)	832	608	73400	714.3	628.6	815.7	815.8	703.8	725.5	659.0	663.9	621.1	623.2	610.8	608.9	551	19109	1587
5-20-71 (1848)	830	608	75200	715.3	641.1	789.5	807.3	708.6	727.1	661.1	665.4	621.1	623.7	610.6	609.4	550	19086	1572
5-21-71 (1334)	855	606	62800	716.9	642.5	813.1	831.1	708.3	727.5	655.1	661.2	615.0	618.7	605.9	604.7	555	19819	1603
5-21-71 (1349)	859	606	62100	700.7	639.9	815.5	831.8	708.6	729.7	654.5	658.6	615.9	618.4	607.4	606.3	546	17064	1579
5-21-71 (1419)	951	606	63100	715.5	631.8	806.6	829.6	703.7	724.0	651.0	656.8	613.4	616.0	606.0	604.8	521	12915	1555
5-21-71 (1434)	853	608	62800	704.4	623.7	811.8	822.4	708.6	728.2	653.9	657.6	616.4	618.8	608.7	608.0	505	9249	1591
5-28-71 (1131)	866	604	58100	710.4	639.0	815.0	844.5	703.2	726.6	651.3	656.3	615.0	617.0	605.9	604.7	551	19775	1578
5-28-71 (1201)	865	606	57800	696.2	630.6	823.0	849.6	704.2	726.2	652.2	657.4	616.0	617.8	608.1	607.2	535	14832	1589
5-28-71 (1231)	863	607	58000	704.5	622.2	827.1	840.1	701.9	727.6	650.2	654.2	614.3	616.2	607.2	606.3	521	12078	1572
5-28-71 (1301)	865	609	56800	713.8	627.9	817.5	846.8	703.7	727.4	652.5	656.8	616.9	618.9	610.4	609.6	502	9907	1607
8-05-71 (1022)	847	615	70440	694.1	635.5	806.6	821.8	718.8	738.6	666.4	670.6	625.9	628.6	615.6	614.9	487	8530	1619
8-05-71 (1340)	892	615	58731	711.0	656.1	811.7	857.6	712.3	756.6	659.3	664.9	621.5	624.1	615.0	612.8	504	8505	1659
8-05-71 (1519)	869	617	63559	726.2	649.5	820.1	841.2	724.2	749.1	667.4	672.6	626.7	629.0	617.6	617.4	502	8660	1600
8-06-71 (0910)	826	617	69279	709.1	642.2	787.8	810.1	711.6	728.8	633.1	667.5	626.0	628.6	617.5	615.7	484	8039	1667
8-06-71 (1030)	804	617	78804	715.2	640.9	780.2	793.6	711.0	726.5	666.8	669.4	628.6	630.9	617.2	616.4	490	7372	1657
8-06-71 (1109)	785	621	91053	713.7	657.1	768.5	776.3	712.5	725.8	671.0	674.1	632.4	635.5	620.4	619.2	504	7403	1661
8-06-71 (1228)	741	618	94962	679.0	625.3	722.8	733.2	683.1	694.2	655.9	657.8	628.5	630.1	618.7	519.0	528	6651	1672
8-06-71 (1336)	755	618	93854	688.3	629.8	738.1	747.0	691.5	703.2	659.5	663.4	628.3	630.1	617.6	616.7	490	6803	1637
8-06-71 (1432)	762	620	93700	699.5	623.2	748.5	753.4	698.1	708.9	666.4	666.6	630.4	633.1	619.3	618.3	490	6803	1652
8-06-71 (1508)	779	618	94061	707.5	622.1	761.3	770.9	705.7	719.2	667.5	670.8	630.6	633.5	617.9	616.8	480	7716	1610
8-06-71 (1546)	790	621	94632	705.7	628.4	769.7	780.6	712.4	726.2	672.8	676.7	634.7	637.8	622.7	621.6	497	8182	1653
8-09-71 (0851)	836	618	74485	717.0	661.0	805.6	816.3	716.3	736.3	668.7	673.0	628.2	631.0	619.5	618.4	486	8583	1652
8-09-71 (0927)	825	620	80251	703.4	654.2	791.3	809.4	716.3	736.1	671.1	677.1	631.4	643.3	619.4	618.4	497	8837	1666
8-09-71 (1020)	813	619	82580	710.6	625.0	758.3	802.1	717.4	735.1	670.9	675.9	630.0	633.4	618.0	616.6	496	8757	1633
8-09-71 (1057)	803	619	85909	708.7	633.5	781.0	793.7	714.0	729.7	670.8	674.8	631.6	634.7	619.2	618.2	497	8612	1652
8-09-71 (1338)	839	613	66940	707.2	640.2	799.9	817.4	713.3	734.8	661.7	666.7	622.4	625.0	612.6	611.9	493	8407	1617
8-09-71 (1415)	849	617	67507	714.4	667.4	806.3	825.0	712.8	734.9	663.7	668.0	625.7	628.3	616.5	615.8	499	8400	1666
8-09-71 (1451)	857	618	66157	716.7	673.1	814.7	826.8	716.1	739.2	664.8	669.9	626.0	628.6	617.0	616.2	501	8297	1668
8-09-71 (1526)	868	616	61971	726.4	671.9	813.3	849.3	711.3	738.1	661.0	664.7	622.0	624.7	613.6	612.7	499	8367	1636
8-09-71 (1602)	866	617	63735	725.4	650.4	823.5	849.9	724.1	747.1	666.7	672.5	625.3	628.0	616.1	615.2	498	8499	1665
8-10-71 (0827)	912	613	47835	751.9	637.7	854.4	881.9	714.9	741.6	654.1	657.9	619.6	621.2	610.9	610.7	490	7622	1674

*"Edge" refers to average sodium temperature in edge flow channel (see Figure 5-3), "cent." has a similar meaning.

Table B-2 (Continued)

8-10-71 (0901)	900	611	49994	725.2	652.6	850.2	868.1	714.1	742.7	653.7	657.1	618.1	619.7	608.8	608.8	494	7587	1649
8-10-71 (0935)	890	610	52236	734.8	655.8	847.0	866.3	717.8	743.4	654.1	658.7	615.2	618.1	606.7	606.5	481	7370	1609
8-10-71 (1008)	883	611	54171	729.2	638.7	836.5	859.7	715.4	740.5	657.5	661.6	619.6	621.3	609.6	609.5	501	7731	1649
8-10-71 (1042)	870	612	54492	720.8	651.5	822.4	842.4	710.6	733.6	654.3	657.1	619.0	620.9	609.3	609.2	506	8224	1647
8-10-71 (1116)	859	612	54549	697.7	648.8	811.3	836.6	707.8	731.3	654.0	657.7	619.0	620.5	609.6	609.6	500	6998	1649
8-10-71 (1149)	835	614	56651	710.6	658.0	799.4	813.7	701.8	720.8	652.9	655.2	620.6	622.2	611.4	611.5	509	6788	1665
8-10-71 (1313)	845	615	59206	720.2	653.6	816.6	824.0	709.7	732.4	657.6	661.8	620.5	622.9	610.6	610.1	486	6573	1639
8-10-71 (1527)	822	616	63488	700.6	632.0	791.1	807.3	702.1	721.5	654.8	659.2	622.1	624.3	612.2	611.8	507	7248	1658
8-10-71 (1601)	813	616	67683	721.8	629.6	783.1	797.1	704.6	724.4	658.1	661.2	622.2	624.6	611.2	610.8	502	6637	1632
8-13-71 (1009)	903	603	39243	715.6	630.7	829.0	862.0	688.6	710.3	633.7	636.6	608.8	609.4	600.7	601.0	492	6105	1588
8-13-71 (1042)	885	605	39749	724.0	625.1	818.0	842.7	683.5	706.0	631.2	633.0	606.7	607.2	597.9	597.9	500	6125	1572
8-13-71 (1115)	873	607	43293	716.9	647.9	814.8	840.1	694.1	716.2	641.0	643.6	614.0	614.8	605.5	605.8	485	6019	1643
8-13-71 (1206)	864	609	46239	715.7	655.0	808.2	827.5	692.7	714.3	642.4	645.4	614.8	615.9	606.5	606.7	490	6998	1639
8-13-71 (1346)	856	610	48015	711.3	640.8	808.0	826.8	694.0	716.3	645.0	648.6	616.5	617.6	608.3	608.5	483	6396	1649
8-13-71 (1420)	840	610	47945	704.3	629.4	791.8	815.0	690.3	709.2	643.1	647.1	617.4	618.1	608.9	609.4	493	5695	1670
8-13-71 (1510)	834	612	49022	705.0	634.4	787.4	815.5	685.5	708.2	639.7	643.8	612.5	614.7	606.0	605.1	481	5918	1603
8-13-71 (1635)	823	608	58537	704.8	646.7	781.5	809.3	697.6	717.4	653.0	656.2	621.0	622.5	611.5	611.6	483	6377	1684
8-17-71 (1328)	815	614	59096	695.8	630.7	775.5	798.9	694.7	712.8	652.1	656.5	621.5	623.2	611.2	611.0	479	6409	1627
8-17-71 (1401)	801	608	60929	687.2	629.4	761.1	785.6	685.1	703.5	645.0	648.4	615.9	617.5	605.8	605.8	481	6381	1566
8-17-71 (1435)	806	608	60996	701.1	642.0	763.6	790.7	686.6	706.5	645.5	648.9	616.7	618.2	609.9	609.6	491	6369	1580
8-17-71 (1509)	786	602	60547	693.2	624.8	753.7	768.1	683.1	694.3	636.9	640.5	609.9	611.3	603.4	603.2	483	6289	1517
8-17-71 (1543)	789	608	65915	686.2	618.1	748.2	776.0	684.3	707.3	647.0	648.6	617.6	619.1	610.3	610.0	485	6617	1590
8-18-71 (0903)	898	611	56185	728.4	640.3	839.2	871.0	719.3	746.6	659.3	665.0	619.8	622.1	612.0	611.3	492	8445	1602
8-18-71 (0937)	885	613	57513	749.7	665.6	840.3	855.6	721.7	746.5	661.6	667.5	621.8	624.1	613.5	612.9	482	7915	1618
8-18-71 (1010)	874	612	60309	721.3	647.9	827.9	848.5	716.0	742.6	661.0	664.9	622.0	624.1	613.4	612.7	491	8595	1614
8-18-71 (1151)	797	613	67072	691.4	638.0	768.3	780.7	693.5	710.1	651.7	655.3	620.4	622.5	612.8	612.4	466	6387	1604
8-18-71 (1225)	797	616	77902	708.2	653.5	766.0	786.3	701.6	718.8	660.5	665.1	626.7	629.0	617.1	616.1	467	7288	1625
8-18-71 (1315)	774	612	83714	690.7	633.9	744.3	761.4	687.6	703.6	653.6	656.5	622.5	624.8	613.3	612.4	493	7537	1580
8-18-71 (1349)	783	615	83350	690.4	637.9	751.2	765.5	693.5	708.8	657.4	661.1	625.2	627.6	615.8	615.0	482	7672	1606
8-18-71 (1423)	789	619	81753	690.6	633.9	765.0	744.1	700.6	715.9	662.3	665.0	629.1	631.8	619.8	618.9	486	7460	1654
8-18-71 (1530)	842	613	64627	712.4	650.1	798.7	810.2	705.6	726.5	657.3	662.0	622.0	624.3	613.8	613.2	489	7798	1612
8-19-71 (0856)	782	614	73162	680.8	625.7	758.7	766.4	690.4	707.5	652.2	655.9	621.6	623.8	613.7	612.8	454	6245	1597
8-19-71 (0946)	781	614	70075	685.5	640.3	744.8	760.7	684.2	700.4	648.8	652.6	621.1	622.6	613.9	613.4	470	6267	1620
8-19-71 (1020)	778	611	70088	678.3	626.1	750.0	768.6	684.3	699.9	646.6	651.4	618.3	620.0	611.0	610.4	463	6153	1583
8-19-71 (1128)	749	605	76785	669.6	623.2	728.8	740.2	676.5	689.6	642.9	645.8	615.0	616.4	606.9	606.5	480	5342	1534
8-20-71 (1028)	854	616	65643	716.1	683.7	787.9	835.4	711.1	736.7	661.8	666.4	625.4	627.6	617.1	616.4	496	7822	1660

Table B-2 (Continued)
FOR P/D = 3

Test Date	Time	Na Inlet Temp. (°F)	Na Outlet Temp. (°F)	Na Flow (lb/hr)	SODIUM TEMPERATURES Elev.: 508" Temp., (°F) edge	cent.	Elev.: 492" Temp., (°F) cent.	edge	Elev.: 437" Temp., (°F) cent.	edge	Elev.: 377" Temp., (°F) cent.	edge	Elev.: 257" Temp., (°F) cent.	edge	Elev.: 137" Temp., (°F) cent.	edge	Evap. Inlet H_2O Temp. (°F)	Evap. Recirc. Flow, (lb/hr)	Steam Drum Press. (psia)
10-13-71	(1234)*	862	600	62305													470	7841	1635
10-13-71	(1328)	868	599	60327													475	7537	1630
10-13-71	(1432)	880	595	55402													480	8209	1615
10-13-71	(1532)	852	597	63800													470	7841	1620
10-14-71	(0917)	850	600	61866													470	7409	1630
10-14-71	(1002)	840	602	66263													465	7162	1630
10-14-71	(1026)	830	604	69536													465	7664	1615
10-14-71	(1101)	825	605	76156													468	7779	1630
10-14-71	(1147)	817	605	79102													463	7672	1625
10-14-71	(1306)	828	617	77091	733.9	645.4	800.1	813.5	716.8	736.3	670.6	675.7	629.6	632.2	618.6	617.7	468	7122	1627
10-14-71	(1345)	833	618	75303	710.7	657.5	802.5	815.4	718.4	737.5	670.8	674.6	630.9	633.2	619.7	618.8	477	7326	1642
10-14-71	(1424)	859	617	70374	727.7	660.0	820.6	835.8	723.7	747.6	671.5	677.9	629.2	631.6	618.5	617.7	482	7671	1637
10-14-71	(1504)	846	612	69037	724.6	643.6	798.7	327.3	713.4	733.4	664.1	669.2	625.1	627.5	615.3	614.6	497	8358	1612
10-14-71	(1604)	836	618	74872	733.2	646.2	805.3	314.2	716.7	739.2	669.5	674.4	629.8	632.6	619.0	618.3	469	7333	1640
10-15-71	(0843)	848	616	69521	738.1	677.1	816.0	329.2	717.6	738.9	667.7	671.5	627.5	630.0	617.5	616.9	474	7238	1638
10-15-71	(0922)	850	617	69838	717.7	752.7	803.6	333.9	719.2	741.6	667.9	671.0	628.3	630.4	617.9	617.1	469	7282	1640
10-15-71	(1002)	859	615	69512	737.9	637.9	819.0	336.5	720.5	743.9	669.4	672.2	627.8	630.2	617.2	616.5	482	7939	1632
10-15-71	(1042)	868	617	70027	751.3	666.1	830.4	345.0	727.6	753.2	672.5	676.0	629.4	632.0	618.5	617.6	475	7889	1645
10-15-71	(1102)	878	616	66584	729.5	654.7	833.7	356.7	727.3	753.9	672.2	677.3	628.8	631.5	618.4	617.7	476	7632	1648
10-15-71	(1142)	885	616	64513	749.9	653.9	839.0	360.8	728.4	753.5	671.3	677.2	627.9	630.6	617.8	617.3	473	7829	1649
10-19-71	(0942)	857	613	62323	734.3	652.6	810.3	336.2	710.0	733.8	660.6	664.6	622.5	625.3	614.1	613.2	452	6664	1599
10-19-71	(1018)	836	616	64847	737.9	667.8	801.8	310.8	709.4	733.7	661.9	664.3	625.6	628.0	617.4	616.7	480	5882	1647
10-19-71	(1053)	842	615	64728	722.4	634.5	799.2	317.7	708.2	727.9	661.0	664.3	624.3	626.9	616.1	615.4	473	6855	1632
10-19-71	(1129)	851	617	64403	735.2	665.8	815.5	330.0	714.9	738.6	664.1	666.9	625.8	628.1	617.1	616.2	474	6574	1640
10-19-71	(1317)	828	613	68949	722.0	636.1	797.3	313.3	706.7	727.3	660.6	664.4	649.6	625.6	614.0	613.3	482	6506	1600
10-19-71	(1353)	803	615	72093	701.7	630.1	770.1	784.2	699.5	717.2	659.7	661.9	626.6	628.4	617.8	617.2	501	6303	1654
10-19-71	(1429)	828	617	72199	713.2	675.9	787.6	301.8	705.7	725.6	662.5	665.3	627.2	629.5	617.9	617.2	481	6681	1648
10-19-71	(1506)	819	618	72590	719.0	656.5	790.8	303.2	710.9	728.0	665.3	668.5	628.5	630.9	619.2	618.4	478	6513	1660
10-19-71	(1542)	815	616	72230	707.7	641.8	782.0	796.6	704.3	724.5	661.4	665.3	626.0	628.7	617.1	616.2	482	6488	1633
10-20-71	(0857)	864	615	62947	728.2	638.9	814.2	835.4	716.3	740.7	664.0	668.4	625.2	627.7	616.8	615.9	477	7555	1643
10-20-71	(0936)	874	613	60094	753.8	665.6	834.9	851.9	720.4	744.5	663.4	666.0	623.3	625.5	615.1	614.4	478	6660	1630
10-20-71	(1015)	883	607	55486	749.2	651.6	834.2	861.3	712.1	737.4	654.8	657.7	617.0	618.9	610.0	609.4	483	6611	1587
10-20-71	(1055)	894	610	51568	721.9	657.5	836.3	863.9	711.8	734.9	655.8	659.1	620.1	621.8	613.6	613.2	488	6599	1640
10-20-71	(1135)	912	609	47875	745.9	652.0	844.7	861.4	710.2	736.5	652.2	656.6	619.7	620.7	612.8	612.6	487	6612	1666
10-20-71	(1154)	907	610	49620	746.5	647.1	839.4	875.1	712.5	736.7	654.1	659.0	620.1	621.8	613.6	613.1	494	7218	1649
10-20-71	(1314)	910	609	6929	752.1	653.2	843.6	879.7	713.2	743.1	654.9	657.5	618.9	620.5	612.5	611.9	479	6929	1631
10-20-71	(1353)	906	609	51146	745.4	644.9	835.8	867.6	711.5	739.7	653.2	657.3	619.1	619.6	611.6	611.2	475	6814	1621

* The data acquisition system was out of order for the following 9 runs and the listed data was recorded by hand.

Table B-2 (Continued)

10-20-71 (1433)	895	611	53784	743.5	671.3	845.9	868.3	715.8	742.5	657.7	661.3	620.8	621.9	613.4	612.8	475	6752	1630
10-20-71 (1512)	891	614	57368	730.7	649.7	836.7	857.9	716.7	741.3	661.9	667.2	623.7	627.0	616.6	615.9	483	7026	1650
10-20-71 (1552)	875	616	62464	738.2	652.1	831.2	844.2	720.3	746.1	666.5	672.6	625.4	627.3	617.4	616.8	471	7205	1652
10-21-71 (0913)	857	616	62904	730.1	647.3	811.4	824.2	713.9	736.7	663.1	668.1	625.4	628.1	617.5	616.6	475	7033	1651
10-21-71 (1032)	855	614	64605	719.2	654.5	805.4	830.9	713.6	736.9	662.9	666.3	624.8	627.2	616.2	615.4	483	7243	1636
10-21-71 (1152)	856	617	69644	741.7	658.4	820.9	837.6	720.3	745.0	669.6	672.7	628.5	630.9	618.4	617.6	471	7326	1644

Table B-3
DNB THERMOCOUPLE DATA AND RECIRCULATION FLOW RATES

Date	Time	DNB Thermocouples ΔT/C 34 (°F)	ΔT/C 26 (°F)	ΔT/C 25 (°F)	ΔT/C 29 (°F)	Average ΔT (°F)	Recirculation Flow Rates (lb/hr) W	W_o	W_{DNB}
P/D = 6 Swirl Generator Inserts									
8-5-71	1022	0	0	3	0	0.8	8279	8820	7488
8-5-71	1340	0	0	3	0	0.8	8734	9211	7894
8-5-71	1519	3	3	1	2	2.3	8080	8746	7550
8-6-71	1910	0	2	1	1	1.0	8039	8193	7266
8-6-71	1030	12	18	4	5	9.8	7372	8303	8188
8-6-71	1109	16	22	8	8	13.5	7403	8236	8866
8-6-71	1228	5	7	2	2	4.0	6651	7457	6481
8-6-71	1336	5	8	0	0	3.3	6803	7191	6516
8-6-71	1432	11	15	2	2	7.5	6602	8040	7180
8-6-71	1508	6	10	3	3	5.5	7716	8729	7791
8-6-71	1546	8	9	4	4	6.3	8182	8889	8414
8-9-71	0851	7	4	4	3	4.5	8583	9062	8464
8-9-71	0927	0	1	3	2	1.5	8887	9585	8137
8-9-71	1020	0	5	5	0	2.5	8757	9480	8224
8-9-71	1057	4	8	4	2	4.5	8612	9244	8493
8-9-71	1338	4	4	6	6	5.0	8407	8768	8389
8-9-71	1415	4	6	4	2	4.0	8400	9002	8185
8-9-71	1451	3	6	6	8	5.8	8297	8993	8435
8-9-71	1526	6	8	4	4	5.5	8367	8880	8447
8-9-71	1602	6	8	8	6	7.0	8499	9355	8880
8-10-71	0827	6	6	3	4	4.8	7622	8038	7569
8-10-71	0901	8	8	4	2	5.5	7587	8785	7660
8-10-71	0935	10	10	8	6	8.5	7370	8078	7961
8-10-71	1008	6	8	4	5	5.8	7731	8750	7860
8-10-71	1042	2	3	2	0	1.8	8224	8727	7588
8-10-71	1116	0	8	2	0	3.3	6998	7996	6704
8-10-71	1149	6	6	1	2	3.8	6788	7953	6582
8-10-71	1313	10	12	8	3	8.3	6573	7497	7068
8-10-71	1527	8	8	2	2	5.0	7248	7965	7232
8-10-71	1601	12	14	4	4	8.5	6637	8246	7169
8-13-71	1009	6	14	2	0	5.5	6105	6873	6164
8-13-71	1042	10	14	2	2	7.0	6125	7442	6399

Table B-3 (Continued)

Date	Time	DNB Thermocouples ΔT/C 34 (°F)	ΔT/C 26 (°F)	ΔT/C 25 (°F)	ΔT/C 29 (°F)	Average ΔT (°F)	Recirculation Flow Rates (lb/hr) W	W_o	W_{DNB}
8-13-71	1115	8	14	5	2	7.3	6019	7057	6332
8-13-71	1206	5	4	3	1	3.3	6998	6885	6703
8-13-71	1346	8	14	2	3	6.8	6396	7064	6653
8-13-71	1420	8	12	3	4	6.8	5695	7325	5923
8-13-71	1510	6	10	1	0	4.3	5918	6594	5808
8-13-71	1635	12	12	2	3	7.3	6377	7366	6708
8-17-71	1328	8	6	2	2	4.5	6409	7379	6320
8-17-71	1401	8	10	2	0	5.0	6381	6594	6368
8-17-71	1435	8	12	1	1	5.5	6369	7334	6430
8-17-71	1509	2	6	0	3	2.8	6289	6909	5951
8-17-71	1543	2	5	3	3	3.3	6617	7355	6338
8-18-71	0903	0	8	2	3	3.3	8445	8792	8090
8-18-71	0937	10	16	10	6	10.5	7915	8842	8921
8-18-71	1010	4	6	2	3	3.8	8595	8800	8335
8-18-71	1151	10	13	2	3	7.0	6387	7719	6673
8-18-71	1225	8	11	3	2	6.0	7288	8131	7443
8-18-71	1315	2	3	0	1	1.5	7537	7733	6901
8-18-71	1349	6	8	3	0	4.3	7672	8466	7529
8-18-71	1423	5	8	2	3	4.5	7460	8055	7356
8-18-71	1530	6	5	1	5	4.3	7798	8559	7653
8-19-71	0856	8	12	0	0	5.0	6245	7903	6232
8-19-71	0946	10	8	2	2	5.5	6267	7846	6327
8-19-71	1020	8	10	2	2	5.5	6153	7729	6212
8-19-71	1128	14	18	4	5	10.3	5342	7376	5946
8-20-71	1028	10	12	2	2	6.5*	7822	8403	8081
P/D = 3 Swirl Generator Inserts									
10-13-71	1234	10	12	20	10	13.0	7845	8771	9020
10-13-71	1328	1	6	5	2	3.5	7684	8234	7309
10-13-71	1432	0	0	2	0	0.5	8213	8727	7493
10-13-71	1532	6	5	10	4	6.2	7845	8517	8021
10-14-71	0917	3	0	4	2	2.2	7413	8337	7016
10-14-71	1002	2	5	6	2	3.7	7173	7957	6086
10-14-71	1026	3	5	6	2	4	7674	8363	7505

* The average of all these readings for the P/D = 6 insert is 5.091°F.

Table B-3 (Continued)

Date	Time	DNB Thermocouples ΔT/C 34 (°F)	ΔT/C 26 (°F)	ΔT/C 25 (°F)	ΔT/C 29 (°F)	Average ΔT (°F)	Recirculation Flow Rates (lb/hr) W	W_o	W_{DNB}
10-14-71	1101	4	5	8	2	4.7	7040	8009	7736
10-14-71	1147	3	5	6	5	4.7	7800	8529	7629
10-14-71	1306	7	11	16	8	10.5	7121	8415	7854
10-14-71	1345	6	7	10	5	7.0	7407	8648	7592
10-14-71	1424	7	9	14	5	8.7	7731	8829	8212
10-14-71	1504	0	0	0	0	0	8253	8253	7709
10-14-71	1604	3	5	8	3	4.7	7411	8451	7292
10-15-71	0843	4	4	11	6	6.2	7307	8239	7404
10-15-71	0922	4	5	12	3	6.0	7457	8378	7408
10-15-71	1022	3	3	5	2	3.2	7933	8590	7669
10-15-71	1042	3	14	16	6	9.7	7858	8948	8595
10-15-71	1102	7	11	13	2	8.2	7888	8885	8098
10-15-71	1142	6	10	13	6	8.7	7871	8587	8381
10-19-71	0942	1	7	6	4	4.5	6452	7642	6589
10-19-71	1018	8	21	20	18	16.7	5805	7447	7190
10-19-71	1053	3	5	11	3	5.5	6872	7858	6908
10-19-71	1129	9	16	25	13	15.7	6491	8222	7912
10-19-71	1317	8	19	28	10	16.2	6444	8072	7892
10-19-71	1353	4	9	10	6	7.2	6204	7379	6667
10-19-71	1429	5	10	18	5	9.5	6649	8003	7240
10-19-71	1506	8	13	21	10	13.0	6524	8024	7492
10-19-71	1542	3	10	16	7	9.0	6436	7721	6970
10-20-71	0857	1	6	3	1	2.7	7664	8475	7226
10-20-71	0936	8	16	22	10	14.0	6669	8786	7787
10-20-71	1015	8	20	26	8	15.5	6479	8378	7918
10-20-71	1055	6	9	16	8	9.7	6709	8421	7189
10-20-71	1135	6	7	11	9	8.2	6625	7682	7015
10-20-71	1154	4	4	6	3	4.2	7085	7941	7110
10-20-71	1314	2	5	10	2	4.7	6952	8109	6891
10-20-71	1353	8	10	12	5	8.7	6841	8287	7294
10-20-71	1433	7	12	22	12	13.2	6700	8563	7805
10-20-71	1512	5	12	16	1	8.5	7008	8414	7481
10-20-71	1552	3	9	20	7	9.7	7257	8765	7849
10-21-71	0913	3	3	10	4	5.0	6989	8410	7021
10-21-71	1032	2	5	6	4	4.2	7171	8161	7134
10-21-71	1152	4	11	14	4	8.2	7329	8312	7772

Table B-4
REDUCED DEPARTURE FROM NUCLEATE BOILING RESULTS

	Test Date Time	Local Critical Steam Quality, X_c (dimless)	Mass Flow Rate (lb/sec ft^2)	Radial Acceleration, A_R (g's)	Correlation Factor, C (dimless)	Critical Heat Flux, q_c * X 10^6(btu/hr ft^2)	$q_c \cdot C$ X 10^6(btu/hr ft^2)
For P/D=6 :	8-06-71 (0910)	.949	54.0	2.771	.492	.183	.092
	8-06-71 (1030)	.824	60.9	2.653	.523	.222	.116
	8-06-71 (1109)	.809	65.9	2.998	.530	.209	.111
	8-06-71 (1432)	.927	53.5	2.588	.496	.155	.077
	8-06-71 (1508)	.953	57.9	3.213	.494	.165	.082
	8-06-71 (1546)	.928	62.6	3.553	.501	.182	.091
	8-09-71 (0851)	.911	63.0	3.465	.505	.231	.117
	8-09-71 (1020)	.950	61.2	3.557	.496	.194	.096
	8-09-71 (1057)	.891	63.2	3.337	.510	.207	.105
	8-09-71 (1338)	.819	62.4	2.751	.526	.261	.137
	8-09-71 (1415)	.882	60.9	3.037	.510	.255	.130
	8-09-71 (1451)	.857	62.7	3.045	.517	.264	.137
	8-09-71 (1526)	.829	62.8	2.858	.524	.284	.149
	8-09-71 (1602)	.817	66.0	3.067	.528	.285	.151
	8-10-71 (0827)	.821	56.3	2.250	.520	.313	.163
	8-10-71 (0901)	.827	57.0	2.339	.519	.305	.158
	8-10-71 (0935)	.790	59.2	2.305	.530	.311	.165
	8-10-71 (1008)	.831	58.5	2.486	.520	.264	.137
	8-10-71 (1042)	.829	56.4	2.306	.519	.279	.145
	8-10-71 (1116)	.906	49.9	2.150	.496	.240	.119
	8-10-71 (1149)	.878	49.0	1.946	.501	.229	.115
	8-10-71 (1313)	.890	52.6	2.306	.502	.238	.120
	8-10-71 (1527)	.836	53.8	2.130	.514	.232	.120
	8-10-71 (1601)	.875	53.3	2.293	.506	.216	.109
	8-13-71 (1009)	.814	45.8	1.467	.508	.302	.153
	8-13-71 (1042)	.738	47.6	1.300	.526	.300	.158
	8-13-71 (1115)	.795	47.1	1.477	.514	.282	.145
	8-13-71 (1206)	.747	49.9	1.461	.528	.280	.148
	8-13-71 (1346)	.782	49.5	1.577	.520	.268	.140
	8-13-71 (1420)	.823	44.1	1.385	.503	.242	.122
	8-13-71 (1510)	.859	43.2	1.451	.495	.232	.115
	8-13-71 (1635)	.837	49.9	1.837	.510	.229	.117
	8-17-71 (1328)	.887	47.0	1.831	.496	.210	.104
	8-17-71 (1401)	.853	47.4	1.720	.503	.213	.107
	8-17-71 (1435)	.863	47.8	1.795	.502	.214	.108
	8-17-71 (1509)	.808	44.3	1.347	.506	.210	.107
	8-17-71 (1543)	.863	47.1	1.744	.501	.198	.099
	8-18-71 (0937)	.772	66.4	2.764	.540	.314	.169
	8-18-71 (1010)	.857	62.0	2.974	.517	.283	.146
	8-18-71 (1151)	.872	49.6	1.973	.503	.204	.102
	8-18-71 (1225)	.896	55.4	2.592	.503	.199	.100
	8-18-71 (1315)	.933	51.3	2.416	.493	.168	.083
	8-18-71 (1349)	.867	56.0	2.483	.510	.196	.100
	8-18-71 (1423)	.896	54.7	2.532	.503	.189	.095
	8-18-71 (1530)	.871	56.9	2.589	.510	.248	.127
	8-19-71 (0856)	.941	46.4	2.004	.486	.168	.082
	8-19-71 (0946)	.870	47.1	1.766	.500	.187	.094
	8-19-71 (1020)	.899	46.2	1.518	.493	.179	.088
	8-19-71 (1128)	.875	44.6	1.604	.495	.162	.080
	8-20-71 (1028)	.902	60.1	3.096	.506	.231	.117

* Based on inner tube diameter

Table B-4 (Continued)

	Test Date	Time	Local Critical Steam Quality, X_c (dimensionless)	Mass Flow Rate (lb./sec. ft2)	Radial Acceleration, A_R (g's)	Correlation Factor, C (dimensionless)	Critical Heat Flux, q_c * X 10^6 (btu/hr ft^2)	$q_c \cdot C$ X 10^6 (btu/hr ft^2)
For P/D=3:	10-13-71	(1328)	.773	54.4	7.151	.407	.292	.119
	10-13-71	(1432)	.747	55.7	7.018	.413	.310	.128
	10-14-71	(0917)	.802	52.2	7.093	.400	.272	.109
	10-14-71	(1002)	.843	52.0	7.770	.391	.254	.100
	10-14-71	(1026)	.774	55.8	7.559	.407	.262	.107
	10-14-71	(1101)	.816	57.5	8.927	.397	.250	.099
	10-14-71	(1147)	.825	56.7	8.874	.395	.241	.095
	10-14-71	(1306)	.818	58.4	9.246	.397	.254	.101
	10-14-71	(1345)	.879	56.5	9.976	.384	.239	.092
	10-14-71	(1424)	.837	61.1	10.584	.393	.278	.109
	10-14-71	(1504)	.871	57.3	10.100	.386	.255	.090
	10-14-71	(1604)	.911	54.2	9.886	.378	.230	.087
	10-15-71	(0843)	.877	55.1	9.445	.385	.253	.097
	10-15-71	(0922)	.871	55.1	9.327	.386	.257	.099
	10-15-71	(1002)	.891	57.0	10.460	.382	.258	.099
	10-15-71	(1042)	.803	63.9	10.671	.400	.296	.118
	10-15-71	(1102)	.846	60.2	10.514	.391	.291	.114
	10-15-71	(1142)	.789	62.3	9.796	.403	.313	.126
	10-19-71	(0942)	.900	49.0	7.878	.380	.251	.095
	10-19-71	(1018)	.789	53.5	7.209	.403	.260	.105
	10-19-71	(1053)	.858	51.4	7.870	.388	.251	.097
	10-19-71	(1317)	.725	58.7	7.334	.419	.270	.113
	10-19-71	(1353)	.874	48.8	7.380	.385	.207	.080
	10-19-71	(1429)	.850	53.8	8.484	.390	.240	.094
	10-19-71	(1506)	.775	55.7	7.552	.407	.246	.100
	10-19-71	(1542)	.846	51.8	7.789	.391	.229	.089
	10-20-71	(0857)	.863	53.7	8.712	.387	.269	.104
	10-20-71	(1015)	.700	60.3	7.214	.425	.323	.137
	10-20-71	(1055)	.781	53.5	7.062	.405	.313	.127
	10-20-71	(1135)	.761	52.2	6.384	.409	.328	.134
	10-20-71	(1154)	.806	52.9	7.357	.399	.318	.127
	10-20-71	(1314)	.838	51.3	7.470	.392	.314	.123
	10-20-71	(1353)	.762	54.2	6.920	.409	.330	.135
	10-20-71	(1433	.723	52.1	7.134	.419	.328	.137
	10-20-71	(1512)	.829	55.6	8.616	.395	.303	.120
	10-20-71	(1552)	.785	58.4	8.505	.404	.301	.122
	10-21-71	(1152)	.914	57.8	11.304	.377	.245	.092

* Based on inner tube diameter

Table B-5-1
DNB THERMOCOUPLE DATA FOR NUCLEATE BOILING CONDITIONS AND THE EVALUATED EFFECTIVE HEAT TRANSFER COEFFICIENT FOR THE DNB THERMOCOUPLE "INSULATION"

P/D = 6 Swirl Generator Inserts

DATE	(Time)	Na Temp. at 492 in. (°F)	Temp. at DNB T/C's (°F)	Steam Temp. (°F)	Effective U for DNB T/C "Insulation" (btu/hr ft² °F)	Effective Heat Flux X10⁻³ (btu/hr ft²)	Inside Wall Temp., (°F)
8- 6-71	(1910)	810.5	749.0	605.8	2762.6	169.9	627.5
8- 6-71	(1109)	772.8	725.2	607.3	2945.1	140.2	625.2
8- 6-71	(1432)	749.4	710.7	606.5	3206.3	124.1	622.4
8- 6-71	(1508)	760.6	717.2	605.6	3060.5	132.8	622.6
8- 6-71	(1546)	774.1	724.4	606.9	2811.5	139.7	624.8
8- 9-71	(851)	811.6	758.9	607.6	3402.4	179.3	630.6
8- 9-71	(1020)	800.4	747.2	606.6	3135.9	166.8	628.0
8- 9-71	(1057)	788.3	741.5	607.1	3409.3	159.6	627.5
8- 9-71	(1338)	832.2	756.1	601.4	2411.2	183.5	624.9
8- 9-71	(1415)	812.3	760.6	605.9	3546.1	183.3	629.4
8- 9-71	(1451)	819.9	763.8	607.1	3308.8	185.6	630.9
8- 9-71	(1526)	844.7	779.1	608.7	3071.9	201.5	634.5
8- 9-71	(1602)	841.4	779.6	605.7	3328.6	205.7	632.0
8-10-71	(827)	866.6	785.2	602.5	2654.4	216.1	630.2
8-10-71	(901)	874.7	795.7	604.0	2866.3	226.4	633.0
8-10-71	(935)	862.4	793.2	607.2	3174.7	219.7	635.3
8-10-71	(1008)	867.0	794.4	606.5	3056.8	221.9	634.9
8-10-71	(1042)	863.7	786.5	605.4	2773.1	214.1	632.8
8-10-71	(1116)	849.5	779.2	606.5	2905.8	204.3	632.6
8-10-71	(1149)	831.1	766.5	606.1	2940.8	190.0	630.4
8-10-71	(1313)	812.7	763.0	608.2	3689.5	183.4	631.7
8-10-71	(1527)	805.6	747.5	608.8	2832.0	164.5	629.9
8-13-71	(1009)	866.7	779.6	598.1	2466.8	214.9	625.6
8-13-71	(1042)	852.4	767.9	596.1	2410.0	203.6	622.2
8-13-71	(1115)	847.1	770.7	603.2	2596.3	198.4	628.6
8-13-71	(1206)	834.0	761.8	604.1	2588.6	186.9	628.0
8-13-71	(1346)	828.5	758.5	603.4	2627.0	183.9	626.9
8-13-71	(1420)	820.2	752.0	598.1	2678.6	182.7	621.5
8-13-71	(1510)	807.4	747.0	605.5	2780.2	167.9	627.0
8-13-71	(1635)	806.1	742.2	606.7	2517.3	160.9	627.3
8-17-71	(1328)	787.0	735.0	601.3	3056.1	158.9	621.6
8-17-71	(1401)	788.8	732.4	599.6	2799.9	157.9	619.8
8-17-71	(1435)	785.1	727.8	596.9	2718.4	155.8	616.8
8-17-71	(1543)	766.5	712.7	593.6	2639.0	142.0	611.8
8-18-71	(937)	868.1	784.1	601.8	2567.0	215.6	629.4
8-18-71	(1010)	857.5	776.5	604.0	2520.3	204.1	630.1
8-18-71	(1151)	789.1	736.7	605.0	2985.8	156.5	625.0
8-18-71	(1225)	778.4	728.6	603.4	2989.5	148.9	622.5
8-18-71	(1315)	775.8	729.4	606.5	3148.4	146.1	625.2
8-18-71	(1349)	761.8	713.7	597.5	2878.5	138.5	615.2
8-18-71	(1423)	773.2	725.7	601.6	3108.1	147.6	620.5
8-18-71	(1530)	805.0	745.5	605.6	2790.7	166.0	626.9
8-19-71	(856)	763.1	717.2	602.8	2967.2	136.2	620.2
8-19-71	(946)	757.6	712.4	597.9	3018.6	136.4	615.4
8-19-71	(1020)	768.1	718.5	599.5	2856.8	141.7	617.6
8-19-71	(1128)	751.8	709.0	596.7	3128.0	133.9	613.8

Table B-5-1 (Continued)

P/D = 3 Swirl Generator Inserts

DATE	(Time)	Na Temp. at 492 in. (°F)	Temp. at DNB T/C's (°F)	Steam Temp. (°F)	Effective U For DNB T/C "Insulation" (btu/hr ft2 °F)	Effective Heat Flux X10^{-3} (btu/hr ft^2)	Inside Wall Temp., (°F)
10-14-71	(1306)	807.0	749.3	606.1	2944.4	169.9	627.3
10-14-71	(1345)	812.9	749.0	603.2	2707.8	173.0	625.3
10-14-71	(1424)	832.3	762.5	607.8	2625.6	183.3	631.3
10-14-71	(1504)	830.3	757.9	605.3	2498.7	180.9	628.5
10-14-71	(1604)	810.6	749.2	604.8	2790.5	171.3	626.7
10-15-71	(843)	825.7	760.0	606.3	2772.5	182.2	629.6
10-15-71	(922)	816.5	759.6	605.6	3207.9	182.5	629.0
10-15-71	(1002)	826.8	764.8	607.3	3008.9	186.5	631.2
10-15-71	(1042)	842.3	768.6	605.2	2625.6	193.5	630.0
10-15-71	(1102)	800.0	700.0	600.0	1192.8	119.3	615.3
10-15-71	(1142)	856.4	780.9	606.5	2731.9	206.3	632.9
10-19-71	(942)	800.0	700.0	600.0	1192.8	119.3	615.3
10-19-71	(1018)	806.3	742.6	595.0	2753.8	175.4	617.5
10-19-71	(1053)	819.5	752.7	604.5	2631.6	175.8	627.0
10-19-71	(1129)	818.9	755.1	604.3	2803.1	178.8	627.2
10-19-71	(1317)	806.6	747.2	602.0	2901.8	172.4	624.1
10-19-71	(1353)	779.9	725.0	591.9	2887.1	158.5	612.2
10-19-71	(1429)	801.0	742.5	604.3	2805.1	164.1	625.3
10-19-71	(1506)	800.0	738.4	601.8	2634.8	162.3	622.6
10-19-71	(1542)	801.7	738.7	601.8	2581.8	162.7	622.6
10-20-71	(857)	841.6	764.5	606.7	2424.4	186.9	630.6
10-20-71	(936)	850.7	770.5	603.7	2462.9	197.5	629.0
10-20-71	(1015)	858.3	773.8	602.6	2398.7	202.7	628.5
10-20-71	(1055)	846.7	779.4	604.2	3079.9	207.3	630.7
10-20-71	(1135)	856.8	780.5	601.9	2769.7	211.3	628.9
10-20-71	(1154)	800.0	700.0	600.0	1192.8	119.3	615.3
10-20-71	(1314)	872.1	784.9	603.7	2457.2	214.3	631.1
10-20-71	(1353)	874.7	784.7	602.8	2390.3	215.1	630.3
10-20-71	(1433)	866.1	781.2	602.8	2485.9	211.1	629.8
10-20-71	(1512)	858.1	778.3	606.2	2551.3	203.6	632.3
10-20-71	(1552)	845.0	772.0	606.6	2681.9	195.8	631.7
10-21-71	(913)	831.3	762.2	606.7	2666.3	184.2	630.3
10-21-71	(1032)	828.4	762.8	606.3	2826.5	185.4	630.0
10-21-71	(1152)	832.9	762.2	603.9	2653.6	187.6	627.9

Table B-5-2
DNB THERMOCOUPLE DATA NEAR DEPARTURE FROM NUCLEATE BOILING CONDITIONS AND THE CORRESPONDING STEAM SIDE HEAT TRANSFER COEFFICIENT

P/D = 6 Swirl Generator Inserts

DATE	(Time)	Na Temp. at 492 in. (°F)	Temp. at DNB T/C's (°F)	Steam Temp. (°F)	Steam Side Heat Trans. Coefficient (btu/hr ft2 °F)	Effective Heat Flux X10^{-3} (btu/hr ft2)	Inside Wall Temp., (°F)	Local Steam Quality
8- 6-71	(1910)	810.1	752.8	608.3	8299.7	166.2	633.9	0.830
8- 6-71	(1109)	776.3	739.8	609.6	2482.3	105.8	664.2	1.018
8- 6-71	(1432)	753.4	720.8	608.3	2682.1	94.5	653.4	0.996
8- 6-71	(1508)	770.9	729.9	606.8	3975.5	118.9	645.1	0.965
8- 6-71	(1546)	780.6	735.5	609.9	5198.0	130.8	642.1	0.962
8- 9-71	(851)	816.3	762.4	608.9	4815.5	156.3	650.4	0.894
8- 9-71	(1020)	802.1	752.3	607.3	4432.6	144.4	649.0	0.876
8- 9-71	(1057)	793.7	746.4	607.7	4319.0	137.2	648.4	0.875
8- 9-71	(1338)	829.7	763.7	605.6	11588.0	191.3	626.7	0.816
8- 9-71	(1415)	825.0	767.8	609.2	5346.1	165.9	648.9	0.852
8- 9-71	(1451)	826.8	773.4	610.1	3795.2	154.9	662.3	0.875
8- 9-71	(1526)	849.3	782.1	607.9	7268.0	194.9	642.2	0.839
8- 9-71	(1602)	849.9	787.3	609.6	4913.6	181.5	656.9	0.865
8-10-71	(827)	881.9	803.9	609.0	9017.7	226.2	641.1	0.814
8-10-71	(901)	881.1	800.0	606.9	12593.6	235.3	630.8	0.838
8-10-71	(935)	879.3	800.3	605.2	9654.0	229.1	635.6	0.877
8-10-71	(1008)	859.7	792.7	607.8	5494.2	194.3	653.1	0.849
8-10-71	(1042)	850.8	780.6	607.2	9506.6	203.5	634.6	0.746
8-10-71	(1116)	836.6	773.0	608.0	7208.0	184.4	640.8	0.857
8-10-71	(1149)	813.7	761.2	608.7	4482.7	152.2	652.2	0.844
8-10-71	(1313)	824.0	771.0	607.9	3717.6	153.7	660.8	0.979
8-10-71	(1527)	807.3	750.9	608.5	8236.8	163.6	633.9	0.834
8-13-71	(1009)	849.1	781.4	601.6	6431.4	196.2	640.7	0.825
8-13-71	(1042)	834.2	768.6	599.1	7317.2	190.3	632.4	0.782
8-13-71	(1115)	840.1	776.4	605.4	6136.5	184.7	643.9	0.851
8-13-71	(1206)	827.5	761.8	605.1	12008.3	190.5	625.4	0.704
8-13-71	(1346)	826.8	764.5	606.3	8027.3	180.7	635.1	0.825
8-13-71	(1420)	815.0	755.7	607.8	8860.2	172.0	632.6	0.864
8-13-71	(1510)	815.5	756.7	602.5	6769.6	170.5	634.7	0.838
8-13-71	(1635)	809.3	750.6	607.2	10055.5	170.2	628.9	0.896
8-17-71	(1328)	798.9	744.1	605.9	8249.1	158.9	630.6	0.871
8-17-71	(1401)	785.6	731.8	600.4	9905.9	156.0	620.6	0.851
8-17-71	(1435)	790.7	737.1	601.9	8192.2	155.4	626.2	0.874
8-17-71	(1543)	776.0	724.7	600.0	10171.7	148.8	618.7	0.814
8-18-71	(937)	855.6	790.6	605.8	4884.2	188.5	655.2	0.907
8-18-71	(1010)	848.5	777.9	604.6	9899.9	204.7	631.1	0.822
8-18-71	(1151)	780.7	735.7	603.6	4285.3	130.5	642.6	0.926
8-18-71	(1225)	786.3	738.0	604.6	5366.0	140.1	638.0	0.922
8-18-71	(1315)	781.4	716.9	601.1	6899.9	129.0	625.0	0.831
8-18-71	(1349)	765.5	722.6	603.8	5280.5	124.4	634.0	0.845
8-18-71	(1423)	774.1	731.0	607.3	4634.4	125.0	641.8	0.880
8-18-71	(1530)	810.2	753.1	604.6	7044.3	165.6	634.7	0.849
8-19-71	(856)	766.4	728.4	602.4	2973.2	110.2	649.8	0.938
8-19-71	(946)	760.7	721.8	603.9	3847.6	112.8	641.4	0.882
8-19-71	(1020)	768.6	723.4	602.2	6032.5	131.1	630.0	0.911
8-19-71	(1128)	740.2	706.7	596.1	2991.5	97.1	637.7	1.019

Table B-5-2 (Continued)

P/D = 3 Swirl Generator Inserts

DATE	(Time)	Na Temp. at 492 in. (°F)	Temp. at DNB T/C's (°F)	Steam Temp. (°F)	Steam Side Heat Trans. Coefficient (btu/hr ft² °F)	Effective Heat Flux X10⁻³ (btu/hr ft2)	Inside Wall Temp., (°F)	Local Steam Quality
10-14-71	(1306)	813.5	759.7	606.9	3808.6	145.3	655.7	0.866
10-14-71	(1345)	815.4	758.9	608.3	4717.3	152.5	649.7	0.855
10-14-71	(1424)	835.8	776.4	607.9	3840.0	160.4	661.4	0.852
10-14-71	(1504)	827.3	757.3	605.6	14691.1	189.0	622.1	0.723
10-14-71	(1604)	814.2	757.3	608.4	5050.1	153.6	647.3	0.837
10-15-71	(843)	829.2	765.6	608.2	6394.0	171.7	642.6	0.836
10-15-71	(922)	833.9	765.9	609.1	9308.5	183.6	634.3	0.824
10-15-71	(1002)	836.5	766.6	607.7	10200.8	188.7	631.4	0.788
10-15-71	(1042)	844.9	780.9	608.6	4581.6	172.8	656.9	0.840
10-15-71	(1102)	856.7	784.8	608.9	6808.0	194.1	645.4	0.852
10-15-71	(1142)	860.8	787.6	608.9	6887.0	197.6	645.6	0.803
10-19-71	(942)	836.3	763.0	605.4	15930.7	197.9	621.3	0.812
10-19-71	(1018)	810.8	766.1	608.7	2178.1	120.7	679.6	0.947
10-19-71	(1053)	817.7	758.6	607.7	5568.4	159.6	644.4	0.795
10-19-71	(1129)	830.0	774.5	608.3	3265.8	149.8	667.0	0.860
10-19-71	(1317)	813.3	756.8	605.0	4577.0	152.5	647.7	0.865
10-19-71	(1353)	784.2	736.8	608.7	4462.1	128.0	645.4	0.842
10-19-71	(1429)	801.8	749.1	608.7	4712.4	142.3	647.3	0.886
10-19-71	(1506)	803.2	755.8	609.5	2994.6	128.0	664.2	0.862
10-19-71	(1542)	796.7	747.2	607.2	3847.3	133.6	651.7	0.855
10-20-71	(857)	835.4	767.9	608.9	8217.9	182.2	637.3	0.746
10-20-71	(936)	851.9	790.8	607.6	3265.0	165.0	672.3	0.830
10-20-71	(1015)	861.3	786.4	603.6	6876.1	202.2	641.2	0.850
10-20-71	(1055)	863.9	785.7	608.7	10651.6	211.1	634.1	0.801
10-20-71	(1135)	861.4	790.0	610.1	5965.3	192.8	651.5	0.749
10-20-71	(1154)	875.1	789.7	609.4	20185.5	230.6	624.0	0.721
10-20-71	(1314)	879.7	794.2	607.5	14221.7	230.8	628.3	0.760
10-20-71	(1353)	867.6	788.9	606.6	9162.9	212.5	636.3	0.765
10-20-71	(1433)	868.3	793.5	607.5	6327.7	202.0	648.4	0.811
10-20-71	(1512)	857.9	784.4	609.1	7744.2	198.4	641.9	0.831
10-20-71	(1552)	844.2	784.3	609.2	3510.6	161.7	668.2	0.815
10-21-71	(913)	824.2	768.4	609.6	3795.3	150.7	660.4	0.906
10-21-71	(1032)	831.0	764.8	608.0	7954.6	178.7	636.8	0.965
10-21-71	(1152)	837.6	772.1	608.5	6151.2	176.8	645.3	0.922

Table B-5-3
DNB THERMOCOUPLE DATA FOR FILM BOILING CONDITIONS AND THE CORRESPONDING STEAM-SIDE HEAT TRANSFER COEFFICIENT

P/D = 6 Swirl Generator Inserts

DATE	(Time)	Na Temp. at 492 in. (°F)	Temp. at DNB T/C's (°F)	Steam Temp. (°F)	Steam Side Heat Trans. Coefficient (btu/hr ft² °F)	Effective Heat Flux X10⁻³ (btu/hr ft²)	Inside Wall Temp., (°F)	Local Steam Quality
8- 6-71	(1910)	798.9	763.3	608.3	1626.6	103.1	689.4	1.079
8- 6-71	(1109)	779.3	763.1	607.6	493.5	47.0	729.5	1.125
8- 6-71	(1432)	757.4	746.3	605.8	350.7	32.2	723.3	1.155
8- 6-71	(1508)	774.9	752.4	606.8	844.2	65.2	705.7	1.145
8- 6-71	(1546)	788.6	761.2	608.9	1066.2	79.5	704.3	1.083
8- 9-71	(851)	824.3	799.6	608.9	658.8	71.6	748.1	1.067
8- 9-71	(1020)	806.1	772.8	609.3	1311.5	96.6	703.5	0.983
8- 9-71	(1057)	796.7	764.5	607.7	1329.4	93.4	697.6	1.004
8- 9-71	(1338)	821.4	778.0	605.6	1961.6	125.9	687.7	1.032
8- 9-71	(1415)	833.0	804.3	608.2	782.2	83.2	744.4	1.137
8- 9-71	(1451)	834.8	801.4	609.1	1011.2	96.9	731.7	1.086
8- 9-71	(1526)	846.4	815.1	608.9	825.6	90.8	749.7	1.149
8- 9-71	(1602)	855.9	817.3	609.6	1128.2	111.9	736.6	1.050
8-10-71	(827)	907.3	856.9	609.0	1317.4	146.2	751.0	1.024
8-10-71	(901)	880.1	837.0	606.9	1144.2	125.0	746.7	1.085
8-10-71	(935)	891.5	852.3	603.2	871.1	113.6	770.1	1.050
8-10-71	(1008)	865.7	818.7	607.8	1548.7	136.3	720.5	1.022
8-10-71	(1042)	860.9	838.6	605.2	442.4	64.6	792.0	1.204
8-10-71	(1116)	844.6	817.5	605.0	645.4	78.6	760.9	1.080
8-10-71	(1149)	819.7	803.4	606.7	371.9	47.3	769.4	1.114
8-10-71	(1313)	831.0	811.0	605.9	454.5	58.0	769.2	1.087
8-10-71	(1527)	815.3	792.2	608.5	632.6	67.0	744.1	1.100
8-13-71	(1009)	868.8	837.7	600.6	670.3	90.1	772.7	1.131
8-13-71	(1042)	847.8	826.6	601.1	434.1	61.4	782.3	1.230
8-13-71	(1115)	842.6	813.9	606.4	723.0	83.3	753.9	1.216
8-13-71	(1206)	845.5	820.2	607.1	586.2	73.4	767.3	1.160
8-13-71	(1346)	842.8	818.5	605.3	555.4	70.5	767.7	1.197
8-13-71	(1420)	829.0	809.7	607.8	443.3	56.0	769.4	1.067
8-13-71	(1510)	829.5	813.2	604.5	346.4	47.3	779.2	1.255
8-13-71	(1635)	817.3	794.6	606.2	597.2	65.8	747.3	1.157
8-17-71	(1328)	810.9	783.6	605.9	838.3	79.2	726.8	1.133
8-17-71	(1401)	795.6	774.8	600.4	588.6	60.3	731.6	1.230
8-17-71	(1435)	800.7	769.1	602.9	1166.5	91.6	703.5	1.132
8-17-71	(1543)	786.0	767.2	602.0	553.1	54.5	728.2	1.235
8-18-71	(937)	865.6	835.6	603.8	659.0	87.0	772.8	1.064
8-18-71	(1010)	857.5	800.4	604.6	2762.1	165.6	681.3	0.997
8-18-71	(1151)	787.7	771.6	603.6	444.2	46.7	738.1	1.134
8-18-71	(1225)	794.3	773.7	604.6	605.5	59.7	730.9	1.179
8-18-71	(1315)	767.4	747.4	600.1	701.2	58.0	706.0	1.168
8-18-71	(1349)	776.5	761.1	603.8	456.1	44.7	729.1	1.120
8-18-71	(1423)	782.1	765.5	607.3	498.1	48.1	731.0	1.086
8-18-71	(1530)	824.2	802.1	601.6	531.2	64.1	756.0	1.112
8-19-71	(856)	772.4	760.9	600.4	312.4	33.3	737.0	1.232
8-19-71	(946)	769.7	759.3	603.9	288.5	30.2	737.7	1.320
8-19-71	(1020)	776.6	759.6	601.2	512.5	49.3	724.3	1.248
8-19-71	(1128)	744.2	728.2	594.1	587.7	46.4	695.2	1.241

Table B-5-3 (Continued)

P/D = 3 Swirl Generator Inserts

DATE	(Time)	Na Temp. at 492 in. (°F)	Temp. at DNB T/C's (°F)	Steam Temp. (°F)	Steam Side Heat Trans. Coefficient (btu/hr ft2 °F)	Effective Heat Flux X10^{-3} (btu/hr ft2)	Inside Wall Temp., (°F)	Local Steam Quality
10-14-71	(1306)	819.5	799.4	605.9	449.7	54.3	760.4	1.021
10-14-71	(1345)	821.4	791.2	607.3	832.9	81.5	732.6	0.990
10-14-71	(1424)	841.8	814.4	605.9	610.1	74.0	761.1	1.037
10-14-71	(1504)	834.3	810.2	605.3	527.0	65.1	763.4	1.172
10-14-71	(1604)	822.2	804.2	606.4	382.0	48.6	769.2	1.059
10-15-71	(843)	834.2	794.1	608.2	1282.3	108.3	716.3	0.992
10-15-71	(922)	843.9	817.7	608.1	570.9	70.7	766.7	1.074
10-15-71	(1002)	846.5	816.1	608.7	708.7	82.1	756.9	1.041
10-15-71	(1042)	854.9	820.9	608.6	804.2	91.8	754.7	1.007
10-15-71	(1102)	866.7	832.9	607.9	734.2	91.3	767.0	1.039
10-15-71	(1142)	868.8	834.1	607.9	756.4	93.7	766.4	1.023
10-19-71	(942)	848.3	823.0	603.4	513.2	68.3	773.8	1.028
10-19-71	(1018)	819.8	809.6	606.7	192.6	27.5	789.8	1.145
10-19-71	(1053)	827.7	806.1	605.7	471.2	58.3	764.1	1.014
10-19-71	(1129)	838.0	815.5	605.3	467.2	60.7	771.7	1.021
10-19-71	(1317)	821.3	797.7	603.0	547.7	63.7	751.9	1.085
10-19-71	(1353)	797.2	784.1	605.7	295.9	35.4	758.7	1.088
10-19-71	(1429)	813.8	795.1	605.7	422.1	50.5	758.8	1.111
10-19-71	(1506)	813.2	795.3	608.5	406.8	48.3	760.6	1.059
10-19-71	(1542)	804.7	786.4	606.2	437.0	49.4	750.9	1.048
10-20-71	(857)	847.4	830.4	606.8	308.5	45.9	797.3	1.172
10-20-71	(936)	861.9	845.8	605.6	266.5	43.5	814.4	1.118
10-20-71	(1015)	873.3	842.4	601.6	591.5	83.4	782.1	1.183
10-20-71	(1055)	876.9	843.7	607.7	670.2	89.6	778.9	1.129
10-20-71	(1135)	873.4	849.0	609.1	438.7	65.9	801.3	1.121
10-20-71	(1154)	885.1	838.2	608.4	1171.9	126.6	746.7	1.063
10-20-71	(1314)	893.7	851.2	606.5	908.4	114.7	768.2	1.064
10-20-71	(1353)	881.6	851.7	603.6	544.7	80.7	793.3	1.181
10-20-71	(1433)	878.3	838.5	605.5	885.2	107.5	760.9	1.078
10-20-71	(1512)	867.9	838.6	607.1	580.8	79.1	781.4	1.117
10-20-71	(1552)	852.2	835.8	608.2	289.7	44.3	803.8	1.087
10-21-71	(913)	839.2	821.6	606.6	336.5	47.5	787.3	1.162
10-21-71	(1032)	841.0	813.0	606.0	634.3	75.6	758.6	1.158
10-21-71	(1152)	847.6	818.8	607.5	641.1	77.8	762.7	1.124

APPENDIX B-2
SUPERHEATER PERFORMANCE DATA

Table B-6
SUPERHEATER THERMAL PERFORMANCE RESULTS

Date	Time	Overall Heat Transfer Coefficient, (btu/hr ft^2) Experiment	Overall Heat Transfer Coefficient, (btu/hr ft^2) Predicted	Na Inlet Temp. (° F)	Thermal Power (kW_t)	Steam Drum Press. (psia)
3-30-71	(1728)	362	265	936	407	1587
3-31-71	(0430)	356	260	937	397	1555
3-31-71	(1536)	357	260	928	390	1601
3-31-71	(1551)	363	264	930	400	1621
3-31-71	(1606)	369	268	940	425	1644
3-31-71	(1635)	383	280	941	453	1693
5-20-71	(1327)	327	238	932	335	1612
5-20-71	(1458)	362	260	907	374	1618
6-08-71	(1153)	369	270	954	439	1647
6-08-71	(1524)	387	283	952	478	1655
6-08-71	(1908)	397	286	949	478	1660
7-24-71	(2056)	377	274	937	435	1651
7-25-71	(0354)	381	277	933	440	1657
7-25-71	(1228)	368	267	927	407	1630
7-12-71	(1932)	373	272	935	426	1650
7-22-71	(0540)	365	266	935	412	1624
7-23-71	(0856)	371	270	936	424	1658
7-24-71	(0625)	380	285	931	437	1652
7-31-71	(0251)	387	285	959	487	1617
7-31-71	(2221)	370	269	933	418	1648
8-02-71	(2324)	384	290	908	412	1615
11-03-71	(0815)	376	276	942	442	1632
7-31-71	(0210)	376	275	946	445	1655
12-04-71	(0115)	357	260	935	396	1657
12-10-71	(0243)	352	257	933	384	1625

Table B-7
SUPERHEATER THERMAL PERFORMANCE DATA

		Sodium Side																	Steam Side		
Date	Time	W_{Na}	T_{in}	T_{out}	T/C 1	T/C 2	T/C 3	T/C 4	T/C 5	T/C 6	T/C 7	T/C 8	T/C 9	weigh-ted AVG.	T/C 10	T/C 11	T/C 12	T/C 13	T/C 14	T_{in}	T_{out}	W_s
3-30-71	(1728)	53296	934.6	846.5	839	845	846	843	843	851	861	858	840	846.7	904	914	919	869	867	603	907	5078
3-31-71	(0430)	52311	936.8	849.1	843	849	848	852	847	853	863	861	843	851.2	908	916	921	886	880	600	911	4918
3-31-71	(1536)	47692	927.9	842.2	835	839	842	842	839	844	855	852	834	842.3	898	907	913	879	868	604	902	4928
3-31-71	(1551)	49611	929.6	842.5	835	841	839	846	837	846	857	854	840	844.1	899	909	914	875	868	606	903	5056
3-31-71	(1606)	49884	940.2	845.7	842	852	853	845	844	853	864	862	841	846.8	908	918	924	884	874	608	912	5183
3-31-71	(1635)	59447	940.8	856.1	851	858	855	858	853	860	872	869	852	858.7	912	921	927	887	870	611	916	5536
5-20-71	(1327)	47392	932.0	852.0	847	851	851	852	849	856	866	864	848	853.6	905	913	917	873	863	605	906	4193
5-20-71	(1458)	54451	906.7	834.2	829	834	833	837	830	839	848	846	829	836.3	882	889	894	855	843	605	882	4901
6-08-71	(1151)	52817	953.5	853.2	850	855	854	858	854	860	871	869	849	857.8	920	931	938	900	888	608	923	5220
6-08-71	(1524)	56038	951.8	850.3	845	851	851	855	847	856	869	867	843	854.0	916	928	936	884	875	608	918	5684
6-08-71	(1908)	56963	948.5	848.5	843	854	849	856	849	856	868	864	844	853.9	915	927	934	896	881	609	926	5773
7-24-71	(2056)	55072	936.7	853.9	844	853	851	854	852	856	867	866	847	854.4	908	917	922	884	869	608	910	5359
7-25-71	(0354)	57025	933.4	848.9	839	845	844	847	841	850	861	859	839	847.2	903	913	919	880	865	608	906	5457
7-25-71	(1228)	54844	926.5	847.6	840	847	843	847	842	850	860	858	840	847.4	899	908	913	848	863	606	901	5127
7-12-71	(1932)	53969	934.6	854.0	847	851	851	854	848	857	868	866	848	854.6	907	915	920	880	868	608	916	5277
7-22-71	(0540)	53630	934.6	853.9	848	855	850	857	850	857	869	867	848	856.3	908	916	920	885	871	606	916	5102
7-23-71	(0856)	55094	935.6	853.0	847	853	850	856	847	855	868	864	847	849.7	907	916	922	884	871	608	915	5230
7-24-71	(0625)	57293	931.4	848.4	845	848	846	850	847	852	864	861	843	846.3	903	912	918	873	864	608	911	5459
7-31-71	(0251)	52812	958.9	858.3	855	859	860	862	853	865	875	874	855	857.4	925	937	945	900	889	605	936	5783
7-31-71	(2221)	55741	932.5	844.6	839	844	842	847	842	848	859	858	840	842.1	902	912	919	878	863	608	915	5188
8-02-71	(2324)	59716	907.8	841.7	833	840	837	842	837	844	853	851	836	837.1	885	892	896	859	841	605	890	5510
11-03-71	(0815)	56158	941.6	846.7	842	848	846	846	844	851	863	858	841	848.8	908	919	926	885	877	606	910	5417
7-31-71	(0120)	55373	946.4	851.8	848	852	848	856	849	856	867	866	846	854.5	914	925	931	890	882	608	916	5382
12-04-71	(0115)	51489	934.5	851.1	843	847	850	851	851	855	865	863	845	851.5	904	912	917	863	863	608	916	4888
12-10-71	(0243)	52003	933.2	847.7	841	847	846	849	847	852	863	860	843	844.7	902	912	918	878	867	606	915	4773

APPENDIX B-3
STEAM-SIDE STABILITY DATA

Table B-8-1
DATA FOR THE BAYONET TUBE EVAPORATOR WITH THE P/D = 3 INSERT
(PARTIALLY INSULATED BAYONET TUBES)
RECORDED DURING THE STEAM-SIDE STABILITY TESTS AT 1100 TO 1200 kWt

Run #1, 12-07-71

STEAM SIDE												SODIUM SIDE								
TIME	lb/hr		degrees F				psig			psi		GPM	degrees F							
	W_R	X_e	T_W	T_B	T_G	T_S	P_i	P_O	P_D	ΔP_P	ΔP_A	W_{Na}	T_{in}	T_{508}	T_{492}	T_{437}	T_{377}	T_{257}	T_{137}	T_{out}
1342	8020	0.65	493	519	535	606	1601	1591	1597	10.0	8.0	130	834	690	800	705	650	620	611	609
1401	6770	0.76	476	508	526	605	1596	1590	1596	6.3	5.5	130	836	670	790	704	652	620	609	608
1421	5740	0.93	420	484	510	608	1598	1596	1602	2.6	1.5	131	836	630	803	706	654	620	612	612
1441	4740	1.19	420	484	510	608	1610	1609	1616	1.6	1.1	130	847	770	835	810	734	637	620	615
1501	4140	1.42	421*									130	870	813	800	847	828	792	710	638
1521	4270	1.31	430									140	864	805	853	843	825	797	725	655
1541	3840	1.30	426									139	875	818	869	855	839	815	774	683
1601	9100	0.50	499	517	530	590	1420	1403	1409	17.0	10	112	840	655	795	685	629	600	591	590

*The remaining numbers not defined due to periodically varying conditions

Table B-8-2
DATA FOR THE BAYONET TUBE EVAPORATOR WITH THE P/D = 3 INSERT
(PARTIALLY INSULATED BAYONET TUBES)
RECORDED DURING THE STEAM-SIDE STABILITY TESTS
AT APPROXIMATELY 1400 TO 1500 kWt

Run #2, 12-08-71

STEAM SIDE												SODIUM SIDE								
TIME	lb/hr		degrees F				psig			psi		GPM	degrees F							
	W_R	X_e	T_W	T_B	T_G	T_S	P_i	P_O	P_D	ΔP_P	ΔP_A	W_{Na}	T_{in}	T_{508}	T_{492}	T_{437}	T_{377}	T_{257}	T_{137}	T_{out}
0945	9045	0.72	482	509	525	602	1576	1561	1564	16.0	10	158	840	675	810	720	665	622	611	609
1004	7800	0.88	461	495	517	607	1619	1609	1613	10.0	7.0	168	839	680	812	722	669	626	614	612
1024	7040	0.97	440	482	508	608	1631	1625	1629	6.0	5.0	166	843	704	820	730	673	629	615	614
1044	5960	1.17	421	477	503	606	1588	1586	1591	2.0	1.5	167	843	730	837	814	774	653	623	618
1104	5260	1.32	418*									184	846	803	842	828	817	787	724	649
1124	5130	1.24	417									189	860	812	857	843	830	806	761	680
1143	6830	0.75	419	474	502	607	1609	1603	1605	6.0	5.0	162	830	772	822	805	788	723	648	634

*The remaining numbers not defined due to periodically varying conditions.

Table B-8-3
DATA FOR THE BAYONET TUBE EVAPORATOR WITH THE P/D = 3 INSERT (PARTIALLY INSULATED BAYONET TUBES) RECORDED DURING THE STEAM SIDE STABILITY TESTS AT APPROXIMATELY 800 TO 900 kWt

Run #3, 12-08-71

STEAM SIDE												SODIUM SIDE								
TIME	lb/hr		degrees F				psig			psi		GPM	degrees F							
	W_R	X_e	T_W	T_B	T_G	T_S	P_i	P_O	P_D	ΔP_P	ΔP_A	W_{Na}	T_{in}	T_{508}	T_{492}	T_{437}	T_{377}	T_{257}	T_{137}	T_{out}
1342	6980	0.62	503	531	546	609	1643	1637	1640	6.0	5.0	102	840	670	790	692	640	616	608	607
1402	4470	1.03	447	500	523	608	1611	1608	1613	2.5	2.0	103	849	698	815	703	641	615	610	609
1422	2182	2.09	421*									102	857	805	851	841	827	799	755	643
1442	2520	1.67	429									104	885	830	877	865	851	823	788	680
1502	5050	0.67	434	492	517	640	1623	1621	1623	2.0	0.6	102	827	780	820	795	792	653	623	620

*The remaining numbers not defined due to periodically varying conditions.

APPENDIX C
ANALYSIS

C-1 TUBE WALL TRANSIENT ANALYSIS

In order to investigate the transient behavior of the heater tube wall, a finite difference model to be solved on the computer was constructed. Since the swirl generator was positioned midway between the two DNB thermocouples, the plane through the swirl generator is a plane of symmetry (Figure 5-10), and only one-half segment is considered (Figure C-1). The steam-side heat transfer coefficient denoted by $h_i(\phi,t)$ on Figure C-1 is a function of time and angular position the time behavior of h_i being the principal parameter to be varied in this study. In the transition region the steam-side surface may be alternately in nucleate boiling with a very high h_i or in film boiling corresponding to film blanketing and a very low h_i. The film blanketing may occur over only part of the surface, and this intuitively will result in a lower temperature fluctuation in the wall. The transient heat conduction problem will now be considered in more detail.

Transient Conduction Problem

Consider the transient heat conduction problem described by the following system of equations.

$$\frac{\partial^2 T}{\partial r^2} + \frac{1}{r}\frac{\partial T}{\partial r} + \frac{\partial^2 T}{\partial \phi^2} = \frac{1}{\alpha}\frac{\partial T}{\partial t} \quad \text{in } r_i \leqslant r \leqslant r_o \qquad \text{(C-1)}$$

$$o \leqslant \alpha \leqslant \pi$$

$$t > o$$

Boundary Conditions:

$$k\frac{\partial T}{\partial r} = h_i\ (t,\phi)\ (T - T_i) \qquad r = r_i \qquad \phi = o \text{ to } \pi \qquad \text{(C-2)}$$

$$k\frac{\partial T}{\partial r} = h_o\ (\phi)\ (T_o - T) \qquad r = r_o \qquad \phi = o \text{ to } \pi \qquad \text{(C-3)}$$

$$\frac{\partial T}{\partial \phi} = o \quad \text{at } \phi = o \quad r_i \leqslant r \leqslant r_o \qquad \text{(C-4)}$$

$$\frac{\partial T}{\partial \phi} = o \quad \text{at } \phi = \pi \quad r_i \leqslant r \leqslant r_o \qquad \text{(C-5)}$$

Initial Condition

$$T = T\ (r,\phi) \text{ at } t = o \qquad \text{(C-6)}$$

The nodal grid of Figure C-1 was adapted and then the radial and angular coordinates are given by

$$r = r_i + (i - 1)\ \Delta r \qquad \text{(C-7)}$$

$$\phi = (j - 1)\ \Delta\phi \qquad \text{(C-8)}$$

Denote the temperature of a point at time t and at time $t + \Delta t$ by

$$T\ (r,\phi,t) = T_{ij}$$

$$T\ (r,\phi,t + \Delta t) = T^1_{ij}$$

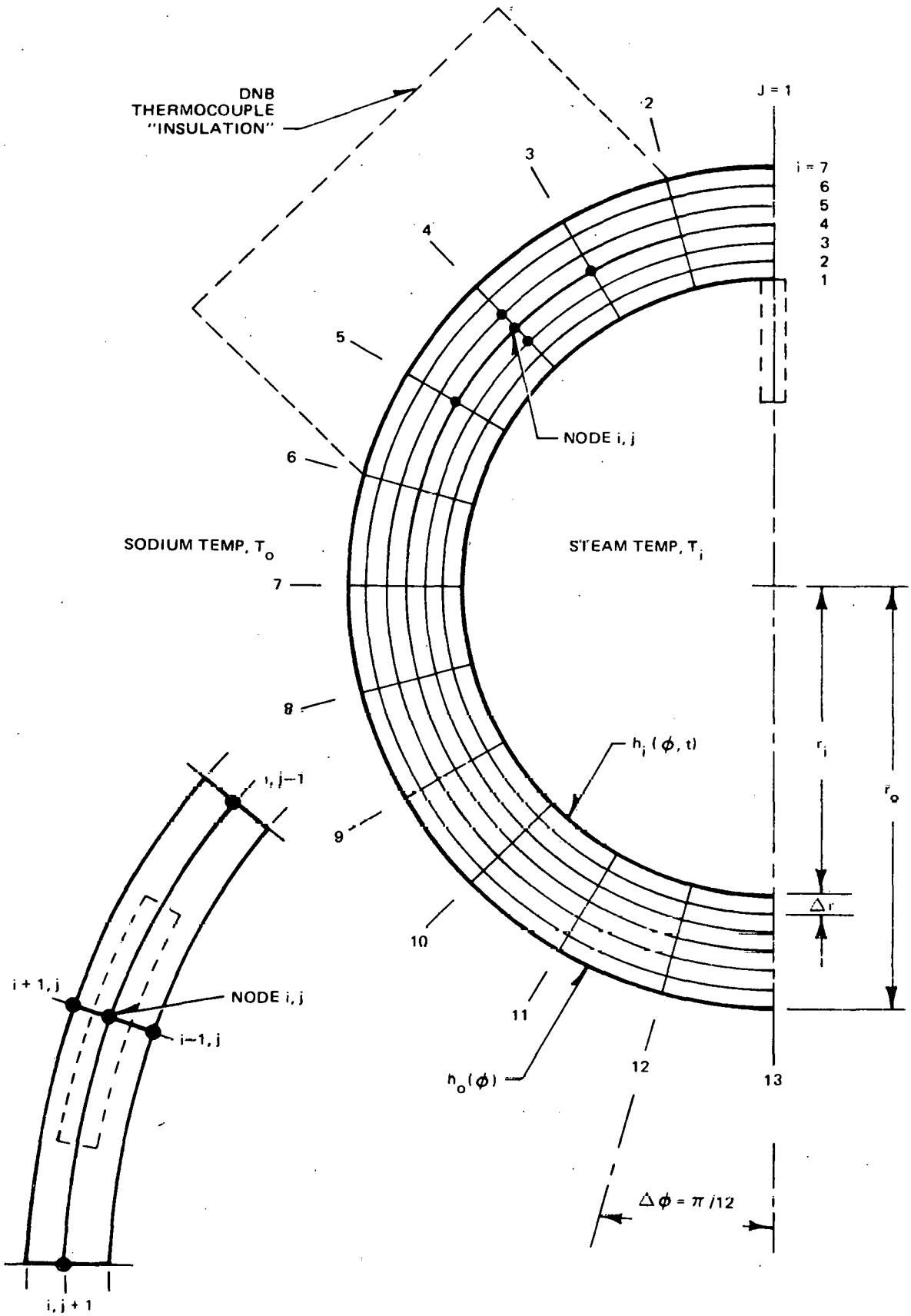

Figure C-1. Computer Model Used in the Transient Heater Tube Wall Analysis

Following the approach taken in Reference 44, the finite difference approximation of the heat conduction problem at node ij (see the enlarged sketch of node ij in Figure C-1) is

$$T_{ij}^{1} = M_r \left(1 + \frac{\Delta r}{2r}\right) T_{i+1,j} + \left(1 - \frac{\Delta r}{2r}\right) T_{i-1,j} + M_\phi \left(T_{i,j+1} + T_{i,j-1}\right) + \left(1 - 2M_r - 2M_\phi\right) T_{ij} \tag{C-9}$$

where

$$M_r = \alpha \ \Delta t/(\Delta r)^2 \tag{C-10}$$

$$M_\phi = \alpha \ \Delta t/(r\Delta\phi)^2 \tag{C-11}$$

For stability of the solution to be assured, the coefficient of the T_{ij} term in Equation C-9 must be $\geqslant 0$. This yields for maximum time step at this node

$$\Delta t \leqslant 1/(2\alpha \ (1/(\Delta r)^2 + 1/(r\Delta\phi)^2) \tag{C-12}$$

The corresponding requirement for a surface node results in smaller time step than this, and the smallest possible time step was used in the analysis to assure stability.

The temperatures of the steam and in the sodium were held fixed at 605°F and 855°F, respectively. The sodium-side heat transfer coefficient was set equal to 4000 Btu/h-ft²-°F for all nodes except nodes j = 3, 4 and 5, where the heat transfer coefficient was taken equal to the effective overall heat transfer coefficient of 2900 derived from the P/D = 6 insert experimental data in subsection 5-4. The validity of this boundary condition was checked against actual temperature measurements by comparing the calculated wall temperature at j = 4 to the temperature reading from the corresponding DNB thermocouple for particular measured outside and inside temperatures and heat transfer coefficients.

The steam-side surface heat transfer coefficient was assumed to vary between a fully nucleate boiling coefficient of ~12000 Btu/h-ft²-°F and a pure film boiling coefficient of 500 Btu/h-ft²-°F. The total inside surface was subjected to this variation according to saw-tooth, sine-wave and square-wave functions over a range of frequencies as described in subsection 5-4. When part of the surface was subjected to this variation while the remainder of the surface was kept at an average value of the limiting heat transfer coefficients mentioned before, the resulting temperature fluctuation was slightly smaller; therefore, the worst condition of variation over the total surface was used in the study.

Due to the DNB thermocouple "insulation," the local heat flux near the j = 4 node is slightly lower than at other angular locations and the magnitude of the wall temperature fluctuation was found to be approximately 7% lower near the j = 4 than at node j = 7. The reported temperature fluctuations are therefore the largest possible.

C-2 SINGLE TUBE STABILITY ANALYSIS

A computer code was used to investigate the cyclic flow oscillations occurring in the bayonet tube steam generator. The oscillations occur when the steam in the upper cootion of the annulus becomes superheated. When the superheat becomes high enough, boiling may start in the bayonet tube. The resulting accelerating two-phase flow in the bayonet tube will decrease the head and increase the friction pressure drop, which results in decreasing flow. This causes a further increase of the superheat in the annulus, thus higher quality in the bayonet tube and yet lower flow. This is called flow-heat transfer divergence. Flow-heat transfer divergence ends when the vapor region in the bayonet tube expels the liquid downstream before subcooled water rushes through the bayonet tube again.

This explanation of cyclic flow oscillations was verified by using a mathematical model of a single bayonet tube to substantiate flow-heat transfer divergence. The object of the code was to prove that, for amounts of superheat in the annulus sufficiently in excess of saturation temperature, boiling occurs in the bayonet tube. The code would show that the resulting two-phase flow friction pressure drop decreases the flow rate, which further increases the heat transfer per unit mass rate, continuing increases in void fraction and friction pressure drop (i.e., flow-heat transfer divergence).

The bayonet tube is a vertical tube approximately 590 in. in length with an i.d. of 0.501 in. and an o.d. of 0.625 in. Details of the bayonet tube and the insulation used in the upper portion are shown in Table 4-1 and in Figure 4-9.

Fluid conditions corresponding to stability run number 1 given in Table B-8-1 were selected for investigation. Heat transfer coefficients used were 280 Btu/h-ft²-°F in the insulated section and 1000 Btu/h-ft²-°F in the single wall tube region. The uniform tube wall temperature at the beginning of the simulation was 608°F (boundary condition number 1, Figure C-2). The superheat profile increased this temperature by 200°F over the upper portion (Figure C-2, BC 2). The slip ratio for homogeneous flow was 1.5 and the pipe friction factor was 0.02. The code assumes that the tube walls have no heat capacity. Since the code uses a macro-slip model, flow regime oscillations are precluded. Enthalpy is treated as a function of temperature only. Fluid properties were calculated at a reference pressure and considered constant.

The fundamental equations of the code, conservation of mass, momentum, and energy, were adapted from the finite difference linearization approximation used by Meyer and Rose[40] and will not be repeated here.

Void fraction, effective slip flow density, and the friction pressure drop relations were also the same as those used in Reference 40.

The criterion for choosing the time step size was stability. Stability of the basic energy equation was established by standard methods. The solution of the bayonet tube temperature profile, etc., was found by first finding the effective slip flow density for each node using qualities and void fractions of the previous time step. This density value and the heat flux resulting from the temperature difference of last step's fluid temperature profile and the imposed tube wall temperatural profile yield the nodal enthalpy. Nodal quality, void fraction, and temperature are calculated from this enthalpy value. Each node's local flux correction factor, or density change, is calculated from the new void fractions.

The previous time step's flow resistance is then used to find the current time step's mass flow rate. An integration of the local flux correction factors is applied to the average mass flow rate yielding the mass flux rate at the inlet. The succeeding mass flux rates are calculated by applying the local flux correction factor in sequence. The friction pressure drop and the elevation pressure drop per node are calculated using the new nodal mass flux rates and the present nodal void fraction. The sum of the friction and elevation pressure drops is the flow resistance. Now, the necessary quantities are known to start the next time step.

The simulation was started by making initial estimates of mass flow rate, enthalpy, etc., for each node. These values plus the inlet enthalpy and uniform tube wall temperature allowed the simulation to reach steady-state in 10 sec. Then, the superheated profile given by BC 2 in Figure C-2 was imposed on the system. The flow decreased as the driving force decreased (Figure 7-33), showing flow-heat transfer divergence. The program was terminated when flow reached approximately 50% of the steady-state value.

C-3 DNB CORRELATION FACTOR

The multiplier used to correlate the DNB data as discussed in Section 5 and given by Equation 5-15 is:

$$C = (D_H/D_O)^{0.7} \, (G/G_O)^{0.45}/(1 + A_R)^{0.25} \qquad \textbf{(5-15)}$$

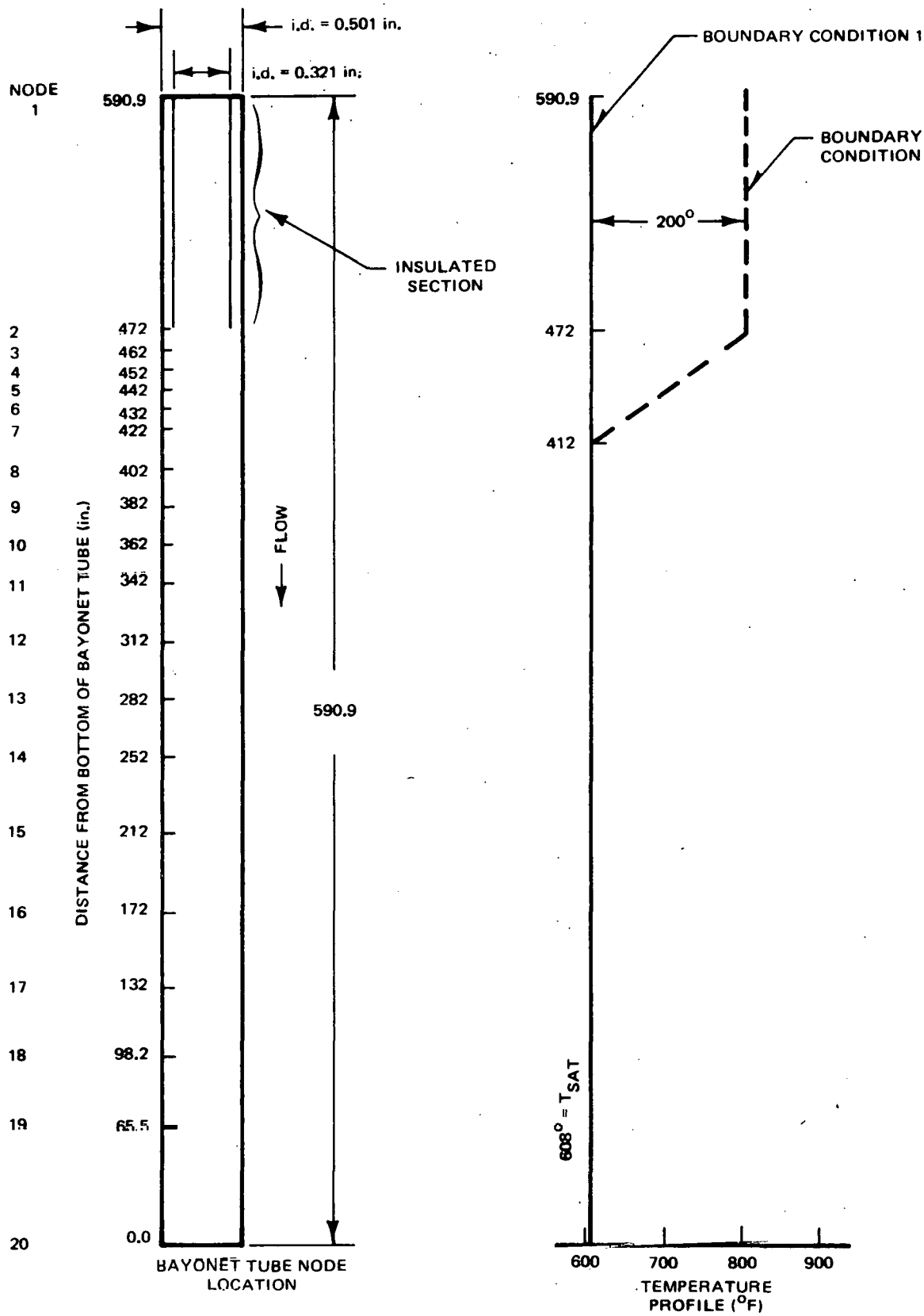

Figure C-2. Computer Model Used in the Single Tube Stability Analysis

A parameter of interest in the analysis of the experimental boiling data is the radial acceleration, A_R in Equation 5-15, developed by the insert in two-phase flow in the thin liquid film at the tube wall. An expression for this radial acceleration, expressed as a multiple of the standard gravitational acceleration g, was obtained in Reference 37. It was assumed that the liquid fraction in the two-phase flow occupied a negligible fraction of the flow area.

The radial acceleration is then given by:

$$A_R = (XG/\rho_g S \Pi D/P)^2 \; 2/Dg \qquad \textbf{(C-1)}$$

Equation 5-15 was evaluated for P/D ratios of 6 and 3 using Equation C-1 when the slip ratio S of the high-pressure two-phase mixture was approximated by:

$$S = (\rho_f/\rho_g)^{1/2} \qquad \textbf{(C-2)}$$

The results are shown in Figures C-3 and C-4 for difference mass flow rates. These curves are convenient when applying the DNB design limit given by Equation 5-17.

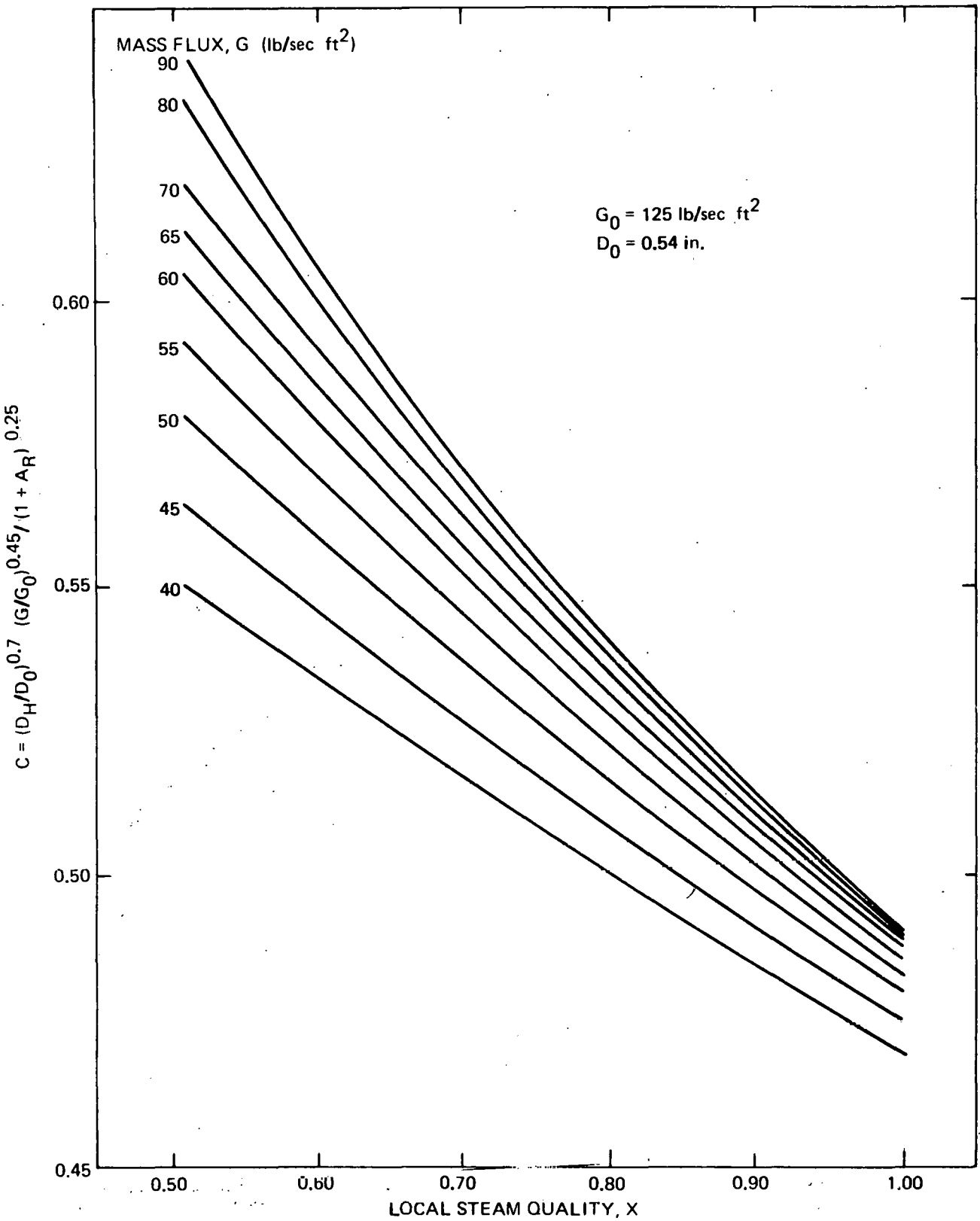

Figure C–3. Multiplication Factor in the DNB Correlation for the P/D = 6 Insert

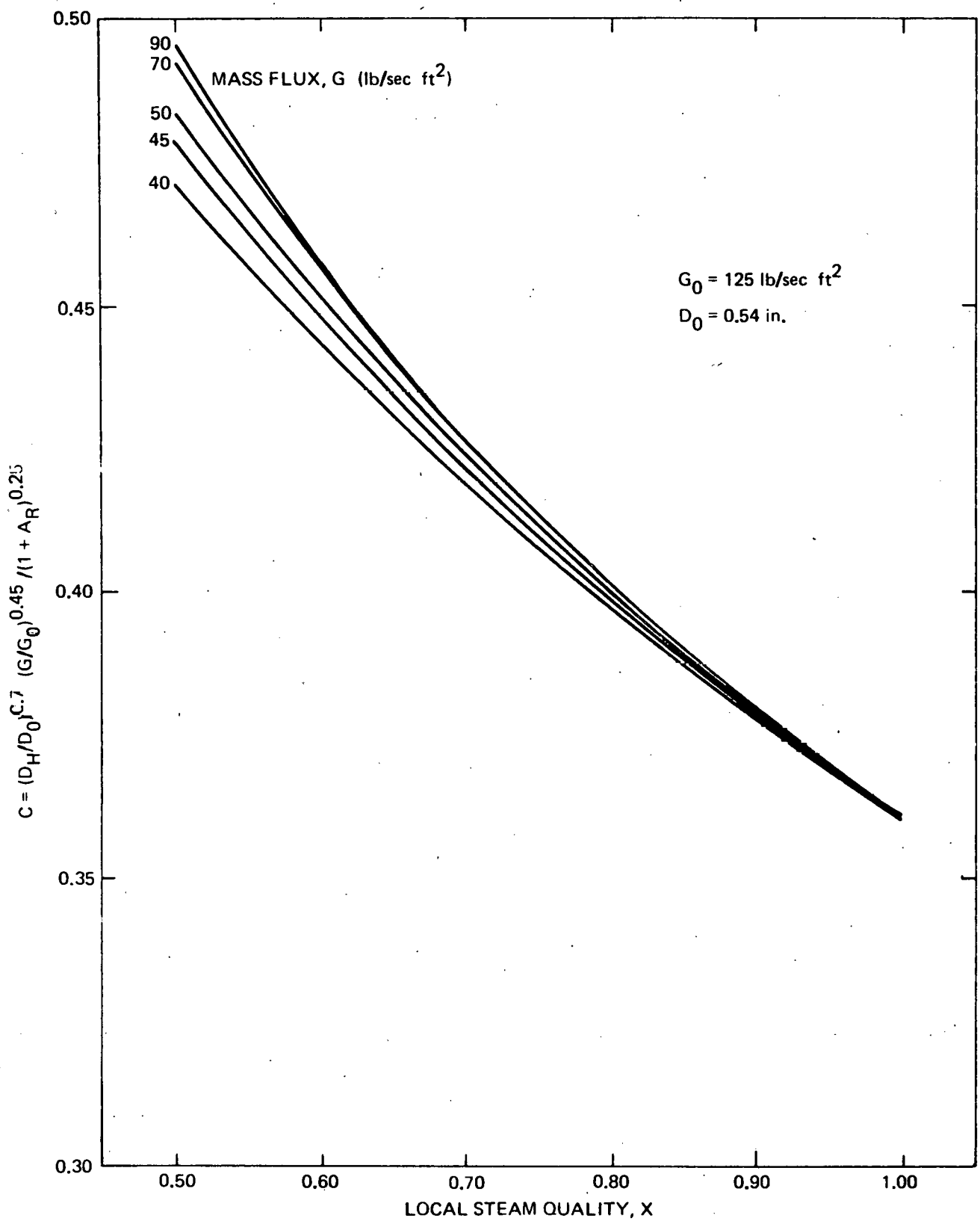

Figure C–4. Multiplication Factor in the DNB Correlation for the P/D = 3 Insert

DISTRIBUTION

Director, Contracts Division U. S. Atomic Energy Commission San Francisco Operations Office 2111 Bancroft Way Berkeley, California 94704	1
RDT Site Office U. S. Atomic Energy Commission General Electric Company 310 DeGuigne Drive Sunnyvale, California 94086	1
Division of Reactor Development and Technology, Headquarters U. S. Atomic Energy Commission Washington, D. C. 20545 Attn: Director	2
Division of Technical Information Extension U. S. Atomic Energy Commission P. O. Box 62 Oak Ridge, Tennessee 37831	204

BREEDER REACTOR DEPARTMENT
SUNNYVALE, CALIFORNIA 94086

Expanding the World's Energy Reserves

GENERAL ELECTRIC